INVESTIGATION OF TWO-PHASE FLOW DURING LIQUID DISPLACEMENT IN MICROCHANNELS: EXPERIMENTS AND CFD SIMULATIONS

by

YU LU

A thesis submitted to
The University of Birmingham
for the degree of
DOCTOR OF PHILOSOPHY

School of Chemical Engineering
The University of Birmingham
United Kingdom
May 2018

Abstract

Microfluidic systems, where sub-millimetre channels are used, attract attention because the benefit they offer such as very high surface area to volume ratio, very limited consumption of materials and the precise control of the flow features or droplets formation. However, the study of pressure-driven displacement flows, which have applications in the coating of channels, oil recovery and channel cleaning, has not been systematically explored in these systems. This thesis presents a study of the behaviour of liquid-liquid two-phase flows in microchannel during the displacement of one liquid by another, i.e. when a pre-filled liquid is displaced by the injection of the second liquid.

Liquid displacement using immiscible (silicone oil and water or glycerol solutions) and miscible fluid pairs (water or glycerol solutions) were carried out. The kinematic viscosities of the fluids used range from 1 to 100 cSt. Three types of straight channel and a T-junction channel, with various channel sizes ranging from 100 to 200 μm, were tested. The visualisation of flows was realised by using a water-soluble dye, a microscope and a high-speed camera. The flow activities at the interface between the two fluids were mainly investigated, such as the study of the liquid film thickness left on wall after the advancing of the displacing fluid and the occurrence of different types of unstable flow regime. Three regimes were identified (stable, axisymmetric unstable and asymmetric unstable for immiscible fluid pairs; stable, wavy unstable and completely unstable for miscible fluid pairs) and their occurrence was illustrated via flow pattern maps of capillary number vs viscosity ratio (immiscible) or Reynolds number vs viscosity ratio (miscible). The addition of surfactants (sodium dodecyl sulfate, SDS, and Polyether modified Polysiloxane, PmP) in the displacing fluid was also studied. The surfactants were found to bring a thinning effect on the thickness of liquid film on the wall due to the

dynamic interfacial tension effects and the circulatory flows near fluid tip. The occurrence of unstable flows is not affected by the addition of surfactant if the alteration of interfacial tension has been taken into consideration. Within the fluids used in this study, the viscosity ratio between the displaced and displacing was found to not affect the film thickness left on the wall, but it did influence the appearance of interfacial instabilities. A microchannel with hydrophobic wall was also tested. It was shown to affect the occurrence of unstable flow patterns but not the film thickness. In the T-junction channel, an increase of film thickness was found after the displacing fluid passing through the junction. It was also noticed that the addition of SDS in the displacing fluid did not bring additional effects on the film thickness apart from the change in interfacial tension in T-junction channel experiments, because equilibrium interfacial tension was achieved within the timescale of the experiments.

CFD simulations are applied largely in the study of fluid mechanics with the ability to confidently predict flow behaviour from computational methods being the ultimate goal. In this study, the experimental results were used to validate CFD simulations carried out using the Fluent package incorporating the multi-phase Volume of Fluid (VoF) model. Good agreement between simulation and experiment results was achieved both qualitatively and quantitatively. Additional information of the flow features, which were not observable in the experiments, were provided from simulation results.

Acknowledgements

First and foremost, I would like to thank my supervisor Professor Mark Simmons. He is such a kind, knowledgeable and insightful person, without his constant support and valuable guidance, I would never be able to achieve this much.

I would like to thank the School of Chemical Engineering at University of Birmingham and the EPSRC "MEMPHIS" grant (EP/K003976/1) for supporting my PhD studentship. I appreciate the inspiring researches carried out in the "MEMPHIS" project.

I would like to thank Dr. Nina Kovalchuk, Dr. Federico Alberini, Dr. Emilia Nowak and Dr. Zhizhao Che who provided important help and suggestions at different stages of my research.

Last but not least I would like to thank the support from my parents and my girlfriend Hongya, who certainly made my PhD journey more enjoyable.

Table of contents

List of Tables

List of Figures

Nomenclature

A	A constant associated with calculating surfactant's CMC
A_2	Cross-section area of fluid 2
A_c	Cross-section area of channel
At	Atwood number
a	Apparent film thickness on the wall
a_{tran}	Width of the transitional regime
a_{mean}	Mean film thickness
$a_{diagonal}$	Film thickness at diagonal
B	A constant associated with calculating surfactant's CMC
Bo	Bond number
C	A constant associated with the correlation factor of Du Noüy Ring method.
c	Surfactant concentration
Ca	Capillary number
Ca'	Modified capillary number
Ca_2	Capillary number based on the velocity and viscosity of fluid 2
D	Characteristic length of channel
D_H	Hydraulic diameter of channel
F	Vertical force applied on plate or ring when measuring surface tension
F_g	Gravitational parameter
Fr	Froude number
fc	Correction factor when calculating surface tension using the Du Noüy Ring method
G_G	Gas mass velocity for two-phase pipe flows
G_L	Liquid mass velocity for two-phase pipe flows

g	Gravity acceleration
H	Channel height
I_{st}	Instability number
k_{wor}	Permeability to water at residual oil saturation
LA	Laplace constant for determining microchannels
L	Width of the Wilhelmy plate
L_e	Entrance length
M	Endpoint mobility ratio
m	Percentage of liquid layer left on wall
Ng	Gravitational number
n	The number of carbon atoms in the tail of surfactant molecule
P	Perimeter of the cross-section of channel
P_2	Perimeter of the cross-section of fluid 2
P_c	Surfactant packing parameter
Pe	Peclet number
P_{max}	Maximum pull of the ring, Du Noüy Ring method.
p	Pressure
Q_2	Injection flowrate of fluid 2
R	Radius of the ring, Du Noüy Ring method.
Ra	Surface Roughness
R_C	Radius of channel
Re	Reynolds number
Re_2	Reynolds number using properties of fluid 2
R_S	Dimensionless radius of interface
r	A constant associated with calculating surface tension at certain temperature
r_t	Radius of Fluid 2 tip curvature

r_w	Radius of the wire of the ring, Du Noüy Ring method.
T	Temperature
T_0	Critical temperature of material
T_K	Krafft temperature for surfactant
t	Thickness of the Wilhelmy plate
t_B	Bubbling time of maximum bubble pressure method
t_L	Lifetime of maximum bubble pressure method
t_D	Deadtime of maximum bubble pressure method
U_G, U_L	Superficial velocity for gas and liquid
u	Mean velocity of flow
$u_2(')$	(Modified) fluid 2 velocity
u_{tip}	Tip velocity

Greek

α	Aspect ratio of rectangular channel
β	Channel inclination angle from vertical
Γ	Surface excess from Gibbs equation
γ	Surface tension of a fluid
γ_0	Surface tension without surfactant
γ_s	Equilibrium surface tension
γ_{st}	Surface tension with surfactant at surface age t
γ_{t0}	Surface tension at temperature 0 K

λ	A parameter associated with the density value of gas and liquid in two-phase pipe flows
ν	Kinematic viscosity of fluid
$\Delta\rho$	Density difference
θ_w	Contact angle of heavy liquid on the container wall, Wilhelmy plate method
μ_2	Dynamic viscosity of Fluid 2
ρ_2	Density of Fluid 2
σ	Interfacial tension between two fluids
σ_0	Interfacial tension without surfactant
σ_s	Equilibrium interfacial tension
σ_{st}	Interfacial tension with surfactant at surface age t
Φ	A constant associated with the estimation of interfacial tension
ψ	A parameter associated with the density and viscosity values of liquid in two-phase pipe flows

Chapter 1 INTRODUCTION AND MOTIVATION

Microfluidics handle very small amount of liquids (10^{-9} to 10^{-10} L) in systems with typical dimensions of tens to hundreds of micrometres (Whitesides, 2006). It is a rapid expanding research area because of the benefits offered compared with large scale apparatus, such as low material consumption, short observation time, high surface area to volume ratio, as well as its various potential practical applications. The relatively easy and precise control and the manipulation of multiphase flows is one of the most important advantages that microfluidics provides. This was realised in the earliest developments of the field and a great number of researches have been conducted using microfluidics to fulfil flow separation (Pamme (2007), Yamada, et al. (2004) and Huh, et al. (2007)), the generation of complex droplets (Thorsen, et al. (2002), Okushima, et al. (2004) and Atencia and Beebe (2005)), chemical reaction (Kobayashi, et al. (2004) and Shestopalov, et al. (2004)) or biological studies (Sia and Whitesides, 2003).

Fluid displacement, which commonly refers to the pressure-driven displacement of one fluid by another in various types of ducts, pipes or channels, attracts research interests due to its important application in industries such as for transport of crude oil, oil recovery, food-processing, channel cleaning, coating, as well as flow of magma inside the earth. (Redapangu, et al., 2012). It is well known that the instability presents itself when the displacing fluid is less viscous than the displaced one and this leads to the reduction of displacing efficiency because unfavourable mobility profile at the front of the displacing fluid (Petitjeans and Maxworthy, 1996). The very first study on the instability is believed to be done by Yih (1967), who numerically studied planar flow, and pipe flows were first studied by Hickox (1971). Balasubramaniam, et al. (2005) examined the instability during displacement of miscible fluids

in a vertical cylindrical tube and they observed the interface to be a sinuous shape for downward displacement and a spike shape for upward displacement.

The presence of surfactant, which alters surface or interfacial tension and in some cases, provides dynamic surface/interfacial tension effects, is important in the researches of immiscible multiphase flows because of the applications such as oil recovery and formulated liquid product manufacture. Previously the effects of surfactant on bubbles (Olgac and Muradoglu (2013), Ratulowski and Chang (1990)) and core flooding experiments (Skauge, et al. (1992) and Wang, et al. (2013)) have been investigated which is highly related to oil recovery applications. For the problem of fluid displacement, which a time-dependent problem, where the dynamics at the interfaces between phases are more of interest, the effects of surfactant are not yet thoroughly explored.

The ultimate aim of any fluid mechanics project is to develop the physics and modelling framework such that any experimentation can be carried out *in silico* with absolute confidence. Computational Fluid Dynamics (CFD) is an effective and important tool fluid mechanics research, yet further developments are needed to fully elucidate the physical impact of surfactants in interface tracking models and in multiphase flows involving deformable interfaces in general. Within the scope of this project, the commercial CFD package Fluent will be used to determine the capabilities and limitations of the current framework.

1.1 Aims and objectives

This present study is concerned with the study the displacement of a more viscous fluid by a less viscous fluid in microchannels both via experiments and computational simulation. The motivation is to examine how fluid properties such as the viscosity and interfacial tension play a role in the phenomena observed; for the latter fluid pairs which are immiscible, and thus have

a finite interfacial tension, and miscible (where interfacial tension is negligible) are studied and the influence of surface active chemicals (surfactants) are also explored. Since microchannels are manufactured with a range of cross sectional shapes, and also sizes, the effect of changing these parameters is also examined. The aims and objectives of this study are thus to:

1. Determine and classify the flow patterns observed during fluid displacement in straight channels as a function of key parameters (channel geometries, wall conditions, fluid properties and flow conditions) and generate generalised predictive flow regime maps based on the appearance of different types of instabilities.
2. Explore how the interfacial behaviour influences the rate of displacement of the displaced fluid, looking in particular at the shape of the tip of the displacing fluid and the thickness of the residual film left on the channel wall.
3. Explore how the addition of surfactant, and in particular how the effects of dynamic surface tension might influence the physics observed.
4. Produce CFD simulations which are validated by the experimental results as well as providing information that may not be observable in experiments.
5. Examine how the displacement process is influenced by the presence of a bend (i.e. in a T-junction).

1.2 Thesis outline

Chapter 2 reviews the fundamental research work carried out in relevant areas including microfluidics, multiphase flows, surfactants and CFD. Chapter 3 describes the channels, equipment and set-up in the experiments as well as the materials used. Some fluid properties characterisation methods including surface/interfacial tension and dynamic surface tension measurement are also explained. In addition, the computer software used in this study and some

processing procedures carried out using the software are described. Chapter 4 provides and discusses the experimental results using straight microchannels. One purchased and two lab-made microchannels were used for fluid displacement experiments carried out with both immiscible and miscible fluid pairs. Chapter 5 lists the theory and settings used in the CFD simulation of this study, followed by the simulation results using three geometries of microchannels. Quantitative and qualitative comparison between experimental and simulation results are provided. Chapter 6 introduces a junction channel and the two injection modes for fluid displacement experiments using the junction channel. A brief CFD simulation using the cross-section shape of the junction channel but in a straight channel configuration was carried out, to explore the cross-section shape of interface between two fluids in this non-circular channel.

1.3 Publications and presentations arising from this work

Journal papers

Lu, Y., Kovalchuk, N.M., Simmons, M.J.H. Residual film thickness following immiscible fluid displacement in non-circular microchannels at large capillary number, *AIChE J., accepted for publication on 2nd April 2018.*

Conference papers and presentations

Lu, Y., Simmons, M.J.H., Experiment and Computational Simulations of Liquid-Liquid Interfacial Instabilities upon Flow Displacement in Microchannels, International Conference on Multiphase Flow ICMF 2016, 22-27 May, Firenze, Italy.

Lu, Y., Simmons, M.J.H., Experiment and Computational Simulations of Liquid-Liquid Flow Displacement in Microchannels, 68th APS-DFD, Boston, MA, CA November 22-25, 2015.

Lu, Y., Nowak, E., Simmons, M.J.H., Percival, J., Pain, C.G., Influence of surface properties and miscibility upon displacement flow in microchannels, 67th APS-DFD, San Francisco, November 23-25, 2014.

Chapter 2 LITERATURE REVIEW

Introduction

Fundamentals and applications of microfluidics are first reviewed in §2.1, followed by discussions of multi-phase flows in §2.2, including different types of multi-phase flows, flow pattern regimes, flow visualisation and characterisation techniques and specifically more attention is given on fluid displacement, flows at junctions and interfacial instabilities. Surface science principles including surfactant, critical micelle concentration, surface/interfacial tension and their measurement techniques are reviewed in §2.3. Finally, §2.4 discusses Computational Fluid Dynamics (CFD) including fundamental introduction, main solvers and models, current available commercial CFD packages and open source codes and specifically reviews of CFD simulations and numerical studies of fluid displacement.

2.1 Microfluidics

2.1.1 Introduction

Microfluidics attracts both research and practical manufactural interest since the recognition of the outstanding features it provides. Research using devices made with micro-scale mechanics technology origins from around early 1970's (Gravesen, et al., 1993). Traditional materials for fabricating microfluidic devices are silicone, glass, polymer-based and paper-based materials. Various techniques are required for the fabrication of microfluidic devices which are material dependent, including photolithography, thin-film deposition, etching for silicone-based devices and soft lithography, micromoulding, microcontact printing for glass/polymer-based devices (Lei, 2014). Fabrication from silicone or glass provide benefits especially where applications

require high temperature resilience, accurate construction of channels or pores or high aspect ratio structures. High thermal conductivity of silicon is also preferred to provide a uniform temperature distribution (Lliescu, et al., 2012). Lliescu, et al. (2012) provide a practical guide on the choice of microfluidic fabrication processes based on application requirements, shown in Table 2.1. They also provide a detailed summary of the material and fabrication techniques used in each fabrication processes.

Table 2.1 Guide on choosing microfluidic fabrication processes based on application requirements. (Lliescu, et al., 2012)

Step	Selection to be made			Possible processing routes and criteria for their selection (preferred process options are shown in bold)	
				Route A	Route B
1	Materials involved in the microfabrication process			• **Glass/glass** (take this route if the application requires optical transparency of the device)	• **Glass/silicon** (a more common and well established route)
2	Patterning method	Microchannels		• **Wet etching** in HF/HCl • Dry etching (recommended only if vertical walls or high aspect ratio structures are required)	• **Dry etching** of the silicon • For complex microfluidic devices requiring multiple channel layers, the silicon wafer can be patterned on both sides and via holes etched through the wafer to connect them; alternatively, the glass can be patterned (by wet etching) as well as the silicon.
		Through-holes for fluidic ports		• **Wet etching** • **Sand-blasting** • Drilling	• **Dry etching** • Laser-drilling • Sand-blasting
3	Bonding method	No electrical connection	The device operates above ~200 °C	• **Fusion bonding** • Anodic bonding with metallic or a:Si layer	• **Anodic bonding**
			The device operates at or below ~200 °C	• **Adhesive bonding** • Anodic bonding with metallic or a:Si layer • Fusion bonding	• **Anodic bonding** • Adhesive bonding
		With electrical connection	The device operates above ~200 °C	• **Anodic bonding** (the thickness of the metallic layer can be critical) • Bonding using an intermediate layer	• **Anodic bonding** (the thickness of the metallic layer can be critical)
			The device operates at or below ~200 °C	• **Adhesive bonding** • Anodic bonding (the thickness of the metallic layer can be critical)	• **Adhesive bonding** • Anodic bonding (the thickness of the metallic layer can be critical)
4	Fluid connections			• Permanent: push-fit tubing into polymer ports (optionally fix with glue or PDMS) • Permanently attached ferrule with removable capillary tubing (e.g., Nanoport) • Temporary: push-fit capillary tubing into PDMS device (permanent if PDMS is plasma-treated) • Mechanically clamped chip-holder	

2.1.2 Microfluidic research aspects

One of the research disciplines of microfluidics that has drawn a lot attention is micro- or nano-scale flow characterisation, especially for multiphase flows. Microfluidic multiphase flows take the advantages of large surface (interface) areas and short mixing times. Momentum, inertial, viscous and gravity forces are considered to be the traditional characterization parameters in microfluidics. These are represented respectively by dimensionless parameters of Reynolds number ($Re = Du\rho/\mu$), Weber number ($We = \rho u^2 D/\sigma$), capillary number ($Ca = \mu u/\sigma$) and Bond number ($Bo = \Delta\rho g D^2/\sigma$), where ρ, σ, u are the density, surface tension, velocity of fluid and D is the characteristic length (channel diameter). Gunther and Jensen, 2006) produced a comprehensive graph showing the influence of these dimensionless numbers (*We*, *Ca* and *Bo*) with respect to interfacial forces in microfluidic multiphase systems (Figure 2.1). More details about multiphase flow in microfluidic system (microchannels) are discussed in §2.2.2.

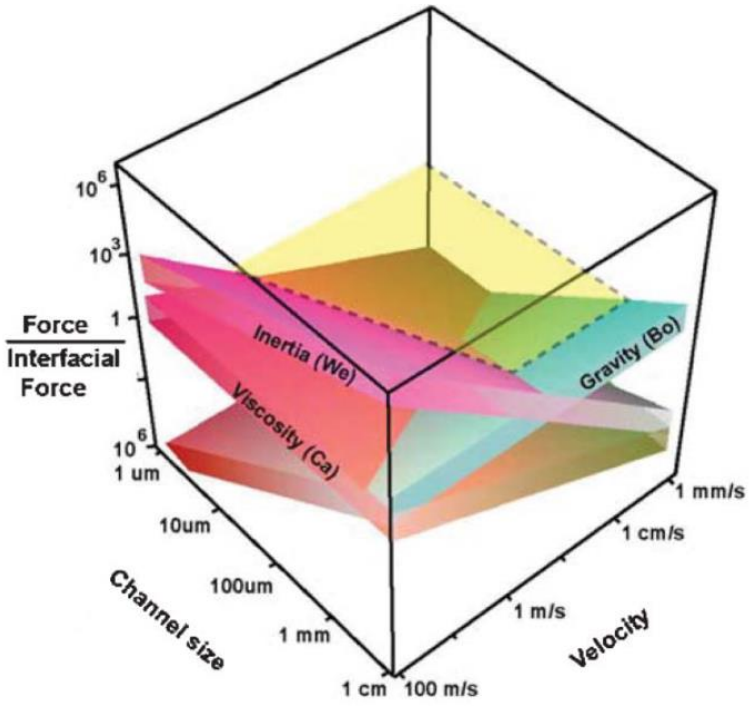

Figure 2.1 The influence of inertial, viscosity and gravity forces with respect to interfacial forces in microfluidic multiphase systems. Image taken from Gunther and Jensen (2006).

Stone et al. (2004) summarised the representing driving forces used in the processes of manipulation flows in microfluidics (Table 2.2).

Table 2.2 External forces and fields used in microfluidic flows manipulation (Stone, et al., 2004).

Driving force	**Subcategorization**
Pressure gradient ∇p	
Capillary effects	Surface tension, γ Thermal Electrical (electrocapillarity)
	Surface tension gradients, $\nabla\gamma$ Chemical Thermal Electrical Optical
Electric fields **E**	DC electro-osmosis AC electro-osmosis Dielectrophoresis
Magnetic field/ Lorentz forces	Magnetohydrodynamic stirring
Rotation	Centrifugal forces
Sound	Acoustic streaming

An important part of microfluidic multiphase flows is continuous flow separation or interface control, especially in the field of bioanalytical chemistry, due to the small volume required and well-developed techniques of fabricating microfluidic devices leading to precise control of flows (Pamme, 2007). Pamme (2007) summarised the subcategories of continuous flow separation microfluidic methods, such as pinched flow fractionation, hydrodynamic filtration, continuous flow filtration and lateral displacement. Teh, et al. (2008) gives a thorough review of drop-focused covering detailed aspects such as droplet generation methods, materials, mixing in droplets, droplet sorting, phase change in droplet and droplet applications. Figure 2.2 depicts the production of functionalised droplets using microfluidic devices. These droplets

generated can be used to transport content, perform chemical reactions, etc. Chemical reactions can be valuable especially for those studies where reagents are very expensive or only available in very small amounts, such as drug delivery and DNA-related analysis. More detailed aspects of multi-phase flows in microchannels are discussed in §2.2.2.

(a)

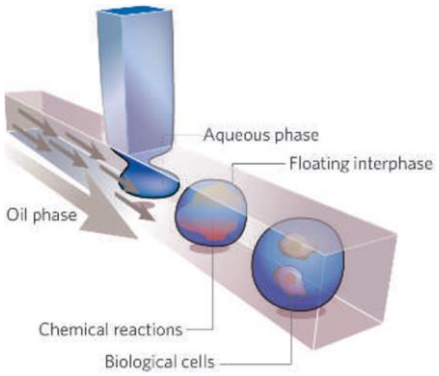

(b) (c)

Figure 2.2 (a) Illustrative image of a microfluidic device for the production of functionalised droplet (Atencia and Beebe, 2005); (b) and (c): A T-junction microfluidic channel used for generating double emulations (Okushima, et al., 2004).

2.2 Multiphase flows

2.2.1 Introduction

The term *multiphase flows* refer to the concept of having more than one phase or component in the flow system of interest. Thus multiphase flows can be loosely classified into categories based upon the number and type phases present in the flow: two-phase flows include liquid/gas

flows, gas/solids flows, liquid/liquid flows and three-phase flows might encompass gas/solid/liquid flows. Different flow patterns can be present based upon the system configuration, orientation and operating conditions (particularly whether the flow of each phase is laminar or turbulent), typically characterised as *separated*, *intermittent*, *continuous* or *dispersed*. For example, the gas phase can be present as a separated phase or bubbles; if the gas bubbles occupy most of the cross section of the channel they can be considered as an intermittent phase, as in *plug* or *slug* flow, if they form a continuous (horizontal) layer then the flow may be *stratified*, or if bubbles are much smaller than the channel diameter, they exist as a dispersed phase in *bubbly* flow. Hybrid regimes are possible such as *annular* flow which is characterised by a continuous fast-moving gas core where the liquid phase is present as a film on the pipe wall and also dispersed as drops-interchange of the liquid between the film and drops is driven by the entrainment of drops from the liquid film due to interfacial shear of the gas and deposition of the drops back into the film.

In liquid-liquid flow, analogous flow regimes exist although in the latter the liquid takes the form of droplets rather than bubbles (Simmons and Azzopardi, 2001). More detail is given of these flow regimes and their relevance to this work in the discussion below. The reason for studying multiphase flows is very obvious as virtually almost all industrial processes encounter multiphase flows problems. Therefore the capability to predict multiphase flow phenomena is of considerable interest from both industrial and academic viewpoints.

2.2.2 Types of Multiphase flows problems

As mentioned above, multiphase flows are generally categorised by the phases and the number of phases involved. The multiphase flows in channels with at least a few centimetres in diameter (gravity effects are considered) are first discussed. Then multiphase flows in microchannels,

which have been studied greatly in recent years due to the differences in flow phenomena observed in channels with diameters smaller than a few millimetres (very little gravity effects) are described. Circular channels are the most studied cross-sectional shape (e.g. pipe) but other geometries such as rectangular channel also attracts some research interest. The problem of fluid displacement, where the channel is pre-filled with a static fluid and the second fluid is injected into the channel, is separately discussed in §2.2.4.

Liquid/gas and liquid/liquid flows in pipe

Considerable research has been carried out studying liquid/gas flows in pipes of different diameters, cross-section shapes, wall roughness and incline angles of pipes, as well as different fluid properties (e.g. liquid viscosity, surface tension and density) and operational conditions, such as Mandhane, et al. (1974), Mcquillan and Whalley (1985), Spedding and Spence (1993), Coleman and Garimella (1999), Ohnuki and Akimoto (2000) and Serizawa, et al. (2002).

Flow patterns describe the geometric appearance of the phases in multi-phase flows, identifying different flow patterns and the conditions under which these patterns take place is the starting point of understanding the mass, momentum and energy transfer of the flows (Brennen, 2005). One of the earliest work of classifying the flow regimes of liquid/gas flows in horizontal pipes was carried out by Hoogendoorn (1959), who concluded five flow patterns for horizontal pipe: *plug flow*, the presence of gas bubbles of plugs in pipe with thicker liquid layer at the lower part of pipe than the upper part; *Stratified flow*, complete separation of liquid and gas with gas flows at the top of smooth liquid surface; *wavy flow*, the presence of waves at the liquid surface when gas velocity is increased; *slug flow* (or *plug flow*), the presence of large liquid surface fluctuation represented by liquid touching the upper pipe; *annular flow*, gas flows at the core along the pipe leaving an annular liquid layer and *froth flow*, the presence of gas bubbles dispersed in liquid phase. Later works suggest an addition pattern of *bubble flow* (or *bubbly*

flow) and the froth flow is more often referred as *dispersed flow*. Figure 2.3 shows the schematics of the flow patterns mentioned above. In particular, the large bubbles in the slug (plug) flow are referred as Taylor bubbles, which have attracted significant interest since Taylor's seminal paper in 1961 (Taylor, 1961).

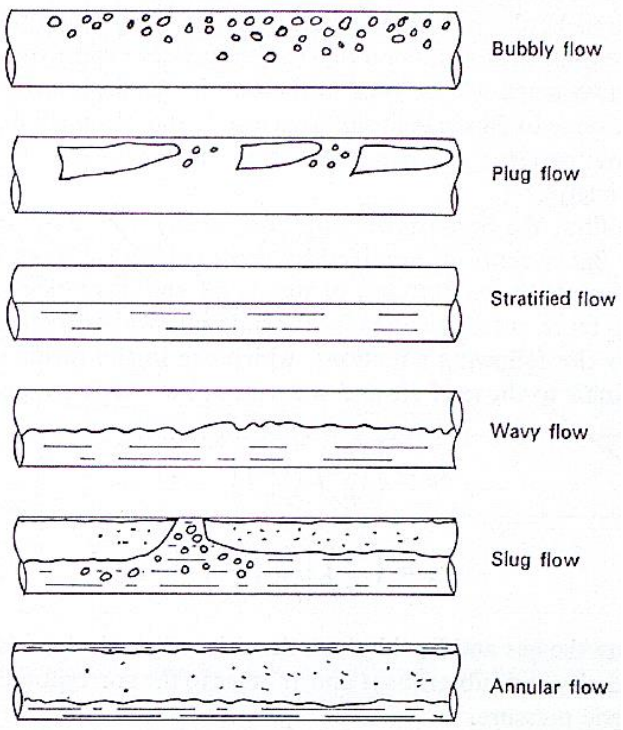

Figure 2.3 Flow patterns of liquid/gas flows in horizontal pipe (Hewitt and Hall-Taylor, 1970).

Flow regime maps are widely used to reflect the existence of flow patterns on a graph with the axes representing the fluid properties of two phases so the boundaries of each regimes can be marked. The flow regime maps for different pipes and different fluids are different when simple dimensional axes are used, numerous studies have been carried out to produce generalised flow regime maps that are valid over a range of conditions. Various fluid properties or modified parameters are used to plot flow regime maps such as the G_G/λ and $G_L\lambda\psi/G_G$ used by Baker (1954), where G_G and G_L are the superficial mass velocities for gas and liquid, λ and ψ are two

parameters based on the physical properties of liquid and gas; the mixture velocity-gas percentage coordinates system used by Hoogendoorn (1959); the liquid and gas mass velocity system used by Govier and Omer (1962) and Weisman, et al. (1979); the superficial momentum flux of liquid and gas system used by Hewitt and Roberts (1969); the superficial liquid and gas velocity system used by Mandhane, et al. (1974). Figure 2.4 is an example of flow regime map in horizontal pipe produced by Weisman, et al. (1979). Different flow patterns are marked and put into flow regimes. The grey areas in the graph are the transition regions where flow patterns were hard to categorised into either side of the regimes or the patterns were unreproducible.

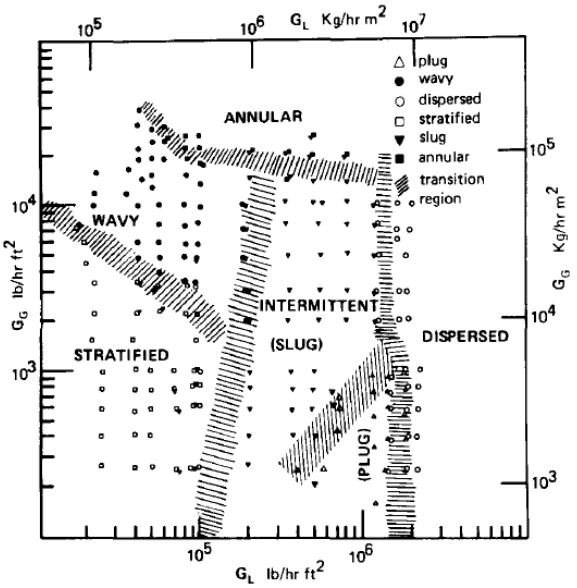

Figure 2.4 Flow regime map for liquid/gas flows in a 5.1 cm horizontal pipe, the liquid is 150 cp glycerol solution. (Weisman, et al., 1979).

The flow patterns in a heated horizontal pipe is a special case of the liquid/gas two-phase flow due to the generation of vapour. Figure 2.5 is a schematic sketch of the two-phase flow in a heated horizontal pipe with a relatively low inlet velocity (< 1 m s^{-1}) and the asymmetric nature of the flows in this type of pipe is weakened at higher inlet velocity.

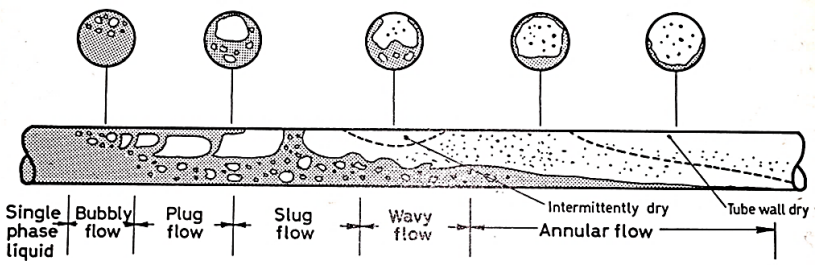

Figure 2.5 Flow patterns in a heated horizontal pipe (Collier, 1981).

In terms of liquid/gas flows in vertical pipes. Figure 2.6 illustrates the four flow patterns for upwards flows: *bubbly flow*, the presence of discrete gas bubbles in liquid body; *slug flow (or plug flow)*, the presence of large bubbles, which is termed as Taylor bubbles, with nearly the same width as the diameter of channel; *churn flow*, the complete destruction of the slug flow, and *annular flow*, the phenomena of a liquid layer on the pipe wall with a stream mainly of gas flows in the centreline of pipe (Hewitt and Hall-Taylor, 1970). Depending on the form of entrained water droplets, the term *wispy-annular flow* is sometimes used to represent the existence of irregular wisps of large agglomerated liquid droplets, in comparison to the separated small entrained liquid droplets in annular flow. Hewitt and Hall-Taylor (1970) also suggest that for downwards vertical flows, bubbly flow and annular flow are possible with slug flow occurring at high liquid flow rates.

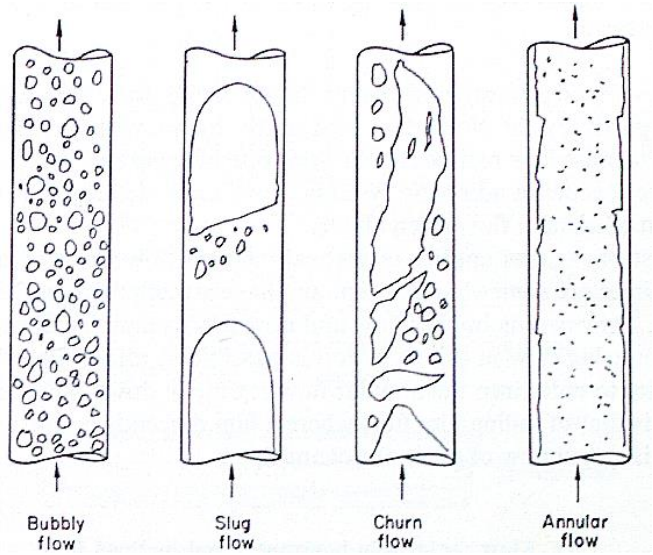

Figure 2.6 Flow patterns of liquid/gas flows in vertical pipe (upwards flow) (Hewitt and Hall-Taylor, 1970).

One of the early attempts to systematically develop numerical models to predict flow regimes is the work carried out by Taitel, et al. (1980). In addition, experimental work has also been done in order to compare theoretical flow regime transitions, where good agreement was achieved (see Figure 2.7a). Prediction of flow regimes has focused on the analysis of transition regions between two defined flow patterns. Early researches include Radovcich and Moissis (1962) and Griffith and Snyder (1964), who both studied the transition from bubbly flow to slug flow. Figure 2.7b shows the flow regime maps in pipe with relatively small inner diameter (4.08 mm) developed from the experimental results from Mishima and Hibiki (1996) as well as two numerical prediction of the regime boundaries.

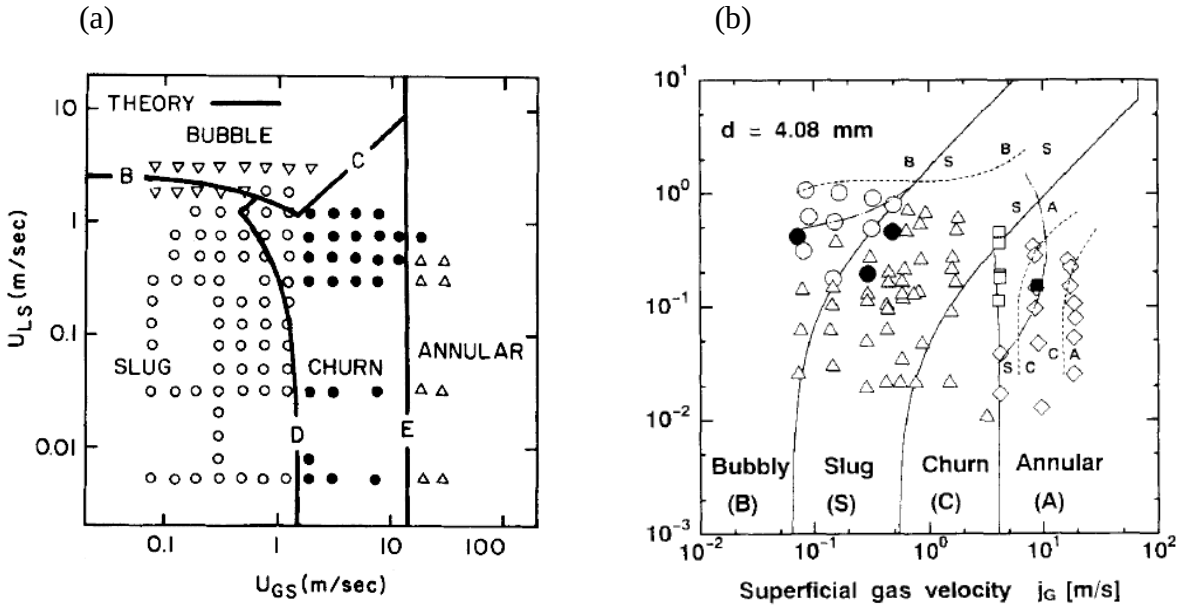

Figure 2.7 (a) Flow regime map for upwards vertical flows in a 2.5 cm pipe, both experimental (symbols) and theoretical predictions (lines) are shown (Taitel, et al., 1980). (b) Flow regime map in a vertical pipe of 4.08 mm inner diameter with symbols are experimental results from Mishima and Hibiki (1996), the solid lines are the regime boundaries predicted using the criteria of Mishama and Ishii (1984) and the dashed lines are the regime boundaries predicted by Barnea, et al. (1983).

Taitel, et al. (1980) explained the mechanism of the transition from bubbly to slug flow as the coalescence and agglomeration of dispersed bubbles to form Taylor-type bubbles when the gas flow rate is increased. Bubble void fraction is used as the key parameter to determine this transition. Generally the void fraction for this transition is considered to be 0.25 to 0.3 (Griffith and Snyder, 1964). This value has also been estimated by only considering the physical geometry of the packing of small bubbles, by assuming all bubbles in the bubbly flow are uniform spheres and coalescence starts to take place rapidly when the space between two bubbles is less than a certain threshold. This threshold is considered to be half the bubble radius by Taitel, et al. (1980) or the bubble diameter by Mishama and Ishii (1984). For the slug to churn flow transition, the liquid slug between two consecutive Taylor bubbles is not long enough to stay stable to separate two Taylor bubbles and oscillatory movement is observed for

the liquid film around and between Taylor bubbles (Taitel, et al., 1980). The length of the slug between two Taylor bubbles is used as an indicator of this transition in numerical studies and Taitel, et al. (1980) stated that a stable slug requires a minimum slug length to pipe diameter ratio of 16 and they have also provided a correlation of calculating the entry length for churn flow. Woods and Hanratty (1996) considered the condition for a stable slug in horizontal flow based upon a mass balance of fluid uptake into the liquid slug, versus the liquid shedding from the rear, a modification of the earlier work of Dukler and Hubbard (1975).

For the churn-annular flow transition, a commonly accepted way to predict this regime is by looking at the entrained liquid droplets being carried by the upwards flowing gas. Thus the minimum gas flowrate (or velocity) needed to suspend liquid droplets are calculated from the force balance of gravity and drag on the droplet.

Similar to the horizontal case, the flow patterns in a heated vertical pipe is a special case of the liquid/gas two-phase flows. More than one flow regimes are presented in a heated pipe. Figure 2.8 is an illustrative graph of the flow patterns take place in a heated pipe (Collier, 1981). The changes of flow patterns are due to the deviation of thermodynamic equilibrium state because of the presence of radial temperature profiles. In this case, if the change of local flow conditions is larger or smaller, the regions of some certain flow patterns may appear to be enlarged or shortened (or completely disappeared). Collier (1981) states that the slug flow pattern in a heated pipe would normally only exists in a long pipe and may not been observed at all in short pipes.

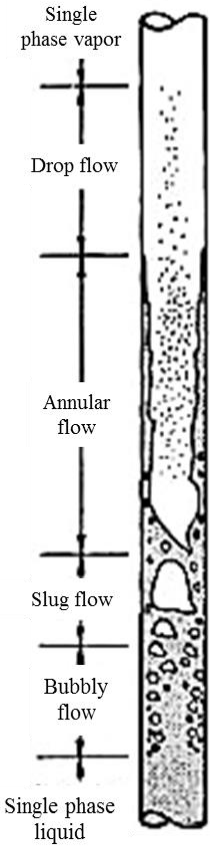

Figure 2.8 Flow Patterns in a vertical heated channel (Collier, 1981).

Liquid/solid and gas/solid flows

These two types of two-phase flows generally refer to the flows that a bulk liquid or gas continuous phase carrying dispersed solid particles. The term *Particle-laden flows* is used to describe these types of flows. Sometimes solid particles are purposely introduced in flow systems as the tracing media to reflect to motion of the bulk fluid such as the Particle Image Velocimetry (PIV) technique, which typically applies particles with 1 to 100 μm in diameter, and the novel Ghost Particle Velocimetry (Buzzaccaro, et al., 2013), in which nanoparticles are used.

Based on the interactions between particles, three categories of particle-laden flows are defined: collision-free flow (dilute phase flow); collision-dominated flow (medium concentration flow) and contract-dominated flow (dense phase flow) (Tsuji, 2000).

Multiphase flows in microchannels

As mentioned above, multiphase flows are greatly studied in microfluidic systems. Unlike conventional two-phase flows described above that applies to pipes with diameters of at least a few centimetres, two-phase flows in channels with diameters of the orders of millimetre or micrometre attract researchers' attention because the lack of the effects of gravity and the increased effects of wall conditions, interfacial and surface properties of fluids. Due to the diameter constraint, the flows observed are generally laminar in nature, with the Reynolds number, Re < O(10). To classify a channel as "microchannel", several criteria have been proposed. The Laplace constant, which represents the ratio of surface tension and gravity forces: $La = \sqrt{\frac{\gamma}{g\Delta\rho}}$ (Serizawa, et al., 2002), to be larger than D_H, which is the hydraulic diameter of channel; or Eotvös number (also referred as Bond number *Bo*), $Eo = \frac{g\Delta\rho D^2}{\gamma}$ (Brauner and Maron, 1992), to be smaller than $(2\pi)^2$ or the confinement number $Co = \frac{LA}{D_H}$ (Kew and Cornwall, 1997), to be greater than 0.5 are recommended for microchannel effects, such as negligible gravity effects, to present.

Figure 2.9 shows the flow pattern regimes observed by Serizawa, et al. (2002) in 25 μm silica and 100 μm quartz microchannels. Four flow regimes are noted for the 25 μm channel: bubbly flow, slug flow, liquid ring flow and liquid lump flow. Five flow regimes are noted for the 100

μm channel: bubbly flow, slug flow with liquid droplets on wall, liquid ring flow, liquid lump flow and droplet flow.

(a)

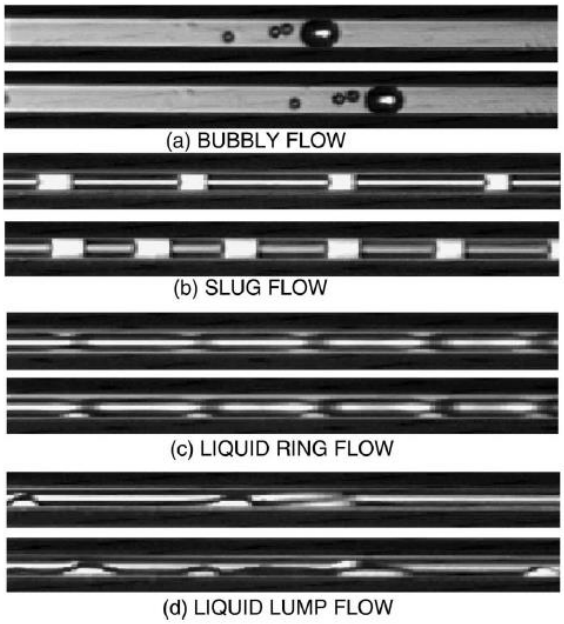

(b)

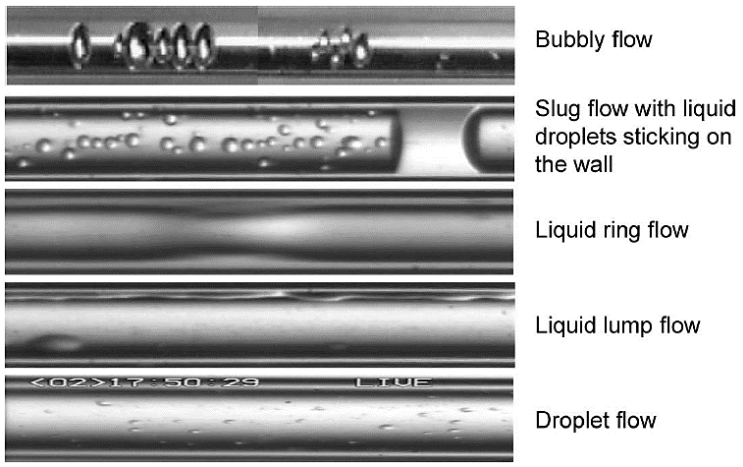

Figure 2.9 Liquid/gas flow pattern regimes observed in (a) 25 μm silica channel and (b) 100 μm quartz channel (Serizawa, et al., 2002)

Han, et al. (2015) studied specifically annular flow (total mass flux from 100 to 500 kg $m^{-2}s^{-1}$) in microchannels of 0.3, 0.5 and 1.0 mm. They observed three flow patterns: annular-ring, annular-ripple and annular-wavy flow. A correlation of film thickness was developed and compared with experimental data, measure by laser focus displacement meter:

$$\frac{\mathrm{a}}{R_C} = 1 - \frac{f_G}{f_L} \bullet \frac{\rho_G U_G^2}{\rho_L U_L^2} \qquad \text{(Equation 2.1)}$$

Where a is the film thickness, R_C is channel radius, U_G and U_L are the superficial velocity for gas and liquid, f_G/f_L is the ratio of friction factors for gas and liquid phase:

$$\frac{f_G}{f_L} = \begin{cases} 0.228\left(\frac{\mathrm{Re}_L^{1.39}}{\mathrm{Re}_G^{0.69}}\right) & \text{(Laminar gas flow)} \\ 0.0548\left(\frac{\mathrm{Re}_L^{1.39}}{\mathrm{Re}_G^{0.47}}\right) & \text{(Turbulent gas flow)} \end{cases} \qquad \text{(Equation 2.2)}$$

Flow regime maps of liquid/gas flows are also developed by a number of studies, however because of the different diameter and material of channels used, the variation of flow regime pattern headings, these flow regime maps show relatively large variations in terms of the transition of flow regimes. For example liquid/gas flows experiments carried out in a 100 μm horizontal channel Kawahara, et al. (2002) did not observe the bubbly flow regime as Serizawa, et al. (2002) suggested. Therefore Hassan, et al. (2005) developed a universal flow regime map for liquid/gas flow in microchannels with diameter less than 1 mm, shown in Figure 2.10. They characterise flow regimes according to two main categories and the transition between these two: the surface tension dominated regimes and the inertia dominated regimes. Four flow regimes are named under this criterion: bubbly, intermittent, churn and annular.

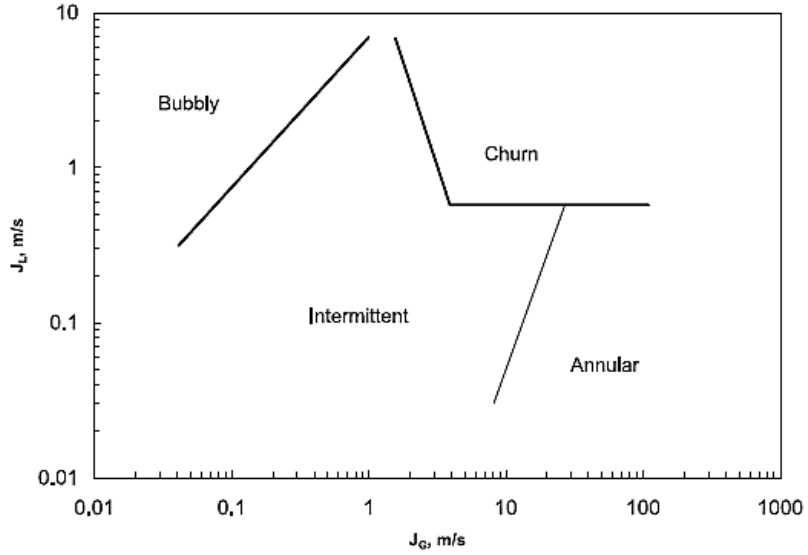

Figure 2.10 Universal flow regime map for liquid/gas flows in microchannel less than 1 mm, developed by Hassan, et al. (2005). J_G and J_L are the superficial velocity of gas and liquid phase.

Multiphase flows in channels of noncircular cross-section shapes

A number of studies have been carried out concerning the flow patterns and flow regime maps using channels with non-circular cross-section shapes such as triangular and rectangular (including square) channels. Sadatomi, et al. (1982) studied air/water flows in vertical non-circular channels including four sizes of rectangular channel, an isosceles-triangular channel and a concentric annular channel. They observed three flow patterns including bubble, slug and annular flows and the flow pattern transitions are not affected greatly when changing channel geometries when the hydraulic diameter (D_H) is greater than about 10 mm. On the other hand, Li, et al. (2014) carried out two-phase flow experiment using nitrogen-water in vertical upwards rectangular and equilateral-triangular channels with the same D_H and concluded that for channels with smaller diameters, the change of channel cross-section shapes greatly influence the transitions of flow patterns (Figure 2.11). Comparable results were obtained by Chung, et al. (2004) who carried out two-phase flow experiment in horizontal channels with even smaller

sizes (96 μm square channel and 100 μm circular channel) and found significant variation on the transitions of flow patterns.

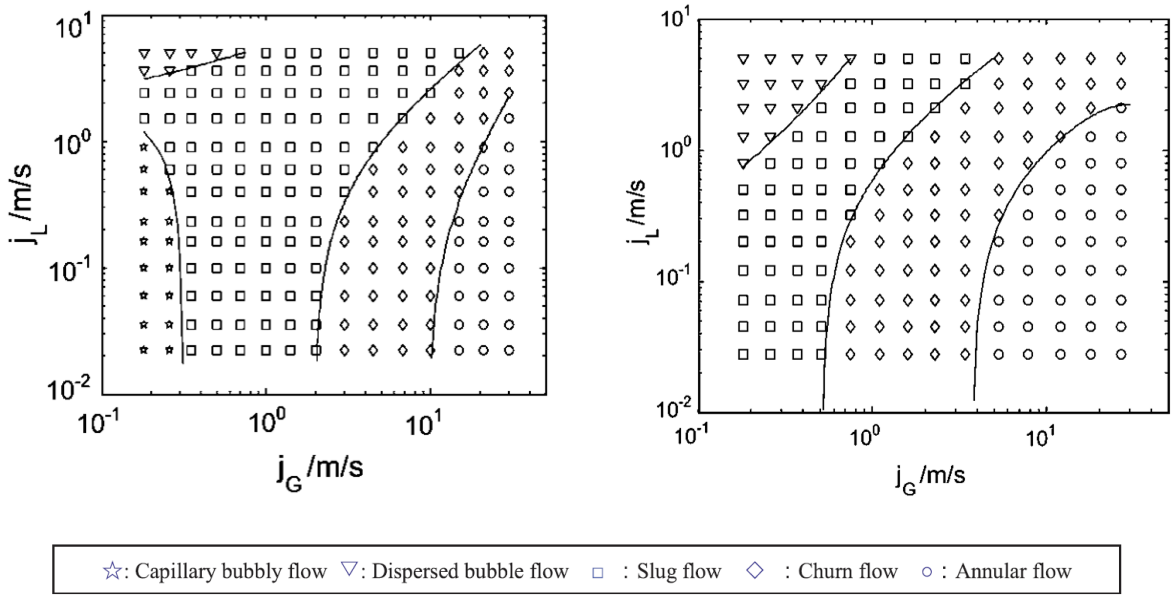

Figure 2.11 Flow pattern map of nitrogen/water two-phase flows in vertical upwards equilateral-triangular (left) and rectangular (right) channels, both channels are with the same D_H = 2 mm. (Li, et al., 2014).

Rectangular channels are the most used cross-section shape in the study of multi-phase flows in noncircular channels. Apart from the orientation of channel (inclination angle, vertical or horizontal channel) and D_H, a geometrical parameter is generally used: aspect ratio (or ratio of sides) (α), which is the ratio between the height and width of the cross-section of channel. Troniewski and Ulbrich (1984) studied the two-phase liquid/gas flow in 10 sizes of vertical upward rectangular channels, with D_H ranging from 7.45 to 13.1 mm, α ranging from 1/10 to 12. They first found that the value of α has effects on the appearance of flow patterns. For example, for horizontal flow, the stratified flow regime does not occur for $\alpha \leq 0.1$. They have also concluded that for α range 1 to 12, there exists a universal flow regime map for vertical upward flows. Coleman and Garimella (1999) compared the two-phase flow in horizontal

channels with circular channel (D = 5.5 mm) and rectangular channel with very similar D_H (5.36 mm) and developed flow regime maps for both cases. They found a shift in flow regime transitions, shown in Figure 2.12. Fluid displacement studies have also been carried out in noncircular channels which is reviewed in §2.2.4.

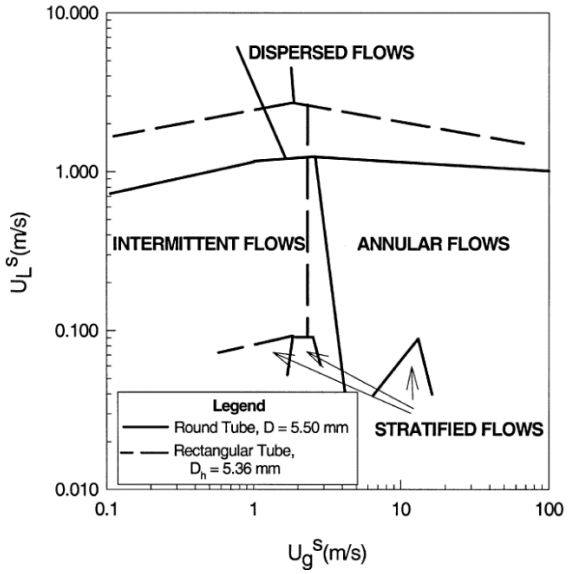

Figure 2.12 Comparison of flow regime maps of water/air two-phase flow in circular and rectangular channel with very similar hydraulic diameter. (Coleman and Garimella, 1999).

Some research has been carried out using rectangular channel with very small height (mini gap). Xu, et al. (1999) conducted air/water flow experiment in vertical channels with 12 mm in width and 0.3, 0.6 and 1.0 mm in height (gap). They have mainly observed, for channels with 0.6 and 1.0 mm gap, bubbly, slug, churn and annular flow patterns as expected only finding the bubbles in the bubble and slug flow are flattened to be two-dimensions in shape. However, for the channel with 0.3 mm gap, bubbly flow does not occur, instead two new patterns are identified: slug-droplet and annular-droplet flow. These two patterns take place as liquid droplets always appear to attach on the wall at low liquid flowrates. Another important geometry for small scale

multi-phase flows is the *Hele-Shaw* cell, which referred to the geometry of the small gap between two plates. This is briefly discussed in §2.2.4.

2.2.3 Flow visualisation and characterisation techniques

According to Smits and Lim (2012), dye and smoke visualisation are the oldest techniques in fluid mechanics. For liquid flow, the main techniques are dye techniques, rheoscopic fluid and electrolytic precipitation. The flow visualisation for gas flow commonly involves using smoke tunnel, smoke generator, smoke-wire technique or Titanium tetrachloride. Conventional dye, laundry brightener, milk and fluorescent dye are the most commonly used dye techniques.

For microscale flows, according to Sinton (2004) there are mainly four categories of techniques for the visualisation of microscale flows: particle-based flow visualisation methods, scalar-based flow visualisation methods, indirect gaseous flow visualisation techniques and point-detective scanning techniques. Laser Doppler Velocimetry (LDV), Particle Streak Velocimetry (PSV) and Particle Image Velocimetry (PIV) are the three most commonly used methods in microfluidic studies.

2.2.4 Fluid displacement and instabilities

Fluid displacement has drawn researchers' attention due to its important role in industry both for manufacture e.g. the coating of capillaries, injection moulding, mechanical lubrication and ensuring hygiene (minimisation of contamination) in fluid changeover. Various geometries and fluids (miscible or immiscible, including gas) have been studied with research aspects such as the wall thickness, interfacial instabilities, channel inclination, non-Newtonian fluids properties, velocity field measurement, etc. This has been studied both experimentally and theoretically, the latter by computational simulation or numerical analysis. §2.2.4 discusses the experimental studies of fluid displacement and reviews general instabilities with particular focus on the

instabilities take place in fluid displacement processes. Numerical study and CFD simulations are discussed later in §2.4.

Experimental study of fluid displacement

For immiscible fluid displacement, with gas-assisted fluid displacement being the earliest approach, the intention is to understand coating or cleaning processes. Therefore, the thickness of liquid film left on the wall after the displacing fluid's injection is the critical factor and has been studied the most and earliest in the area of fluid displacement studies. Fairbrother and Stubbs (1935) were among the first researches that study the liquid layer left on the wall after the prefilled liquid being pushed by another liquid. The fraction of liquid left on the wall is shown by expression

$$m = \frac{4(D-a)a}{D^2} \qquad \text{(Equation 2.3)}$$

where D is the inner diameter of tube and a is the film thickness on the wall. When a is very small, this parameter may be simplified to:

$$m = \frac{4a}{D} \qquad \textbf{(}\text{Equation 2.4)}$$

They suggested this fraction may be related to the square root of the capillary number, Ca, where:

$$Ca = \frac{\mu u}{\sigma} \qquad \text{(Equation 2.5)}$$

where μ is viscosity, u is velocity of advancing flow (bubble) and σ is the interfacial tension. The correlation developed by Fairbrother and Stubbs (1935) is flawed, since it came from very

limited experiment data (very small capillary number) and the capillary number cannot exceed 1 as *m* will be bigger than 1 which is not technically possible. Marchessault and Mason (1960) developed an empirical equation of

$$m = 2\sqrt{\frac{\mu}{\sigma}}(\text{-}0.05+0.89\sqrt{u}) \qquad \text{(Equation 2.6)}$$

$$\text{Or } m = -0.1\sqrt{\frac{\mu}{\sigma}} + 1.78\sqrt{Ca} \qquad \text{(Equation 2.7)}$$

The seminal work by Taylor (1961) extended Fairbrother and Stubbs (1935)'s work using 2 mm and 3 mm tube, studied capillary number up to 1.9. Taylor (1961) proposed an asymptotic value of m to be around 0.55 but the actual empirical equation was not developed. Bretherton, (1961) concluded the equation to be

$$m = 2.68Ca^{2/3} \qquad \text{(Equation 2.8)}$$

However this correlation only works for very small capillary number of less than 0.01. Irandoust and Andersson (1989) obtained a theoretical equation of

$$m = 0.72(1 - e^{-3.08(Ca\text{^}0.54)}) \qquad \text{(Equation 2.9)}$$

They verified their finding from experimental results of *Ca* up to 2.0. Aussillous and Quere (2000) revisited Taylor's experimental data and developed a model which has good fit to Taylor's data as well as their own experimental results:

$$m = \frac{2.68Ca^{2/3}}{1+3.35Ca^{2/3}}, \qquad \text{(Equation 2.10)}$$

which is referred as Taylor's law.

Quintella, et al. (2007) and Soares, et al. (2008) extended the study of liquid film on wall from liquid/gas and Newtonian liquid/liquid to Non-Newtonian fluid pairs, as well as investigated the effects of viscoelastic properties. Some of these results are summarised in Table 2.3.

Table 2.3 Literature correlations for film thickness

Reference	Correlation	Range of applicability
Fairbrother and Stubbs (1935)	$\frac{a}{D} = 0.25Ca^{0.5}$	$Ca \leq 0.09$ (Stated by Bretherton (1961))
Bretherton (1961)	$\frac{a}{D} = 0.67Ca^{2/3}$	$Ca \leq 0.01$
Data from Taylor (1961) Correlation fitted by Aussillous and Quere (2000)	$\frac{a}{D} = \frac{0.67Ca^{2/3}}{1+3.35Ca^{2/3}}$	$Ca \leq 1.4$
Irandoust and Andersson, (1989)	$\frac{a}{D} = 0.18(1-e^{(-3.08Ca^{0.54})})$	$Ca < 2.0$

The effects of viscosity ratio for immiscible displacement is studied by Soares, et al. (2005). Shown in Figure 2.13 are the results of the fraction of liquid left on wall plotted against viscosity ratio for difference capillary number cases. It can be seen for small capillary number cases the viscosity ratio has very little effects and for higher capillary number cases only small viscosity ratio values have influences on the results.

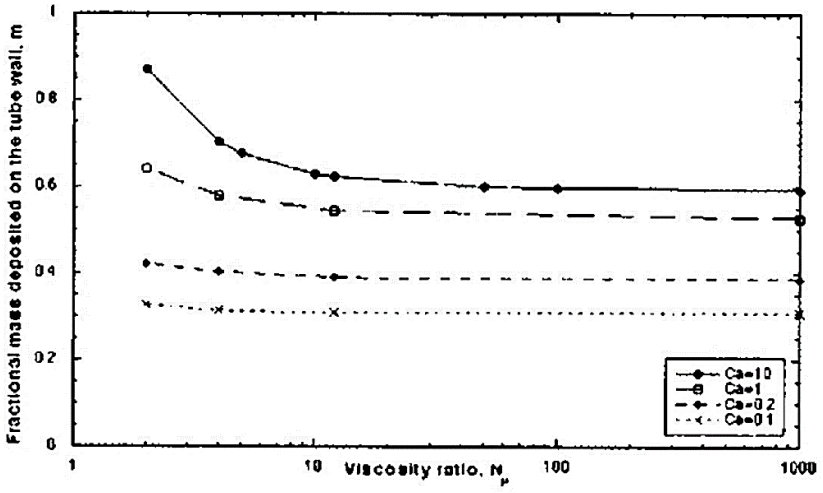

Figure 2.13 Fraction of liquid film left on the all plotted against viscosity ratio for different capillary number cases. (Soares, et al., 2005)

The influences of channel size on the thickness of liquid film on the wall have been studied by several researchers and similar conclusions have been obtained. As shown in Figure 2.14, at low capillary number, the ratio of liquid film thickness to channel radius (or diameter) is not affected greatly by channel size but at higher capillary number this ratio tends to decrease when the channel size becomes smaller.

(a) (b)

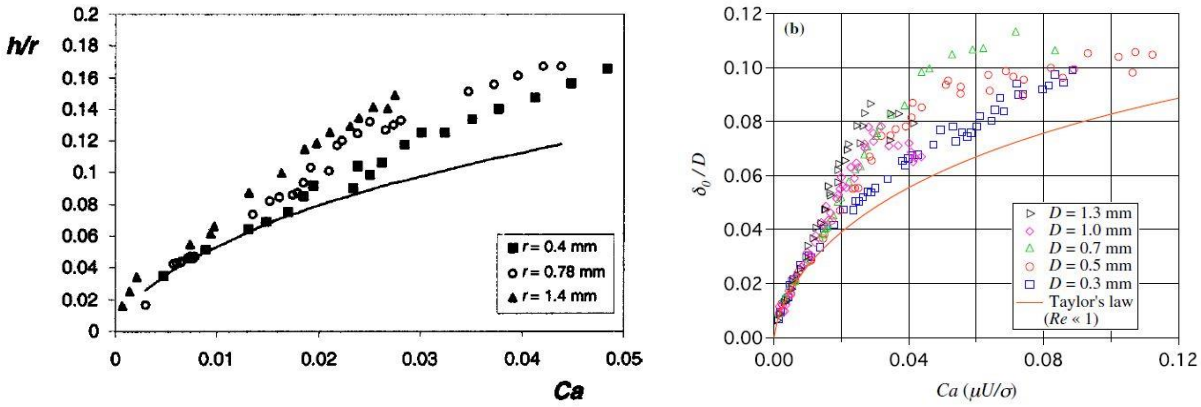

Figure 2.14 Results of studying the effects of channel size on the thickness of liquid film left on the wall by (a) Aussillous and Quere (2000), (the solid line being the Taylor's law) and (b) Han and Shikazono (2009a).

For miscible fluid pairs, Kuang, et al. (2003) carried out experiment of the displacements of a more viscous silicone oil by a less viscous silicone oil, in pipes of 1 to 4 mm in diameter. The fraction volume of the more viscous fluid left on the wall is characterised by

$$m = 1 - u / u_{tip} \qquad \text{(Equation 2.11)}$$

where u is the mean velocity and u_{tip} is the tip velocity. They chose three dimensionless groups Atwood number ($At = (\rho_1 - \rho_2)/(\rho 1 + \rho_2)$, where ρ_1 and ρ_2 are the density of the two fluids), Peclet number ($Pe = Du/D_f$, where D_f is the mass diffusion coefficient) and a gravitational parameter ($F_g = gd^2\Delta\rho / v_2 u \rho_2$). They clarified that it is not practically true that the thickness of the liquid left on the wall stays constant for the entire displacement process, thus m is a diagnostic measurement of the fluid left on the wall after the passage of the finger shape tip. They concluded that for large Pe, m is only affected by At but for small Pe, m tends to depend on all parameters (including the diameter of pipes). Taghavi, et al. (2012) carried out miscible displacement experiment using a denser fluid to displace a light fluid in an inclined pipe and found small viscosity ratio leads to higher displacement efficiency, which is characterized by the front velocity of displacement. They have also developed a flow regime map using (Fr, $Re\ cos\beta/Fr$) coordinates system, where Fr is the Froude number and β is angle of inclination from vertical.

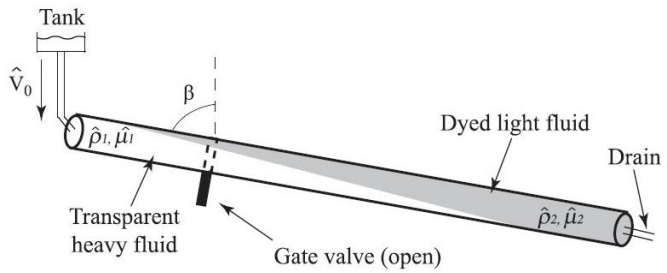

Figure 2.15 Schematic of experimental set-up of miscible displacement in an inclined pipe (Taghavi, et al., 2012).

Kolb and Cerro (1991) studied the coating of a capillary of square cross-section by filling the capillary with a viscous fluid then injecting air into the capillary, which essentially is a fluid displacement process. They stated the interface in the radial plane can be either axisymmetric or asymmetric, which is characterised by the radius of interface viewing from sides or diagonal planes of the square capillary, shown in Figure 2.16a and Figure 2.16b shows the measurement of these radii plotted against capillary number showing the transition from asymmetric to axisymmetric shape of the interface on the radial plane. This study has also concluded that the radius of the interfacial cap (regime AB in Figure 2.16c) decreases as the capillary number increases and the transition region (BC in Figure 2.16c) between the interfacial cap and the uniform film thickness regime becomes larger as the capillary number becomes larger, which is in agreement with what Bretherton (1961) suggests. Shown in Figure 2.16c are capillary number 0.04, 0.2 and 1.2.

(a)

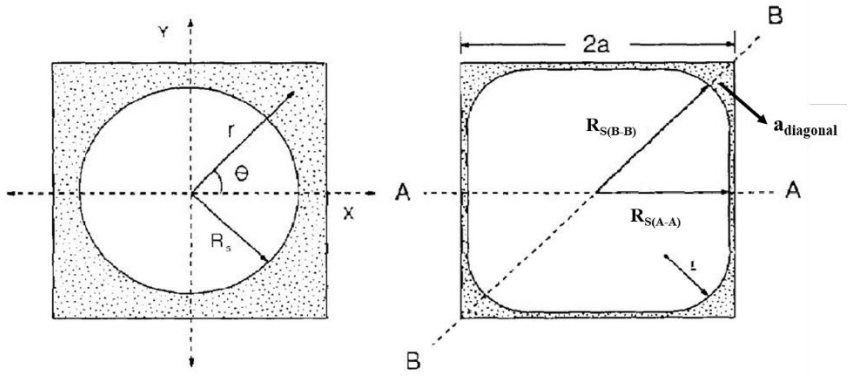

(b)

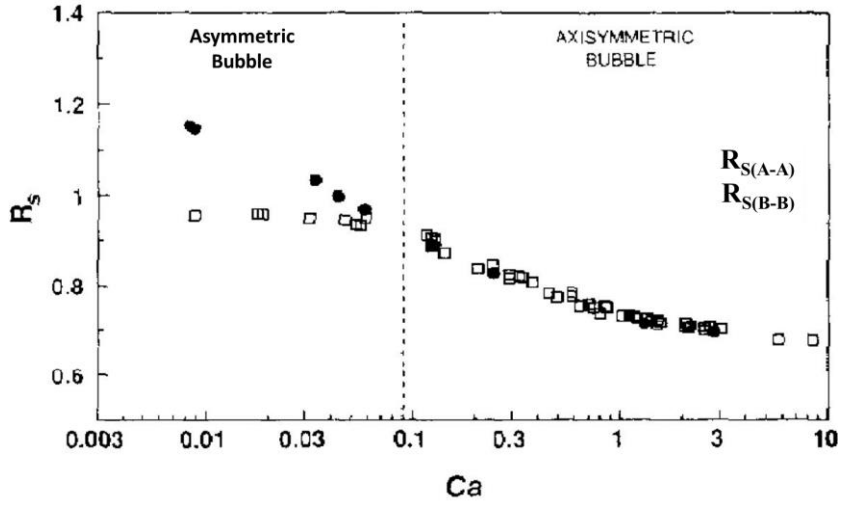

(c)

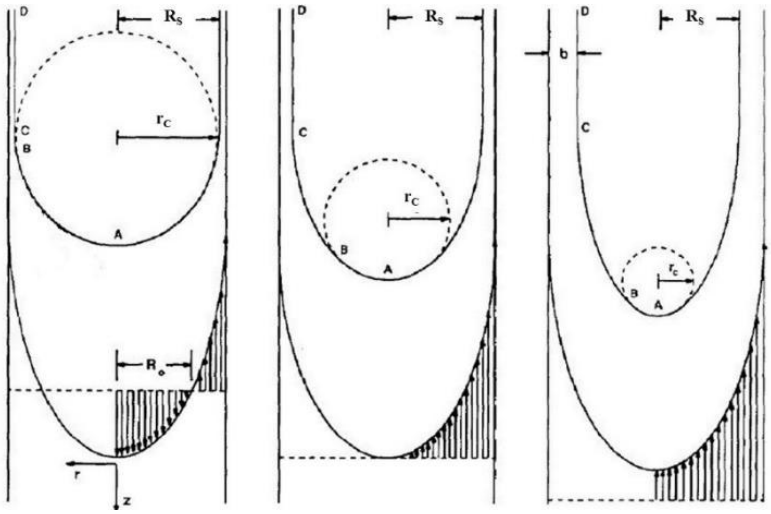

Figure 2.16 Fluid displacement of viscous fluid by air, figures adapted from the study of Kolb and Cerro (1991), (a) Schematic of axisymmetric and asymmetric interface at radial plane; (b) Radii of interface at radial plane viewing from sides (A-A) or diagonal planes (B-B) of the square capillary plotted against capillary number; (c) the radius of interface cap (regime AB) decreases with the increasing of capillary number, which is 0.04, 0.2 and 1.2 in the figure.

The $R_{S(A\text{-}A)}$ and $R_{S(B\text{-}B)}$ are the dimensionless radius:

$$R_{S(A-A)} = 1 - \frac{2a}{D_H} \quad \text{(Equation 2.12)}$$

$$R_{S(B-B)} = \sqrt{2} - \frac{2a_{diagonal}}{D_H} \quad \text{(Equation 2.13)}$$

Where $a_{diagonal}$ is the actual distance from the centre of the cross-section of channel to the interface at the diagonal plane and *a* is the distance from the centre to the interface at the sides of channel. It can be seen from Figure 2.16b that $R_{S(A\text{-}A)}$ stays almost constant at very close to 1 and $R_{S(B\text{-}B)}$ gradually decreases before these two radii become the same. Comparably, Han and Shikazono (2009b) also studied the measurement of film thickness on wall in micro square channel with 0.3, 0.5 and 1.0 mm in D_H, using a laser focus displacement meter. They confirmed the behaviour of constant side film thickness and increasing diagonal film thickness before the interface becomes axisymmetric. They also developed an empirical correlation of how these two radii depends on *Ca* and *We*, and claimed the correlation predicts the experimental data with ±5% accuracy:

$$R_{(S(B-B))} = 1.171 - \frac{2.43Ca^{2/3}}{1 + 7.28Ca^{2/3} - 0.255We^{0.215}} \text{ (for } Re < 2000) \quad \text{(Equation 2.14)}$$

$$R_{S(A-A)} = \begin{cases} 1 & (R_{S(B\text{-}B)} > 1) \\ R_{S(B-B)} & (R_{S(B\text{-}B)} \leq 1) \end{cases} \quad \text{(Equation 2.15)}$$

The empirical equation for liquid film thickness for circular channel developed also by Han's group (Han and Shikazono, 2009a and 2009b) can be used to compare the liquid film thickness

for the situations of using the same liquid and channels with different (square and circular) but the same hydraulic diameter:

$$\frac{a}{D_H} = \frac{0.67Ca^{2/3}}{1+3.13Ca^{2/3}+0.504Ca^{0.672}Re^{0.589}-0.0352We^{0.629}} \qquad \text{(Equation 2.16)}$$

Kamisli and Ryan (2001) carried out displacement experiments using two types of Newtonian fluids and two types of non-Newtonian fluids (shear-thinning and viscoelastic) displaced by gas. They found the fraction of non-Newtonian fluids left on wall depends greatly on the rheological properties and noted the development of quantitative models.

Instabilities at the interfaces between the displacing and displaced fluid have been observed for both immiscible and miscible cases, these are discussed in the next section.

Interfacial instabilities

General two-phase interfacial instabilities have been studied using a large range of geometries and fluids. Boomkamp and Miesen (1996) gave an overview of the two-phase instabilities in parallel flow and classified the instabilities to be five main categories: Rayleigh-Taylor instability (Figure 2.17a), Miles-instability, shear mode instability, internal mode instability and instability induced by tangential disturbances which includes viscosity-induced instability, gravity induced instability and viscosity-gravity-induced instability.

The term viscous fingering (Figure 2.17b) is used to describe the unstable flows, which is believed to relate to the viscosity variation between phases, occur during the displacement of fluids in porous media. Homsy (1987) gave a very detailed review on the mechanism behind viscous fingering phenomena. Petitjeans and Maxworthy (1996) suggest that viscous-based instabilities appear when a more viscous fluid displaced by a less viscous one. This has been

validated by a number of studies including Chakrabarty and Bentsen (1991) who developed a criterion based upon a dimensionless Instability number for the tubular porous media systems:

$$I_{St} = \frac{\mu_w u(M - 1 - Ng)D^2}{k_{wor}\sigma_e}\left(\frac{M^{2/3}+1}{2M^{2/3}}\right) \qquad \text{(Equation 2.17)}$$

which is derived from partial differential equations describing the evolution of the macrosurface between oil and water, for immiscible displacement in tubular cores, where μ_w is the viscosity of water, u is superficial velocity, M is the endpoint mobility ratio, Ng is gravitational number, D is the core diameter, k_{wor} is the permeability to water at residual oil saturation, σ_e is the effective interfacial tension. They also gave the critical value of 13.56, below which the displacement was believed to be stable. This critical value comes from the criterion provided by Bentsen (1985): $\gamma_w^2 > \gamma_{wgom}^2$, where γ_w is the eigenvalue for water regions and γ_{wgeom} is the minimum geometric eigenvalue.

Scoffoni, et al. (2001) studied the displacement of a more viscous fluid by a miscible, less viscous fluid in a vertical cylindrical tube and observed interfacial instabilities (Figure 2.17c). Similarly but under the opposite protocol, Balasubramaniam, et al. (2005) studied the displacement of a less viscous fluid by a miscible, more viscous fluid in vertical cylindrical tube, at a relatively low flow velocity range and observed the appearance of sinuous instability at some flow conditions Figure 2.17d. They also obtained controversial results with Yih (1967) and Hickox (1971) that in the cases of vertical miscible displacement the viscosity ratio alone does not have the determinant effects on the sinuous instability. However, even though large numbers of studies were carried out focusing on interfacial instabilities, very little literature can be found focusing how interfacial instabilities influence the cleaning process as well examining their 3-dimensional nature.

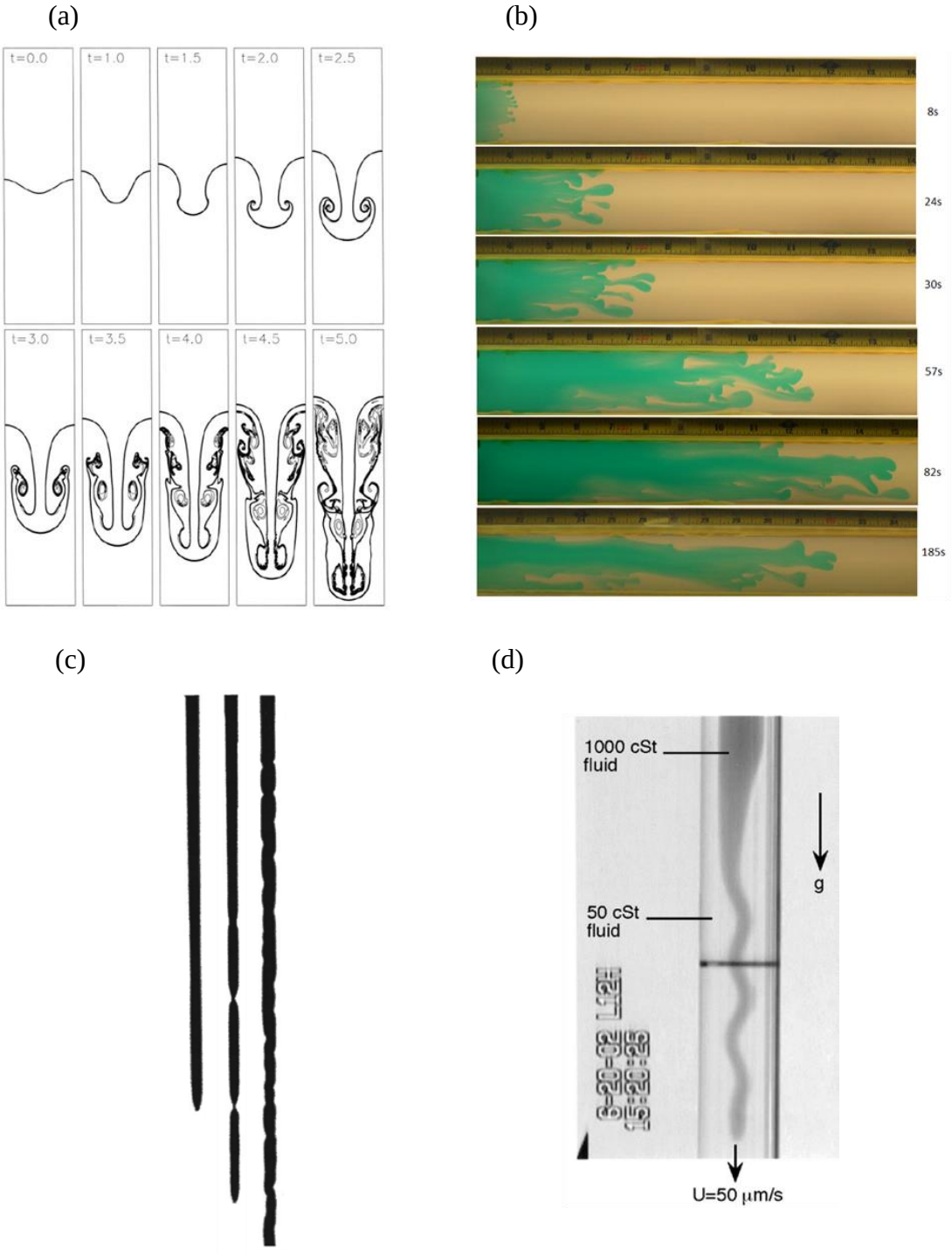

Figure 2.17 (a) Numerical simulation of Rayleigh-Taylor instability using Lattice Boltzmann scheme (He, et al., 1999); (b) Experimental images of viscous fingering from water penetrates 88.2% glycerol solution in a Hele-Shaw cell of 5 cm wide (Malhotra and Sharma, 2014); (c) Interfacial instabilities from displacement experiment of a more viscous fluid by a less viscous one in a vertical cylindrical tube (Scoffoni, et al., 2001). (d) Sinuous unstable flow from downward displacement experiment of 50 cSt silicone oil by 1000 cSt silicone oil in a 3-mm vertical cylindrical tube. (Balasubramaniam, et al., 2005).

2.3 Surfactant, surface and interfacial tension

2.3.1 Introduction of surfactant and micelles

There are two main characteristics used to define a surfactant: the first is that it must generate a molecular aggregate in solution and secondly its molecules must be attracted to and absorb onto the surface or interface of a solution or between two phases (Nakama, 2017).

Some other terminologies used to describe such surfactant are amphiphiles, surface-active agents, tensides and paraffin-chain salts (Schramm, et al., 2003). According to Schramm, et al. (2003), the term of *surfactant* was initially a trade mark of surface-active products from the RAF Corporation. Surfactants are applied in a very wide range of industries including food, consumer products (such as laundry detergents, house and personal care products), lubricants, pharmaceuticals, agricultural applications and fuel additives.

A typical surfactant molecule has a hydrophilic group and a hydrophobic chain. The hydrophilic group of the molecule is also called head group or polar group while the hydrophobic end of the molecule is referred as the tail (Kulkarni and Shaw, 2016).

Micelles are the unique self-organised microstructure formed when adding surfactant in aqueous systems, given the concentration of surfactant exceed a certain level, which is called critical micelle concentration (CMC). The process for micelles to form for surfactant in aqueous solution is called micellization. Figure 2.18a shows a typical schematic of the structure of a micelle and Figure 2.18b is a Transmission Electron Microscope (TEM) image of the micelles of a triblock amphiphilic copolymer poly(δ-valerolactone)/poly(ethylene glycol)/poly(δ-valerolactone) (VEV).

(a) (b)

Figure 2.18 (a) Schematic sketch of the structure of a micelle (Menger, et al., 1998). (b) TEM image of doxorubicin loaded VEV micelles (Nair K, et al., 2011).

Different shapes of micelle structures exist as the results of different structures of the surfactant molecules, such as spherical, cylindrical, hexagonal, cubic lamellar, inverted cylindrical and inverted spherical (Kulkarni and Shaw, 2016). Some parameters are used to characterise the physical structures of micelles: interface curvature, critical packing parameter (CPP) and hydrophile-lipophile balance (HLB). Figure 2.19 shows the relationship between these parameters and the structures of micelles (Miyake and Yamashita, 2017).

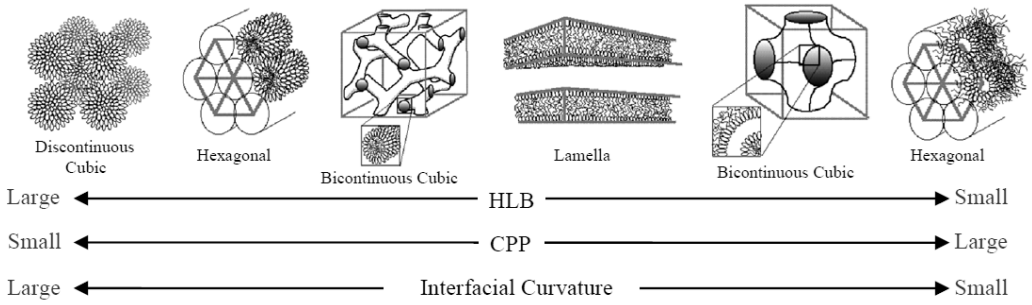

Figure 2.19 Examples of the relationship between three characterisation parameters (interfacial curvature, CPP and HLB) and the structures of micelles (Miyake and Yamashita, 2017).

The surfactant packing parameter is defined by Israelachvill, et al. (1976) as

$$P_c = v / a_0 l \qquad \text{(Equation 2.18)}$$

where *v* and *l* are the volume and length of the hydrophobic tail of surfactant molecule and a_0 is the optimal surface area per amphiphile, with which the free energy per amphiphile in a micelle is at its minimum. Israelachvili, et al. (1976) also concluded the critical packing parameter of spherical micelles is 1/3, above which non-spherical shapes start to form. The critical values of this parameter for cylindrical and planar bilayers forms of micelles are 1/2 and 1, respectively. Based on the information given by Israelachvili, et al. (1976), Table 2.4 summarises the relationship between the packing parameter and the forms of self-assembly structures.

Table 2.4 Summary of the relationship between surfactant packing parameter and self-assembly structures from information provided by Israelachvill, et al. (1976).

Critical packing parameter	Expected self-assembly structure
<1/3	Spherical micelles
1/3 to 1/2	Cylindrical micelles
1/2 to 1	Flexible bilayers and vesicles
1	Planer bilayers
>1	Inverted micelles

The approach of analysing HLB was first created by Griffin (1949), who attempted to link the molecular structure of surfactant to its practical behaviours and provided some methods to calculate HLB values. HLB values are practically important for choosing surfactant for specific applications. Shinoda and Saito (1969) summarised the choosing of surfactant based on their HLB values for various applications:

Table 2.5 General guidance on choosing surfactant based HLB values for various applications (Shinoda and Saito, 1969).

HLB range	Application
3 to 6	W/O emulsifiers
7 to 9	Wetting agents
8 to 18	O/W emulsifiers
3 to 15	Detergency
15-18	Solubilising agents

2.3.2 Types of surfactant

Typically, there are two main categories of surfactant, depending on the properties of the polar head group: ionic surfactant and non-ionic surfactant (such as Polysorbate 20: $C_{58}H_{114}O_{26}$). Ionic surfactants can be further subcategorised into three types:

Anionic surfactant, with its hydrophilic group bearing a positive charge. Such as sodium dodecyl sulfate ($CH_3(CH_2)_{11}SO_4Na$) and sodium lauryl sulfate ($CH_3(CH_2)_{11}(OCH_2CH_2)_nOSO_3Na$).

Cationic surfactant, with its hydrophilic group bearing a negative charge. Such as dodecyl trimethyl ammonium chloride ($CH_3(CH_2)_{11}NH_3Cl$) and Dodecyltrimethylammonium bromide ($CH_3(CH_2)_{11}N(CH_3)_3Br$).

Amphoteric (Zwitterionic) surfactant, the molecules of which carry both negative and positive charges. Such as Cocamidopropyl betaine ($C_{19}H_{38}N_2O_3$) and dodecyl betaine ($C_{16}H_{33}ClNNaO_2$).

Apart from the above surfactant categories some novel synthesized surfactants are being added into the area such as the Gemini surfactant, which contains, in sequence, a long hydrocarbon

chain, an ionic group, a spacer, another ionic group and another hydrocarbon chain (Figure 2.20). This surfactant is synthesised and named by Menger and Littau (1991).

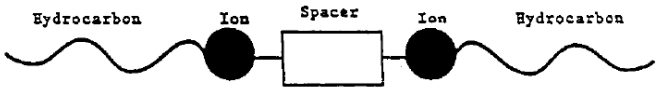

Figure 2.20 Schematic of Gemini surfactant molecule (Menger and Littau, 1993).

Surfactants can also be classified based on their solubility, those which are aqueous soluble are called hydrophilic surfactants and those which are lipids soluble are called hydrophobic or lipophilic. Most ionic surfactants are soluble in the aqueous phase while some non-ionic surfactants are hydrophilic and some are hydrophobic. The HLB value aforementioned can be used as a quantified indicator of the ability of attracting water for hydrophilic group and the ability to attracting oil for hydrophobic groups, thus it can be used to estimate the solubility of surfactants (Nakama, 2017). The concept of *Krafft temperature* point (T_K) is an important parameter that relates to the effect of temperature on the solubility of surfactant (Figure 2.21). For an ionic surfactant, below T_K, when the micellization does not start, the solubility is determined by the crystal energy and the heat of hydration of the system (Myers, 1992). Above T_K the solubility of surfactant increases greatly, due to presence of micellization (Schramm, et al., 2003). Figure 2.21 shows a diagram illustrating the determination of K_T, below which no CMC curve is presented because no micellization process exist and the sudden increase in surfactant solubility when temperature is above K_T.

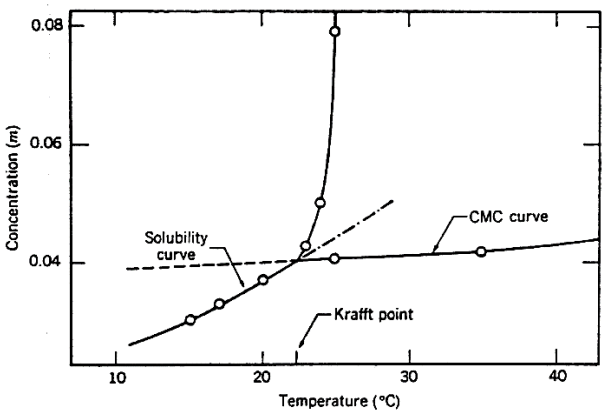

Figure 2.21 Illustration of the Krafft temperature point of surfactant (Shinoda, et al., 1965).

2.3.3 Critical Micelle Concentration

Factors influencing the CMC

The CMC values of surfactant are mainly affected by molecular properties such as the nature of hydrophobic tail and head group, but some external factors also influence the CMC value such as temperature, pH and the existence of other additives in the system.

The length of hydrophobic chain of surfactant molecules is a dominant element of CMC. Myers (1992) stated that for straight-chain hydrocarbon surfactants, the CMC drops to half its previous value with the addition of each methylene group and the phenomena exists until the number of carbon atoms reaches about 16. When the number of carbon atoms is above 16 straight-chain hydrocarbon, the effect of chain length becomes insignificant and this effect stops its presence when the number of carbon atoms is above 18. Mukerjee (1967) suggests this may be the results of the coiling of long hydrophobic chains in water. For non-ionic and Zwitterionic surfactant, according to Rosen (2004), the effect on changing CMC when increasing methylene groups is much greater, the CMC value drops to the one tenth of its previous with the addition of two

methylene groups. Klevens (1953) provided an empirical equation of the relation between CMC value and the number of carbon atoms for straight chain (both cationic and anionic) surfactant:

$$\log CMC = A - Bn \qquad \text{(Equation 2.19)}$$

Where n is the number of carbon atoms in the hydrophobic chain, A and B are both empirical constants for particular conditions of homologous series, temperature and pressure, etc. Some values of A and B are also reported by Klevens (1953):

Table 2.6 Some values of A and B for equation 2.19. (Klevens, 1953)

Surfactant type	Temperature (˚C)	A	B
Alkane sulfonates	40	1.59	0.294
Alkane sulfonates	50	1.63	0.294
Alkyl sulfates	45	1.42	0.295
Alkyl ammonium chlorides	45	1.79	0.296
Alkyltrimethy ammonium bromides	60	1.77	0.292

The effect of hydrophilic group on CMC values is also found to be important. Table 2.7 lists some examples of how CMC values change with different hydrophilic head on same hydrophobic tail. Myers (1992) states that for a C_{12} hydrocarbon surfactant with a non-ionic head group the CMC value is in the scale of 0.0001 M while an ionic head group with the same hydrophobic chain the CMC value is in the scale of 0.001 M. For anionic surfactant, it was found for the same hydrophobic tail and head group such as anionic lauryl sulfates, the CMC values decrease in the order of $Li^+ > Na^+ > K^+ > Cs^+ > N(CH_3)_4^+ > N(C_2H_5)_4^+ > Ca_2^+ \approx Mg_2^+$. For cationic surfactants, such as dodecyltrimethylammonium and dodecylpyridinium halides, the CMC values are found to be decrease in the order of $F^- > Cl^- > Br^- > I^-$. (Mukerjee, 1967).

Table 2.7 Examples of different CMC values with different hydrophilic group on same hydrophobic tail (Fendler, 1982).

Hydrophobic tail	Hydrophilic head	Temperature (˚C)	CMC (mM)
$C_{12}H_{25}$	COOK	25	12.5
	SO_3Na	25	8.1
	$N(CH_3)_3Br$	25	16
$C_{16}H_{23}$	$N(CH_3)_3Cl$	30	1.3
	$N(CH_3)(C_2H_4OH)_2Cl$	30	1.0
C_8H_{17}	OCH_2CH_2OH	25	4.9
	$(OCH_2CH_2)_2OH$	25	5.8
C_9H_{19}	$COO(CH_2CH_2O)_9CH_3$	27	1.0
	$COO(CH_2CH_2O)_{16}CH_3$	27	1.8
$C_{10}H_{21}$	$O(CH_2CH_2O)_8CH_3$	30	0.6
	$O(CH_2CH_2O)_{11}CH_3$	30	0.95

Other factors influence the CMC value of surfactant including the existence of electrolyte. It was found for both cationic and anionic surfactants, the existence of electrolyte leads to a decrease of CMC values and this has much less significant effect for non-ionic and Zwitterionic surfactants (Rosen, 2004). The effectiveness of electrolyte on the change of CMC for anionic surfactant is in the order of: ½ SO_4^{2-} > F^- > BrO_3^- > Cl^- > Br^- > NO_3^- > I^- > CNS^-, for cationic surfactant is in the order of: NH^{4+} > K^+ > Na^+ > Li^+ > ½ Ca^{2+} (Ray and Nemethy, 1971).

The effect of temperature on CMC values is strongly associated with the fact that increased temperature causes the decrease of the hydration of water of the hydrophilic head group, which helps the micellization. On the other hand, increased temperature also varies the isolated water molecules around hydrophobic groups, which disrupt the micellization processes. Thus, the

effect of temperature appears to cause the lowering of CMC and then increase when further increase temperature (Rosen, 2004), which has been observed from a number of experimental studies such as the results shown in Figure 2.22 (Mohajeri and Noudeh, 2012).

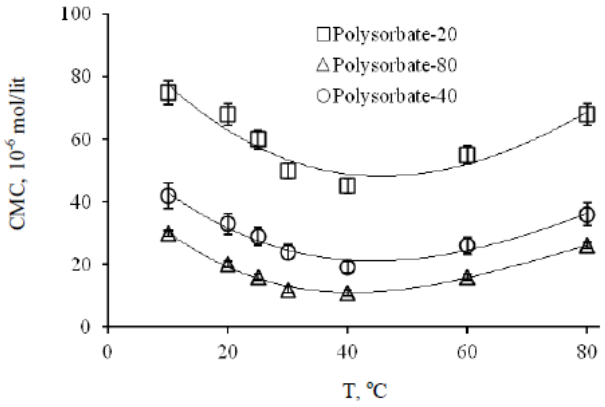

Figure 2.22 Results of measuring CMC values of non-ionic surfactant polyoxyethylene sorbitan fatty acid esters (polysorbate) effected by temperature.

Importance of CMC and how to determine CMC

The CMC value is very important as some physical properties of surfactant solution change dramatically after surfactant concentration exceeds the CMC. Figure 2.23 shows the plot generated by Presto (1948) of the change of some physical properties with the change of concentration of surfactant sodium lauryl sulfate. Thus, it is widely accepted that the general method of obtaining CMC values for a surfactant is to plot important properties against the surfactant concentration (Schramm, et al., 2003). In order to precisely determine the CMC of a surfactant, large amount of researches have been carried out, using the most widely applied methods of measuring surface tension, measuring conductivity and fluorescence spectroscopy (dye method), such as Shimizu and Iwatsuru (1988), Wilhelm, et al. (1991), Patist, et al. (2000), Perez-Rodrıguez, et al. (1998) and Mehta, et al. (2005). Mukerjee and Mysels (1971) summarised some other methods of determining CMC values of surfactants without additive

the solution such as the measurement of the refractive index, diffusion coefficient, viscosity, streaming current, calorimetric methods, the Kraft Point Solubility methods, potentiometric measurement. Some methods of measuring CMC with the help of additive, suggested by Mukerjee and Mysels (1971), include the of change of solubility of water-insoluble compounds with the presence of surfactants, the methods based on interfacial phenomena and methods observing the change of flocculation rate of a suspension.

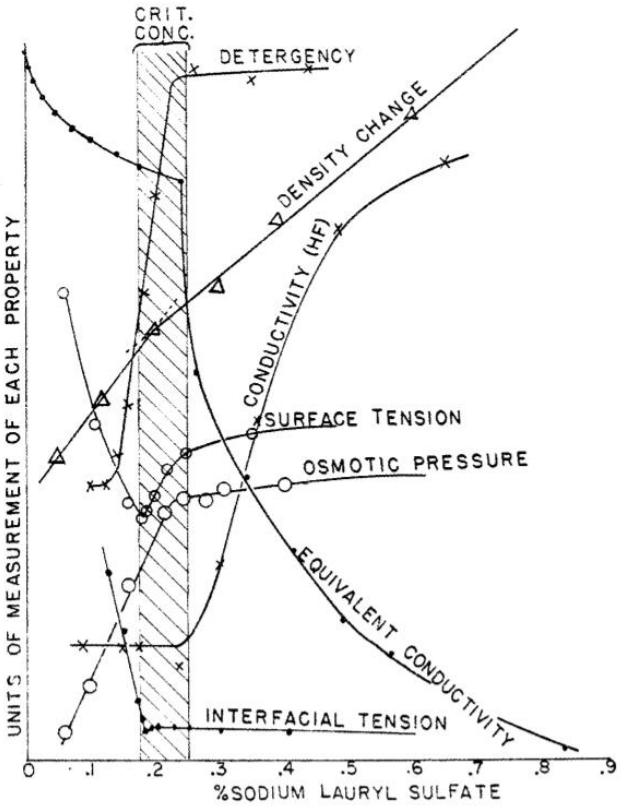

Figure 2.23 Physical properties change with surfactant concentration for Sodium lauryl sulfate (Presto, 1948).

2.3.4 Surface and interfacial tension and measurement techniques

The interface generally refers to the imaginary plane between the two phases in contact and have atoms or molecules on both sides of the plane (Ebnesajjad and Landrock, 2014). The generation of surface tension comes from the concept that the molecules cause unbalanced

forces at surfaces because the last layer of molecules does not have other identical molecules to interact with. Therefore the non-zero net force towards the bulk needs to be counteracted to increase the surface area and the energy consumption required to drive the increase of surface are is called the *free surface energy*. *Surface tension* (ST) is the cohesive force required to fulfil the above process, which has the unit of energy per unit area or the forces per unit length. Similarly for surfaces present between two immiscible fluids, the relevant parameter is called *interfacial tension* (IFT). Due to the theories mentioned above, surfaces thus tend to contract their minimum surface area which is the thermodynamically favourable condition (Rapp, 2016).

The effect of temperature on surface tension was studied by Guggenheim (1945) who concluded an empirical equation:

$$\gamma = \gamma_{t0}(1-\frac{T}{T_0})^{1+r} \qquad \text{(Equation 2.20)}$$

Where γ_{t0} is the surface tension at temperature 0 K, T_0 is the critical temperature of the liquid and r is a constant which is reported to be 2/9 by Guggenheim (1945) and 0.21±0.015 by Ferguson (1923).

Some studies of estimating interfacial tension value from the surface tension values of both phases have been carried out. Girifalco and Good (1957) provided an equation of estimating interfacial tension between phase 1 and 2:

$$\sigma_{12} = \gamma_1 + \gamma_2 - 2\Phi(\gamma_1\gamma_2)^{1/2} \qquad \text{(Equation 2.21)}$$

Where σ_{12} is the interfacial tension between phase 1 and 2, γ_1 and γ_2 are the surface tension of phase 1 and 2, respectively and Φ is a constant given by:

$$\Phi = -\frac{\Delta G_{12}^{a}}{(\Delta G_{1}^{a}\Delta G_{2}^{a})^{1/2}} \qquad \text{(Equation 2.22)}$$

Where ΔG_{12}^{a} is the free energy of adhesion for the interface between phase 1 and 2, ΔG_{1}^{a} and ΔG_{2}^{a} are the free energy of cohesion for phase 1 and 2 respectively. Griffith and Snyder (1964) also provided some values for this constant, which ranges from 0.5 to 1.2, for systems of water and an organic liquid.

Drelich, et al. (2002) summarised five conventional categories of methods for measuring liquid-liquid interfacial tension including: direct measurement using a microbalance; measurement of capillary pressure; analysis of capillary gravity forces; gravity-distorted drops and reinforced distortion of drop (Figure 2.24).

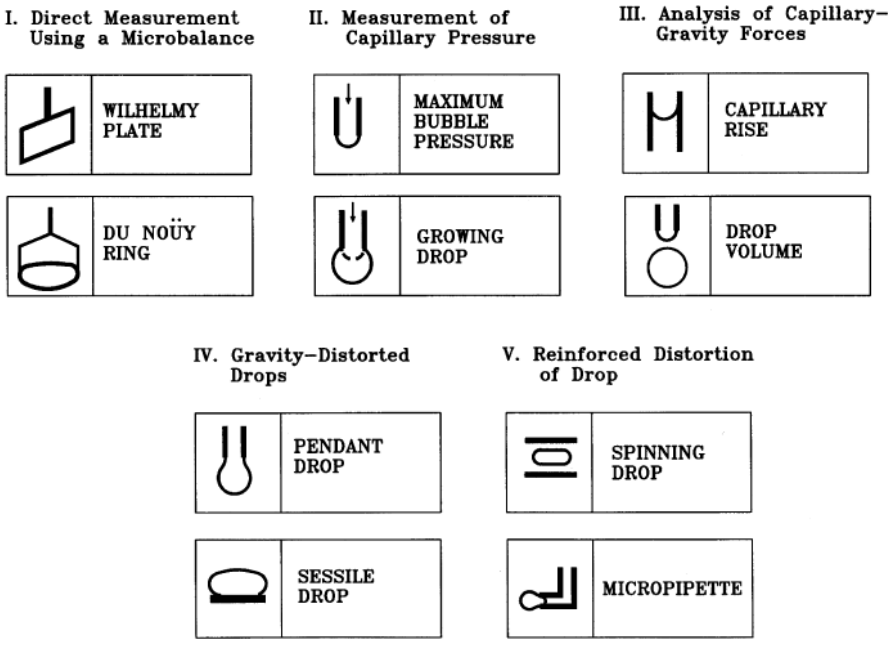

Figure 2.24 Summary of the methods of measuring liquid-liquid interfacial tension.

A newly developed method of measuring interfacial tension is microfluidic tensiometry that has been studied in the past decade. Microfluidic systems are designed to measure interfacial

tension (including dynamic interfacial tension) through analysing the shape deformation and velocity variation of droplets at certain geometries. In the presence of surfactant, surface-active monomers are first being adsorbed to assist to generation of droplets then the adsorbed surfactant helps in stabilising the droplets. Droplets formation and control geometries are designed such as T-junction channel (Brosseau, et al., 2014); Y-junction channel (Steegmans, et al., 2009 and Muijlwijk, et al., 2016); and the novel geometry proposed by Martin and Hudson (2009), which allows precisely control of the formation rate of droplets, space between droplets, overall flowrate and droplet height (see Figure 2.25).

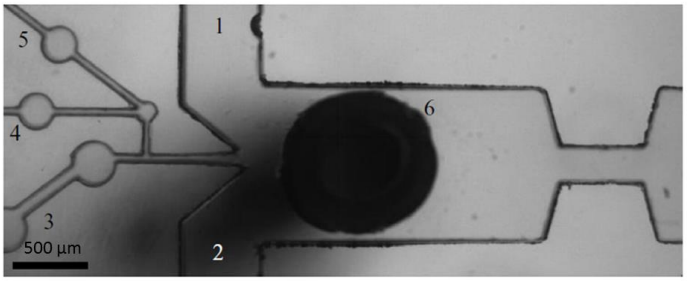

Figure 2.25 The microfluidic system designed for measuring interfacial tension showing inlet 1, 2 and 3 for controlling continuous phase, inlet 4 and 5 for aqueous phase and inlet 6 for controlling droplets heights (Martin and Hudson, 2009).

The Wilhelmy plate method, developed by Wilhelmy (1864) and the Du Noüy ring methods, first published by Lecomte du Noüy (1919) are the traditional and most widely used techniques for measuring surface and interfacial tension, especially when these properties need to be measured over a long period of time. However, one of the well-known possible source of error for the Wilhelmy plate method comes from the wetting properties on the plate of the liquid being measured. The basics of these two measurement methods are discussed below.

The Wilhelmy plate method

Figure 2.26 illustrates the operation of the Wilhelmy plate method (Ebnesajjad and Landrock, 2014). The plate is placed at a fixed position in contact of the surface of liquid and then the vertical force applied on the plate is measured by measured by microbalance. The equation below is used to calculate the surface tension of liquid:

$$\gamma = \frac{F}{P \bullet \cos\theta} \qquad \text{(Equation 2.23)}$$

Where F is the force applied on the plate, θ is the contact angle of the liquid in contact of the measuring plate and P is the perimeter of the plate, which equals to $2\times(t+L)$.

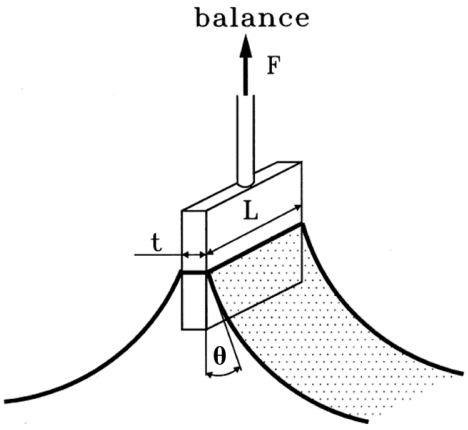

Figure 2.26 Schematic of the Wilhelmy plate method. (Ebnesajjad and Landrock, 2014)

Zero contact angle between the plate and liquid is the basis of this method, thus it is suggested to use roughened plate, such as platinum or platinum-iridium alloy plate (Gaonkar and Neuman, 1984).

Furlong and Hartland (1979) studied the effect of wall wettability of the container used for the measurement of ST or IFT using Wilhelmy plate method. They concluded that the effect is the largest when θ_w, the contact angle of the heavy phase on the container wall, is 0° and the smallest

when θ_w is 90°. They also found the effect is significant when using a thicker plate or a smaller container to fill the liquid, the effect is greater when measuring IFT than measuring ST and these criteria were provided: the effect is considered to be significant when $t(\Delta\rho g/\sigma)^{0.5}$ is big or $x_w(\Delta\rho g/\sigma)^{0.5}$ is small, where t is the thickness of the plate, x_w is the distance between the centre of plate and container wall, $\Delta\rho$ is the density difference between the two phases.

The Du Noüy Ring method

Figure 2.27 illustrates the schematic of the operation of the Du Noüy Ring method (Ebnesajjad and Landrock, 2014). Similar to the basic equation for determining surface tension using the Wilhelmy plate method, the basic equation for the ring method (Equation 2.13) requires a correction factor f_c:

$$\gamma = \frac{F}{P \bullet \cos\theta} f_c \qquad \text{(Equation 2.24)}$$

Zuidema and Waters (1941) provided an equation to calculate the correction f_c:

$$f_c = 0.725 + \left(\frac{0.00363}{\pi^2 R^2} \times \frac{P_{\max}}{\Delta\rho} + C\right)^{0.5} \qquad \text{(Equation 2.25)}$$

Where R is the radius of the ring, C is a constant depending on the radius of the wire of the ring (r_w) and the radius of the ring: C = 0.04534-1.679 (r_w/R), P_{max} is the maximum pull on ring, determined from the microbalance. Empirical values of the correction factor are provided by Harkins and Jordan (1930), covering data from sixteen rings with the radii of the wires from 0.009 to 0.05 cm and the radii of the rings from 0.4 to 0.8 cm. These data have been integrated into recent software of tensiometers using the Du Noüy Ring method such as the K100, K11 and K20 models of tensiometer from KRÜSS Gmbh (2017). Similar to the Wilhelmy plate

method, it is preferred that a perfect wettability (zero contact angle) of the denser fluid on the ring surface (Drelich , et al., 2002). Thus similar materials as the Wilhelmy plate method are recommended. Another recommendation to increase the accuracy of the results from this method includes make sure the ring lies on a plane and the plane of ring is horizontal (parallel to the surface of liquid) (Harkins and Jordan, 1930).

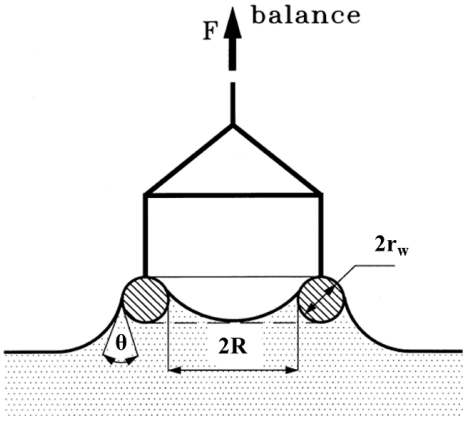

Figure 2.27 Schematic of the Du Noüy Ring method. (Ebnesajjad and Landrock, 2014).

2.3.5 Surface and interfacial tension with surfactant

Due to the presence of surfactant, adsorption takes place at the surface or interface causing the decreasing of surface or interfacial tension. Accordingly the phenomena of the surface/interfacial tension that depends on the surface/interfacial age is referred as dynamic surface or interfacial tension. The time for the surface or interfacial tension to reach an equilibrium state ranges from milliseconds to days (Eastoe and Dalton, 2000). The equilibrium is a state under which the flux of adsorption of surfactant monomers at the surface or interface equals to the desorption flux. Understanding of the kinetics of adsorption processes or the change of interface excess concentration is needed in order to make accurate deduction of these from the measurement of dynamic surface tension measurement. Two main theories for monomer transportation and adsorption are: (1) the *diffusion (only) controlled* theory, in which

monomers are diffused from the bulk to the subsurface (an imaginary surface a few molecular diameters away from the surface/interface) then instantly adsorbed at the interface and (2) the *mixed kinetic-diffusion* theory, which assumes the existence of a potential barrier when monomers are diffused at the subsurface before being adsorbed at the interface (Eastoe and Dalton, 2000). Traditionally the Gibbs equation below is the conventional theory of expressing surface excess of adsorption:

$$\Gamma = -\frac{1}{nRT} \times \frac{d\gamma}{d\ln(c)} \qquad \text{(Equation 2.26)}$$

Where R is the gas constant, T is the absolute temperature in Kelvin, c is surfactant concentration, n = 1 for non-ionic surfactants or ionic surfactants in the presence of excess electrolyte and n = 2 for 1:1 ionic surfactants (Eastoe and Dalton, 2000). Experimentally, the methods of measuring the amount of absorbed monomers include the *radiotracer method*, which involves measuring the radioactivity at the interface when radioactive chemicals such as soft β-emitter ^{14}C or ^{35}S, are added into surfactant solutions (Dixon, et al. (1949), Tajima, et al. (1970)); the neutron reflection method (Rennie, et al. (1989), Lu, et al. (1993), Taylor, et al. (2002)) and the *dropping-pipette method* reported by Donnan and Baker (1911).

The measurement or prediction of the dynamic surface tension of surfactant in aqueous phase has been carried out by a number of researchers using various method such as Fainerman and Miller (1995), Manglik, et al. (2001), Yoshimura, et al. (2013), etc. Drelich, et al. (2002) summarised the time ranges available for different surface/interfacial tension measurement techniques (Table 2.8). Although it is claimed by Franses, et al. (1996) that the available time range for the oscillating jet method is commonly 10 to 100 ms, with possibilities to reach 1 to

500 ms and the minimum surface age the maximum bubble pressure method deals is 0.1 to 1 ms.

Table 2.8 list of the time range available for various common surface/interfacial tension measure methods (Drelich , et al., 2002).

Method	Time range
Wilhelmy plate	>10 s
Du Noüy ring	>30 s
Pendant drop	>10 s
Sessile drop	>10 s
Drop volume/weight	1 s–20 min
Maximum bubble pressure	1 ms–100 s
Growing drop/bubble	>10 ms
Oscillating jet	1–10 ms
Pulsating bubble	5 ms–0.2 s

The maximum bubble pressure method

The maximum bubble pressure method, which was first proposed by Simons (1851), is one of the most widely used techniques to measure short-time dynamic surface tension values. It is operated by blowing air bubbles from a capillary which is inserted into the liquid being measured and the maximum pressure of air bubble is measured by pressure sensor. The fundamental equation for calculating surface tension is the law of Laplace:

$$p = \frac{2\sigma}{r_c} + \rho g h \qquad \text{(Equation 2.27)}$$

Where p is the max bubble pressure, σ is surface tension, r_c is the radius of capillary, h is the height from the tip of capillary to the liquid surface. The time from the start of generating an

air bubble to the moment the bubble reaches its maximum bubble pressure is referred as *lifetime* (t_L) and the time for subsequent growth of the bubble until it breaks or detaches from the capillary is called the *deadtime* (t_D) (Koval'chuk, et al., 1998). The bubbling time (t_B), between the detachment from capillary tip of two bubbles is $t_B = t_L + t_D$. The lifetime is the characteristic age of liquid surface with regards to dynamic surface tension measurement. It has been shown that the moment of maximum bubble pressure reached corresponds to the hemispherical shape of the bubble for pure liquid but this is not necessarily true when surfactants are present (Horozov, et al., 1996). Generally these time intervals are determined by the pressure signal of the air in capillary as the t_L to be the increasing part of curve and t_D to be the decreasing part of curve (see Figure 2.28). A significant improvement of the accuracy of measurement can be achieved by analysing the oscillation of air flow rate through the capillary during the generation of bubbles especially for dynamic surface tension measurement of lifetime less than 10 ms. This method of determining lifetime has been applied by some commercial maximum bubble pressure tensiometers such as SINTERFACE BPA (Fainerman, et al., 2004).

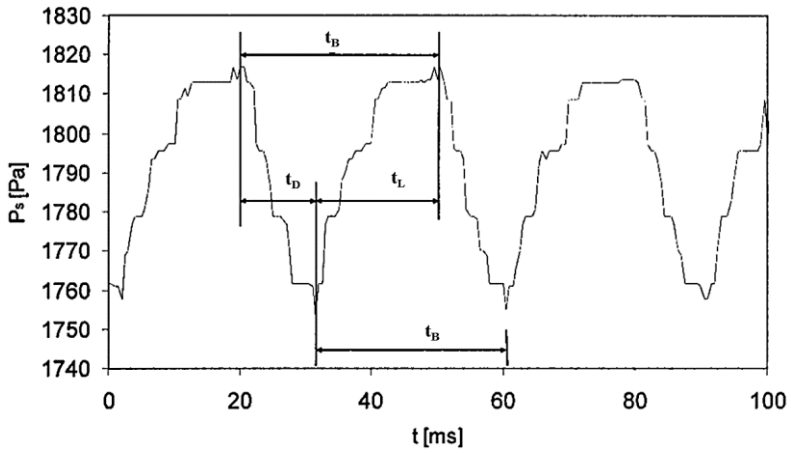

Figure 2.28 An example of the pressure signal of air in capillary for the maximum bubble pressure method (Adapted from Fainerman, et al. (2004)).

Dynamic surface tension measurement of sodium dodecyl sulfate (SDS)

Studies on various aspects of the properties and performance of the surfactant of sodium dodecyl sulfate (SDS) has been carried out in a number of researches due to its important industrial/commercial application such as the solubilisation, dispersion and stabilisation of drugs and detergent formulation (Fairnerman, et al., 2010). The dynamic surface tension effects have been studied relatively extensively by a number of different measuring methods such as Owens (1969) using the oscillating jet method; Casandra, et al. (2017), using the pendant bubble method; Iliev and Dushkin (1992) or Mysels (1986), both using the maximum bubble pressure method. The Owens (1969) dynamic surface tension measurement ranges from 1 ms to 6 ms, concluding that the ST value of SDS solution over CMC, at 15 ˚C, has a rapid drop from around 72 mN m^{-1} to about 50 mN m^{-1} at 3 ms then gradually decreasing towards the equilibrium ST value, which is 36.1 mN m^{-1} measured by the ring method. Some assumptions are made in Owens (1969)'s research such as at time zero the ST value of the solution equals to the ST value of the pure solvent, which is water in the study. Iliev and Dushkin (1992)'s measurement of dynamic ST values range from around 10-20 ms to 250 ms. Their results suggest for SDS solutions above CMC, a drop of ST value of about 4 mN m^{-1} from time 10 ms to time 30 ms then stays level thereafter at equilibrium ST of around 40 mN m^{-1}. Casandra, et al. (2017)'s study of dynamic ST of SDS solution has an extensive time range of from 1 to over 100 s and has concluded for an SDS solution with concentration below CMC (e.g. 4.0×10^{-6} mol cm^{-1}), a drop of ST value from 52 mN m^{-1} at time 1 s to 48 mN m^{-1} at time around 300 s. Relevant work carried out by (Mysels, 1986) provided an empirical equation to calculate the equilibrium ST value of SDS:

$$\gamma = 68.49 - 6.516\ln c - 3.353\ln^2 c \qquad \text{(Equation 2.28)}$$

Where γ is the ST (mN m^{-1}) and c is the concentration in mM. However, this correlation has its obvious defect because it has only been verified in the range of concentration less than 7 mM, which is lower than the CMC value of SDS water solution. The CMC of SDS water solution has been provided by various studies to be 8 to 8.2 mM (Zhang, et al. (1996), Chattopadhyay and London (1984), Mukerjee and Mysels (1971)).

Lunkenheimer and Czichocki (1993) studied the stability of SDS solution (1×10^{-3} M) by measuring the surface tension, using a ring tensiometer, of the solution after a three-year period of storage under daylight and room temperature. They found that under certain conditions such as the SDS to be "surface-chemically pure", process of SDS solution degradation is very slow that after three years' of storage the surface tension of the solution is almost the same as previous measurement, with only small variation of short-time dynamic surface tension.

2.3.6 Surfactant in multiphase flows

The effect of dynamic surface tension and the thus time-dependent features that surfactants bring attracts attention in the world of multiphase flows. For example, in Enhanced Oil Recovery (EOR) technology, it is well known that the introduction of surfactant can lower the interfacial tension and increase the mobility of oil to achieve better displacement of oil for extraction. It is stated the oil-water interfacial tension needs to be reduced by 6 orders of magnitude to provide efficient improvement of oil recovery results (Ayirala and Rao, 2004).

Olgac and Muradoglu (2013) studied the effect of surfactant on the film thickness of long bubbles in capillary tube using a finite-different/front-tracking method and found a thickening effect for the film thickness. They stated this may be due to the uneven distribution of surfactant at the uniform film thickness region and at the bubble front. The higher surfactant concentration

at the uniform film thickness region, leading to lower interfacial tension, cause the presence of Marangoni stress that pushes more liquid into the uniform film thickness region.

2.4 Computational Fluid Dynamics

2.4.1 Introduction to CFD

Computational Fluid Dynamics (CFD) is a powerful tool to study fluid dynamics phenomena, heat or mass transfer and chemical reactions by numerical solution of the governing conservation and transport equations (e.g. Navier-Stokes). CFD is applied in a very wide range of studies that involve the analysis of at least one form of liquid. CFD simulations validated by experiment results not only can be used to predict flow features but also CFD enables researchers to discover activities that are not easy or even impossible to observe. Hirsch (2007) describes a CFD system generally has these main components: 1. The selection and construction of mathematical models; 2. The discretization of space domain and equations; 3. The analysis of the stability, accuracy of numerical scheme; 4. The solution of numerical domain; 5. Post-processing to produce graphic results. Components 2 to 4 are summarized as an element "Solver" in CFD system (Versteeg and Malalasekera, 1995). Figure 2.29 is a chart illustrating these components.

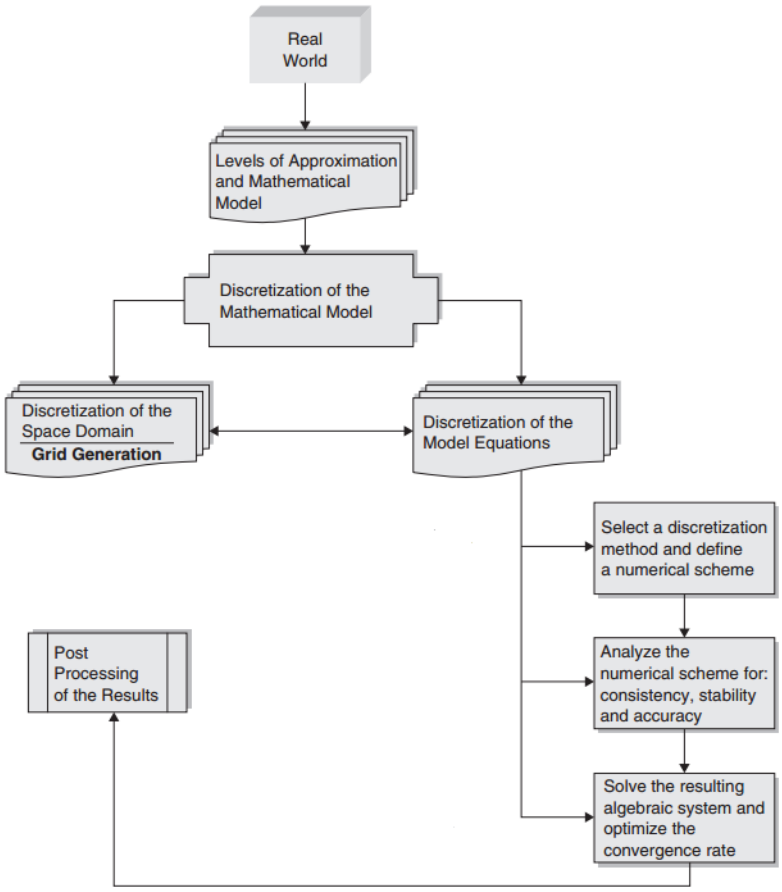

Figure 2.29 Illustrative chart of the components of a CFD system (Hirsch, 2007)

2.4.2 CFD solvers

The governing equations are the core of solving CFD problems. Three parameters must be conserved in order to complete the process of calculations: conservation of mass, momentum and energy (Jamshed, 2015). Finite element method (FEM), finite volume method (FVM) and Finite Difference Method (FDM) are three main solvers used in CFD calculations. FDM is the oldest CFD calculation method which is now believed not to be suitable for complex or multi-dimensional geometries due to the fact that it builds the discretization of partial differential equations (PDEs) by using a topologically square network of lines (Peiro and Sherwin, 2005). The drawbacks of FDM stimulated the use of integral formulation of PDEs which led to the

development of FEM and FVM. Many studies have focused on the comparison of these solvers, especially FEM and FDM. Figure 2.30 illustrates how different FEM and FVM handle the calculation. Jeong and Seong (2014) compared FVM based software ANSYS CFX and Fluent with FEM based codes ADINA and concluded that FVM based calculations give similar simulation results even using different mesh types (hexahedron or tetrahedron) while FEM based calculations are affected by mesh types. They also suggest the calculation time for the same number of mesh cells of FEM based calculations is around 5 times for FVM based methods. What worth noting is these methods are not always independently used for complex simulation problems. A hybrid method which combines FDM and FEM for simulation casting processes was proposed by Si, et al. (2003) where FDM is applied for heat flow analysis and FEM is used for thermos-elasto-plastic stress analysis.

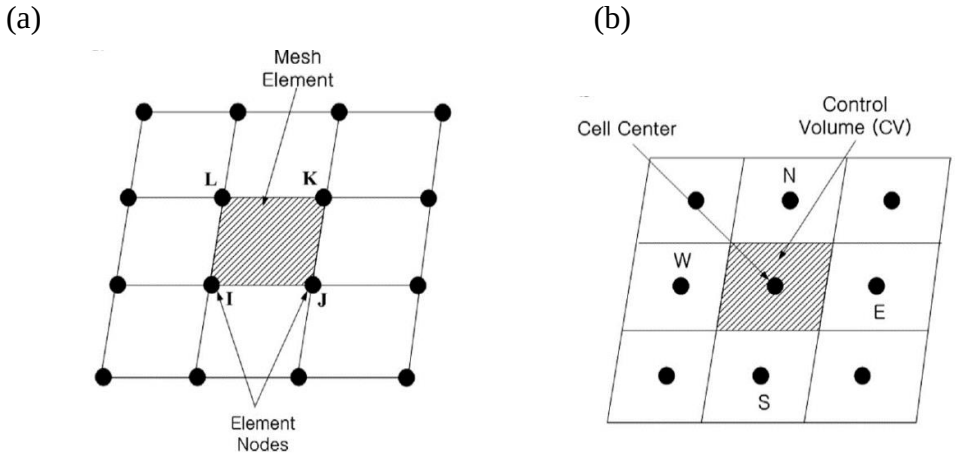

Figure 2.30 Comparison of representative structured mesh analysed by (a) FEM and (b) FVM (Jeong and Seong, 2014)

2.4.3 Navier-Stokes equations

The Navier-Stokes equations are the backbone of the analysis of the motion of fluid. They consist a series of non-linear partial differential governing equations. This system was the

integration of various researches from various physical hypothesis by Navier (1927), Poisson (1831), Saint-Venant (1843) and Stokes (1880).

In Cartesian co-ordinates (*x, y, z*) with velocity components *u*, *v*, *w*, the Navier-Stokes momentum equations can be written as:

$$\rho(\frac{\partial u}{\partial t}+u\frac{\partial u}{\partial x}+v\frac{\partial u}{\partial y}+w\frac{\partial u}{\partial z})=-\frac{\partial p}{\partial x}+u(\frac{\partial^2 u}{\partial x^2}+\frac{\partial^2 u}{\partial y^2}+\frac{\partial^2 u}{\partial z^2})+\rho g_x \quad \text{(Equation 2.29)}$$

$$\rho(\frac{\partial u}{\partial t}+u\frac{\partial v}{\partial x}+v\frac{\partial v}{\partial y}+w\frac{\partial v}{\partial z})=-\frac{\partial p}{\partial y}+u(\frac{\partial^2 v}{\partial x^2}+\frac{\partial^2 v}{\partial y^2}+\frac{\partial^2 v}{\partial z^2})+\rho g_y \quad \text{(Equation 2.30)}$$

$$\rho(\frac{\partial u}{\partial t}+u\frac{\partial w}{\partial x}+v\frac{\partial w}{\partial y}+w\frac{\partial w}{\partial z})=-\frac{\partial p}{\partial z}+u(\frac{\partial^2 w}{\partial x^2}+\frac{\partial^2 w}{\partial y^2}+\frac{\partial^2 w}{\partial z^2})+\rho g_z \quad \text{(Equation 2.31)}$$

And the continuity equation is:

$$\frac{\partial u}{\partial x}+\frac{\partial v}{\partial y}+\frac{\partial w}{\partial z}=0 \quad \text{(Equation 2.32)}$$

For a channel with non-circular cross-section, Boussinesq (1868) suggested that in an elliptical channel with constant pressure gradient *p*:

$$w(x,y)=\frac{pa^2b^2}{2\mu(a^2+b^2)}(1-\frac{x^2}{a^2}-\frac{y^2}{b^2}) \quad \text{(Equation 2.33)}$$

Where *a* and *b* are the semi-major and semi-minor axis.

2.4.4 Main CFD models and the modelling multiphase problems

CFD solvers typically categorise flows as laminar or turbulent, steady or transient, single-phase or multi-phase (Andersson, et al., 2015). These categorises determine the basis of choosing

different physical models in order to solve different problems. In ANSYS Fluent, various model options are available which are termed multiphase models, energy equations, laminar model, different turbulent models, radiation models, heat exchange models, etc. One of critical importance to the research presented in this thesis are the multiphase closure models, since the flows are laminar and do not involve reaction or heat exchange.

For multi-phase flow problems, two main approaches are generally considered: the Euler-Lagrange and the Euler-Euler approach. The Euler-Lagrange model treats the phases as the continuum, by solving Navier-Stokes equations, and the dispersed phase, in which individual particles or bubbles are modelled through the calculation of flow field (Andersson, et al., 2015). This approach is applicable for the cases with very small volume fraction of dispersed phase such as problems of spray drying, liquid fuel combustion, some particle-laden flows.

On the other hand, the Euler-Euler approach treats all phases as continuous phase. Constitutive relations need to be provided from empirical information to close the momentum equations. The volume of fluid (VoF) model, the mixture model, the Eulerian Model and porous bed models are the main multiphase Euler-Euler models (Andersson, et al., 2015). Andersson, et al. (2015) also gives a universal guidance on choosing the model for multi-phase problems, shown in Figure 2.31.

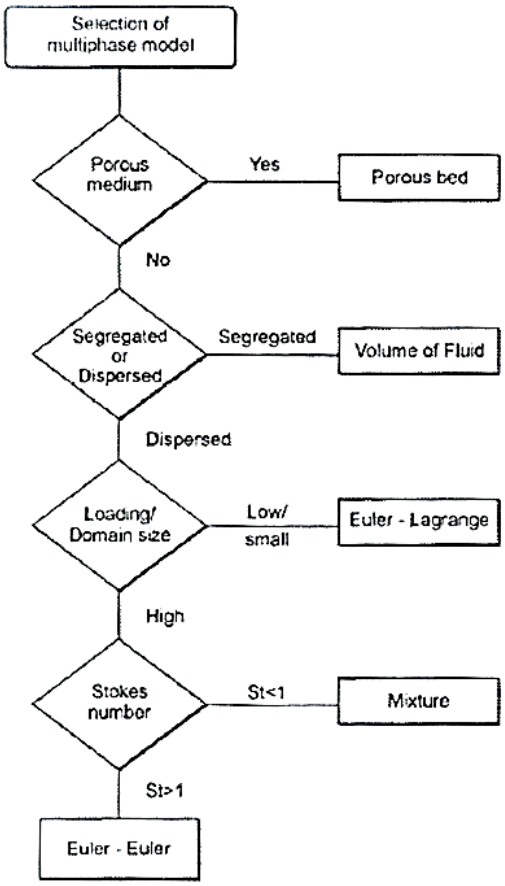

Figure 2.31 Choosing the appropriate multi-phase model by Andersson, et al. (2015).

Multiphase VoF model has been used for situations with free boundary configurations, free surfaces or the interfaces between two fluids. VoF describes the location of interfaces using the values of volume fraction on a grid-cell basis. Figure 2.32 shows a simple example of how VoF reconstructs interfaces. Large number of studies have applied VoF model or developed VoF-based modified model to solve various problems (Leandro, et al. (2016), Pathak and Raessi (2016), and Fleckenstein and Bothe (2013)).

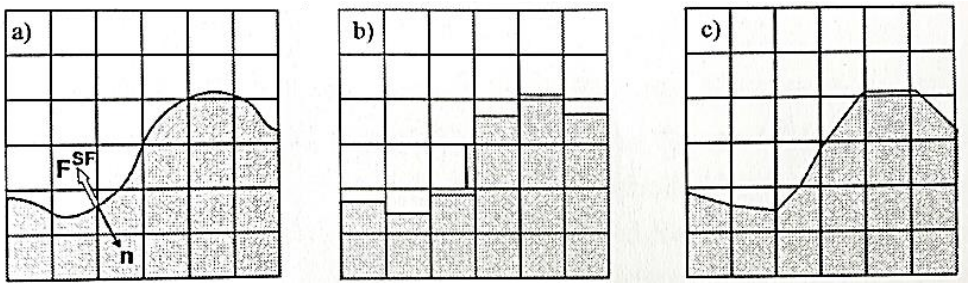

Figure 2.32 Illustrative images of how VoF method track interfaces; (a) actual interface, (b) volume fraction values calculated by VoF model and (c) the linear reconstruction of the interface. (Image by Andersson, et al. (2015)).

A number of researches have been conducted to numerically study multiphase flow in different geometries of duct, pipe or channel. Solving continuum Navier-Stokes equations is a conventional method of modelling displacement flows. Sahu, et al. (2009) applied Navier-Stokes equations together with a convective-diffusion equation in the study of miscible displacement in inclined channels. Alternatively, the Lattice Boltzmann method (LBM) is occupied in the study of flow displacement. Redapangu, et al. (2012) summarised four notable multiple flow LBM approaches: the colour segregation method of Gunstensen, et al. (1991) and Shan and Chen (1993); the free energy method of Swift, et al. (1995) and He, et al. (1999).

2.4.5 Current open source codes and commercial CFD packages

A number of commercial CFD packages began to be available for researchers from early 1980s and a rapid growth has been seen of such CFD packages during the past 35 years (Jeong and Seong, 2014). These include OpenFOAM, OpenFlower, GADGET, Fluent, and FLOW3D. There has been significant recent consolidation in the industry, for example the purchase of CFX by ANSYS in 2003, who are the owners of Fluent.

2.4.6 Existing CFD simulations of fluid displacement or similar processes

Oliveira and Meiburg (2011) who applied the Navier-Stokes equations in the simulation of 3-D miscible displacement in Hele-Shaw cells, are believed to be the first researchers who used 3D Navier-Stokes for displacement studies in this geometry.

Researchers at Indian Institute of Technology have carried out various numerical studies of the fluid displacement problems including immiscible displacement (2D simulation by Redapangu, et al. (2012), 3D simulation in square channel by Redapangu, et al. (2013), miscible displacement (Mishra, et al., 2012) and non-Newtonian fluid displacement (Swain, et al., 2015). Lattice Boltzmann method has been greatly applied to simulation the displacement flows and shown good result including the simulation of interfacial instabilities (shown in Figure 2.33). Figure 2.33a (Redapangu, et al., 2013) shows the results of 3D numerical simulation of immiscible fluid displacement in a inclined square channel. Isosurface representing the interface between the two fluids are illustrated. Related dimensionless groups are Re = 100, At = 0.2, Fr = 5, Ca = 29.9 and the inclination angle is 45˚. The viscosity ratio (displaced fluid/displacing fluid) is 10. Figure 2.33b is showing the 2D numerical simulation of miscible displacement. The flow phenomena is a Kelvin-Helmholtz type instability (Sahu, 2013).

(a)

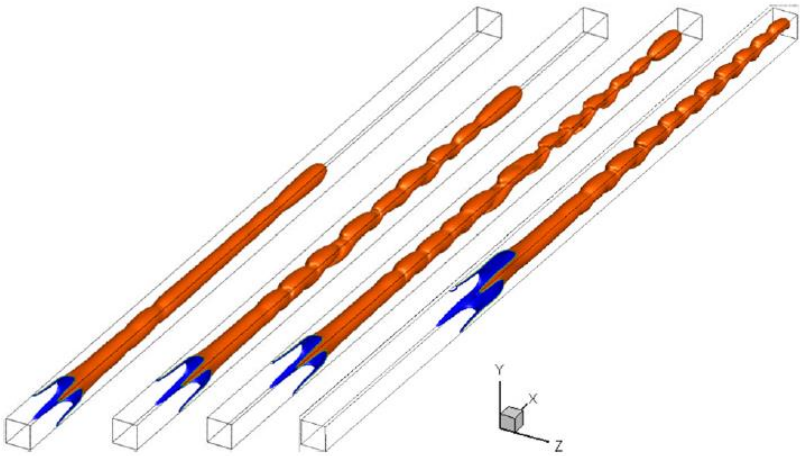

(b)

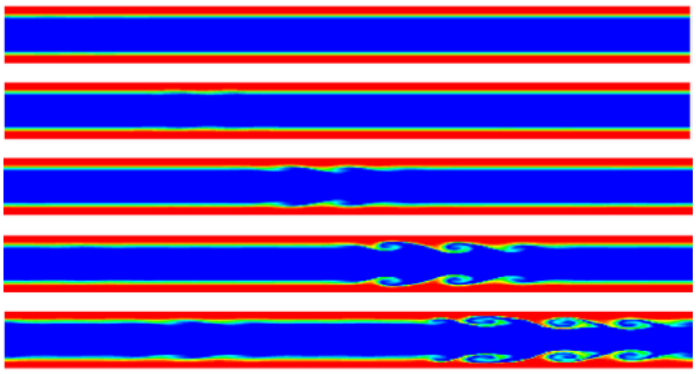

Figure 2.33 3D simulation of immiscible fluid displacement in square channel by Redapangu, et al. (2013), showing interfacial instabilities between two phases. (b) 2D simulation of miscible flow by Sahu (2013), showing the KH-type 'roll-up' instabilities.

The simulations of other type two-phase flows have also been attempted by a great number of researches. Li and Angeli (2017) used ANSYS Fluent to simulation the generation of Taylor plug flows in microchannels. They have observed the circulation patterns and the increase of radial velocity at the front and tail positions of a plug, Figure 2.34b.

(a)

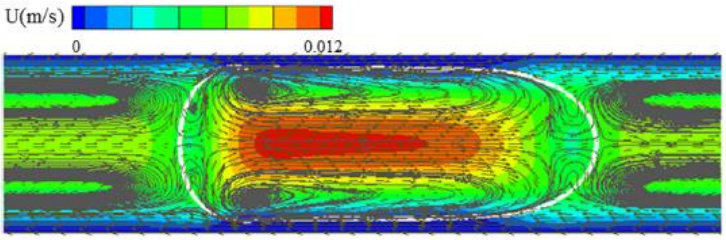

(b)

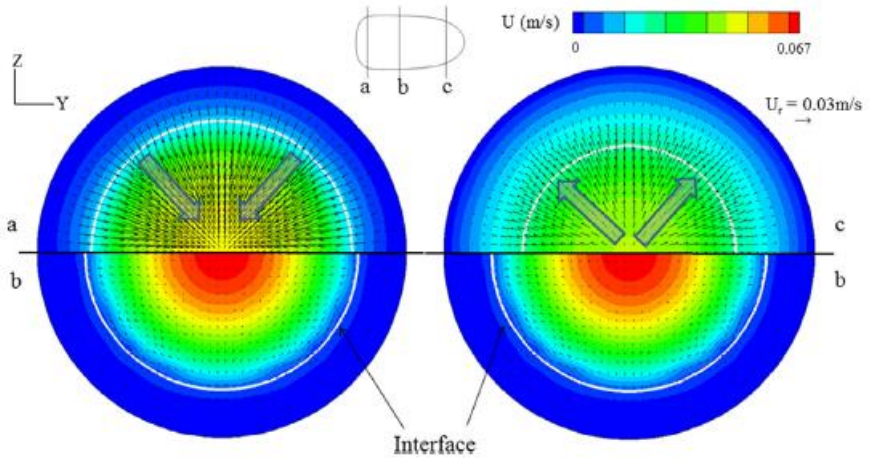

Figure 2.34 Simulation results using Fluent showing (a) circulation flows and (b) the increase of radial velocity at front and tail regimes of a plug. Li and Angeli (2017)

The numerical analysis of the volume of confined non-wetting bubbles or droplet in microchannels, based on surface energy minimization, was carried out by Musterd, et al. (2015). The only input for accurately estimating the volume of bubbles or droplets are the geometrical parameters such as the width and height of channel, and top-view bubble length. Only the "quasi-static" situation where the movement of droplet is low enough to neglect the deformation due to viscous and inertial forces ($Ca < 5\times10^{-3}$ and We < 1 as guidance was stated) was simulated. The full approach is shown in Figure 2.35a. Musterd, et al. (2015) have also validated their models in the three common geometries in microfluidics with the code Surface Evolver, developed by Brakke (1992), and obtained very good agreement. Figure 2.35b shows the 3D

rendered view and 2D top view of the droplets shapes in three most commonly used microchannel geometries: a trapezoidal channel, a rectangular channel with rounded corners and a rectangular channel.

(a)

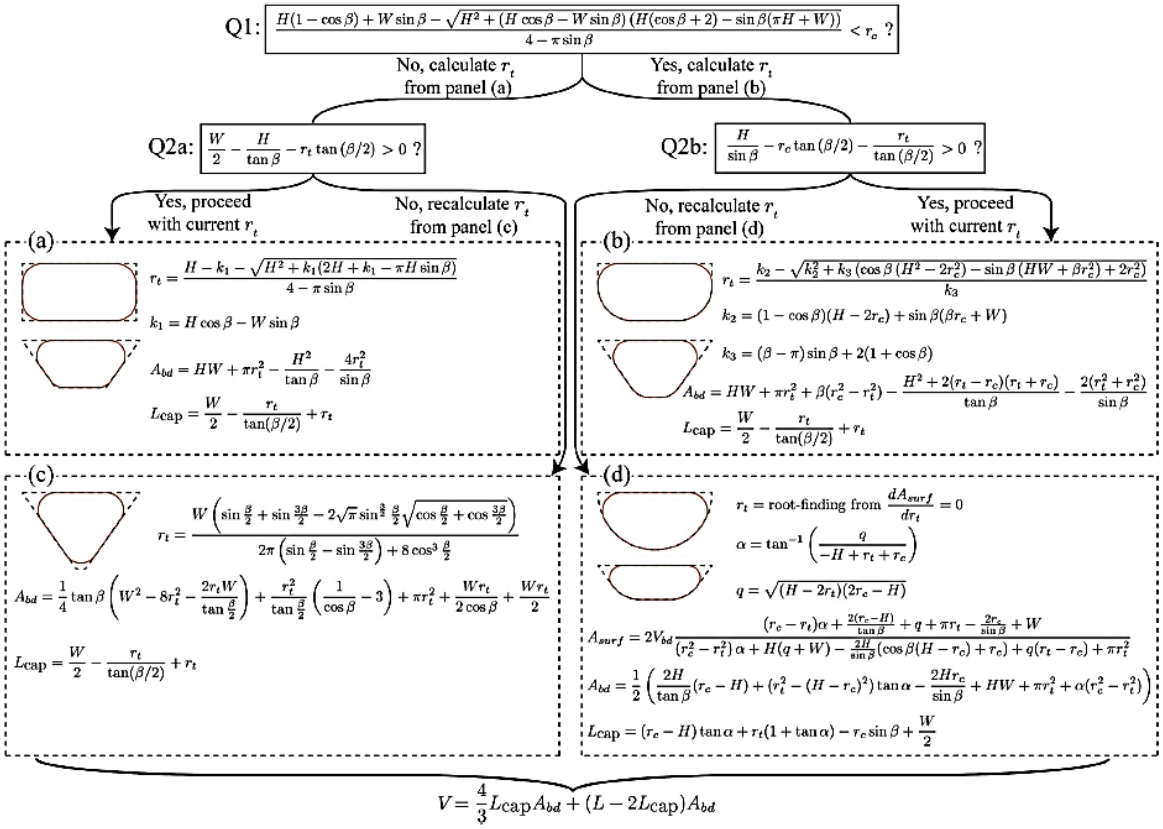

(b)

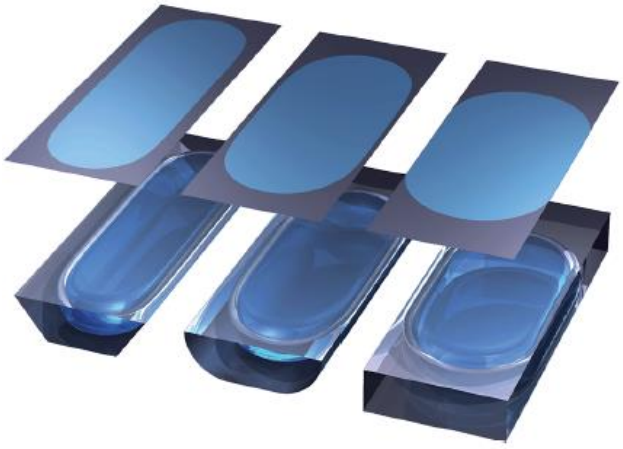

Figure 2.35 (a) Models for estimation the volume of bubble or droplets in microchannels, using input of geometrical parameters and bubble length; and (b) results showing the 3D view and relevant top view of droplets in three most common channels: a trapezoidal channel, a rectangular channel with rounded corners and a rectangular channel (Musterd, et al., 2015).

2.5 Summary

This chapter reviews some of the literature contents relevant to this study. Flows in micro- scale channels and multiphase flows related topics are described first, followed by information on fluid surface science and CFD.

Although some insight to the two-phase pipe flow from previous works, the understanding of fluid displacement in non-circular microchannels is also not yet complete. For example, the overall film thickness left on the wall around a Taylor bubble has not been greatly investigated. A universal method for describing the film thickness at the whole cross-section plane is in need. This is important for applications such as oil recovery and channel coating. The predictive tools in multiphase flows developed were also in some extent restricted to certain parameters of the system. Conflicting conclusions may be drawn depends on specific systems used, operating conditions and characterisation approaches. The systematic information occurrence flow regimes based on interfacial phenomena has not yet been reported for fluid displacement type flows.

In addition, CFD remains a very powerful method for fluid mechanics analysis. Choosing the most appropriate CFD tool, solvers and models and the realisation of experimental phenomena in CFD simulation is an attractive approach in developing validated *in silico* models. Therefore CFD simulation study was carried out, details in Chapter 5.

Chapter 3 MATERIALS AND METHODS

Introduction

This Chapter describes the experimental material used in the study and the methods of main experiments and the analysis. The details of the microchannels are listed in §3.1. Straight channels include the purchased channel (near-semicircular shape, §3.1.1) and lab-made channels (circular and square, §3.1.2). Details of the junction channel are described in §3.1.3. §3.2 shows the equipment used for the main experimental and the set-up. The detailed procedures of the main experiment are in §3.3. The materials used in this study are described in §3.4 as well as the relevant measurements made to determine properties of the fluids such as the values of equilibrium and dynamic interfacial tension. Finally, the software used in the experiment and data analysis are listed in §3.5.

3.1 Microchannels

Four geometries of microchannel were investigated in this project (Table 3.1): (1) Near-semicircular straight channel (width × depth: 205 × 100 μm) (2) Circular straight channel (200 μm or 100 μm diameter). (3) Square straight channel with (200 × 200 μm). (4) T-junction channel (main channel width × depth: 390 × 190 μm, junction width × depth: 195 × 190 μm).

Table 3.1 Summary of microchannels used in project

	Cross-section shape	Size
Straight channel	Near-semicircular	width × depth: 205 × 100 μm
	Circular	200 μm diameter
		100 μm diameter
	Square	200 × 200 μm
T-junction channel	Wide	main channel width × depth: 390 × 190 μm junction width × depth: 195 × 190 μm

3.1.1 Straight near-semicircular channel

The near-semicircular channels are the straight channels on a microchip from Dolomite (Figure 3.1, Dolomite® Microfluidics). The cross-section of the channel is a near-semicircular shape with 205 μm in channel diameter and 100 μm in channel depth. The total length of channel is 22.5 mm. The microchip device consists of the chip itself and accessories that enable the inlet and outlet tubing to be securely and precisely attached to the channel. The picture of the microchip, a schematic of the cross-section of the channel and the accessories include a metal frame and two connectors shown in Figure 3.1.

(a) (b)

Figure 3.1 (a) Near-semicircular channel and relevant microchip. (b) Accessories for microchip: frame and connectors

Channels with both hydrophilic and hydrophobic surfaces are available from Dolomite® and are used in the project. Dolomite does not provide information on the exact coating reagent used to achieve hydrophobicity and relevant contact angle values as these are proprietary. However another product they supply (Pico-Glide™) is stated to be similar to the one used for coating the hydrophobic channel used in this project. The average contact angle of water drop on glass surface treated with Pico-Glide™ is 107 degrees. Other detailed specifications of the channel and microchip are listed in Table 3.2.

Table 3.2 Specifications of near-semicircular channel and relevant microchip

Internal channel cross- section	Width × Depth: 205 × 100 μm
Channel length	22.5 mm
Surface roughness (Ra)	5 nm
Microchip size (L × W × H)	22.5 × 15.0 × 4 mm
Microchip top layer thickness	2.0 mm
Microchip base layer thickness	2.0 mm
Material	Glass
Fabrication process	HF etching and thermal bonding

3.1.2 Straight circular and square channels

Both of these two geometries of microchannels were made in the laboratory. Two sizes of circular channels were fabricated. Preparations prior to the fabrication process include cutting glass capillaries to desired length, cleaning glass microscopic slides and capillaries.

The lab-made devices consist of a round (I.D. 200 μm, O.D. 330 μm or I.D. 100 μm, O.D. 170 μm) or square borosilicate glass capillary (200 × 200 μm), which serves as the main channel for carrying out experiment, inserted in a square capillary (400 × 400 μm) and the space between two capillaries are filled with water. These glass capillary microchannel devices are made by the following steps: (1) an outer square glass capillary (5.5 cm in length) is placed on a microscope slide, making sure one of the flat sides is placed flat on the surface of the microscope slide. Tape or sticker is used to temporarily fix the capillary to the desired position; (2) the capillary (round or square, approx. 7 cm in length) is inserted in the outer square capillary, making sure enough room is left for inlet tubing to be fitted on later; (3) inlet tubing (PTFE) is attached; (4) glue (5 Minute Epoxy, Devcon) is applied to seal one end of the outer square

capillary and the inlet tubing. From this step the device needs to be placed on the microscope as adjustment may be needed, before the glue is completely hardened, to make sure the inner capillary is placed in the middle of the outer one for better observing during experiment; (5) water is injected carefully to fill the space between the outer and inner capillary. It is sometimes very challenging to fill water to the whole length of the channel because at the step one end of the outer capillary is sealed. Thus in these cases water is filled to the length that is long enough to cover the area of observation.; (6) glue is applied to the seal the other end of outer capillary and further secure the position of all components. The device may needs to be placed onto microscope as further adjustment may be needed to ensure the inner capillary stays at a desired position. Finally the device is checked by injecting water into the inlet tubing to ensure no blockage or leakage occurs.

All glass capillaries used are made of standard borosilicate glass without any surface treatment.

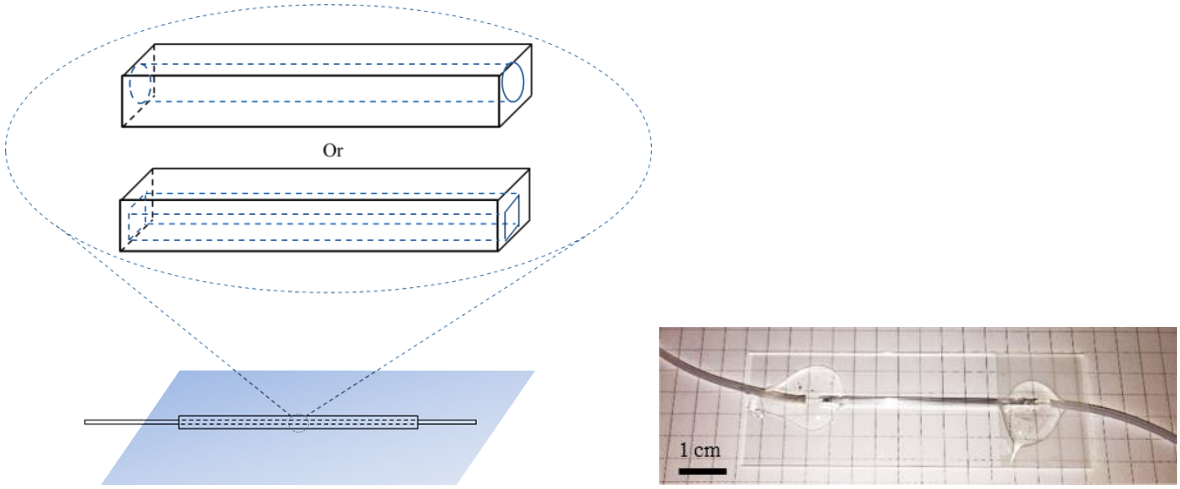

Figure 3.2 Straight circular or square channel

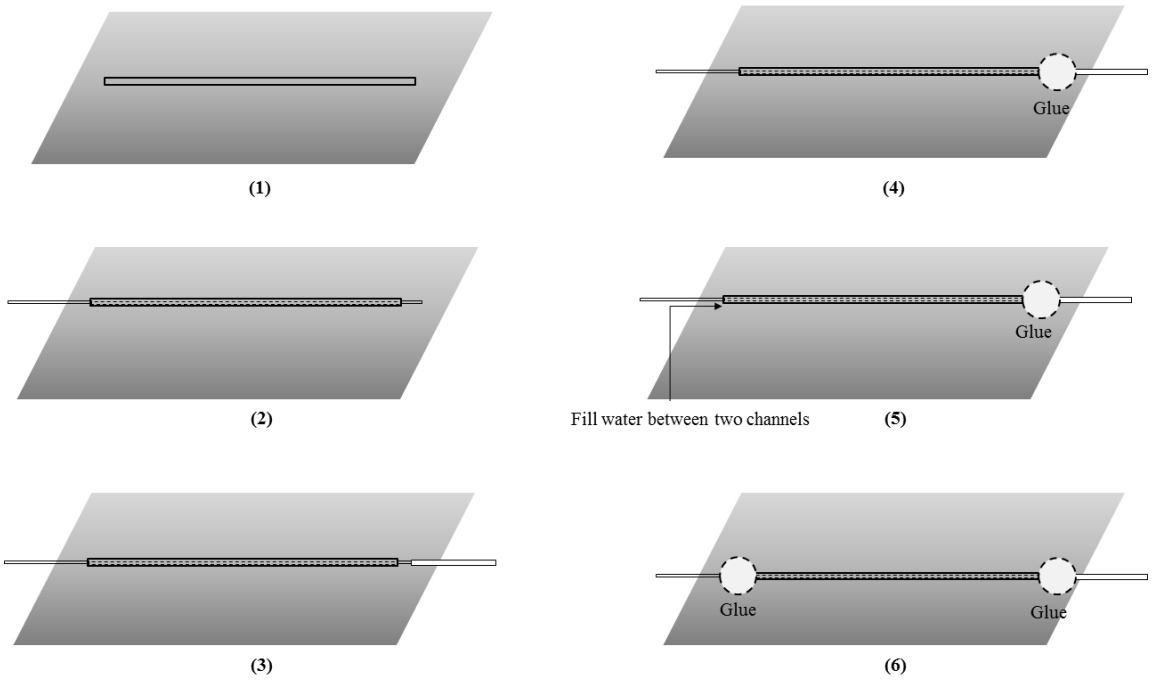

Figure 3.3 Fabrication process of circular or square channel

3.1.3 Junction channel

The T-junction channel is on another microchip from Dolomite. The T-junction channel consists of the junction part and the wide channel part. The wide channel part of the T-channel has size 390 × 190 μm (width × depth) and the junction has size 195 × 190 μm (width × depth). Note here the dimensions of the main wide channel is used to describe the channel dimensions and the dimensions of the wide channel were used in the calculation of parameters such as *Re* and *Ca*. The hydraulic diameter of the main wide channel is calculated to be 266.3 μm (Cross-section area, $A_c = 6.6\times10^4$ μm^2, perimeter $P = 996.6$ μm). Other detailed specifications are listed in Table 3.3.

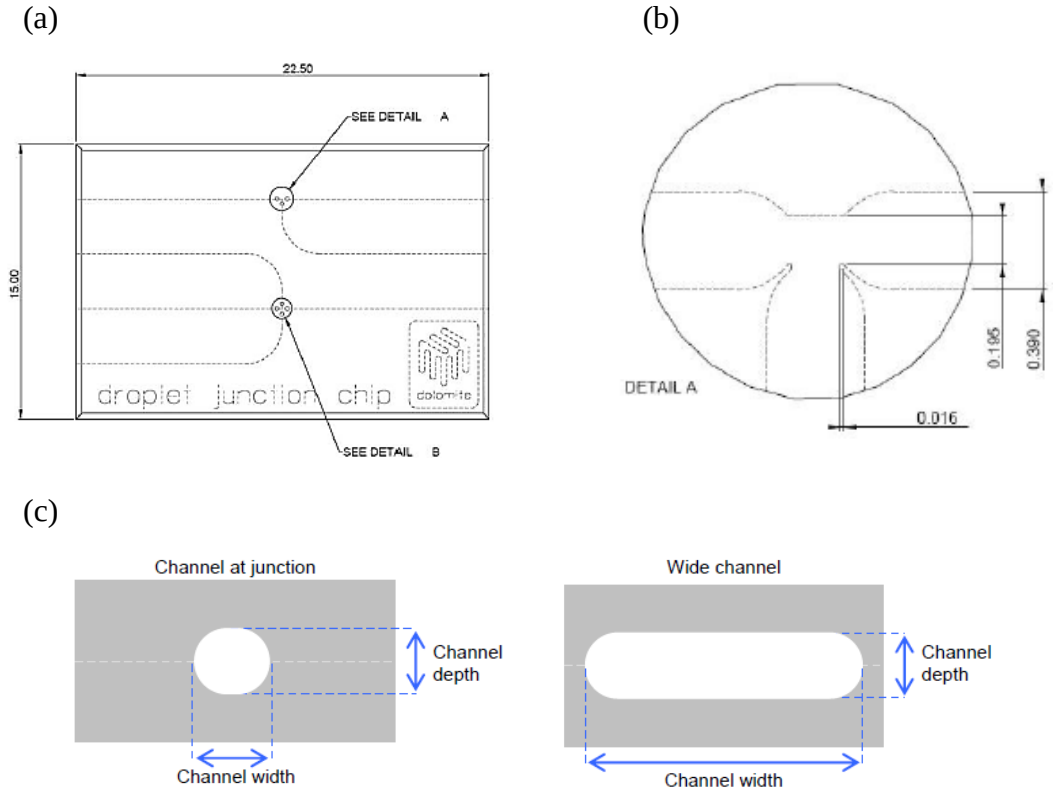

Figure 3.4 (a) The microchip with T-junction channel; (b) Detail at the T-junction (unit in figure: mm); (c) Cross-section shape of the main channel and channel junction.

Table 3.3 Specification of T-junction channel and relevant microchip.

Main channel cross-section	Width × Depth: 390 × 190 µm
Channel junction cross-section	Width × Depth: 195 × 190 µm
Channel length	22.5 mm
Channel length after junction	11.25 mm
Surface roughness (*Ra*)	5 nm
Microchip size (L × W × H)	22.5 × 15.0 × 4 mm
Microchip top layer thickness	2.0 mm
Microchip base layer thickness	2.0 mm
Material	Glass
Fabrication process	HF etching and thermal bonding

3.2 Experimental setup

Figure 3.5 shows experimental setup in this project. A microscope (Nikon TE2000-s) with a high-speed camera (Photron FASTCAM SA3 or SA5) attached to it is used for visualisation and image recording. The precise injection flowrate of fluid 2 is controlled by syringe pump (Harvard PHD 2000). Syringes with Luer-Lock tip™ from BD and needles with size 25G × 5/8" from AGANI™ are used. White light (Microtec Fibre Optics MFO-90) is used as light source illuminating the channel from above and experimental images are recorded through objective lens facing up towards the channel. Tests were carried out for an optimal set-up for illumination. Figure 3.6 shows the pictures of the microscope, syringe pump and high-speed camera used in this study.

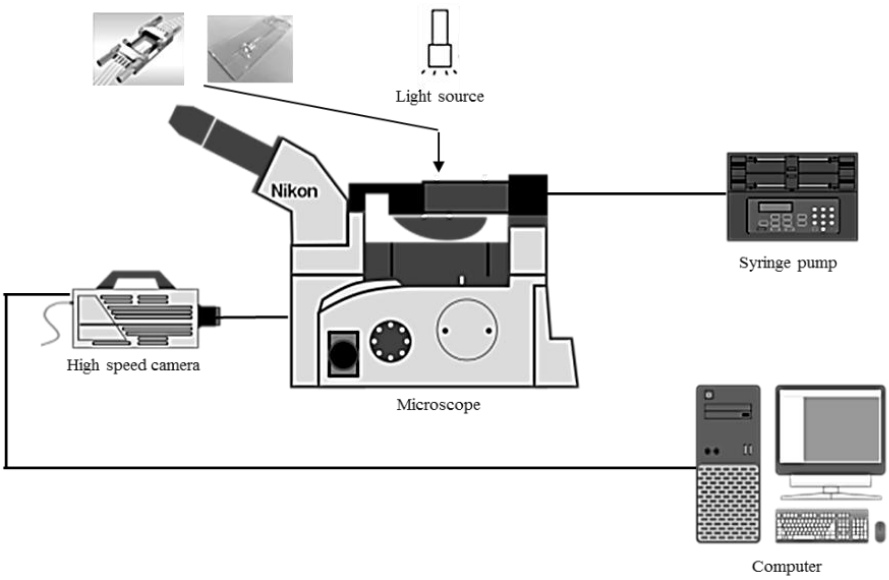

Figure 3.5 Fluid displacement experiment rig setup.

(a)

(b) (c)

Figure 3.6 (a) The Nikon TE2000-s microscope used in the study; (b) Harvard PHD 2000 syringe pump; (c) Photron FASTCAM SA3 camera.

Two models of high-speed camera used in this project are Photron FASTCAM SA3 and SA5. Recording resolution, frame rate and shutter speed are set depending on the channel being used and flowrate of flows. Typically frame rates of 3000 fps (frames per second) were chosen for slower flow recordings and 6000 fps was chosen for faster flow recordings. The combination of SA3 camera and the 4x objective lens provides a pixel size of 2.16 μm. The combination of SA5 camera and the 4x objective lens provides a pixel size of 2.57 μm. Therefor using in this study the minimum length the SA3 and SA5 models can resolve are 2.16 and 2.57 μm respectively. The SA5 model provides bigger resolution at the same frame rate or longer recording time at the same frame rate and resolution settings, compared to SA3. Some typical resolution, frame rate and recording time combination for the two models of camera are summarised in Table 3.4.

Table 3.4 Examples of camera settings.

Model	Frame rate (fps)	Max. resolution	Recording time using max. resolution (s)	Typical resolution used	Recording time using typical resolution (s)
SA3	3000	1024×1024	3.64	640×640	9.32
	6000	1024×1024	1.82	640×640	4.66
SA5	3000	1024×576	3.23	512×512	7.28
	6000	1024×256	3.64	512×512	3.64

All experimental images are recorded at the position of approximately 2/3 of the total channel length away from the inlet to ensure the flow phenomena are fully developed. Shah and Bhatti (1987) gave the entrance length for laminar flow: $L_e = 0.06ReD = 12.3$ mm using the diameter of channel and largest *Re* in this study, for turbulent flow: $L_e = 1.359Re^{1/4} = 7.6$ mm using the largest *Re*).

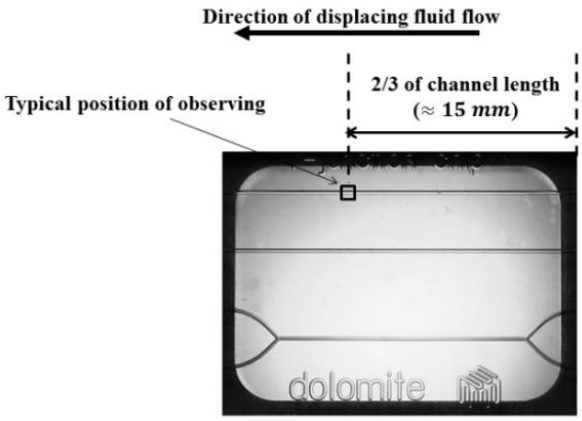

Figure 3.7 Typical position for recording images.

3.3 Experimental procedure

3.3.1 Straight channel procedure

Fluid displacement for straight channel experiment is carried out by prefilling the channel with the fluid to be displaced (fluid 1) from the inlet tubing and then the displacing fluid (fluid 2) is injected into the channel from the same tubing. To prevent air bubbles going into the channel three measures are taken. First the syringes for both the injection of fluid 1 and 2 are examined to ensure no air bubbles exist inside the syringes. After the channel is filled with fluid 1, the needle of the syringe containing fluid 1 is slowly pulled out from the inlet tubing while gently pushing the syringe, which ensures fluid 1 covers the tip of the tubing. In addition, the syringe pump carrying the syringe of fluid 2 is started pushing at a very low flowrate before the needle is connected to inlet tubing. Then the needle is attached to the inlet tubing swiftly when a droplet of fluid 2 is at the needle tip.

The range of flowrates used in different experiment are listed in Table 3.5, these flowrates are chosen based on the observed flow phenomena of unstable flows, explained in more detail in the Chapter 4.

Table 3.5 Range of flowrate used for different fluid displacement experiment in straight channels (μL min^{-1}).

		Immiscible	Miscible
Near-semicircular channel	Hydrophilic	8-3950	190-12000
	Hydrophobic	5-2400	-
Circular channel	200 μm	9-7200	50-9400
	100 μm	2-470	-
Square channel		25-4500	240-7200

After each fluid displacement experiment, the fluid 2 remaining in the channel needs to be completely cleared before starting a new experiment. This is carried out by first injecting clear water into the channel followed by the injection of air from a large (60 mL) syringe. Then the inlet tubing is replaced because it was found upon testing the water droplets at tubing surface tends to be difficult to be cleared out. Further injection of air is needed to achieve complete cleared channel, judged by observing live images from microscope. This preparation steps are also used for experiment with other channels.

In all experimental conditions fluid 2 is dyed with water soluble dye Nigrosin (10 g L^{-1}), which is a non-transparent black colour dye. PTFE tubing (I.D. 0.5 mm, O.D. 1.6 mm) is used to connect syringe and microchip for both inlet and outlet for all experiment where a microchip is used.

3.3.2 Junction channel procedure

Two injection modes are carried out for T-junction channel experiment. Figure 3.8 shows the first mode. The channel end on the junction side is blocked by close a valve attached to the tubing connected to that end. The valve used is a 2-way in-line valve, supplied to fit two 1/16” O.D. tubing, shown in Figure 3.8. The tubing length between microchip and valve is fixed at 5 cm.

Displacement experiment is carried out by prefilling the whole T-junction channel with Fluid 1 before closing the valve. Then Fluid 2 is injected into the channel from the inlet at desired flowrate controlled by syringe pump.

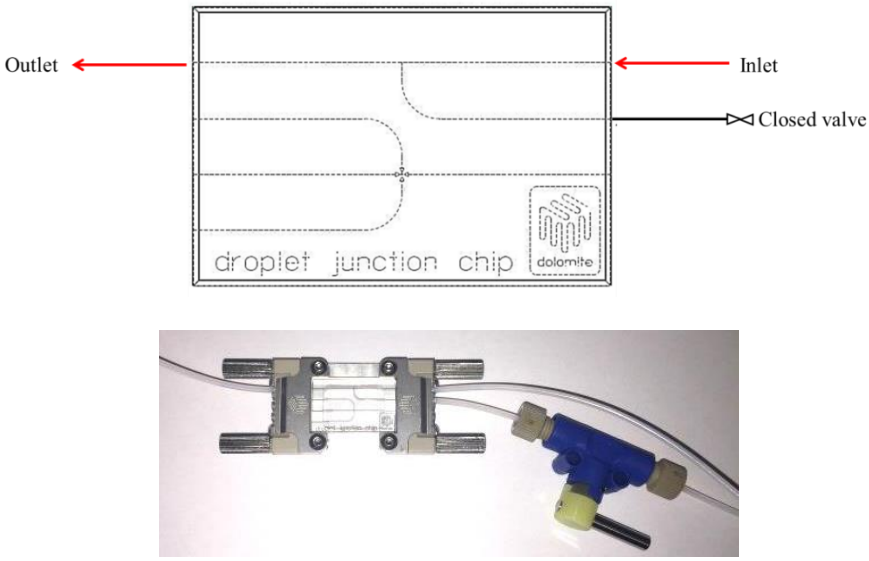

Figure 3.8 T-junction injection mode 1.

Figure 3.9 shows the second injection mode for T-junction experiment. One of the straight channel ends is blocked by a closed valve. Displacement experiment is carried out by prefilling the whole channel with fluid 1 before closing the valve. Then fluid 2 is injected into the channel from the inlet.

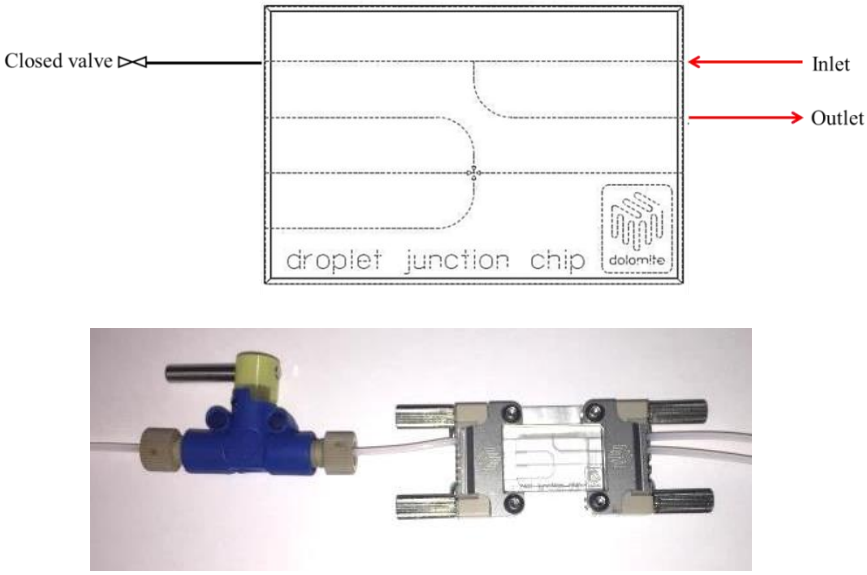

Figure 3.9 T-junction injection mode 2.

3.4 Materials

3.4.1 Fluid pairs

Straight channels

Both immiscible and miscible fluid pairs have been studied with various viscosity ratios. Viscosity ratio values throughout this work are given as the viscosity ratio of fluid 1 to fluid 2. Table 3.6 lists the materials used in the experiments. Silicone oils and water-soluble dye Nigrosin (powder form) are purchased from Sigma-Aldrich Co. LLC. Glycerol solutions are made using 98% wt. glycerol (ReAgent, UK) and viscosity, density data of glycerol-water solution from the Dow Chemical Company. All data are valid at 20-25ºC. SDS stands for Sodium Dodecyl Sulfate and PmP stands for Polyether modified Polysiloxane.

Solutions with SDS and PmP are prepared by adding surfactant and mixing for at least 30 minutes. In all experiment SDS solution concentration is two times its critical micelle concentration (CMC) which is 4.7 g L^{-1} and PmP solution concentration is ten times its CMC which is 1.8 g L^{-1}. Samples are dyed by adding Nigrosin powder into solution and mixing for at least two hours. In all experiment, Nigrosin dye concentration is 10 g L^{-1}.

Table 3.6 materials used in the project.

Fluid 1	Fluid 2	Kinematic Viscosity ratio
100 cSt Silicone oil	Water	100
	2 cSt Glycerol solution (26.0% wt.)	50
	5 cSt Glycerol solution (48.5% wt.)	20
	Water+SDS	100
	2 cSt glycerol solution+SDS	50
	5 cSt glycerol solution+SDS	20
	Water+PmP	100
50 cSt Silicone oil	Water	50
	Water+SDS	50
	2.5 cSt glycerol solution (32.0% wt.)	20
	2.5 cSt glycerol solution+SDS	20
20 cSt Silicone oil	Water	20
	Water+SDS	20
100 cSt Glycerol solution (86.0% wt.)	water	100
	2 cSt Glycerol solution	50
	5 cSt Glycerol solution	50

Junction channel

Three fluid pairs were used in this chapter, all with viscosity ratio of 100. For all three fluid pairs, fluid 1 was always 100 cSt silicone oil and fluid 2 was either water or surfactant-laden

glycerol solutions. SDS with concentration 2CMC was used and the other surfactant used was Polyether-modified Polysiloxane (EVONIK, Ltd., noted as PmP). The concentration of PmP solution used was 10 times its CMC, 1.8 g L^{-1}, which was chosen for improved accuracy due to the low CMC value for PmP.

3.4.2 Interfacial tension measurement

For immiscible fluid pairs, interfacial tensions (IFT) values are measured using a tensiometer (Krüss K100, Figure 3.10) equipped with Wilhelmy plate. Measurement of IFT was made for at least 20 minutes to ensure the IFT measured was at equilibrium. It was found the Nigrosin dye has an effect on the IFT values thus for each immiscible fluid pair, IFT measurement was carried out once without dye and once with dye. IFT values between 100 cSt silicone oil and water dyed with different concentration (0.1, 1, 5, 10 g L^{-1}) of Nigrosin were also measured. In order to test the effect of surfactant concentration on the IFT values, IFT measurements were made between the fluids with fluid 2 containing the surfactant. For SDS, concentration of 2 × CMC (4.7 g L^{-1}) and 10 × CMC (23.5 g L^{-1}) are tested, for PmP concentration of 10 × CMC (1.8 g L^{-1}) and 20 × CMC (3.6 g L^{-1}) were tested. All IFT values measured are shown in the experimental results section.

Figure 3.10 Krüss K100 tensiometer

3.4.3 Dynamic surface tension measurement

Short timescale surface tension depends on the surface age and this was measured using a SINTERFACE BPA-1S Maximum Bubble Pressure Tensiometer (Figure 3.11). The technique was first proposed in 1851 (Simons, 1851). Samples of Nigrosin water solution, water+SDS solution without dye, water+SDS solution with Nigrosin dye and water+PmP solution were measured. All surface tension values measured are shown in the experimental results section (§4.1 and §6.1).

Figure 3.11 SINTERFACE BPA-1S maximum bubble pressure tensiometer

In order to study how stable the SDS and PmP solutions were in terms of surface properties, stability tests were carried out by measuring the short time surface tension immediately, 2 days, 5 days and 9 days after the sample being prepared. The samples were stored in room temperature without direct exposure to sunshine. The equilibrium surface tension value was calculated from all equilibrium values from all measurement.

3.5 Software

Experimental videos were captured using the Photron FASTCAM View (PFV) software from high-speed camera supplier, Photron. PFV is able to precisely select desired capture speed, resolution and shutter speed. It allows captured videos to be saved from selected start and end frame. PFV also served very well as a video player and editor, being able to play videos frame by frame or at selected frame rate. Image J was used to perform some of the measurement and video editing. Matlab was used to perform image processing such as background subtraction and interface identification. Examples of the use of Image J and Matlab image processing are shown below.

3.5.1 Image J and Matlab

The radii of tip curvatures for immiscible displacement were measured by fitting a circle at tip position (Figure 3.12). Image processing software Image J was used: multiple points along the tip of fluid 2 were first chosen manually before Image J could fitting the circle. The error could come from the image capturing method, i.e. the size of pixel and measurement error. Therefore for each experimental image, at least three repeated measurement were carried out. For some experimental images with relatively low contrast between background and target flows, the background image was removed from target image and binarized using Matlab, an example is shown in Figure 3.13.

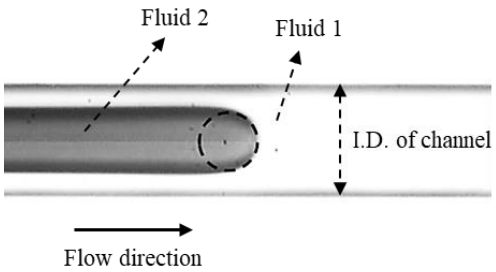

Figure 3.12 Example image of the finger shape flow at the tip of fluid 2 and the measurement of curvature radius (dashed circle).

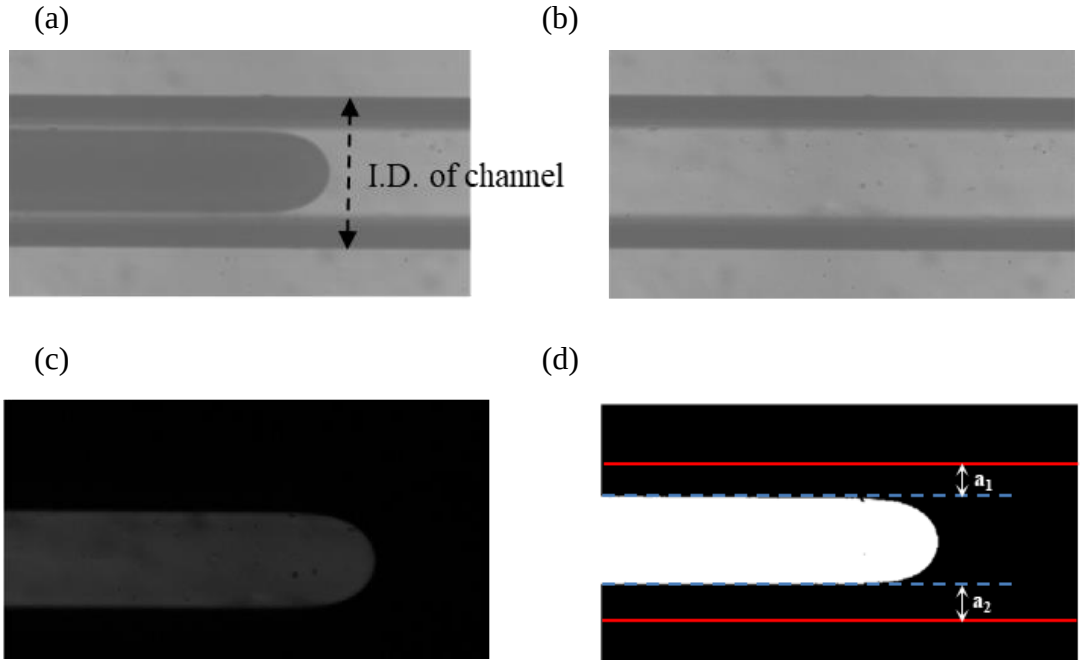

Figure 3.13 Image treatment for better analysis, (a): original target image. (b): background image captured before experiment starts, (c): remove background image from target image, (d): binarized image.

The constant film thickness region was first identified by examining the recorded video, this region usually comes shortly after the tip of fluid 2. The film thickness in this region was used for film thickness measurement, which was referred as initial film thickness in some reported studies (Li, et al., 2013). As shown in Figure 2.13d, the red lines are the position of channel wall by overlapping image in Figure 2.13a and d. The film thickness measurement was carried out by measuring the film thickness at both sides (a_1 and a_2) then take the average value of the two. At least three repeats were conducted. The distortion of channel wall was checked and neglected in this study.

Matlab codes (codes in Appendix B) were also written to identify the interfaces between fluid 1 and 2 for immiscible fluid displacement cases. The stable and axisymmetric unstable regimes here are chosen to study the time it takes to clear all fluid 1 in the channel and the frequency of the appearance of the pinching unstable parts. Figure 3.14a shows the strategy of determining

interfaces by Matlab: a cross-section line is first set at the position very close to the left end of the images (shown as a red line); then Matlab detects the grey scale values in each pixel at this line across the width of the channel; the difference in grey scale values between the adjacent pixels determines the positions of the two interfaces: the positions where maximum and minimum in grey scale differences appear are the positions of the two interfaces. The detailed Matlab codes are in the appendices. By continuously determine the interfaces at that position for each frames of the experimental recording, we then can obtain the information of how the interfaces change. Figure 3.14b is an example result image showing the two interfaces (red and blue curves) identified by Matlab and how close it is to the actual image.

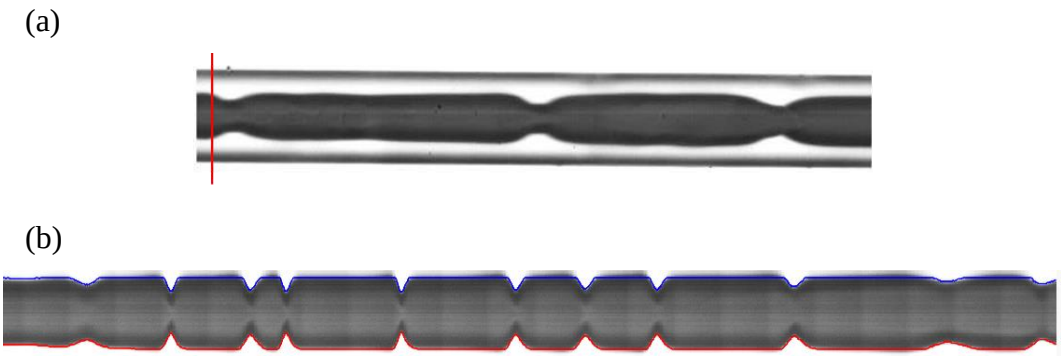

Figure 3.14 (a) The position where the interfaces between fluid 1 and 2 is identified; (b) An example of the interfaces identified by Matlab (blue and red lines). The video processed was from fluid experiment of pair of 100 cSt silicone oil displaced by 5 cSt glycerol solution, Ca_2 = 0.54, in near-semicircular channel.

After the interfaces are identified, the values of film thickness can then be calculated if the pixel size can be provided. By using the camera speed in frames per second, the information of flow times can also be obtained.

Computational Fluid Dynamic (CFD) simulations were carried out using ANSYS Fluent (version 16.1) and Tecplot was used for some data process such as velocity subtraction. Details regarding simulation work of this study are in Chapter 5.

Chapter 4 EXPERIMENTAL STUDIES OF FLUID DISPLACEMENT USING STRAIGHT MICROCHANNELS[1]

Introduction

In this chapter, the experimental results of fluid displacement in straight channels are described. The aims of this work were to understand the dynamics of liquid-liquid flows in the fluid displacement process such as the fluid film left on wall and the interfacial phenomena at the interface between the two fluids. Equilibrium interfacial tension measurement made on the working fluids are given and analysed in §4.1 as well as the measurements made to check for the effect of dye addition upon the interfacial properties, §4.1 lists/describes dynamic surface tension measurements carried out and the estimation method used to attribute dynamic effects to the interfacial tension values. Experimental results using immiscible fluid pairs are explained in §4.3, in which the liquid film thickness left on wall is discussed in §4.3.1, fluid 2 tip curvature is discussed in §4.3.2. §4.4 describes the interfacial instabilities observed during the displacement processes. The effects of viscosity ratio, fluid 2 viscosity, surfactant in fluid 2 and channel geometries and sizes are discussed in §4.3.1, §4.3.2 and §4.4. §4.4.2 describes the results using Matlab image processing. The results of miscible fluid pairs are in §4.5, mainly focused on the interfacial instabilities between two fluids.

[1] Some of the work presented in this chapter has been published in Lu, Y., Kovalchuk, N.M., Simmons, M.J.H. Residual film thickness following immiscible fluid displacement in non-circular microchannels at large capillary number, *AIChE J*, [accepted on 2nd April 2018].

4.1 Interfacial tension between fluid 1 and 2

IFT measurement results carried out using Krüss K100 tensiometer described in §3.4.2 are listed in Table 4.1. Measurement was carried out using fluid 2 with and without Nigrosin to check on the impact of the surface activity of the dye. Water dyed with various concentrations of Nigrosin have also been measured. Concentration of 10 g L^{-1} is chosen to be used in all later measurements and experiments to ensure the contrast different between the dyed and undyed fluids. It was found there were no significant differences on the interfacial tension (IFT) values by varying the surfactant concentration as long as the concentration is above CMC. As described in §2.3.1, properties including interfacial tension becomes constant when the concentration of surfactant exceed its CMC. Concentration of 2CMC (4.7 g L^{-1}) for SDS was used because of its low CMC value and operational accuracy, are chosen in all later measurement and experiment. Estimations of surfactant balance using the maximum adsorption values show that for both these two surfactant solutions, the percentages of surfactant at the interface do not exceed 2%, meaning the surfactant concentrations in fluid 2 bulk are close to their initial values and are above CMC. The IFT values between silicone oil and undyed water (39.5 mN m^{-1}) are in reasonable agreement with literature value of Kanellopoulos and Owen (1971) (~ 42.6 mN m^{-1}). The IFT values between silicone oil and undyed SDS water solution (12.2 mN m^{-1}) are also in good agreement of literature value (~ 12 mN m^{-1}, Kanellopoulos and Owen (1971)). The IFT values between silicone oil and water dyed with Nigrosin (26.7 mN m^{-1}) are in good in agreement with literature value 25 mN m^{-1} (Nowak, et al., 2016).

Table 4.1 IFT (interfacial tension) measurement results

Fluid 1	Fluid 2		Interfacial tension (mN m^{-1})
100 cSt silicone oil	2 cSt Glycerol solution	No dye	35.9
		Dyed with Nigrosin 10g L^{-1}	24.5
	5 cSt Glycerol solution	No dye	33.9
		Dyed with Nigrosin 10g L^{-1}	25.4
	Water	No dye	39.7
		Dyed with Nigrosin 0.1 g L^{-1}	34.1
		Dyed with Nigrosin 1 g L^{-1}	31.7
		Dyed with Nigrosin 5 g L^{-1}	30.1
		Dyed with Nigrosin 10 g L^{-1}	27.1
	Water+SDS	No dye	12.9
		Dyed with Nigrosin 10g L^{-1}	9.9
	2 cSt glycerol solution +SDS	No dye	13.3
		Dyed with Nigrosin 10g L^{-1}	10.7
	5 cSt glycerol solution +SDS	No dye	13.7
		Dyed with Nigrosin 10g L^{-1}	11.3
	Water+PmP	No dye	5.7
		Dyed with Nigrosin 10g L^{-1}	5.6

Table continued on next page

50 cSt Silicone oil	Water	No dye	40.0
		Dyed with Nigrosin 10g L^{-1}	27.6
	2.5 cSt Glycerol solution	No dye	29.4
		Dyed with Nigrosin 10g L^{-1}	26.1
	Water+SDS (2CMC, no dye)	No dye	11.9
		Dyed with Nigrosin 10g L^{-1}	7.5
	2.5 cSt Glycerol solution+SDS	No dye	13.8
		Dyed with Nigrosin 10g L^{-1}	10.6
20 cSt Silicone oil	Water	No dye	38.9
		Dyed with Nigrosin 10g L^{-1}	27.0
	Water+SDS	No dye	11.7
		Dyed with Nigrosin 10g L^{-1}	9.0

4.2 Dynamic surface tension measurement

4.2.1 Nigrosin dye and surfactant SDS

Standard surface tension measurement is carried out using SINTERFACE BPA-1S max bubble pressure tensiometer, as described in §3.4.3 to see if there is a dynamic surface tension effect on the fluid being used in this project. Results are shown in (Figure 4.1 a and b), all surface tension measurement plots are using the life time as surface age. No apparent dynamic effects are observed from both samples containing water dyed with Nigrosin and SDS water solution

(no dye) within the time scale of the measurement of the tensiometer. Water dyed with 10 g L^{-1} Nigrosin has an equilibrium surface tension of 72 mN m^{-1}, which is good agreement of literature value of ~ 71.2 mN m^{-1} (Alvarez, 1998) for pure water. SDS solution (no dye) has an equilibrium surface tension of 40 mN m^{-1}, which is in good agreement with literature value of ~40 mN m^{-1} (Iliev and Dushkin, 1992).

From the stability test (Figure 4.1c) carried out on SDS water solution (dyed with Nigrosin), it was found the surface tension did not change significantly during 9 days of storage and it has an equilibrium surface tension of 37.4 mN m^{-1}. This finding is consistent with other similar stability test (Lunkenheimer and Czichocki, 1993). The standard deviation value of all equilibrium surface tension values measured is 0.23. Based on this result all experiments with surfactant SDS were carried out using samples with an age less than one week. A slightly decrease in surface tension values is found for the sample for stability test, indicating the surface tension drops from 42.5 mN m^{-1} at surface age ~ 0.015 s.

(a)

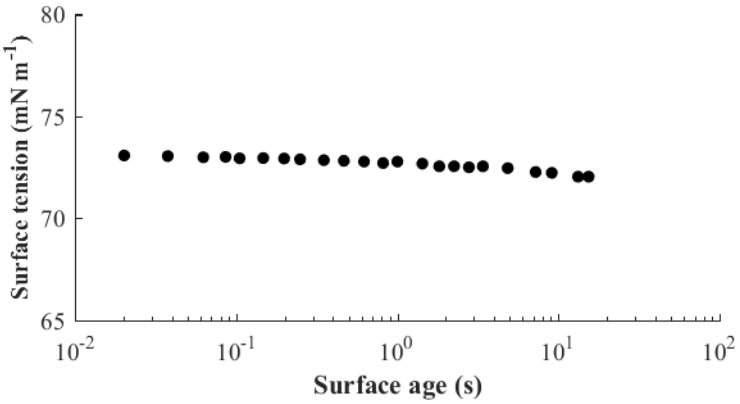

(b)

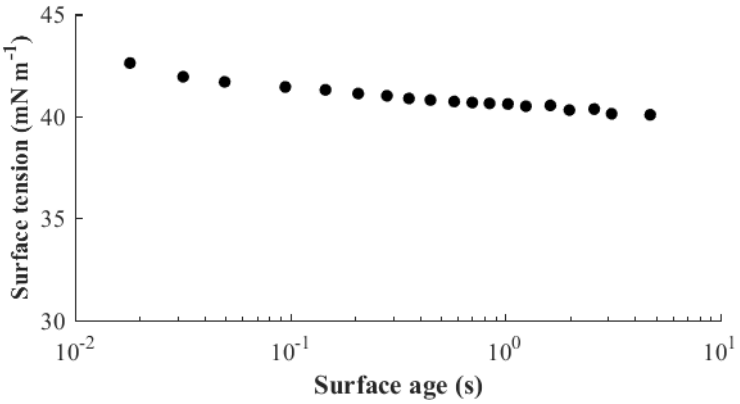

(c)

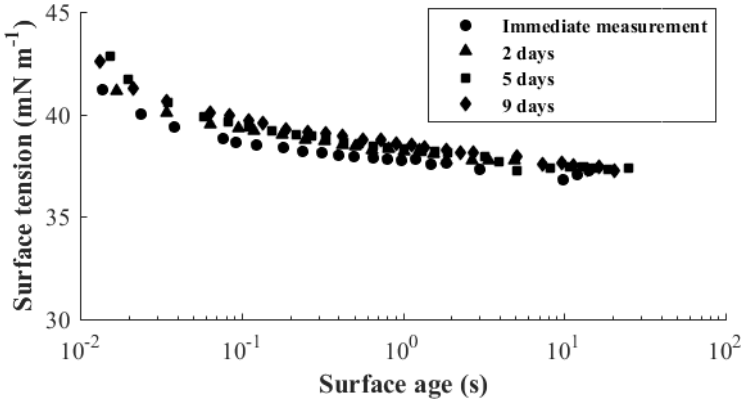

Figure 4.1 Surface tension measurement of (a) water (dyed); (b) Water+SDS (2CMC, without dye) solution; (c) Water+ SDS (dyed) solution.

Short-time mode surface tension measurement, using the same equipment as above, was carried out to measure the surface tension values at surface age smaller than 0.01 second, which is shown in Figure 4.2 . Dynamic surface tension effects are more observable at short surface ages, a drop in the value from 50.5 mN m^{-1} at a surface age of 0.7 ms to 38 mN m^{-1} at surface age of 0.1 s can be observed.

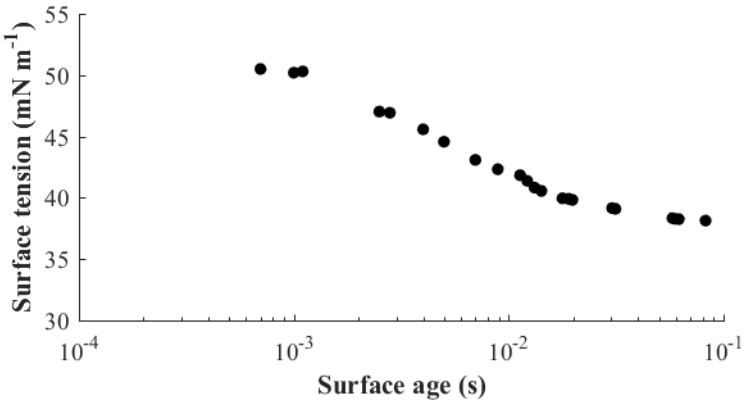

Figure 4.2 Short-time mode surface tension measurement of SDS water solution (concentration two times CMC, dyed with 10 g L^{-1} Nigrosin).

Estimation of dynamic interfacial tension

Thermodynamic equilibrium interfacial tension values are measured using the Wilhelmy plate method. Since there is no equipment available to directly and accurately measure the dynamic interfacial tension values, dynamic interfacial tension values were estimated using the following approach, as reported by Kovalchuk, et al., (2018):

$$\frac{\gamma_0 - \gamma_s}{\sigma_0 - \sigma_s} = \frac{\gamma_0 - \gamma_{st}}{\sigma_0 - \sigma_{st}} \qquad \text{(Equation 4.1)}$$

Where γ_0 is the measured surface tension value of dyed water without surfactant, γ_s is the equilibrium surface tension value of water+surfactant solution (dyed), σ_0 is the interfacial

tension value measured between fluid 1 and dyed water without surfactant, σ_s is the equilibrium interfacial tension value measured between fluid 1 and water + sufactant solution (dyed), γ_{st} is the measured surface tension value of water + surfactant solution (dyed) at specific surface age *t*, σ_{st} is the estimated interfacial tension value between fluid 1 and water + surfactant solution (dyed) at surface age t.

4.3 Immiscible fluid pair displacement

In these experiments, silicone oils with 100, 50 and 20 cSt kinematic viscosity are chosen as fluid 1 (displaced fluid) and water, glycerol solutions with 2 and 5 cSt viscosity are chosen as fluid 2 (displacing fluid). SDS is introduced into fluid 2 in some experiments to study to influence of surfactant.

4.3.1 Liquid film thickness left on wall

The thickness of liquid film left on wall after the advance fluid 2 tip was measured by image J, as described in §3.5. It is noted that the film thickness is dynamic throughout the whole displacement process this the measurement is only taken at the position right after the finger shape fluid 2 tip, which is in some literature called the initial film thickness (Li, et al., 2013).

It has been widely accepted that the liquid film left on wall is not affected greatly by viscosity ratio especially for larger viscosity ratio (>10) cases (Soares, et al., 2005), thus capillary number based on the properties of fluid 1 is used, which calculated from:

$$Ca_1 = \frac{\mu_1 u_2}{\sigma} \qquad \text{(Equation 4.2)}$$

Where μ_1 is the dynamic viscosity of fluid 1, u_2 is the superficial velocity of injected fluid 2 and σ is the interfacial tension between fluid 1 and 2. The superficial velocity of fluid 2 is:

$$u_2 = \frac{Q_2}{A_C} \qquad \text{(Equation 4.3)}$$

Where Q_2 is the injection flowrate of fluid 2, A_c is the cross-section area of channel. However, this superficial velocity is not accurate enough to represent the velocity of fluid 2 especially at initial stage of the injection. This is because fluid 2 passes through a channel with an effectively smaller cross-sectional area due to the (near) stagnant layer of fluid 1 present on the channel walls. The actual or real velocity of fluid 2, u_2' is calculated from dividing the injection flowrate by the cross-section flow area of fluid 2 at the cross-section plan where film thickness is measured. For circular and square channel, it is assumed the cross-section shape of fluid 1 is always circular or very close to circular. For near-semicircular channel the strategy of estimating the cross-section shape of fluid 2 is as follows: when film thickness is small, the cross-section shape of fluid 2 is assumed to be an ellipse shape with the minor axis being the height of channel and the major axis being half the width of fluid 2 (Figure 4.3a); when film thickness is larger than a critical value, the cross-section shape of fluid 2 is assumed to be circular (Figure 4.3b). This critical thickness value is the calculated by half of the value of the width of channel subtract the height of channel which is 52.5 μm.

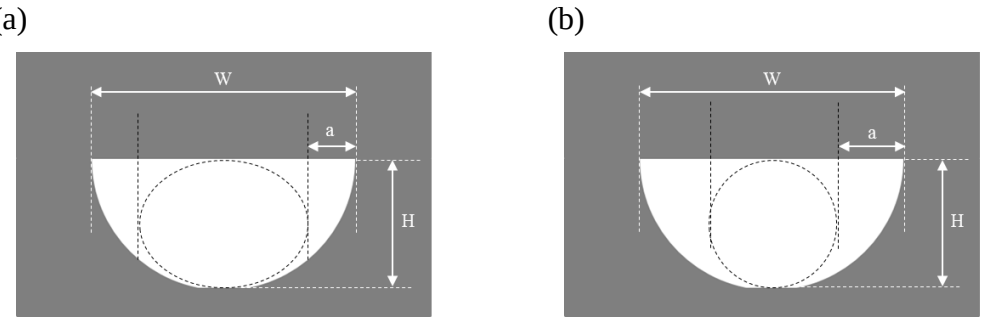

Figure 4.3 Assumptions of the cross-section shape of fluid 2 in near-semicircular channel: (a) Ellipse shape (b) Circular shape. *a* in the figure is the measured apparent film thickness. *W* and *H* are the width and height of channel.

The modified mean velocity of fluid 2 is calculated from:

$$u_2^{'} = \begin{cases} Q_2/\pi(\frac{H}{2})(\frac{W-2a}{2}) & \text{(Near-semicircular channel, a<52.5 μm)} \\ \frac{Q_2}{\pi(\frac{W-2a}{2})^2} & \text{(Near-semicircular channel, a ≥ 52.5 μm)} \\ \frac{Q_2}{\pi(\frac{D-2a}{2})^2} & \text{(Circular and square channel)} \end{cases} \quad \text{(Equation 4.4)}$$

Where a is the measured apparent film thickness, H is the height of semicircular channel and W is the width of semi-circular channel. And the velocity-modified capillary number Ca_1' is:

$$Ca_1^{'} = \frac{\mu_1 u_2^{'}}{\sigma} = \begin{cases} \frac{\mu_1 Q_2}{\pi\sigma(\frac{H}{2})(\frac{W-2a}{2})} & \text{(Near-semicircular channel, a<52.5 μm)} \\ \frac{\mu_1 Q_2}{\pi\sigma(\frac{W-2a}{2})^2} & \text{(Near-semicircular channel, a ≥ 52.5 μm)} \\ \frac{\mu_1 Q_2}{\pi\sigma(\frac{D-2a}{2})^2} & \text{(Circular and square channel)} \end{cases}$$

(Equation 4.5)

For the cases with surfactant added into fluid 2, the interfacial tension value in the equation above depends on the surface age. The estimated dynamic interfacial tension values are used in these calculations. The surface age is estimated by calculating the time it takes for fluid 2 to travel from the inlet to the outlet of channel.

Due to the limitation of experimental set-up, recorded experimental images represent a projected view of the flows therefore only the widest part of flows can be directly seen from images. However for the near-semicircular channel, the film thickness measured by measuring the distance of the widest part of fluid 2 (i.e. apparent film thickness) to the width of channel

obviously does not represent the film thickness at all positions of channel very well. Therefore a *mean film thickness*, a_{mean}, is proposed for near-semicircular channel:

$$a_{mean} = \frac{A_c - A_2}{\frac{1}{2}(P_c + P_2)} \qquad \text{(Equation 4.6)}$$

Where A_C and P_C are the area and perimeter of the cross-section of channel, A_2 and P_2 are the area and perimeter of the cross-section fluid 2. Combining the assumption of the cross-section shape of fluid 2 described above (Figure 4.3), the mean film thickness is calculated from dividing the cross-section area of fluid 1 left on wall by the average length of the perimeters of the contour of fluid 2 and the perimeter of the cross-section of channel:

$$a_{mean} = \begin{cases} \dfrac{A_C - \pi(\frac{H}{2})(\frac{W}{2} - A)}{\frac{1}{2}\{p_c + (\pi(3((\frac{W}{2} - A) + \frac{H}{2}) - \sqrt{(3(\frac{W}{2} - A) + \frac{H}{2})((\frac{W}{2} - A) + \frac{3H}{2})})\}} & (a < 52.5\ \mu m) \\ \dfrac{A_C - \pi(\frac{W}{2} - A)^2}{\frac{1}{2}(p_c + \pi(W - 2a))} & (a \geq 52.5\ \mu m) \end{cases}$$

(Equation 4.7)

The film thicknesses are normalised by the channel hydraulic diameter. The modified capillary number, calculated from Equation 4.5, is chosen to represent more accurate estimation of the viscous effects. The deviation of Ca_1' from Ca_1 based upon the superficial velocity of fluid 2, obviously depends upon the film thickness as shown in Figure 4.4 for three channel geometries for surfactant-free fluid pairs. The ratio of Ca_1' to Ca_1 increases as film thickness increases to a maximum value of ~ 2.6 over the studied range.

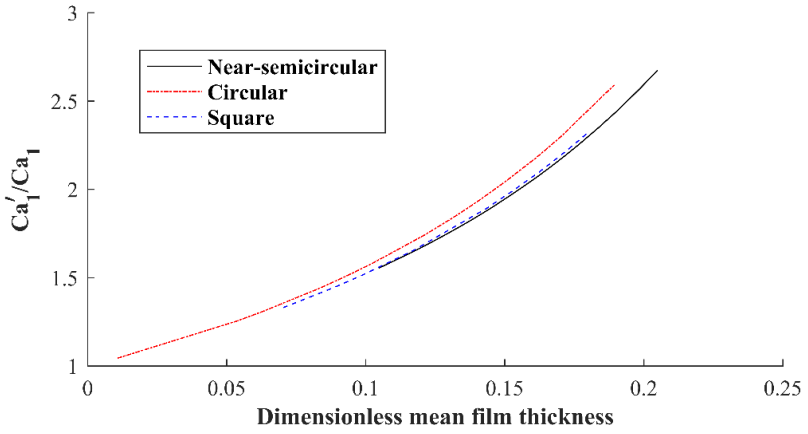

Figure 4.4 The ratio of $Ca_1{}'$ to Ca_1 plotted against dimensionless mean film thickness for near-semicircular, circular and square channel using surfactant-free fluid 2.

Effect of viscosity ratio

Results from experiments using the near-semicircular channel are used to study the effects of viscosity ratio ($\eta = \nu_1/\nu_2$, where ν_1 and ν_2 are the kinematic viscosities of fluid 1 and 2), surfactant and fluid 1 viscosity on the film thickness left on the wall.

The effect of viscosity ratio between fluid 1 and 2 is first studied. Figure 4.5a are the plots of the dimensionless film thickness, which is calculated from the measured apparent film thickness over the hydraulic diameter of the channel, against Ca_1' for the cases of using 100 cSt silicone oil as fluid 1 and 3 fluids as fluid 2 to achieve viscosity ratio of 100, 50 and 20, Figure 4.5b are the plots for cases using 50 cSt silicone oil as fluid 1 and viscosity ratios of 50 and 20. Results using 20 cSt silicone oil and water and fluid 1 and 2 are shown in Figure 4.5c. Fluid 2 without SDS added and with SDS added are both shown. It can be seen from the graph that the data points from three viscosity ratios follows the same trend and therefore the effect of viscosity ratio is neglected. This is also further confirmed from experimental results from circular and square channels. Thus experimental data using the same fluid 1 but different fluid 2 are grouped for the discussion of film thickness. The only effect from using different fluid pairs, although

not significantly, is the variation of interfacial tension values, which can be seen from Table 4.1.

(a)

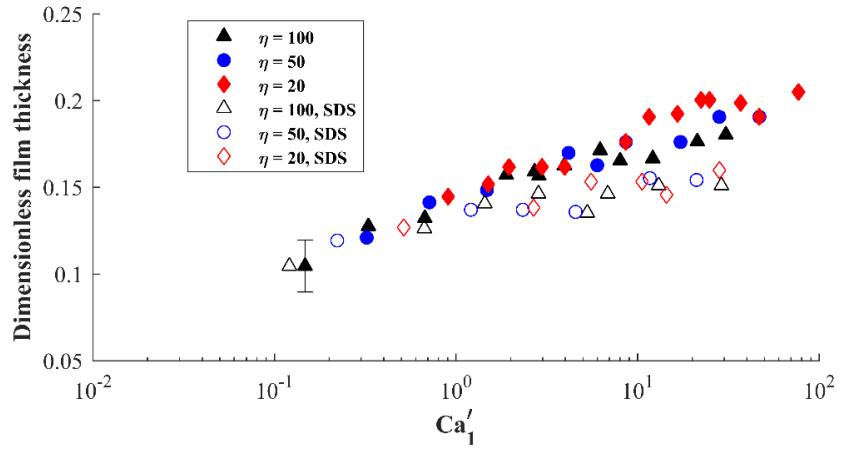

(b)

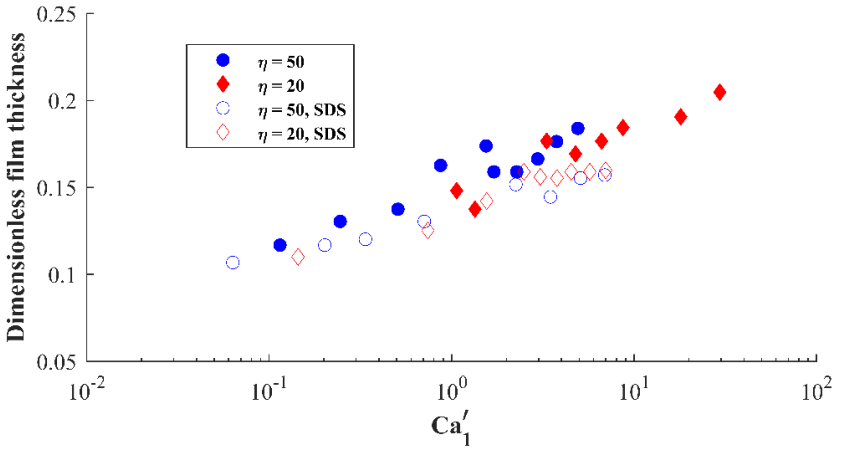

(c)

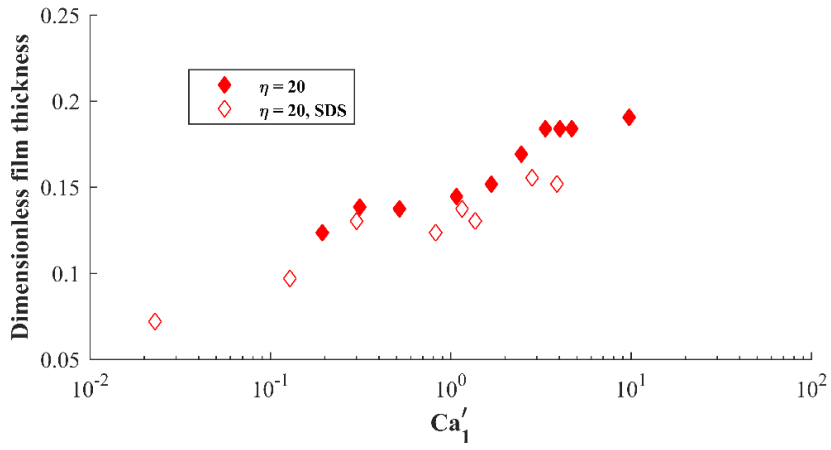

Figure 4.5 Apparent film thickness of three viscosity ratios (the same fluid 1) in near-semicircular channel for (a) 100 cSt silicone oil as fluid 1, (b) 50 cSt silicone oil as fluid 1 and (c) 20 cSt silicone oil as fluid 1. Results using both SDS-free and SDS-laden fluid 2 are shown.

The values of dimensionless film thickness for the near semi-circular channel are compared with literature correlations (reviewed in §2.2.4) to validate the assumptions made above on the shape of the interface between fluid 1 and fluid 2. The dimensionless apparent thickness and mean film thickness are plotted in Figure 4.6 along with literature correlations. Since the effect of viscosity ratio between fluid 1 and 2 is insignificant, the results using 100 cSt silicone oil as fluid 1, which contain three viscosity ratios, are grouped into a single data set. The same has been done to the results for 50 cSt silicone oil as fluid 1, which contains two viscosity ratios. The distance from the inlet to the position where film thickness is measured in the present study is around 17 mm, which is more than 100 times the hydraulic diameter of the near-semicircular channel. This means these literature models, most of which are developed from the measurement or analysis of the film thickness of long bubbles, can be used for comparison. Note the model developed by Irandoust and Andersson (1989) used total average velocity of the two phases, wheres all other models presented in Table 2.3 use bubble velocity to define the capillary number. This is the reason that the results of Irandoust and Andersson (1989) show a shift to the left on graph compared to other models because using bubble velocity results in an increase in the capillary number because bubble velocity is considerably larger than the total flow velocity. Also they studied uprising bubbles in vertical channels where buoyancy influences results.

The large deviation from the literature data indicates that the apparent film thickness does not represent well the overall film thickness across the cross-section of the near-semicircular channel, as expected; the mean film thickness shows good agreement. Using the Taylor's law equation developed by Aussillous and Quere (2000), the average variation between predicted dimensionless film thickness and experimental data, which is calculated from the absolute difference in values to the predicted value ratio, is 7%. Therefore it is proposed that the

assumption of elliptical and circular cross-section shape of fluid 2 interface and the mean film thickness is an acceptable approach to estimate the overall film thickness for noncircular or irregular shape straight channels such as the near semi-circular channel in this study.

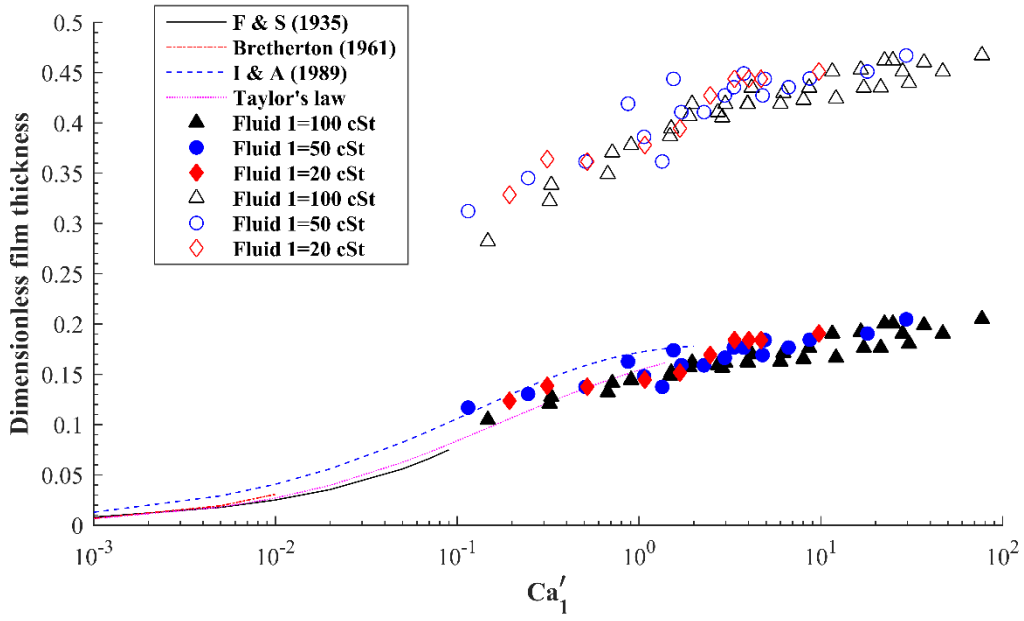

Figure 4.6 Dimensionless apparent film thickness and mean film thickness (calculated using Equation 4.7) in the near-semicircular channel, compared with available models from Fairbrother and Stubbs (1935), Bretherton (1961), Irandoust and Andersson (1989) and the Taylor's law (Aussillous and Quere, 2000). Experimental data are for surfactant-free fluid 2. Filled markers represent results for *mean film thickness* and empty marks represent *apparent film thickness*.

Effect of fluid 1 viscosity

The effect of the choice of fluid 1 is studied by comparing experimental results using fluid 1 with three viscosities: 100, 50 and 20 cSt silicone oil. Similar to the section above, the results for using the same fluid 1 but different viscosity ratios are grouped. Figure 4.7 shows results for both surfactant-free and surfactant-laden fluid 2. From these plots, there is no clear trend of the difference between different viscosities of fluid 1, especially at low capillary numbers. When $Ca' > 1$, the film thickness for 50 and 20 cSt silicone oil appears to be slightly larger

than that of 100 cSt silicone oil and this is observed in both surfactant-free and surfactant-laden cases. These results confirm some literature findings: Han and Shikazono (2009a) studied the displacement of three liquids by air in circular microchannels: water, ethanol and FC-40 liquid, which are respectively ~ 3.7 times and 3 times more viscous than water and ethanol in terms of dynamic viscosity and around 2 times and 1.3 times more viscous than water and ethanol in terms of kinematic viscosity. It was found in the capillary number range from 0 to 0.08 for all three fluids or 0 to 0.15 for ethanol and FC-40, the more viscous fluid resulted in smaller film thickness. This effect gradually grows as capillary number increases.

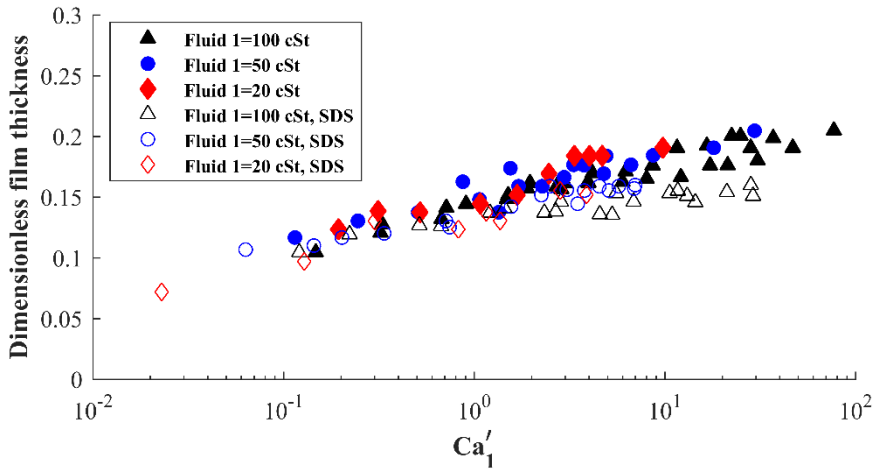

Figure 4.7 Comparison of film thickness using different viscosity of fluid 1 in near-semicircular for SDS-free and (2) SDS-laden cases.

Effect of surfactant

Since the film thickness increases as Capillary number increases, by definition, an increase of viscosity and/or velocity or a decrease of interfacial tension should lead to an increase of the film thickness. For surfactant-laden fluid 2 cases, the most obvious difference that surfactant molecules bring is the change of interfacial tension. It can be seen from Figure 4.7 that even after taking the dynamic interfacial tension effects into consideration (via the calculation of

Ca_1') there is an additional physical effect leading to a thinner liquid film than for the surfactant free cases with the same capillary number, especially at larger capillary number conditions. A possible explanation might be inaccuracies in the estimation of dynamic interfacial tension from Equation 4.1, however other mechanisms may come into play (Figure 4.8).

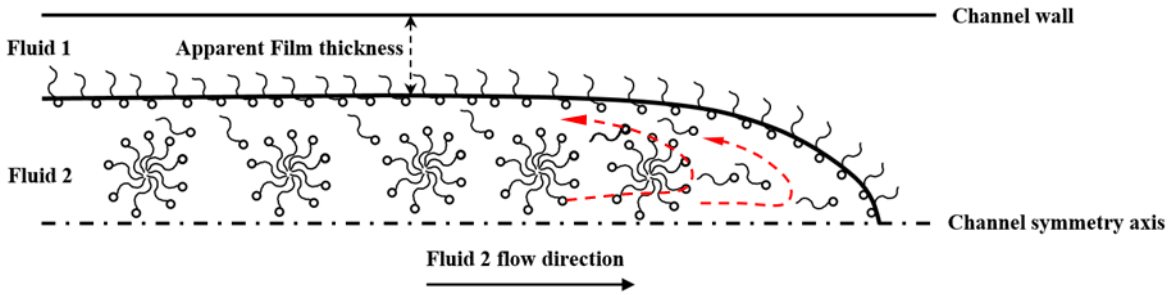

Figure 4.8 Schematic illustration of the problem of surfactant-laden fluid 2 (size of molecules is not to scale).

It is well known that recirculatory flows (Figure 2.34) can develop inside the penetrating fluid tip and also in the displaced fluid, as postulated by Taylor (1961). When flow rate of fluid 2 is small, this effect is small and the new interface between fluid 1 and fluid 2 generated at the channel inlet remains relatively undisturbed. In this case the dynamic interfacial tension, or equilibrium interfacial tension for some small Ca_1' cases, is sufficient to describe the effect of surfactant migration to the new interface, based upon the timescale of the fluid flow i.e. $t = L/u_2'$, and the behaviour is well represented at low values of Ca_1'. However as the fluid 2 flow rate increases, the recirculation effect becomes larger as illustrated by the red arrows in Figure 4.8. In this case the surfactant at the interface at the leading edge of displacement will be convected towards the back leading to depletion at the tip if the bulk diffusion of surfactant from the bulk to the interface is not sufficient to replenish it. This local effect could lead to Marangoni stresses and higher surface tension close to the tip; the consequence of which is a thinner liquid film on the wall. This thinning effect is contrary to findings found in the

numerical simulations by Ratulowski and Chang (1990) and Olgac and Muradoglu (2013) for gas displacing a liquid laden with surfactant; they observed an increase in the film thickness. Reasons for this discrepancy most probably are due to difference in conditions used in mentioned simulations and in the present work. First of all, both numerical studies considered an air bubble moving in the surfactant-laden liquid. In this case the bubble front surface is always in contact with surfactant solution of initial concentration, whereas surfactant depletion occurs along the bubble due to surfactant adsorption from the thin liquid film to the liquid/air interface. In the present study surfactant is situated in the displacing liquid. Therefore depletion can occur at the leading edge of displacement due to Taylor convection. Both numerical studies are related to low capillary numbers $Ca < 10^{-1}$, whereas surfactant-related changes in the film thickness were observed in the present study at $Ca > 1$. Ratulowski and Chang (1990) assumed the equilibrium between the interfacial and bulk surfactant in the uniform film region, but because of high flow rates, equilibration between surfactant in the bulk and at the interface was not achieved yet in the present study at flow rates where the film thinning was observed.

Olgac and Muradoglu (2013) used the effective surface tension related to the average surfactant concentration on the liquid/air interface to calculate the capillary number. Due to the non-uniform surfactant distribution, the film thickness was larger as compared to the film formed by the pure liquid of the same surface tension in the central part of the bubble (quasi-uniform film), but it was smaller than pure liquid film in transition zone near the front of the bubble. For the largest capillary number considered by Olgac and Muradoglu (2013), $Ca = 0.097$, the film thickness for the case of an insoluble surfactant was smaller than that formed by pure liquid with the same surface tension in the quasi-uniform film part. Therefore, based on the results of Olgac and Muradoglu (2013), it can be assumed that by an essential increase of capillary

number and the corresponding decrease of characteristic time of surfactant adsorption, a soluble surfactant can demonstrate the similar behaviour, i.e. produce a smaller film thickness.

Note, the surfactant used in this study is characterised by very fast equilibration at concentrations above CMC when compared with other commonly used surfactants (Wang, et al., 2016). Therefore, a comprehensive study of other surfactants with different CMC values and in a range of concentrations is required to make more general conclusions on the effect of surfactant upon the film thickness. It can be suggested from the discussion above that if an increase in the film thickness is due to depletion of surfactant from the leading edge of displacing liquid then using slower equilibrating surfactants, such as Triton X-100 or hexadecytrimethylammonium bromide (CTAB) (Wang, et al., 2016) should result in further decrease of film thickness, whereas increase in concentration of SDS or other quickly equilibrated surfactant (e.g. dodecyltrimethylammonum bromide, (Kovalchuk, et al., 2018))will eventually increase the film thickness back to the value expected for the capillary number based on surface tension of surfactant solution.

Effect of channel geometry and channel size

The effect of channel shape was studied using two circular channels of 200 and 100 μm inner diameter and a 200 μm square channel. 100 cSt silicone oil is used as fluid 1 and viscosity ratios of 20, 50 and 100 were studied by varying fluid 2 viscosities.

Dimensionless film thickness for both 200 and 100 μm circular channels plotted against Ca_1' is shown in Figure 4.9. The apparent film thickness is used for circular channel, because in this case the mean film thickness is equal to the apparent thickness. The results show that the dimensionless film thickness is larger for the larger channel when $Ca_1' > 1$. A similar trend was observed by Aussillous and Quere (2000), who used channels with diameters from 0.4 to 1.4

mm for $Ca < 0.05$ and by Han and Shikazono (2009b) who used channels of 0.3 to 1.3 mm diameter for $Ca < 0.08$. The results reported by Tsaoulidis and Angeli (2016), who studied the film thickness in 0.5 to 2 mm channels, also suggest an insignificant effect of channel size on the film thickness up to values of $Ca < 0.2$.

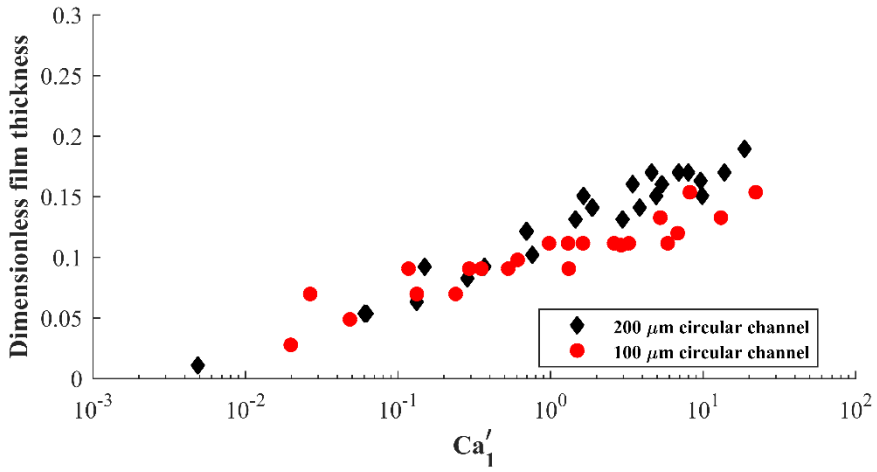

Figure 4.9 Dimensionless film thickness for 200 and 100 μm circular channels. fluid 1: 100 cSt silicone oil, the result for each channel size contains results from three viscosity ratios.

For square channels, the existence of corners causes the film thickness to be non-uniform. Therefore the approach of mean film thickness is also applicable here. Dimensionless apparent and mean film thicknesses are both plotted in Figure 4.10, as well as the model developed by Han and Shikazono (2009b) and Taylor's law (Aussillous and Quere, 2000). Most of the correlations for liquid film thickness do not take channel size into account explicitly and only consider capillary number. However, Han and Shikazono (2009b) have developed empirical equations using both Weber number and Reynolds number in addition to capillary number. Note the curve representing Han and Shikazono (2009b) correlation in Figure 4.10. In addition, by using Equation 2.16, the film thickness values obtained from Han and Shikazono (2009b)

correlation for square channels are calculated on the basis of the mean film thickness, which are also shown in the figure.

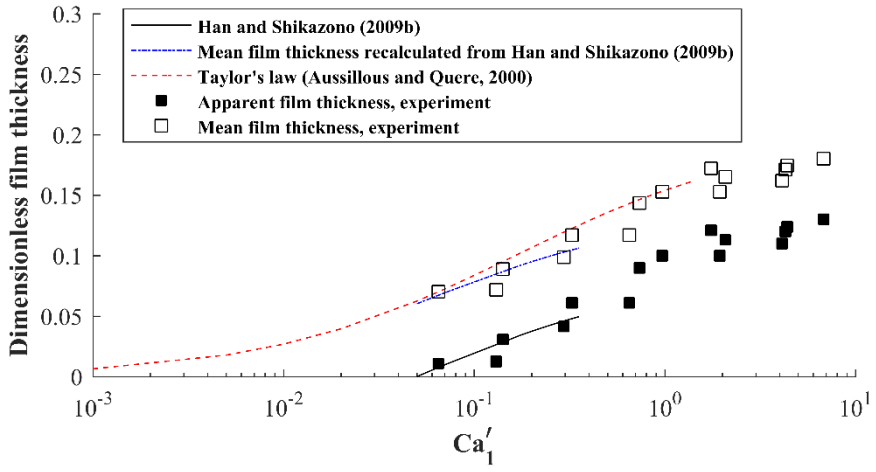

Figure 4.10 Film thickness results for the square channel. Both apparent film thickness and mean film thickness are plotted together with literature models of Taylor' law (Aussillous and Quere, 2000) and models developed by Han and Shikazono (2009b).

It has been shown by Kolb and Cerro (1991) that the thickening of the film in a square channel starts in the corners whereas the film thickness at the sides remains unchanged. Beyond a critical capillary number and a critical film thickness at the corner, the contour of fluid 2 becomes circular and both the liquid film thickness at the corner and at the sides increases with further increase in capillary number. The dashed line in Figure 4.11 is an illustration of the possible contour of fluid 2 interface at smaller capillary numbers. However from the experimental images in this study, under all conditions the images are showing a clear sharp layer of liquid 1 film. This means that under the experimental conditions in this study, which are represented by higher capillary numbers, the contour of fluid 2 is always circular. This can be also assessed from the reported critical capillary number value, which in the experiments by Kolb and Cerro (1991) is $Ca \sim 0.1$ and for Han and Shikazono (2009b) is $Ca \sim 0.02$.

The model of Han and Shikazono (2009b) used here is correlated with the thickness at the sides of the channel, which corresponds to the apparent film thickness measured in this study. By comparing the experimental data with Han and Shikazono's empirical equations, good agreement is found for $Ca < 0.4$, which is the maximum value used in their study. The mean film thickness results are also in line with the recalculated mean thickness based on Han and Shikazono (2009b) correlation. It can be seen that using the apparent film thickness at sides, experimental data does not fit to Taylor's law, which is developed using results in circular channel. However by calculating the mean film thickness using Equation 4.6, the data fits Taylor's law much better. This first proves that the approach of mean film thickness is applicable not only to the near semi-circular channel but also to square channel. Therefore this approach can possibly be used for any non-circular channel if the contour of the interface in the cross-section can be either be known or assumed. In addition, this also agrees the previous finding that under all conditions in this study, fluid 2 presents a circular cross-section shape. This is because the equation for calculating the mean film thickness in square channel uses the assumption of circular interface shape. If the contour of fluid 2 is not circular, using Equation 4.6 will result in an overestimation of the mean film thickness as the thickness at the corner increases (shown as the dot dash circle in Figure 4.11).

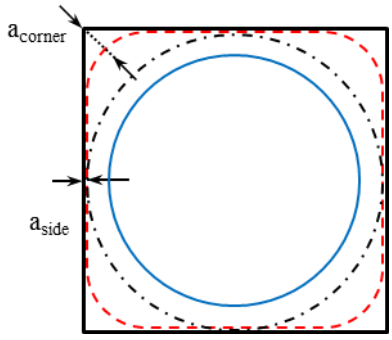

Figure 4.11 Illustration of the cross-section shape of fluid 2 in square channel for smaller capillary number. Red dashed line: possible contour of fluid 2 interface, blue solid line: assumed fluid 2 interface in the mean film thickness approach, dot-dashed line: illustration of the inaccurate estimation of mean film thickness if fluid 2 interface is noncircular.

The comparison of dimensionless film thickness for circular and square channels with the same hydraulic diameter (200 μm) is shown in Figure 4.12. For the square channel, both the apparent and mean film thickness are shown.

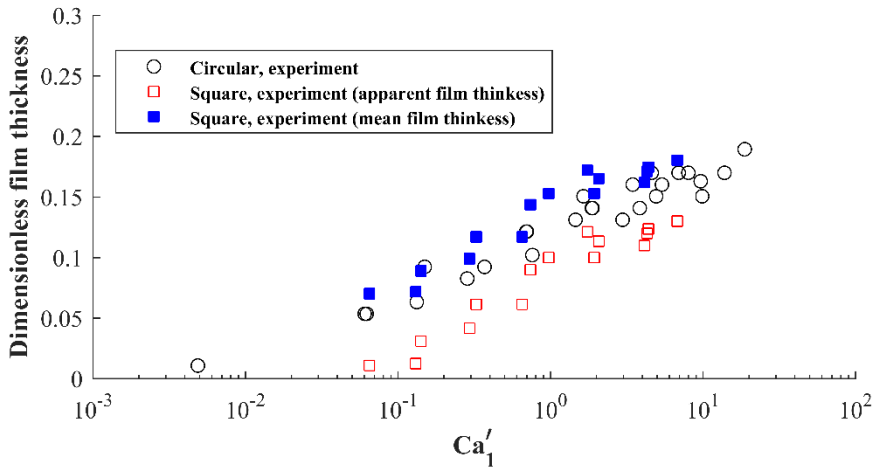

Figure 4.12 Dimensionless film thickness of circular and square channel with 200 um hydraulic diameter.

It can be seen from the figure above that the film thickness results for circular channel are generally larger than the apparent film thickness measured in square channel. This agrees with the results of Han and Shikazono (2009a and b) who also studied both circular and square channels with the same size. The mean film thickness for square channel appears to be slightly larger than the film thickness for circular channel. This is because the method of calculating mean film thickness takes into consideration the corner area, where more liquid is likely to remain than in the circular channel.

Effect of Channel wettability

A microchannel with hydrophobic wall (details in §3.1.1) was used for carrying out fluid displacement experiments. Same fluid pairs (100 cSt silicone oil displaced by water, 2 cSt and

5 cSt glycerol solutions) were used. Film thickness left on the wall was measurement and mean film thickness values were calculated. These results are shown in Figure 4.13, the results using three viscosity ratios are grouped into one set of data. No significant differences appear between the film thicknesses measured using hydrophilic and hydrophobic channel. This could be caused by the fact that the displacing fluid, which is the aqueous phase in this study, does not contact the wall once the entrance length is exceeded. The only point of contact between the aqueous phase and the wall is very close to the inlet of channel. Therefore these results show that within the experimental conditions (are all in the laminar regime), the wettability of channel does not influence the film thickness left on the wall.

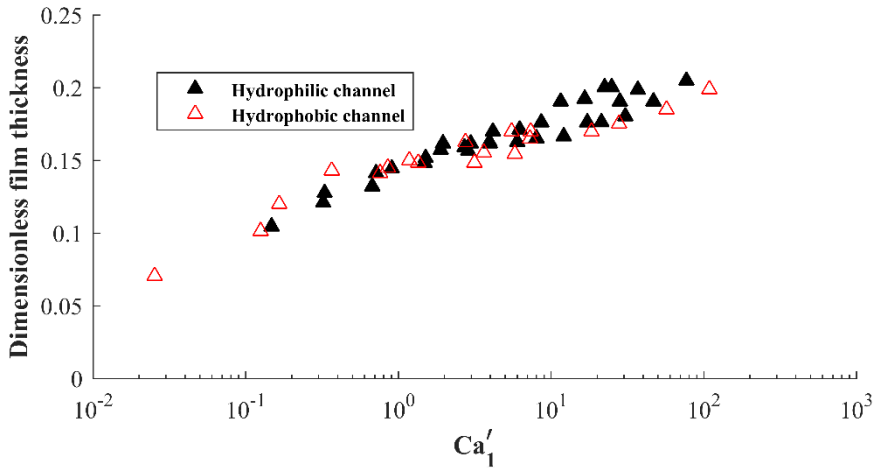

Figure 4.13 Dimensionless mean film thickness measured using hydrophilic and hydrophobic channels.

4.3.2 Fluid 2 tip curvature

In all of the experiments carried out, fluid 2 penetrates fluid 1, first forming a “finger-shape” tip. The radius of the tip curvature has been measured by fitting a circle to this curvature at the tip using Image J, see §3.5 (Figure 3.13).

Effects of viscosity ratio, surfactant and fluid 1 viscosity

The near-semicircular channel (Dolomite microfluidic chip) is used to study the effect of viscosity ratio, the individual viscosity of fluid 1 and whether surfactant is added in fluid 2, where surfactant SDS is chosen. Similar to the measurement of film thickness, the radius of fluid 2 tip curvature is plotted against modified capillary number Ca_1'.

The radius of tip curvature in this study is normalised with the hydraulic diameter of the channel:

$$r_t^{'} = \frac{r_t}{D_H} \qquad \text{(Equation 4.8)}$$

The dimensionless radii of curvature of the fluid 2 tip are plotted against Ca_1' in Figure 4.14. Results from experiment using three different viscosities of fluid 1 are presented for both surfactant-free and surfactant-laden fluid 2 cases. A generally observed trend of decrease of the radius of tip curvature with increasing capillary number is in line with literature findings e.g. Kolb and Cerro (1991), who referred to the tip as bubble cap (region AB in Figure 4.15) and stated increasing capillary number resulted in smaller bubble caps. Similar to the results of film thickness on the wall, the effect of different viscosity ratio is quite small.

(a)

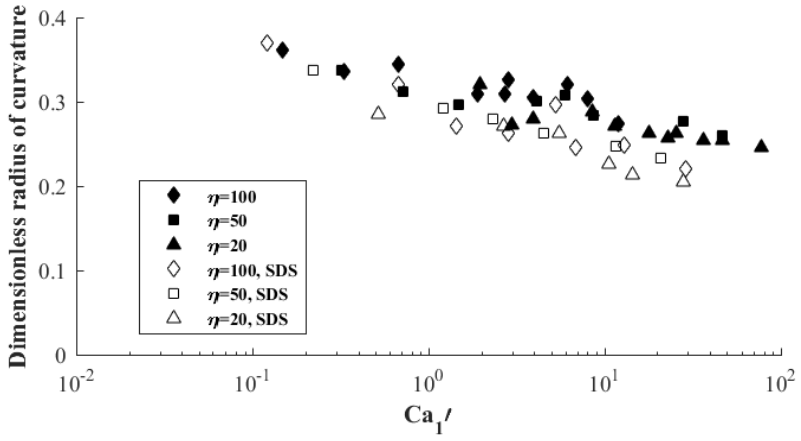

(b)

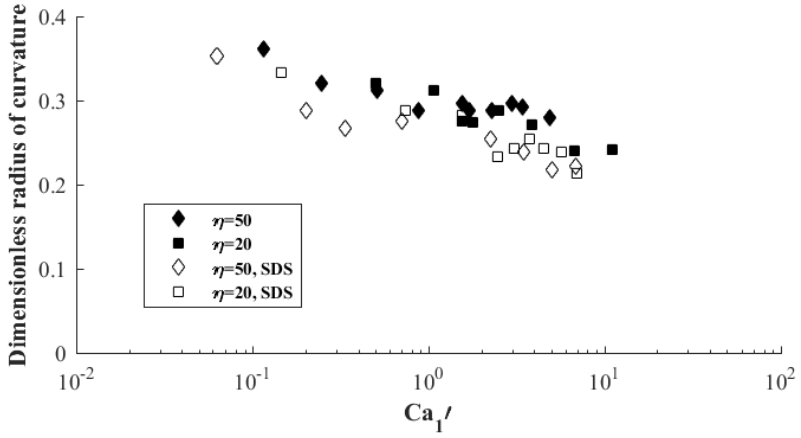

(c)

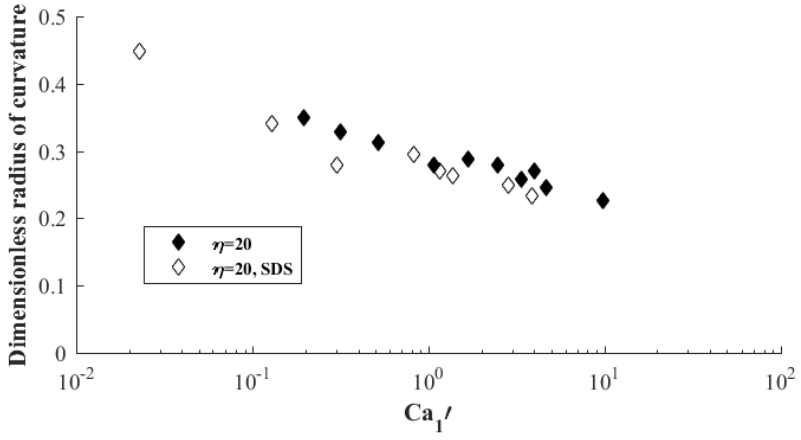

Figure 4.14 Dimensionless radius of fluid 2 tip curvature in immiscible fluid displacement in (a) 100 cSt oil as fluid 1; (b) 50 cSt silicone oil as fluid 1 and (c) 20 cSt silicone oil as fluid 1 (only viscosity ratio of 20), plotted against Ca_1'.

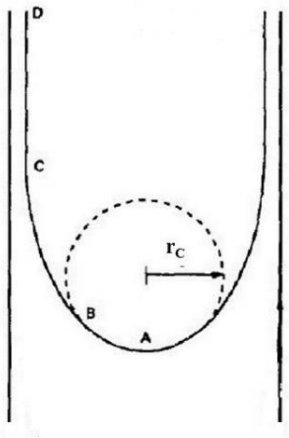

Figure 4.15 Illustration of displacing fluid tip, region AB: bubble, region BC: transitional region and region CD: uniform liquid film region. Adapted from Kolb and Cerro (1991).

In order to see the influences of fluid 1 viscosity, fluid 2 tip curvature results using different fluid 1 are plotted together in Figure 4.16. The results of 100 cSt silicone oil as fluid 1 contains results from using three viscosity ratios, 50 cSt silicone oil as fluid 1 contains results from using two viscosity ratios by varying the viscosity of fluid 2, and 20 cSt silicone oil as fluid 1 contains only 1 viscosity ratio. Similar to the results of film thickness measurement, both surfactant-free and surfactant-laden fluid 2 cases show a decrease in tip curvature radius for the cases of 50 and 20 cSt silicone oil fluid 1 than 100 cSt silicone oil as fluid 1.

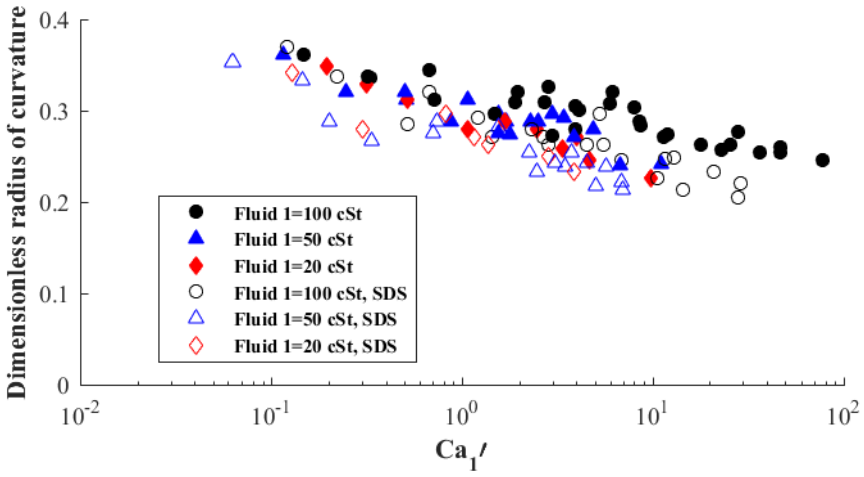

Figure 4.16 Comparison of the dimensionless radius of curvature using different viscosities of silicone oil as Fluid 1 for both surfactant-free and surfactant-laden Fluid 2 cases.

The relationship between fluid 2 tip curvature and the film thickness is shown in Figure 4.17.

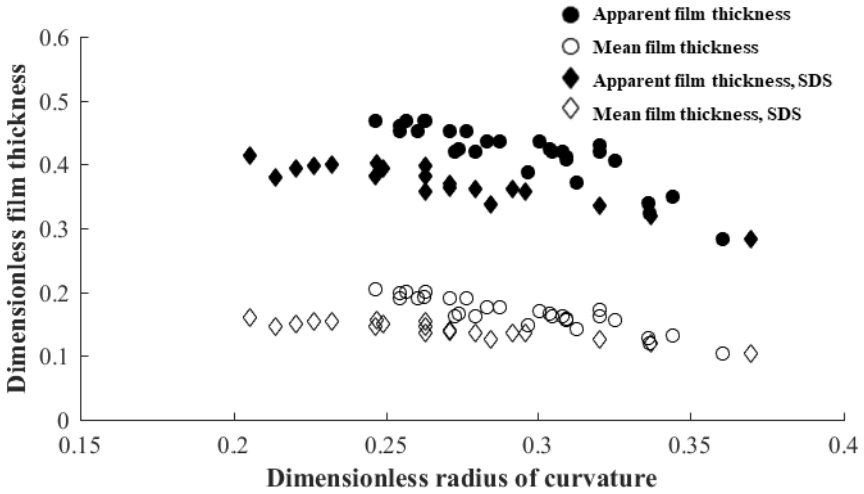

Figure 4.17 Plots of dimensionless film thickness against dimensionless radius of fluid 2 tip curvature, results from near-semicircular channel using 100 cSt silicone oil as fluid 1, Dimensionless film thickness using both absolute measured values and the mean film thickness values are shown.

The relationship between film thickness and fluid 2 tip curvature for three viscosity ratios are shown in Figure 4.18, results using both apparent and film thickness are presented. It can be

seen from these plots that this relationship is hardly affected by the viscosity ratio. For both the cases of using apparent or mean film thickness, data points from three viscosity ratios follow the same trend.

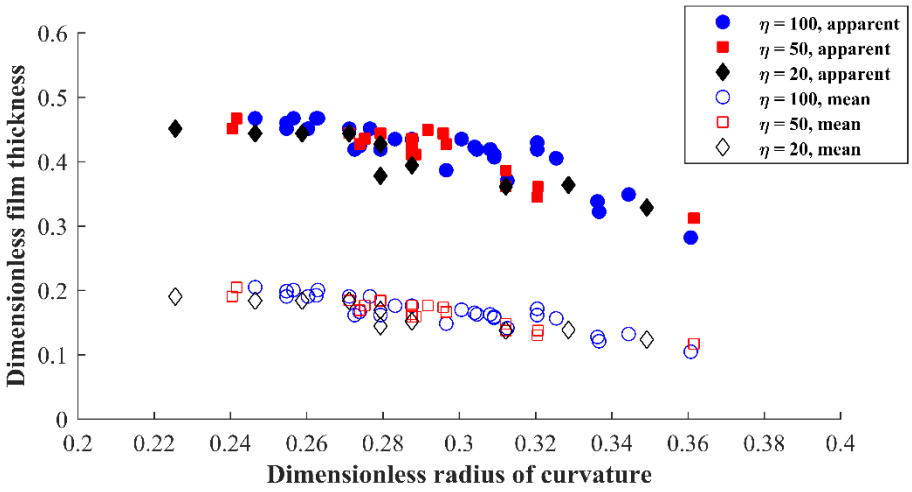

Figure 4.18 Film thickness plotted against fluid 2 tip curvature for near-semicircular channels, three viscosity ratios and the results using both apparent and mean film thickness are shown.

Effects of surfactant addition in fluid 2

It can be seen from Figure 4.16 that the addition of surfactant causes the radius of fluid 2 tip curvature to be slightly smaller than the results obtained using the surfactant-free fluid 2. Combining the previous finding of the thinning effect for film thickness for surfactant-laden fluid 2 cases, the width of transition region (regime BC in Figure 4.15) is plotted against Ca_1' in Figure 4.19. The width of transition regime is also normalised by the hydraulic diameter of channel. These plot shows that by increasing Ca_1', the surfactant added in fluid 2 cause the width of transitional region to stay relatively unchanged (slightly increase) whilst surfactant-free fluid 2 cases show a decrease trend. However this phenomenon does not mean the transition region stays the same because as capillary number increases, the fluid 2 flow front is elongated to form a thicker film thickness and a narrower fluid tip.

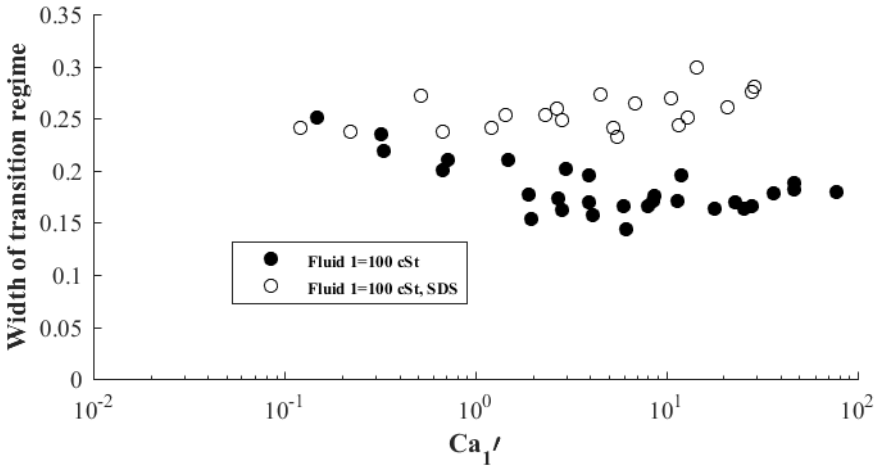

Figure 4.19 Width of transitional regime between fluid 2 tip and constant film thickness region, normalised by channel hydraulic diameter, plotted against Ca for surfactant-free and surfactant-laden fluid 2 cases. Fluid 1 is 100 cSt silicone oil.

Combining the results shown in Figure 4.18 suggests that appearance of larger film thickness is coupled with the appearance of smaller fluid 2 tip curvature. This can also be seen from Figure 4.19 that the slight decrease in the width of the transitional region indicates the increase of the apparent film thickness which can be expressed in a simple from:

$$a = \frac{W - 2r_c - 2a_{tran}}{2} \qquad \text{(Equation 4.9)}$$

Where a_{tran} is the width of the transitional regime. However, as it suggests from Figure 4.19 the width of transitional region present a slight decrease trend over the increase of capillary number, therefore the exact expression of film thickness using Equation 4.9 cannot be obtained. On the other hand, for SDS-laden fluid 2 cases, the width of transition region stays at ~ 0.26 (dimensionless width, equivalent to apparent width of ~ 32.4 μm). This means using Equation 4.9 a linear empirical expression of the apparent film thickness can be contained:

$$a = 67.6 - r_c \qquad \text{(Equation 4.10)}$$

Effects of channel geometry and channel size

The dimensionless fluid 2 tip curvature results from experiments carried out in 200 and 100 μm diameter circular channels are shown in Figure 4.20. It can be observed that for the 200 μm circular channel the measurement of radius of curvature is smaller than is observed for the 100 μm channel.

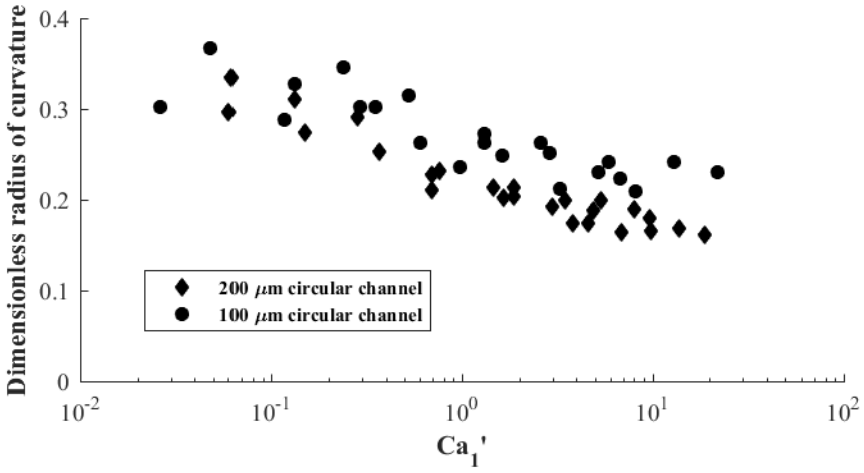

Figure 4.20 Dimensionless radius of fluid 2 tip curvature for circular channels with 200 and 100 μm diameter.

The film thickness versus fluid 2 tip curvature are plotted in Figure 4.21. From the graph the circular channel of these two sizes seem to have very similar effect in terms of the relationship between film thickness and fluid 2 tip curvature. This finding can potentially extend the previous conclusion from the results of near-semicircular channel that the relationship between film thickness and fluid 2 tip curvature is not affected by the use of fluid pairs. This relationship between film thickness and fluid 2 tip curvature does not seem to be affected by the channel size of the same geometry.

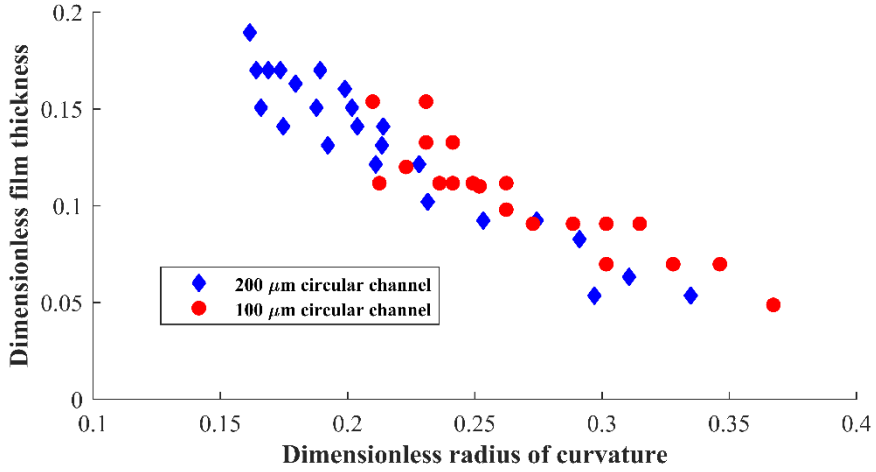

Figure 4.21 Dimensionless film thickness plot against dimensionless radius of curvature for 200 μm and 100 μm circular channels, fluid 1 = 100 cSt silicone oil, surfactant-free fluid 2 cases.

The comparison between circular and square channel with the same hydraulic diameter (200 μm) is shown in Figure 4.22.

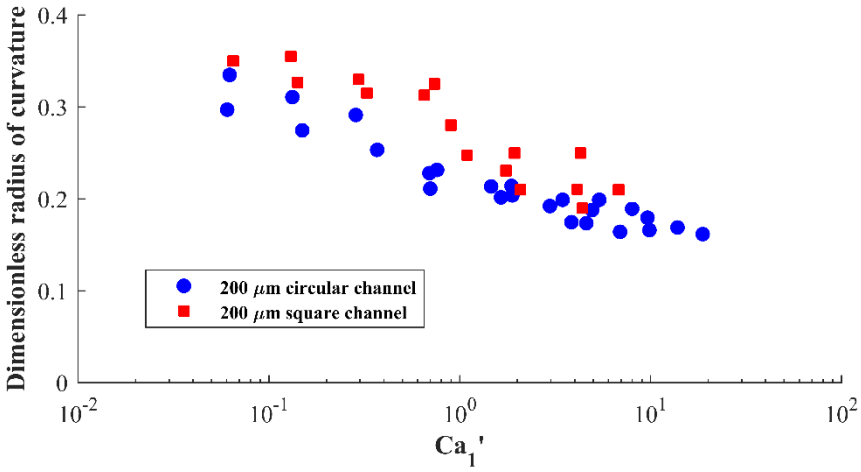

Figure 4.22 Comparison between the dimensionless radius of fluid 2 tip curvature for circular channel of 200 μm diameter and 200 μm square channel.

The relationship between the film thickness and fluid 2 tip curvature for both 200 μm circular and square channels are plotted in Figure 4.23. It can be seen that the results using the apparent film thickness for square channel follows very similar trend to the circular channel whist the

results using mean film thickness show some deviations. This indicates that the relationship between film thickness and fluid 2 tip curvature is not affected by the channel geometry, if the channels have the same hydraulic diameters and the film thickness for square channel is represented by the apparent film thickness.

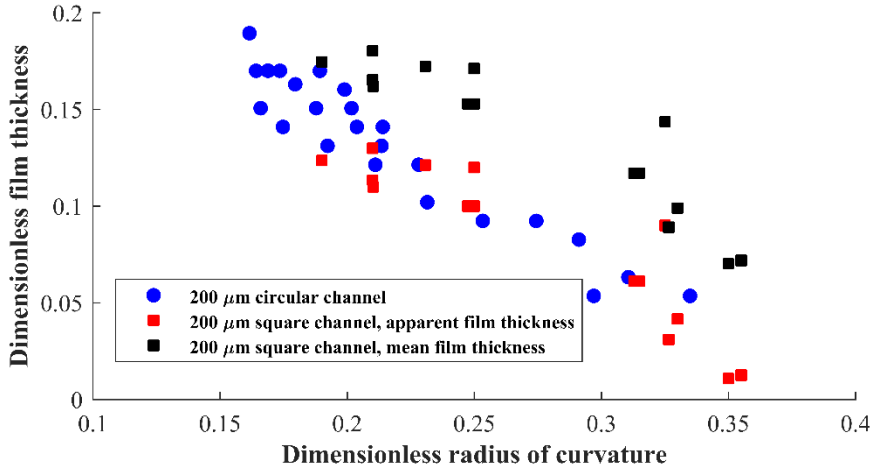

Figure 4.23 Film thickness plotted against fluid 2 tip curvature for both 200 μm circular and square channels. Both apparent and mean film thickness for square channel are plotted.

To check if the finding about the channel effect on the relationship between film thickness and fluid 2 tip curvature from the results for circular and square channels can be extended to near-semicircular channels, plots containing the results for all three types of channels are shown in Figure 4.24. It can be seen that the results for near-semicircular do not follow the same trend as others. Therefore it is concluded that for fluid displacement flow, if the displacing fluid forms a symmetric bullet shape tip, the relationship between liquid film thickness (apparent film thickness for non-circular channel such as square channel) and displacing fluid 2 tip curvature follows the same trend.

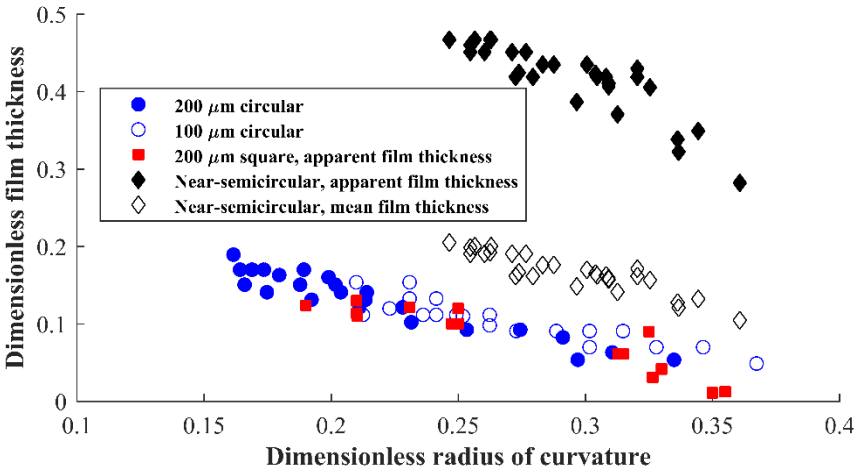

Figure 4.24 Film thickness plotted against fluid 2 tip curvature for three geometries of channels.

4.4 Immiscible cases interfacial instabilities

All the images recorded in the experiments are taken from the view looking vertically upwards through the microscope lens. Thus, and given the nature of non-transparent dye used in fluid 2, these images are in fact the projected (the widest part across the channel) views of interface position through the channel. Different forms of interfacial instabilities have been observed between fluid 1 and 2 following the finger shape tip along the flow, as summarised in Figure 4.25 Three flow regimes are defined for immiscible displacement, shown in Figure 4.25. These regimes are categorised as a function of the following dimensionless groups:

$$\mathrm{Re}_2 = \frac{\rho_2 u_2 D_H}{\mu_2} \qquad \text{(Equation 4.11)}$$

$$Ca_1 = \frac{\mu_1 u_2}{\sigma_{12}} \qquad \text{(Equation 4.12)}$$

$$Ca_2 = \frac{\mu_2 u_2}{\sigma} \qquad \text{(Equation 4.13)}$$

Where ρ_2 is the density of fluid 2, D_H is the hydraulic diameter, σ is the interfacial tension between fluid 1 and 2.

A description of the regimes observed in Figure 4.25 is given below.

Stable regime is the flow regime when no oscillation or interfacial instabilities are observed at the interfaces between fluid 1 and 2 at all times. *Axisymmetric unstable* regime takes place when Re_2 increases. This regime represents the flow behaviour of periodic and axisymmetric interfacial instabilities appear with the axis of symmetry to be the centre line of channel along the flow direction. These instabilities are formed as the axisymmetric pinching behaviour of fluid 2. These instabilities are found to present all the time after its first appearance following the finger shape tip and a short period of stable interfaces. *Asymmetric unstable* regimes take place when Re_2 is further increased. This regime represents complex and asymmetric interfacial instabilities take place between fluid 1 and 2. It is to be noted that the asymmetric instabilities usually take place a short period of time after the onset of the axisymmetric instabilities and these asymmetric instabilities then persist. The three flow regimes observed were found to apply to all immiscible fluid displacement experiment carried out in this project.

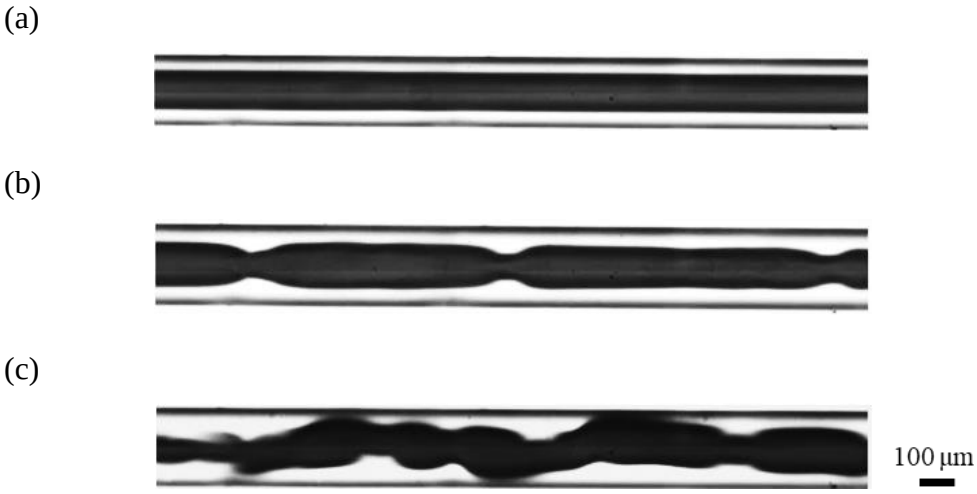

Figure 4.25 Three flow regimes for immiscible fluid pairs, all three images are from the results of fluid displacement in near-semicircular channel 100 cSt silicone oil displaced by water, only changing Re_2 by varying injection flowrate: (a) Stable (Re_2 = 3, Ca_2 = 9.8×10^{-4}), (b) Axisymmetric Unstable (Re_2 = 30, Ca_2 = 9.7×10^{-3}) and (c) Asymmetric Unstable (Re_2 = 60, Ca_2 = 1.9×10^{-2}). Scale bar applies to all images.

Note, unlike the axisymmetric instabilities, there are no key identifiable patterns for the asymmetric unstable regime. Figure 4.26 give some examples of different patterns of asymmetric instabilities observed in immiscible displacement experiment.

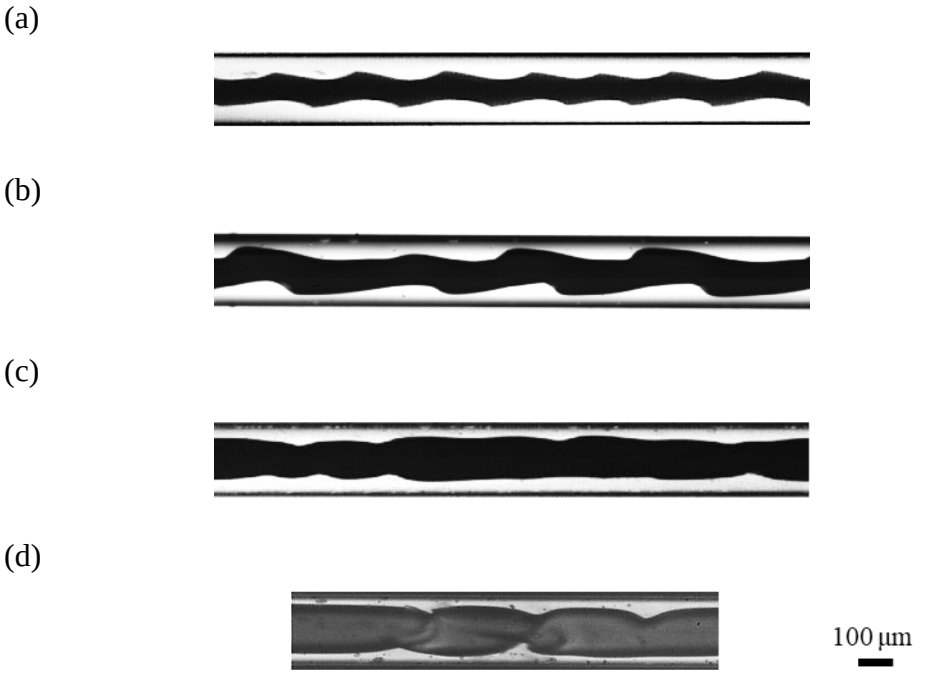

Figure 4.26 Different types of Asymmetric interfacial instabilities observed in immiscible fluid displacement experiment. (a) Fluid 1: 100 cSt silicone oil, Fluid 2: 5 cSt glycerol solution+SDS, Re_2 = 30, Ca_2 = 0.64, in near-semicircular channel; (b) Fluid 1: 20 cSt silicone, Fluid 2:

Water+SDS, Re_2 = 50, Ca_2 = 0.04, in near-semicircular channel; (c) Fluid 1: 100 cSt silicone oil, Fluid 2: water+SDS, Re_2 = 40, Ca_2 = 3.2×10^{-2}, in near-semicircular channel; (d) Fluid 1: 100 cSt silicone oil, Fluid 2: water, Re_2 = 170, Ca_2 = 0.034, in 200 μm circular channel. The scale bar applied to all four images.

4.4.1 Flow regime maps

To characterise the appearance of the different types of instabilities mentioned in above section, flow regime maps are developed to reflect the effects of flow injection condition, channel geometry, channel size, interfacial tension (introduction of surfactant) and channel wall. Unlike the discussion of film thickness on wall in which the initial film thickness after the advancing tip is considered, the interfacial instabilities exist throughout the whole displacement process. Therefore the superficial velocity of fluid 2 (u_2), which is calculated from the injection flow rate and the cross-section area of the channel, instead of modified real fluid 2 (u_2') velocity is used in calculating relevant parameters. In addition, viscosity ratio is an important parameter in discussion of interfacial instabilities because the different behaviour observed of flows with different viscosity ratios and the same operating conditions. Therefore the viscosity of fluid 2 is used in calculating parameters because in this study the varying of viscosity ratio is achieved by changing fluid 2 and fixing fluid 1.

Surfactant free fluid 2.

The flow regime maps for the cases using surfactant-free fluid 2 are shown in Figure 4.27. These flow regime maps are plotted in terms of the viscosity ratios and the capillary number. First it can be observed from Figure 4.27a and b that by using fixed viscosity of fluid 1 and varying fluid 2 viscosity, the transition capillary number decreases with the decrease of the viscosity of fluid 2.

The effect on transition conditions of the fluid pairs with the same viscosity ratios can be also seen from Figure 4.27. Viscosity ratio of 20 is achieved from three fluid pairs and viscosity ratio of 50 is achieved from two fluid pairs. There appears to be no clear trend in behaviour at fixed viscosity ratio despite the use of non-dimensional parameters; hence the fluid viscosity of both phases has to be considered in the analysis.

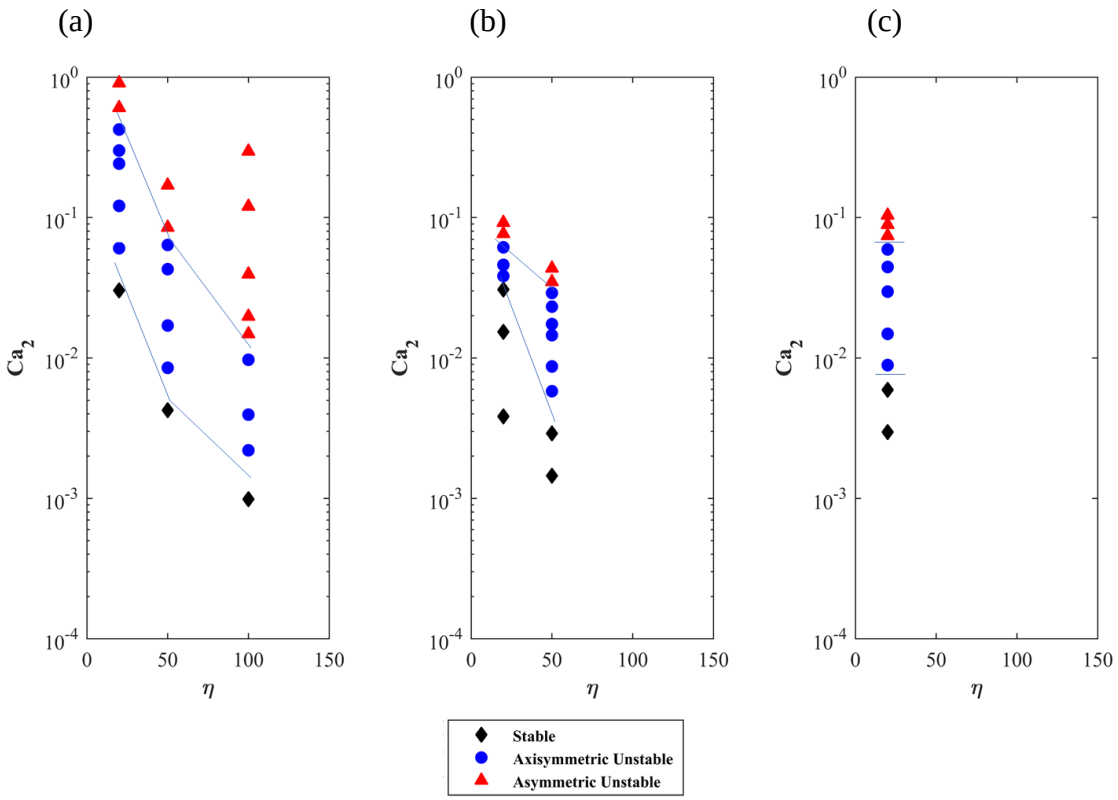

Figure 4.27 Immiscible flow regime map using (a) 100 cSt, (b) 50 cSt, (c) 20 cSt silicone oil as fluid 1 and surfactant-free fluid 2.

To see the influence of fluid 1 on the appearance of interfacial instabilities, Figure 4.28a shows the results using a fixed fluid 2 (water, 1 cSt) but three viscosities of fluid 1 (20, 50 and 100 cSt silicone oil); the increase of fluid 1 viscosity results in a decrease of the transition capillary numbers. From the discussion above it is concluded that the decrease in fluid 2 viscosity or the

increase in fluid 1 viscosity (whist keeping the viscosity of the other phase constant) results in a decrease in the regime transition capillary numbers.

The flow regime map reflecting the effect of the viscosity of fluid 1 when the viscosity of fluid 2 is fixed drives the development of a flow regime map depending of the capillary number based of fluid 1 properties, Ca_1, which is shown in Figure 4.28b.

It can be seen from Figure 4.28b that the transition condition between regimes, characterised by Ca_1, have become very similar for different fluid 1 viscosities. This can be potentially extended to the conclusion: when the viscosity of displacing fluid 2 is constant, for the conditions of viscosity ratio $20 \leq \eta \leq 100$, the transition conditions between three flow regimes are roughly around the same if Ca_1 is used as the characteristic parameter; the transition Ca_1 values between stable, axisymmetric unstable and asymmetric unstable flows are ~0.1 and ~1.

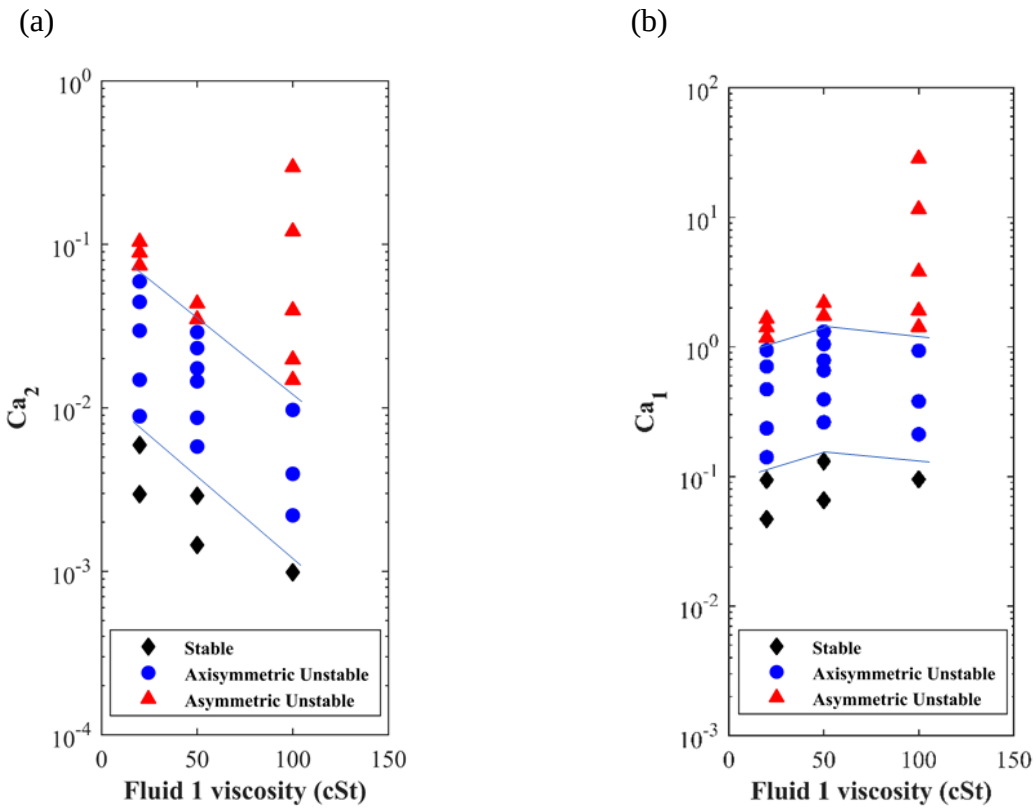

Figure 4.28 (a) Immiscible flow regime map from the results using the fixed fluid 2 (water) and three viscosities of fluid 1, depending on Ca_2; (b) Flow regime map reflecting the effect of fluid 1 viscosity with fixed fluid 2 viscosity, depending on Ca_1.

Surfactant-laden fluid 2

Unlike the analysis of film thickness in this study, where dynamic interfacial tension is used when calculating the capillary number of surfactant-laden fluid 2, the analysis of interfacial instabilities uses equilibrium interfacial tension values estimated from Equation 4.1. This is done because the analysis of interfacial instabilities involves much longer observation time compared to the measurement of film thickness and fluid 2 tip curvature, which is normally from the beginning of fluid 2 injection till the complete displacement of the pre-filled fluid 1 in the channel.

Figure 4.29a shows the flow regime maps for surfactant-laden fluid 2 cases. The comparison between surfactant-free and surfactant-laden fluid 2 cases are shown in Figure 4.29b. It is noted that by overlapping these two regime maps, the transition conditions for these two cases based on Ca_2 are almost identical. Therefore it is concluded that for immiscible fluid displacement, by using the same fluid pairs, the effect of the addition of surfactant in the displacing fluid can be expressed by the variation of equilibrium interfacial tension, which is reflected in calculating capillary number values. In addition to the variation of interfacial tension, the addition of surfactant in fluid 2 also brings morphological variations on the forms of asymmetric unstable flows, as shown in Figure 4.29. However the appearance of these different asymmetric unstable flows is believed to be rather random because of the lack of reproducibility. Due to the 3-dimensional nature of the asymmetric unstable flows, the exact 3-D forms of these instabilities were not obtained in these experiments due to the limitations of the optical set-up.

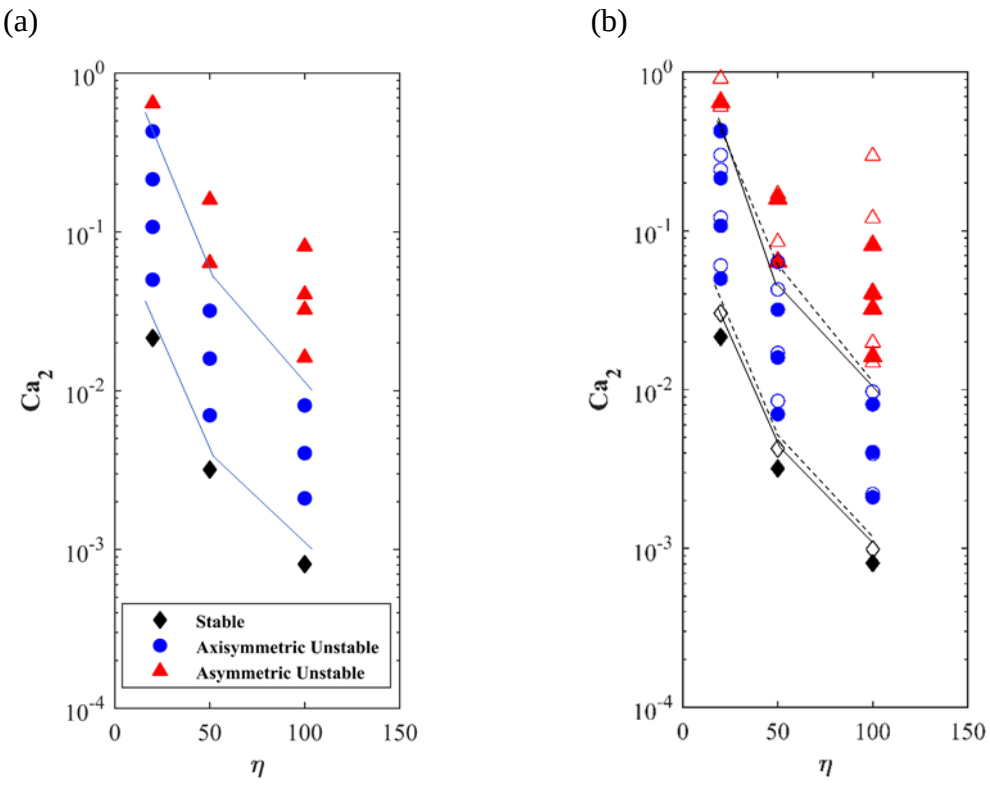

Figure 4.29 (a) Immiscible flow regime maps using 100 cSt silicone oil as Fluid 1 and surfactant-laden fluid 2; (b) comparison between flow regime map of surfactant-free (empty markers) and surfactant-laden fluid 2 (solid markers). Solid lines are the transitions for surfactant-laden fluid 2 cases and dashed lines are the transitions for surfactant-free fluid 2 cases.

Same channel geometry with different channel size

The effect of channel size is studied by using two sizes of circular microchannels: 100 and 200 μm in diameter. Identical fluid pairs and operating procedures were used in these two microchannels. The flow regime maps for these two circular channels are shown in Figure 4.30, which is the overlapped flow regime map of the two maps with the filled markers and solid lines representing the 200 μm channel.

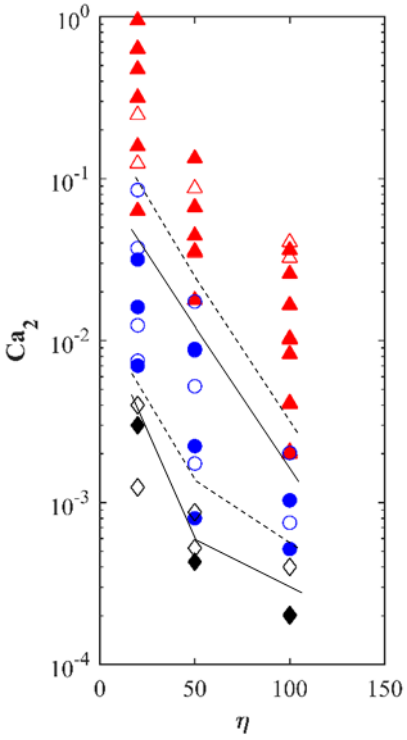

Figure 4.30 Overlapped flow regime maps for the circular channels with 200 and 100 μm diameter. Filled markers and solid lines for 200 μm channel, empty markers and dashed lines are for 100 μm channel.

It can be seen from Figure 4.30 that the transition conditions between flow regimes for 100 μm channel appear a shift up from that for 200 μm channel. This could be caused by the fact that the capillary number used here is calculated from the superficial velocity, from the fluid 2 injection flowrate and the cross-section area of the channel but the real velocity of fluid 2 depends on the film thickness of fluid 1 left one wall. From previous finding (shown in Figure 4.22), the dimensionless film thickness for 200 μm channel is generally larger than that for 100 μm channel. Therefor when Ca_2 values are the same, the real velocity of fluid 2 is higher in the 200 μm channel.

All the flow regime maps shown above also suggest that by using different immiscible fluid pairs, the ranges of the axisymmetric unstable regime, seems to be very similar, given the transition conditions are defined using the same parameters.

Effect of channel geometry

The flow regime maps using microchannels with the same hydraulic diameter (200 μm) but different cross-section shapes (circular and square) are shown below. It can be seen the change of channel geometry causes a significant shift in the transitions between flow regimes. Similar findings were reported for multiphase flows in small scale channels, as described in §2.2.2 (Sadatomi, et al., 1982; Coleman and Garimella, 1999).

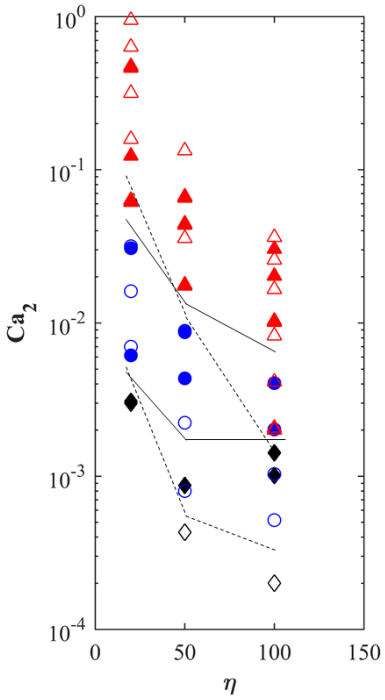

Figure 4.31 Overlapped flow regime maps using 200 × 200 μm square channel (coloured markers and solid line) and 200 μm circular channel (empty markers and dashed line).

Effect of wall wettability

To study the effect of wall wettability on the fluid displacement processes, a near-semicircular channel with the same size and cross-section shape but with a hydrophobic wall was used.

Figure 4.32 is the overlapped flow regime map of the results using hydrophilic and hydrophobic channels where solid markers and solid transition lines are for hydrophilic channel. From Figure 4.32 there exists a decrease in the transition conditions for the hydrophobic channel, represented by the downwards shift of the transition lines. Unlike the finding above using different sizes of circular channels, where the film thickness plays an important role that leads to the difference in the transition conditions, the film thickness for hydrophilic and hydrophobic channels does not show significant differences. In this case the channel inlet where fluid 2 first get contact of the channel wall is believed to be the cause of this difference.

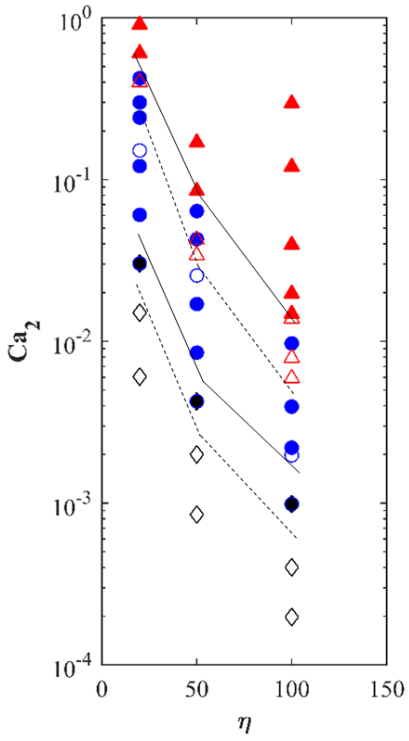

Figure 4.32 Over lapped regime maps of Figure 4.27a (solid markers and solid transition lines) and Flow regime map for hydrophobic near-semicircular channel, using 100 cSt silicone oil as fluid 1 (empty markers and dashed transition lines)

4.4.2 Interfacial film dynamics

As described in §3.5.1, Matlab image process was carried out to identify the interface between fluid 1 and 2, so the dynamics of interfacial film can be analysed.

Figure 4.33 shows the film thickness results from the Matlab image processing for the fluid pair of 100 cSt silicone oil displaced by water in the near-semicircular channel. The time axis shown in the figure starts from the first image processed by Matlab, which is set to the frame just before fluid 2 enters the area of recording. Only the film thickness on the top side is shown because flow conditions are in the stable and axisymmetric unstable regimes. Figure 4.33 shows an initial sharp drop in film thickness at very small flow times, which is due to the detection of the finger shape of fluid 2 tip. All three cases then show a period of unchanged film thickness. This is in line with the previous definition of axisymmetric unstable flows, where axisymmetric instabilities take place after a short period of stable interfacial flows. In addition, the film thickness at the initial stable regimes shows the increase in fluid injection flowrate (represented by Ca_2 here) results in higher film thickness.

For flow conditions of $Ca_2 = 3.9\times10^{-3}$ and 9.7×10^{-3}, axisymmetric instabilities were observed. The peaks of film thickness in Figure 4.33 show the pinching parts of the unstable flows. When capillary number increases, the extent of the shrinkage at the pinching parts of the flow increase. The average film thickness at the pinching parts is 62.3 μm for $Ca_2 = 9.7\times10^{-3}$ and 46.9 μm for $Ca_2 = 3.9\times10^{-3}$. The frequency of the appearance of these pinching parts can also be estimated. 11 peaks appear for the higher capillary number flow with a period of 0.22 second, which corresponds to 50 Hz while for the flow of smaller capillary number condition, it is 35.7 Hz. The results in Figure 4.33 also suggest that the appearance of the peaks is not strictly periodic, meaning the time between each occurrence is not fixed.

The other noticeable finding from the graph is under all conditions, the film initial film thickness after the tip appears a slight drop before becoming constant, meaning the width of fluid 2 experiences initial expansion before shrinking back to form the initial stable flows.

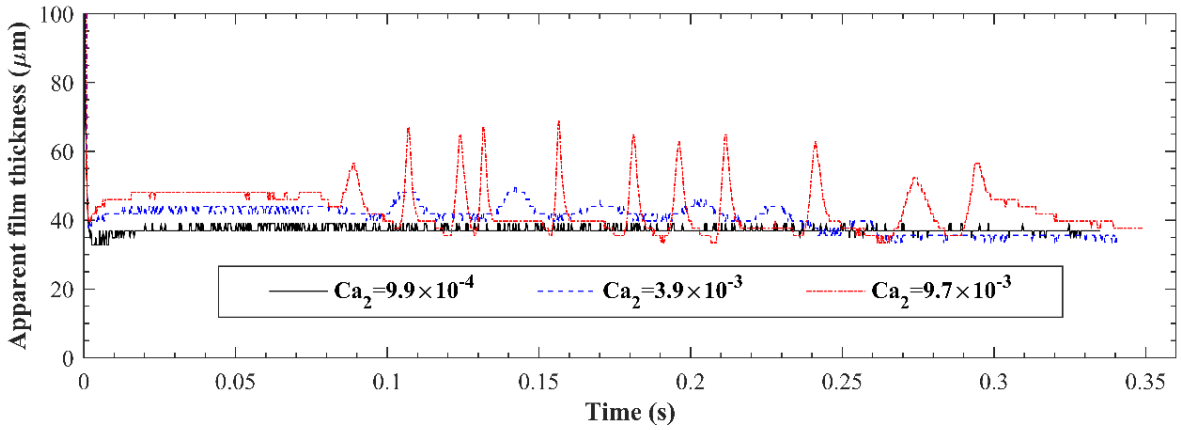

Figure 4.33 Film thickness for fluid pair of 100 cSt silicone oil displaced by water in the near-semicircular channel. Three flow conditions shown.

Similarly, the film thicknesses for fluid pairs of 100 cSt silicone oil displaced by 2 cSt and 5 cSt glycerol solutions are plotted in Figure 4.34. The height of peaks representing the instabilities decreases over time, along with the decrease of the overall film thickness, represented by the feet of the peaks. In addition, for most of the results shown in Figure 4.34 there exist the downwards peak before the initial stable flows. These results also suggest that the presence of instabilities does not assist the displacement in terms of the amount of liquid 1 left on the wall. It takes longer for the film thickness to become constant when fluid 2 injection flowrate is increased, i.e. when unstable flows are formed.

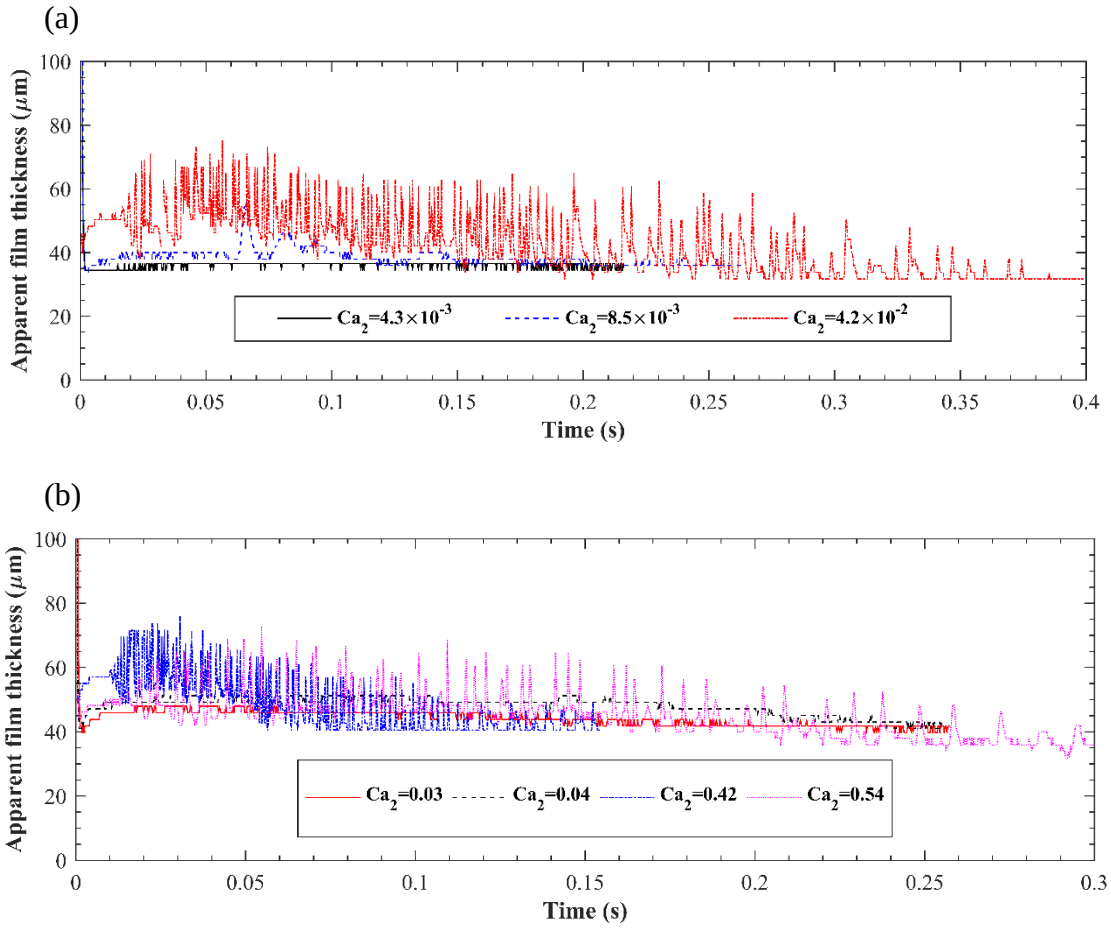

Figure 4.34 Film thickness determined using Matlab image process for the cases of 100 cSt silicone oil displaced by (a) 2cSt glycerol and (b) 5 cSt glycerol solution in semicircular channel.

4.5 Miscible fluid pair displacement

This section discusses the displacement experiment using miscible fluid pair as fluid 1 and 2. Glycerol solution with 100 cSt kinematic viscosity is chosen as fluid 1. Water, glycerol solutions with 2 and 5 cSt viscosity are chosen as fluid 2. The residual liquid film thickness and fluid 2 tip curvature could not be measured precisely due to the diffusion at the interfaces between fluid 1 and 2 therefore only interfacial instabilities are discussed for miscible displacement experiments.

4.5.1 Interfacial instabilities

Identification of different forms of instabilities

Figure 4.35 summarises flow regimes in miscible experiment. Similar to immiscible cases, *stable* regime, with no instabilities or oscillation at the interfaces, is observed at low Re_2. *Wavy unstable* regime takes place when Re_2 is increased. This regime occurs when minor oscillation appears at the interface. It is identified by the following two criteria: first unlike the axisymmetric unstable regime for immiscible cases the wavy instabilities for miscible cases can either be axisymmetric or asymmetric from experimental images. No systematic trend was found in terms of the axisymmetric or asymmetric nature of the instabilities in this regime. Also, these instabilities do not persist, there are intervals of stable interfaces between the appearances of this type of interfacial instabilities. *Completely unstable* regime is observed when Re_2 further increases. This regime is identified by the presence of non-stop, asymmetric interfacial instabilities. Similar to the asymmetric unstable regime for the immiscible cases, the completely unstable regime involves various forms of instabilities between the interfaces of fluid 1 and 2.

The completely unstable regime for miscible displacement represents the appearance of much more complex interfacial instabilities which is similar to the “corkscrew” mode observed by Scoffoni, et al. (2001) from vertical miscible displacement experiment (shown in Figure 4.35c).

Figure 4.35 Flow regimes for miscible fluid displacement experiment. All images are from experiment using 100 cSt glycerol solution as Fluid 1 and water as Fluid 2. (a) Stable: $Re_2 = 43$; (b) Wavy Unstable: $Re_2 = 90$ and (c) Completely Unstable: $Re_2 = 183$.

The occurrence of the "completely unstable" regime shows very time-dependent dynamic flow behaviour, some examples of the evolution of the unstable flows in this regime are shown in Figure 4.36.

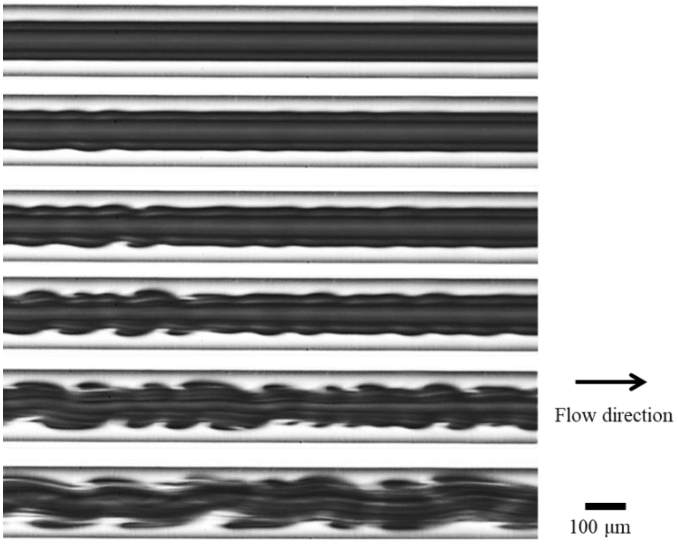

Figure 4.36 Evolution of the "completely unstable" flows, 100 cSt glycerol solution displaced by water, $Re_2 = 300$.

Flow regime maps

The near-semicircular, 200 μm circular and 200×200 μm channels are used for the miscible displacement experiments. For all channels, the identical three fluid pairs are used: 100 cSt glycerol solution as fluid 1, water, 2 and 5 cSt glycerol solutions as fluid 2. Figure 4.37 are the flow regime maps for these three channels. Unlike immiscible displacement where interfacial tension plays an important role (thus capillary number is chosen as the characteristic parameter), no interfacial tension is present at the interfaces of miscible fluid pairs in a physical sense. In this case, Reynolds number is chosen as the characteristic parameter. In addition, the transitions between three flow regimes for miscible cases are harder to define because of the complex flow structures. Therefore those flow conditions result in flow structures that are difficult to categorise are marked as transition region in the flow regime maps.

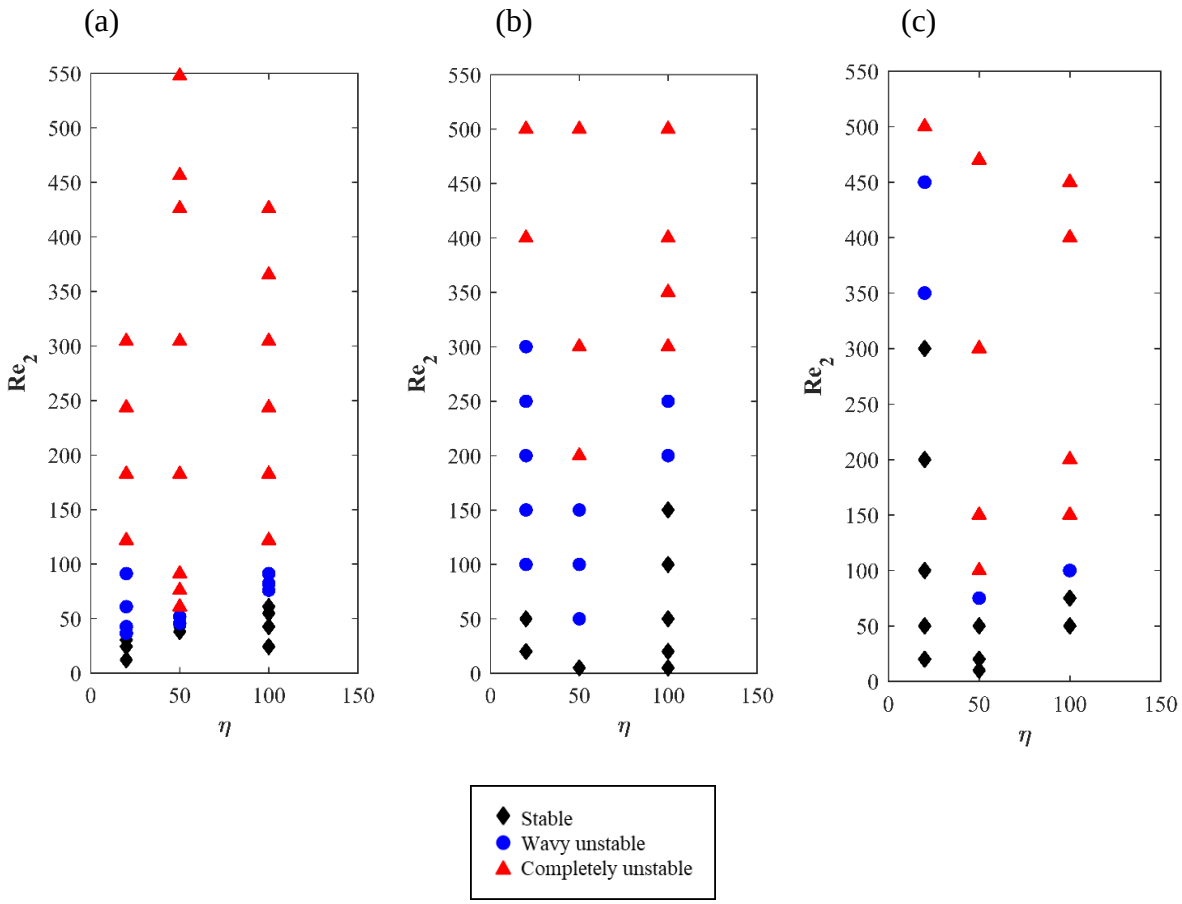

Figure 4.37 Flow regime maps for (a) near-semicircular; (b) 200 μm circular and (c) 200×200 μm square channel. Same fluid pairs are used: fluid 1: 100 cSt glycerol solution, fluid 2: water, 2 and 5 cSt glycerol solutions.

The common feature from the flow regime maps above is that the fluid pair representing viscosity ratio 50 which uses 100 cSt and 2 cSt glycerol solutions as fluid 1 and 2, has the smallest transition *Re* values between the wavy and completely unstable regimes. It can also be seen that using the near-semicircular channel, the hydraulic diameter of which is much smaller than the circular and square channels, resulted in much lower transitions both between stable and wavy unstable regimes and between wavy and completely unstable regimes. This could due to the fact that the same Re_2 values from near-semicircular and circular channel indicates the superficial velocity in the near-semicircular channel is much higher because its hydraulic diameter being much smaller.

4.6 Summary

This chapter discusses the experimental results of the displacement in microchannels with immiscible or miscible fluid pairs. The effects of viscosity ratio, channel geometry and size, wall wettability and the addition of surfactant have been investigated.

For immiscible cases, the range of Ca_1' measured (modified capillary number using real fluid 2 velocity and dynamic interfacial tension for surfactant-laden cases), $0.02 < Ca_1' < 80$, extended the previous reported range. It was found that the initial film thickness, which in general increases with the increase of capillary number, can be estimated more accurately by a method which is referred as the *mean film thickness* for non-circular channels. The cross-section shape of the interface between the two fluids needs to be known or assumed to use this method. A film thinning effect has been observed when a surfactant (SDS) is added into fluid 2, especially for larger capillary number conditions. This is believed to be the result of surfactant redistribution caused by convective flows due to recirculation of fluid in the advancing tip. The radius of the curvature of fluid 2 tip was found to have a reverse correlation with the film thickness, depending on the capillary number. Three flow regimes have been categorised based on the interfacial phenomena observed during the displacement processes. The flow regime maps, characterised by viscosity ratio and capillary number, have been developed. The effect of the addition of surfactant (SDS) was found to be well represented by the capillary number, concluded from the close match between the flow regime maps for surfactant-free and -laden cases.

For immiscible fluid pair displacement, three regimes were defined based on the interfacial activities between the two fluids. Flow regime maps were developed, characterised by viscosity ratio and Reynolds number.

Chapter 5 SIMULATION OF THE DISPLACEMENT OF IMMISCIBLE FLUIDS IN MICROCHANNELS USING COMPUTATIONAL FLUID DYNAMICS (CFD)

Introduction

In this chapter, Computational Fluid Dynamics (CFD) simulations carried out using the commercial package Fluent are described. The aim of this chapter is to use the experiments to validate the flows obtained from this simulation tool as well as providing information that was not obtainable from experiments. §5.1.1 explains the methodology used by Fluent including the detailed setup. Preliminary tests to gain confidence in the simulations by carrying out a mesh independence study (§5.1.2) and the effect of inlet velocity profile (§5.1.3) are first described. The results from the simulation studies using circular, near-semicircular and square channels are discussed in §5.2, §5.3 and §5.4 respectively. Comparisons between CFD simulation results and experimental results focusing on the radius of fluid 2 tip curvature, fluid 1 film thickness and qualitative flow features during the displacement processes such as the interfacial instabilities were carried out, with reasonable agreement observed. The velocity profiles from CFD results also revealed secondary circulation patterns inside the displacing fluid during the process. In addition, §5.2.4 shows that some simulation results obtained have some flow structures (Taylor style plug flow) that were not observed in experiments.

5.1 Methods and theory

As mentioned in §2.4.3, VoF multiphase model was chosen because of its advances in resolving fluid interfaces. The discretization method has a great influence on the accuracy of the

simulation at the interfaces. Fluent (version 16.1) is chosen as the simulation tool in this project because of the variety of discretization schemes available for more accurate and sharper interface simulations. The geometries were drawn using the DesignModeler and the meshing was created using the Meshing facility within the ANSYS stuie. The High-performance Computing facilities at the University of Birmingham (BlueBEAR Linus HPC), accessed using PuTTY, was used for the main calculations. Using 48-72 cores, depending on computing resource availability and individual case calculation speed (affected by geometry, mesh density, flow features, etc.), gives a reasonable compromise between waiting time and calculation speed. An example of the simulation run time is 48 hours for running the simulation for 3×10^{-4} s for the case in Figure 5.13.

Simulations have been carried out only for immiscible fluids pairs. Since no significant difference was observed in terms of the type of interfacial instabilities between fluid pairs (see §4.4) although the occurrence of different instabilities varied as a function of both flow rate and fluid properties, one fluid pair was used for all simulations: 100 cSt silicone oil as fluid 1 and water as fluid 2.

The main objective of the simulation work in the study is to validate the interfacial instabilities that are observed in the experiments. The flow conditions in simulations are purposely chosen to be not close to the transitional conditions found from experiment to maximise the opportunity of getting desired flow features from simulations.

Three channel geometries (near-semicircular, 200 μm circular and 200×200 μm square channels) were used.

5.1.1 Detailed Fluent settings

The detailed 3-D Fluent simulation settings are as follows:

Solver

Two types of solvers are available in Fluent: pressure-based and density-based. Pressure-based solver, with which the momentum and pressure are the primary variables, was chosen in this study. The algorithm that pressure-based solver uses belongs to the "project method" that was introduced by Chorin (1968) to solve incompressible Navier-Stokes equations. In general pressure-based solved is more commonly used for incompressible flow and requires less computing resource input. The pressure-based solver can solve the equations independently since the density of pressure. Absolute velocity formulation was chosen as no rotating domain is present in the current simulation. Transient simulation was carried out because the problem involves time-dependent phenomena such as the unstable motion of the liquid-liquid interface. Further algorithms used within the pressure-based solver are described later in the *solution methods* section.

Model

Euler-Euler multiphase multiphase Volume of Fluid (VoF) model was used in this study. As explained in §2.4.3, the VoF model is commonly accepted to be a good model if the problem involves the description of the position of interfaces.

An explicit VoF scheme was used, providing better solution for time-dependent transient flow behaviour than the implicit scheme. Sharp interface modelling was enabled because only immiscible fluid pairs with a clear interface between the fluids was simulated. To obtain sharp interface is one of the objectives and the basis of comparing simulation with experimental results. Volume fraction cut-off was set to be 1×10^{-6} to ensure the interface was clearly

distinguished. The maximum Courant number (short for Courant-Friedrichs-Lewy number, LFL), which sets the maximum value of the ratio of the sub time step to the minimum transit time, is 0.25. In Fluent VoF model, the sub time step is calculated using

$$\Delta t = C \frac{\Delta x}{u_{fluid}} \qquad \text{(Equation 5.1)}$$

Where Δt is the sub time step, C is the Courant number, Δx is the cell size and u_{fluid} is fluid velocity. The transit time is the smallest value of the times for the fluid to clear out of the cell near fluid interface region.

Fluid 1 (100 cSt silicone oil) is set as the secondary phase, fluid 2 was set as primary phase. The reason for this is Fluent only allows the secondary phase to be patched in the domain, which effectively act as the step of the pre-filling of fluid 1 in the experiment. Surface tension force modelling was enabled in the phase interaction settings and the experimentally obtained interfacial tension values between fluid 1 and 2 were used.

The laminar model was chosen in the viscous model panel because the largest Reynolds number (Re_2) is ~150. All other models were disabled for the simulations.

Material

The fluid properties such as density and viscosity from experimental materials were used.

Boundary conditions

In all cases, wall type boundary was used for all the channel walls. Stationary wall and no slip condition, indicating zero velocity at the wall, were used. The inlet plane was velocity-inlet type to mimic the injection of fluid 2 at fixed flowrate in the experiments. The inlet velocity was set using the fluid 2 injection superficial velocity, obtained from the injection flowrate divided by the cross-section of channel. A User-defined Function (UDF) was used to test the

difference between the inlet velocity with parabolic profile and constant uniform profile, as detailed in §5.1.3. No significant differences were found by comparing the results. A uniform velocity profile inlet was therefore used for all simulations. The outlet was “outflow” type because neither the pressure nor velocities have been measured in the experiments thus this information could not be provided in the simulation.

Solution methods

The SIMPLE scheme, which belongs to the pressure-based segregated algorithms described in the *solver* section, was chosen in the pressure-velocity coupling. The SIMPLE scheme uses a flux and pressure correction for the solution of momentum equations to satisfy the continuity equation. Figure 5.1 illustrates the control volume discussed here. c_0 and c_1 are the cells either on the side or the face *f*.

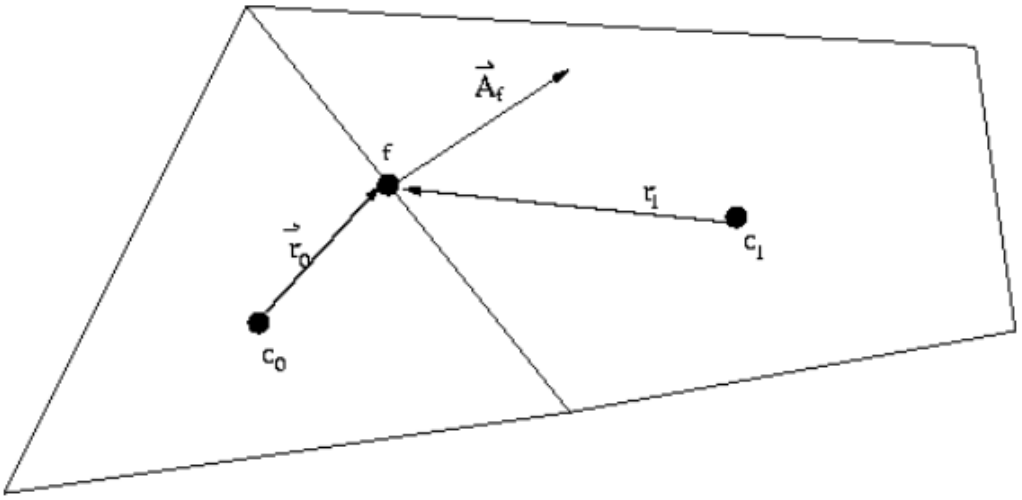

Figure 5.1 Illustration of the control volume.

The integrated continuity equation is written as：

$$\sum_{f}^{N_{faces}} J_f A_f = 0 \qquad \text{(Equation 5.2)}$$

Where J_f is the mass flux through face *f*. A correction face flux J_f' is added to the face flux computed from the momentum equation J_f^* using a guessed pressure field P^* to be the correct face flux:

$$J_f = J_f^* + J_f' \quad \text{(Equation 5.3)}$$

The SIMPLE writes the correction face flux J_f' to be

$$J_f' = d_f (P_{c0}' - P_{c1}') \quad \text{(Equation 5.4)}$$

Where P' is the cell pressure correction. Then Equation 5.3 and 5.4 are substituted in Equation 5.2 to get:

$$\alpha_P P' = \sum_{nb} a_{nb} P_{nb}' + b \quad \text{(Equation 5.5)}$$

Where *b* is the source term of the net flowrate into the cell and α_P is the under-relaxation factor for pressure, which is used to stabilize convergence behaviour. Once Equation 5.5 is solved then the correct cell pressure and face flux can be written as:

$$P = P^* + \alpha_P P' \quad \text{(Equation 5.6)}$$

$$J_f = J_f^* + d_f (P_{c0}' - P_{c1}') \quad \text{(Equation 5.7)}$$

The Least Squares cell-based method, which the solution is assumed to vary linearly, was chosen for the spatial discretization gradient. Only the body-force-weighted and the PRESTO! (PREssure Staggering Option) the available pressure interpolation scheme for the VoF model. In this study the body-force-weighted scheme, which assumes the constant gradient of the

difference between pressure and body forces, was chosen. Second-order upward discretization scheme was chosen to reduce numerical diffusion and achieve higher accuracy. Andersson, et al. (2015) provide an example of how first- and second-order affects the results at an interface:

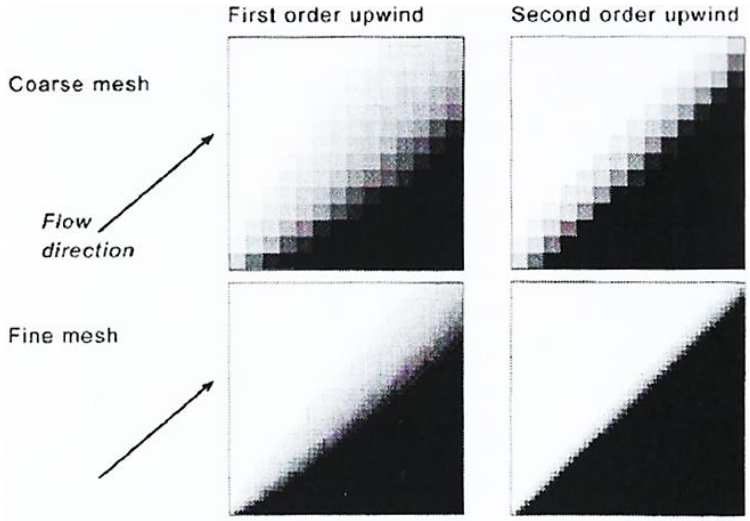

Figure 5.2 The improved description of interface using first and second order upwind discretization schemes (Andersson, et al., 2015).

The Geometric reconstruction scheme was chosen for volume fraction formulation to ensure a smooth and most reality-matching interface. The second-order implicit formulation was chosen for transient formulation, for better accuracy.

Solution controls

Under-relaxation factors were set at a lower value first for easier and more stable convergence then raised in later calculations.

The convergence criteria were set in the residual monitors. 1×10^{-6} was used as the convergence criteria for all residuals (continuity, x-velocity, y-velocity and z-velocity).

Calculation

The time step for calculation varies for different cases. The choice of time step was based on the criterion that convergence was achieved within 10 to 30 iterations.

In this chapter, the characteristic dimensionless groups are Re_2 and Ca_2, both are calculated on the basis of the superficial velocity of fluid 2. The reason for not selecting the modified capillary number, based on real velocity estimated from superficial velocity and film thickness, is that the film thickness measurement from simulation and experimental results does not always match very well. Therefore if the real velocity is used, the capillary number for simulation differs from that for experimental results.

5.1.2 Mesh independence study

Mesh independence studies were conducted by running multiple simulations using exactly the same conditions apart from the mesh density. In this project, an initial mesh was set up as the starting condition of mesh independence study. Simulation is firstly carried out using this initial mesh setting before more simulations are carried out using a finer mesh each time. The details of the mesh setting used for three channels are shown in Table 5.1.

Table 5.1 Meshing settings for three geometries in the mesh independence study.

		Initial	**Mesh 1**	**Mesh 2**	**Mesh 3**	**Mesh 4**	**Mesh 5**
Near-semicircular	No. of cells width-wise	42	61	72	82	-	-
	No. of cells height-wise	24	30	38	46		
	Total nodes	3301100	5397596	6407829	7498260	-	-
	Cell size (μm)	4.9	3.4	2.8	2.5	-	-
Circular	No. of cells along diameter	40	47	55	60	-	-
	Total nodes	2721900	4283664	7392560	14783628	-	-
	Cell size (μm)	5.0	4.3	3.6	3.3	-	-
Square	No. of cells width-wise	33	40	50	59	73	83
	Total nodes	2891156	5044681	6505101	8237580	13087851	18101114
	Cell size (μm)	6.1	5.0	4.0	3.4	2.7	2.4

For the square channel, the initial mesh setting is set with 33 cells along the width and height of the cross-section. This contributes to 2891156 nodes count for the whole geometry (10 mm in length) used in this simulation. Mesh independence studies were then carried out using mesh settings of 40, 50, 59 and 73 along the width and height of the cross-section, contributing to 5044681, 6505101, 8237580, 13087851 and 1810114 nodes count respectively for the whole geometry. The fluid 2 injection condition is u_2 = 0.5 m s^{-1} (Re_2=100). Simulation results at the flow time when the axisymmetric unstable flow appears and fluid 2 travels in exceed the entrance length was chosen (4.74×10^{-3} s).

(a)

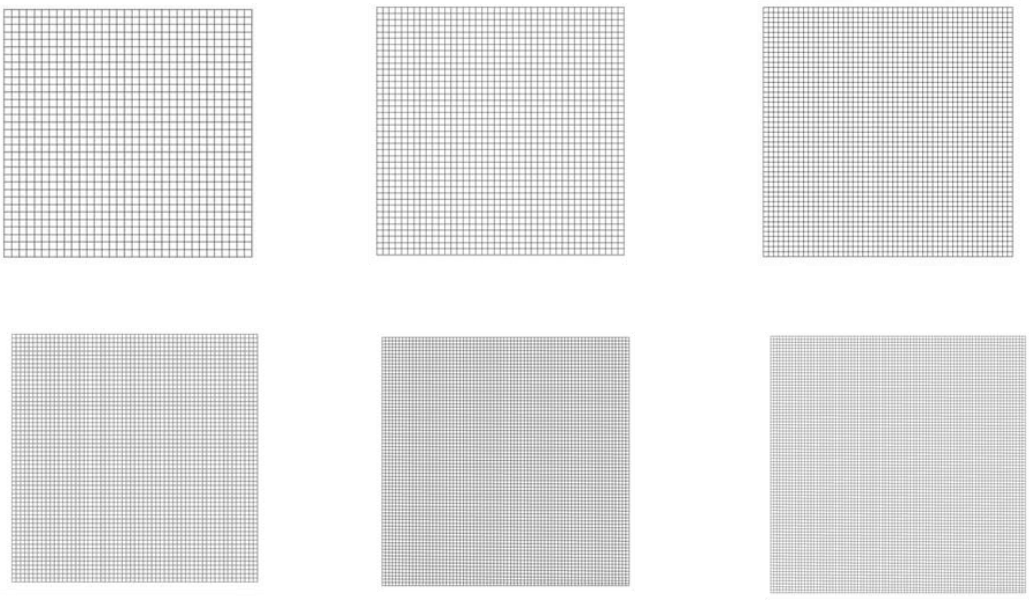

Figure 5.3 Illustration of meshing settings at the cross-section of the channel in the mesh independence study for square channel, showing the increase in mesh density (mesh details in Table 5.1).

The parameters used to check the effects of increasing mesh density are the velocity profile at fluid 2 tip and the width of the interface between two fluids.

The velocity profiles at fluid 2 tip were compared in Figure 5.4. It can be seen that the increase of mesh density are not significantly different once the mesh density exceeds that of Mesh 1.

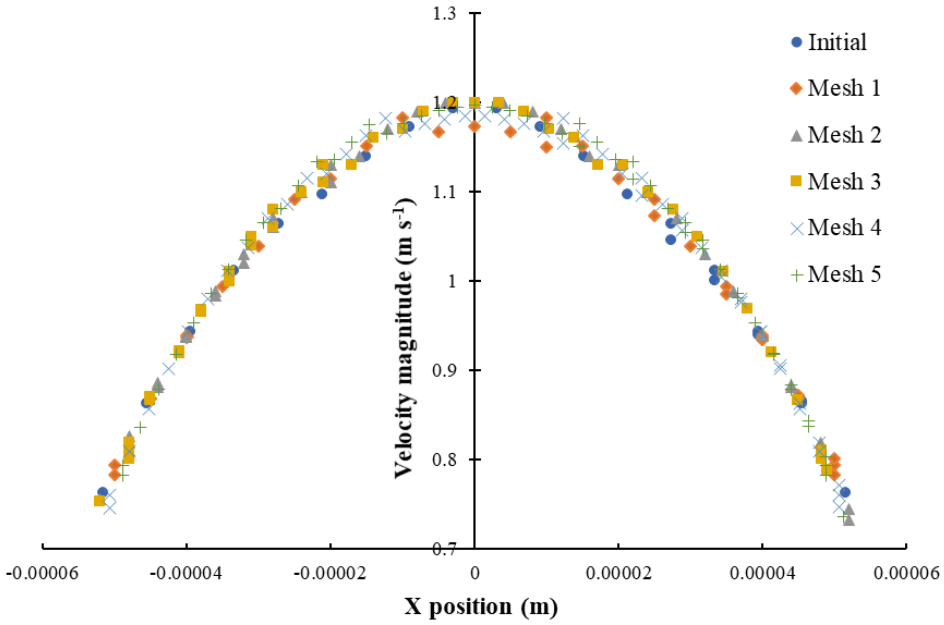

Figure 5.4 Velocity profile taken along the tip of fluid 2 in the mesh independent study using square channel. Detailed meshing settings in Table 5.1.

Figure 5.5 shows the decrease of the width of interface between fluid 1 and 2, observed from the volume fraction contours at the cross-section. The position of this cross-sectional plane is three times the channel width away from the fluid 2 tip. It can be seen from these figures that the width of interface decreases as the mesh density increases. Therefore the actual volume fraction values are used to see how many cells are occupied by the interface then consequently the width of the interface can be obtained.

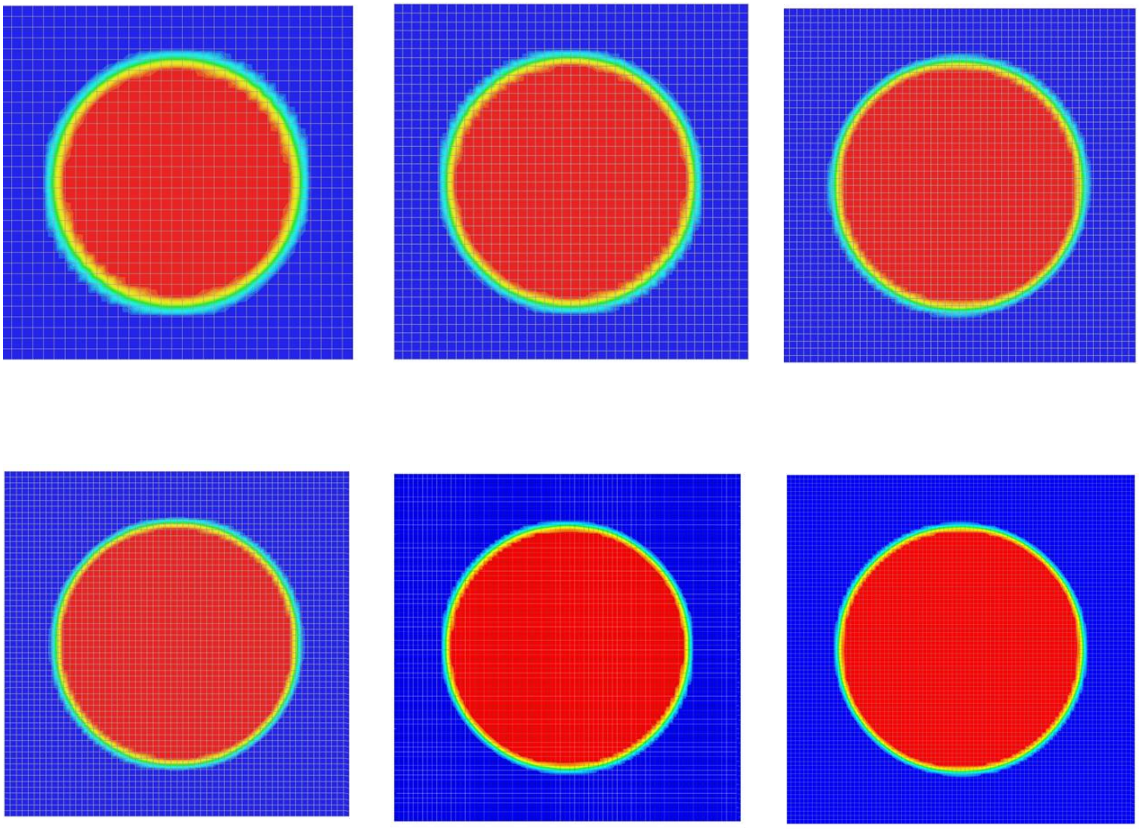

Figure 5.5 Cross-section view of the volume fraction of water (blue is volume fraction 0 and red is volume fraction 1) taken at the cross-section plane at the position of three times channel width away from the tip of fluid 2.

The volume fraction values at the horizontal line of the cross-section view above are plotted in Figure 5.6 for the six cases. Only the volume fraction values at the one of the two interfaces, where the volume fraction values are between 0 and 1, are shown. It was shown that using the current settings the interface resolved within 2 or 3 cells. The gradient between the lines of these interface cells represent the width of the interface. When mesh density increases from the initial setting to mesh 4, the gradient increases. However the increase of mesh density from Mesh 4 to Mesh 5 does not result in a further increase of the gradient. Therefore the mesh independence is achieved, Mesh 4 has been used for further calculations.

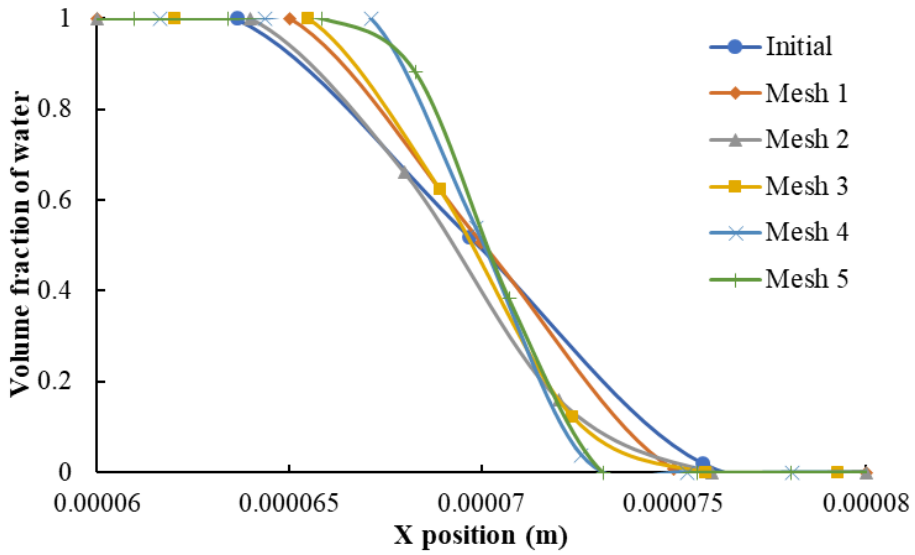

Figure 5.6 Volume fraction of water at the central horizontal line of the view in Figure 5.5, only the one side of the interfaces where volume fraction values are between 0 to 1 are shown.

In addition, the flow behaviour from the cases using different mesh densities are shown in Figure 5.7 by the iso-surface of volume fraction contours. Both the 3-D view and the 2-D view from the volume fraction values taken at the vertical middle plane of the channel are shown. It can be seen the flow behaviour, judging from the appearance of instabilities does not change much from the results using mesh 4 and 5, which also suggests the achievement of mesh independence.

(a)

(b)

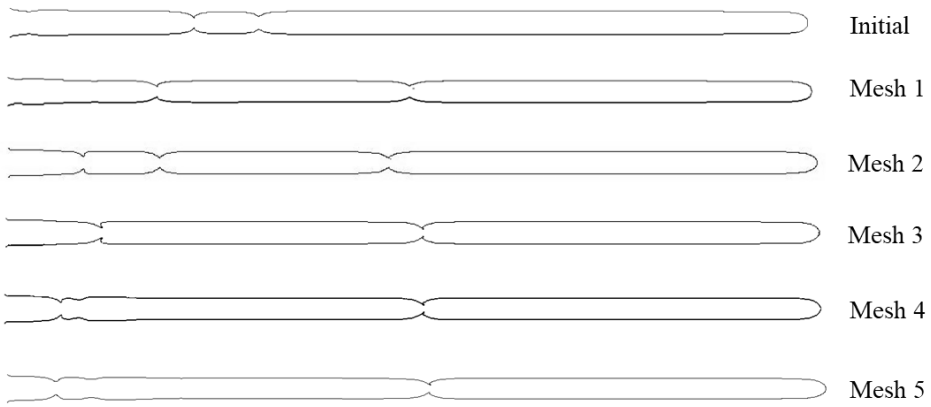

Figure 5.7 Different simulation results from simulations using different mesh settings for square channel (All results taken at flow time 4.74×10^{-3} s after fluid 2 entering the channel). (a) 3-D view: isosurface of volume fraction and (b) 2-D view from volume fraction contour at the vertical middle plane of channel.

For circular channel, the initial mesh setting is set with approximately 40 cells along the diameter of the channel cross-section, contributing to 2721900 nodes count for the whole geometry (10 mm in length). Mesh density was increased in order to achieve mesh independence by using approximately 47, 55, 60 cells along the diameter of cross-section, contributing to 4283664, 7392560 and 14783628 nodes respectively for the whole geometry. Simulation results at flow time 5×10^{-3} s were used to check if mesh independence has been achieved. It was believed that mesh independence was achieved using the mesh setting with 55 cells along the diameter and 7392560 nodes in total. For near-semicircular channel, the initial mesh setting has 42 and 24 cells along the width and height of the channel, which is 3301100 nodes in total. Mesh density was increased to 61, 72 and 82 cells along the width and 30, 38 and 46 cells along height before achieving mesh independence.

Similar to the square channel, the width of interface was used as the main parameter to decide the complete of mesh independence study. Flow behaviour was also checked to confirm the mesh density. For both circular and near-semicircular channel, the mesh density of "mesh 3" (see Table 5.1) was used for further simulations.

5.1.3 Inlet with parabolic velocity profile

C programme codes were written and applied in Fluent as the UDF input to create the parabolic velocity profile at inlet. The codes are shown in appendices. Circular channel was used for this test and all settings were identical apart from the inlet velocity profile. A constant uniform inlet velocity profile set at $u_2 = 0.5$ m s^{-1}, which is the mean velocity for the parabolic velocity profile, which was also used. Figure 5.8a is the illustration of the parabolic inlet velocity profile and Figure 5.8b and c are the results from the two cases of the contours (at flow time 5×10^{-3} s) based on water volume fraction at the horizontal central plane of the channel. It can be seen the results

are almost identical. This is explained by the development length (entrance length) being very small. The development length is ~1.8 mm using the largest *Re* in the simulations (Calculated using Shah and Bhatti (1987), see §3.2). Therefore the constant flat inlet velocity profile is used for all future simulations.

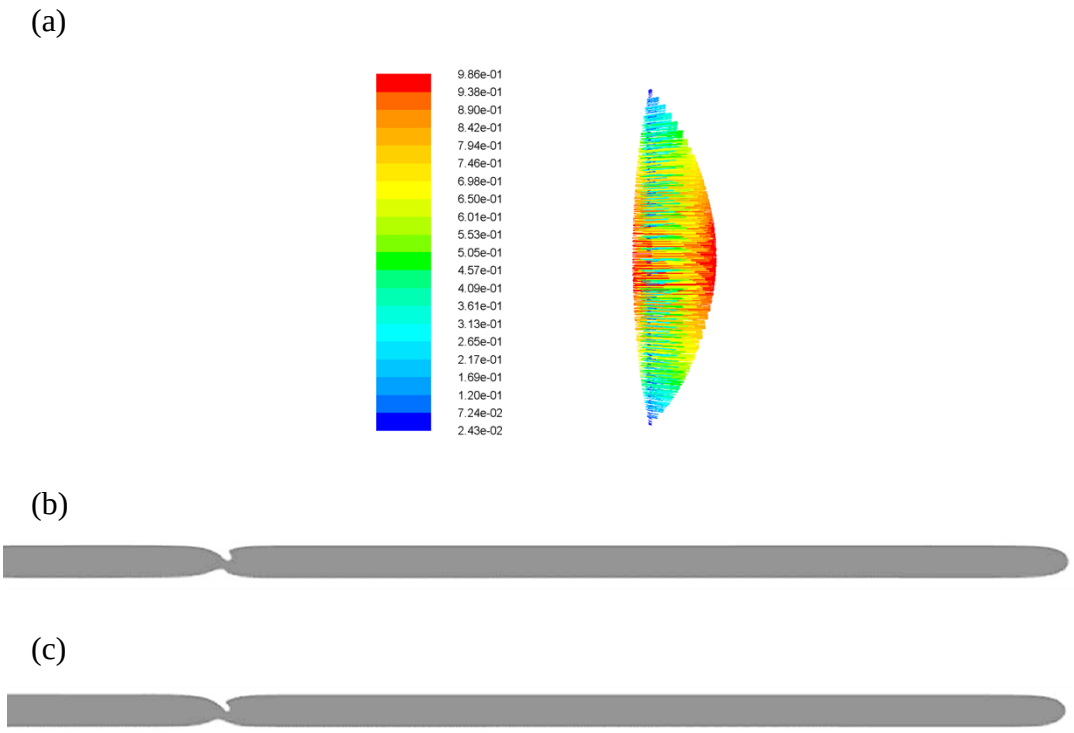

Figure 5.8 (a) Illustration of parabolic inlet velocity profile, velocity unit m s^{-1}, and the comparison of inlet with (b) parabolic velocity profile and (c) constant uniform profile. 200 μm circular channel was used and graphs shown are at flow time 5×10^{-3} s.

5.2 Simulation results for circular channel

The meshing settings following the conclusion from the mesh independence study mentioned above were used for all simulations. For the circular channel immiscible displacement cases, all three flow regimes have been obtained from simulations, as briefly illustrated in Figure 5.9. Detailed analysis of these simulation results is in the following paragraphs.

Figure 5.9 Three forms of interfacial instabilities achieved from simulations in circular channel. Left: Stable, Re_2 = 5, Ca_2 = 0.001, water fraction contour taken at middle horizontal plane; middle: Axisymmetric Unstable, Re_2 = 100, Ca_2 = 0.02, iso-surface; Right: Asymmetric Unstable, Re_2 = 170, Ca_2 = 0.034, iso-surface. Arrows show flow directions. The flows shown are part of the entire channel (fluid 2 has not reached the channel outlet).

5.2.1 Circular channel stable regime

The stable regime from simulation resulted in a flow that the width of fluid 2 is the same as the diameter of the channel. This is because the very small fluid 2 injection flowrate used. This phenomenon has also been seen in experiment (Figure 5.10a). However the contact between fluid 2 and the channel wall for simulation and experimental results are not exactly the same, as shown in Figure 5.10b. This could due to the fact that in simulations apart from no slip boundary condition for the wall, no other characteristics such as the contact angle between the wall and fluid 2 have been used. Despite the difference in the contact between fluid 2 and the wall, the dimensionless radius of fluid 2 tip curvature measurement shows good agreement with the experiments, from simulation the result is ~0.34 and from experiments the result is ~0.31.

(a) (b)

Figure 5.10 (a) Experimental image showing the fluid 2 occupies the entire width of the channel, no fluid 1 film thickness can be seen. (b) CFD results for comparison. Flow conditions: Re_2 = 5, Ca_2 = 0.001.

5.2.2 Circular channel axisymmetric unstable regime

Evolution of unstable flows

The evolution of axisymmetric instabilities in circular channel from simulation is shown in Figure 5.11a. The measurement of fluid 2 tip curvature and film thickness of fluid 1 left on wall were carried out using the simulation results, using the same strategy used for the experimental measurements (Figure 5.11b). The dimensionless film thickness from simulation results is ~0.16. The dimensionless film thickness measurement for the relevant experiment using the same flow condition (Ca_2 = 0.02) is ~0.14, resulting in a difference of 4 μm, i.e. less than the size of two pixels considering the smallest pixel resolution in experiments. The dimensionless fluid 2 tip curvature from simulation results is 0.14 whilst experimental result was 0.17, resulting in a difference of 6 μm.

(a)

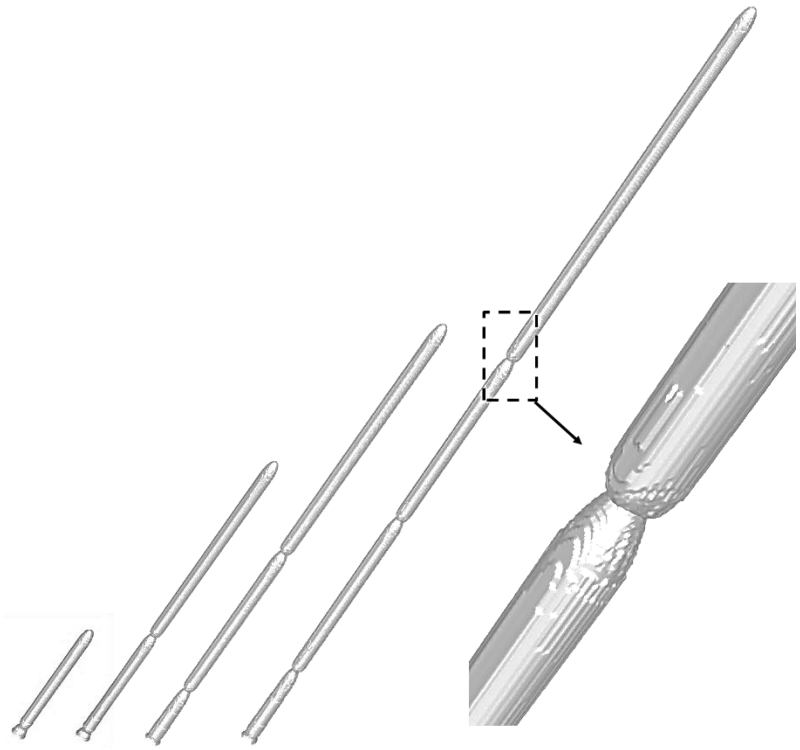

(b)

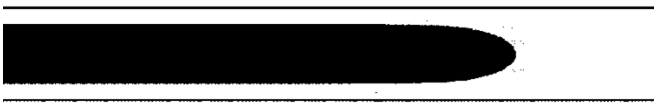

Figure 5.11 (a) Evolution of the iso-surface generated based on water volume fraction indicating the water/oil interface at different times. Axisymmetric instabilities from immiscible simulation in near-semicircular channel, viscosity ratio = 100, Re_2 = 170, from left to right: flow time t = 9.14×10^{-3}, 1.16×10^{-2}, 1.31×10^{-2} and 1.66×10^{-2} s. A zoom-in image of the axisymmetric instabilities on the right. (b) The image from simulation results for the measurement of film thickness and fluid 2 tip curvature from simulation results.

Change of instability flow pattern

The simulation results show that the pinching parts in the axisymmetric unstable flows change in form after fluid 2 travels through the entire channel. The results shown above were obtained at times before fluid 2 exited the channel. This change in form is shown in Figure 5.12c as well as the comparison between the results from simulation and experiment for this flow regime.

The simulation images shown are the same view with that for experiment and images in Figure 5.12b. The screenshots in Figure 5.12b are purposely binarized to imitate the effect that the experimental images are two-dimensional projected view of flow of the dyed fluid 2 flows. It can be seen from Figure 5.12a and c that the appearance of the axisymmetric unstable flow from simulation resembles better the experiments after fluid 2 has exited the channel. The exact reason for this is not clear. However, it may be caused by the much shorter channel length in CFD simulation than in the experiments. In experiment, the location where the images were recorded was approximately 2/3 of the channel length away from the inlet (15 mm) while the length of channel in CFD simulation was 10 mm. It is possible that this type of interfacial instability needs longer development time in CFD simulations to form similar appearance from experimental images.

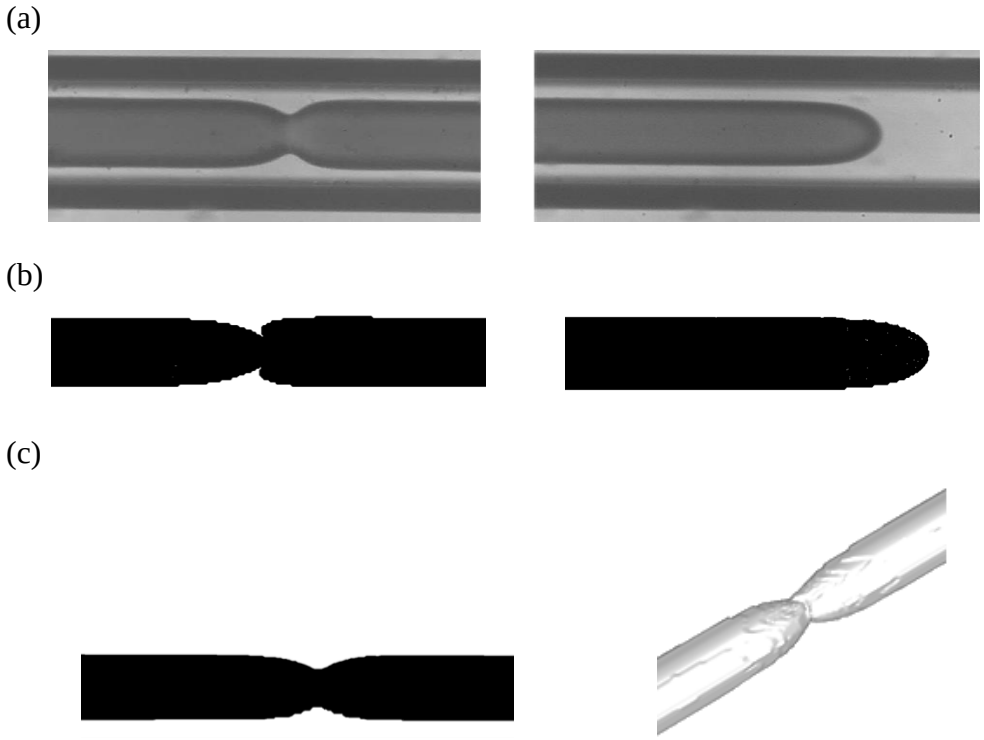

Figure 5.12 In circular channel. (a) Experimental results for axisymmetric unstable flow regime; (b) simulation results at instability part from simulation results, fluid 2 travels through the entire channel; (c) simulation results at instability part from simulation results, after fluid 2 travels through the entire channel. Flow conditions: $Re_2 = 100$, $Ca_2 = 0.02$.

Velocity profiles

The simulated mean velocity of fluid 2 are also compared with the real mean velocity estimated from experimental results by considering the cross-section area occupied by fluid 2. For this particular flow condition (Flowrate 942 μL min^{-1}) the theoretical superficial velocity at the inlet, which is calculated from the flowrate and cross-section area, is 0.5 m s^{-1}. The estimated real fluid 2 velocity when it travels to the position where film thickness was measured, is 0.97 ms^{-1} from experimental results and 1.11 m s^{-1} from simulation results. This may due to the fact that the estimation of real fluid 2 velocity did not take the unstable region, which has smaller cross-section area, into consideration.

The other important feature which was not able to be measured in the experiments, is the velocity profile at the unstable part of the flow. Figure 5.13 shows the velocity profile taken at the horizontal middle plane of the channel as well as the flow interface based on volume fraction. These results reveal that although topologically the flow appears to be axisymmetric unstable, the motion of the fluid 2 flow can be asymmetric and much more complicated. A sinuous curve in the velocity along the axis of the channel can be observed. In addition, the velocity at the unstable part of the flow appears to be the biggest along the whole channel, which is believed to be one of the reason accounting for the slight deviation of the estimation of mean velocity in experiment from simulation results.

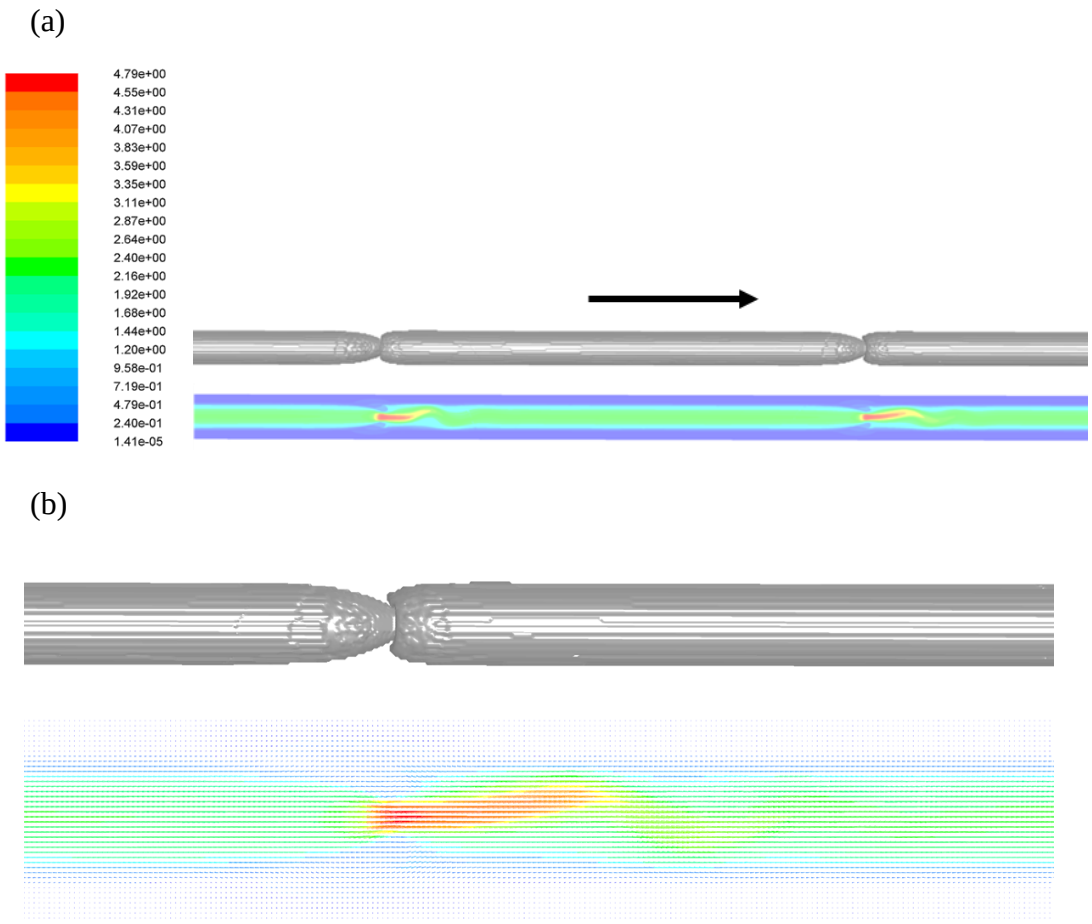

Figure 5.13 Simulation results reveals the velocity profile at the unstable part of the flow. Flow time: 1.66×10^{-2} s. Velocity data taken at the horizontal middle plane of the channel. (b) is a close-up view of the vectors of (a), which shows the contour of velocity profile. Flow direction from left to right. All velocity profiles in this study are the velocity of the velocity of the mixture of fluid 1 and 2. Velocity unit: m s^{-1}. Arrow indicates flow direction.

The velocity fields within the channel cross-section at three different chosen positions are shown in Figure 5.14. The velocity vectors only show the combination of *x*- and *y*- velocities, which are the horizontal and vertical velocities; *z*- velocity, which is the axial velocity along the channel direction, is subtracted and the velocity contours show the total velocity magnitude. The three positions are: (a) close to fluid 2 tip, (b) in the middle between two unstable flow pinching parts and (c) at the pinching part of unstable flow.

The velocity at the position close to fluid 2 tip shows more outward radial velocity than the velocity fields taken at position b, which shows strong axial velocity but low radial velocity. The radial velocity presented near fluid 2 tip assisted mass transfer therefore in the surfactant-laden cases, the film thickness and tip curvature measurement are affected by uneven distribution of surfactant molecules. The velocity fields at position c show the velocity at the location close to the centre is much larger than off-centre positions. Also it shows very strong radial velocity at near centre as well as some inwards radial velocity at off-centre positions.

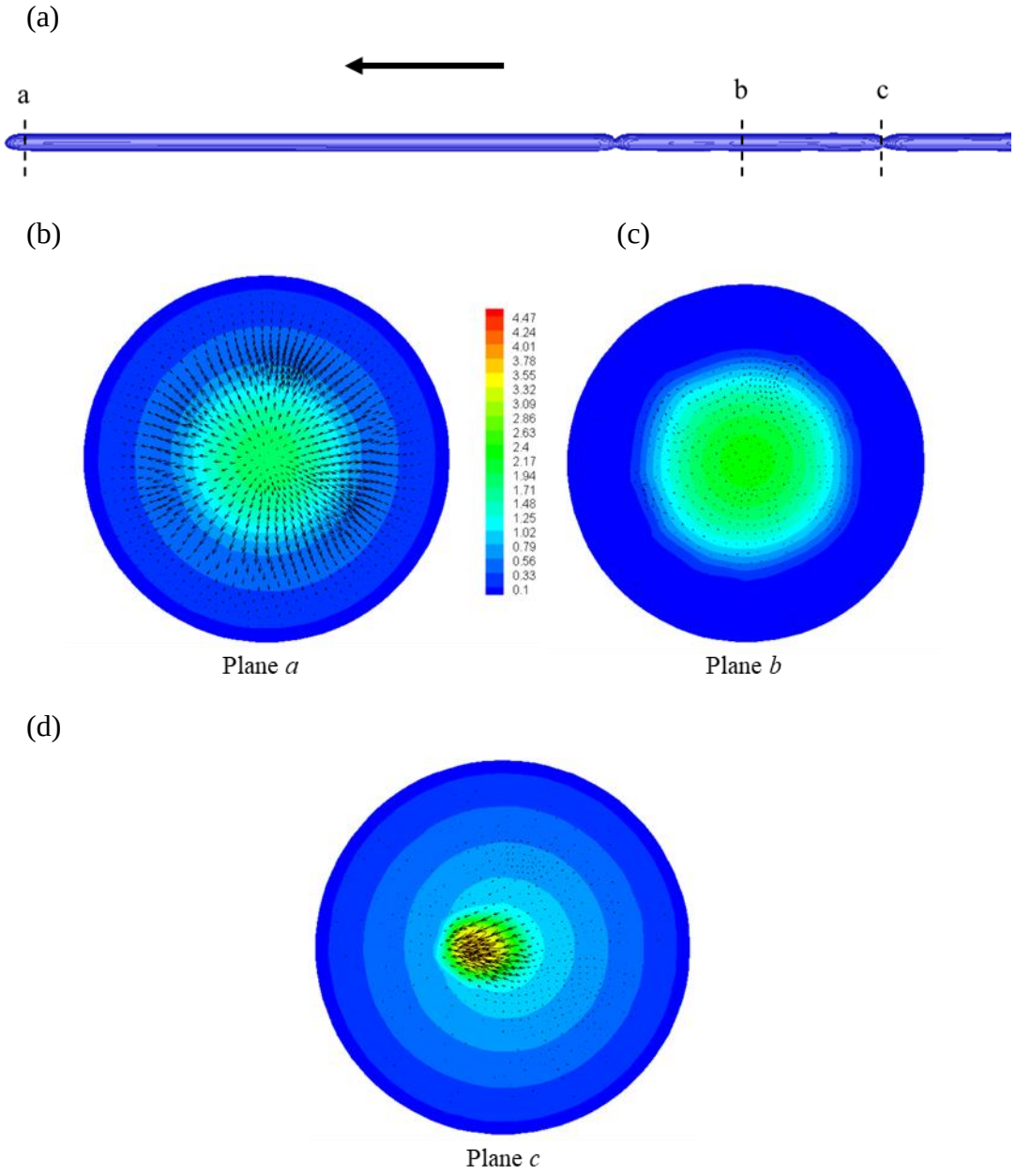

Figure 5.14 Cross-sectional velocity fields at three positions: (a) the three cross-sectional positions, (b) near fluid 2 flow tip, (c) in the middle of two flow pinching parts ad (d) at the unstable flow pinching part. Velocity vectors showing radial velocity and velocity contours showing overall velocity magnitude. Legend in (b) applies to all figures, unit m s^{-1}. Arrow indicates flow direction.

The velocity at the central vertical line in the plane *b* in Figure 5.14, where is believed to be far enough from both the fluid 2 tip and the pinching unstable part, is shown in Figure 5.15. The velocity is normalised by maximum velocity at the line and the distance from the central line is

normalised by channel diameter (*r* is the radial position). The positions where the velocity starts to suddenly increase is at the interface between fluid 1 and 2.

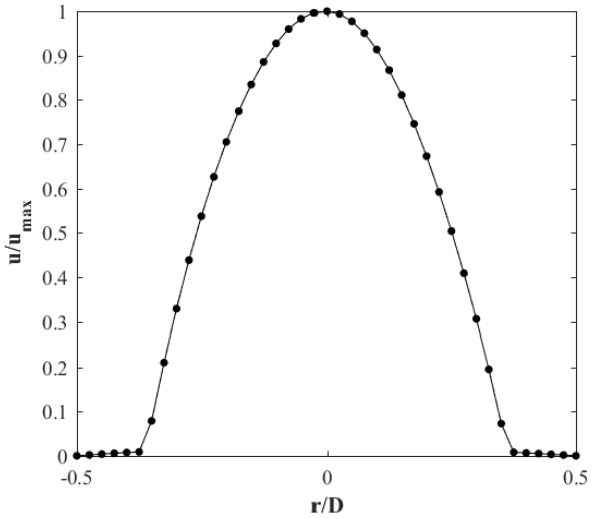

Figure 5.15 Velocity profile at the vertical central line at the position b plane in Figure 5.14.

5.2.3 Circular channel asymmetric unstable regime

Figure 5.16 shows the simulation results of the evolution of asymmetric instabilities in circular channel. Fluid 2 tip curvature and film thickness measurement were also obtained from the simulation. These results were also validated by experimental finding of the existence of a short axisymmetric unstable regime before the asymmetric unstable flows starts to appear, as seen in the fourth flow image in Figure 5.16.

The dimensionless film thickness measurement from simulation result is ~0.11 while the experimental result for the same flow conditions is ~0.16. The dimensionless fluid 2 tip curvature is ~0.23 from simulation result and ~0.19 from experimental result.

Figure 5.16 Simulation results using 200 μm circular channel. Evolution of the iso-surface generated based on water volume fraction indicating water/oil interface at different times. Asymmetric instabilities from immiscible simulation in near-semicircular channel, viscosity ratio = 100, Re_2 = 170, Ca_2 = 0.034, from left to right: flow time t = 1.03, 2.53, 4.00 and 5.60 ($\times 10^{-3}$ s). A zoom-in image of the asymmetric instabilities on the right.

Velocity profiles and comparison with experimental results

The three-dimensional views of these instabilities are revealed in Figure 5.17, where the flow contours at the horizontal and vertical middle plane of the channel are shown. Similar forms of interfacial instabilities were captured in experimental images (Figure 5.18). As mentioned previously, these images are the projected view of flows, thus only with simulation results it is possible to observe the behaviour of these unstable flows from different views.

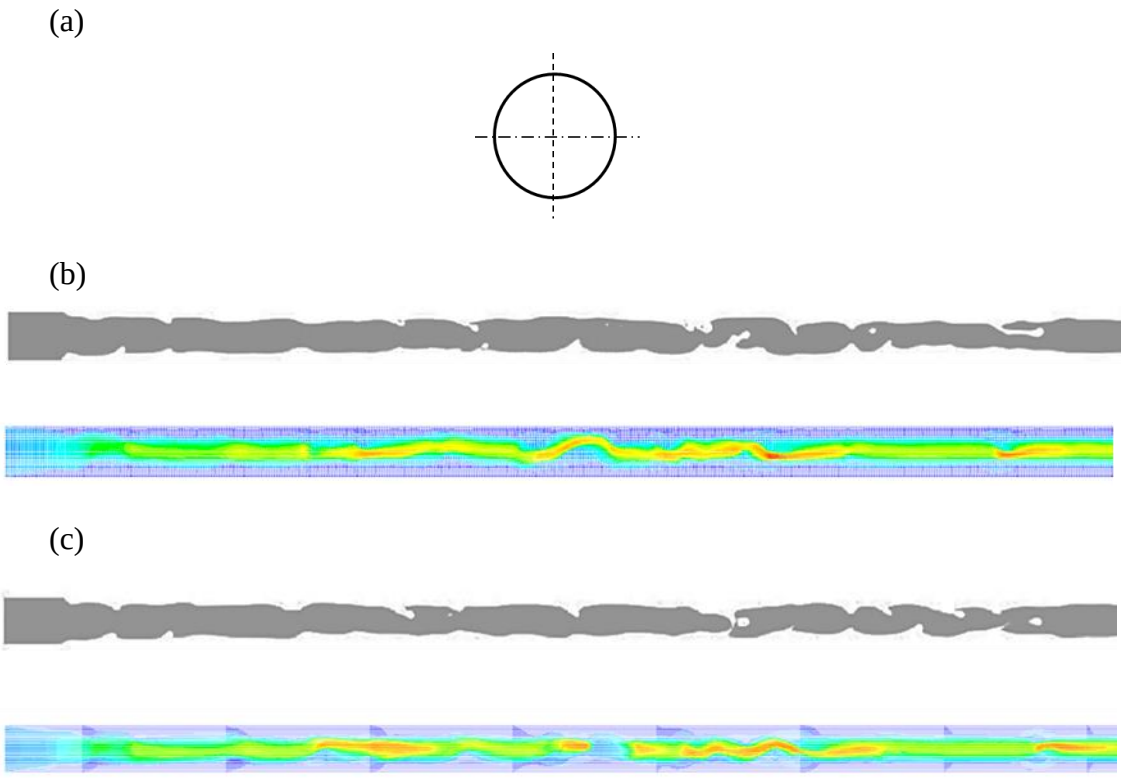

Figure 5.17 Simulation results using 200 μm circular channel. Volume fraction contours and velocity vectors taken at (b) the vertical plave indicated in (a); (c) the horizontal plane indicated in (a). Same flow conditions from the fourth image in Figure 5.16, flow time 5.6×10^{-3} s.

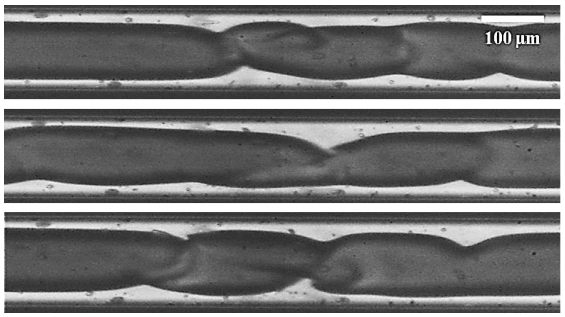

Figure 5.18 Experimental images from immiscible displacement experiment using the same flow conditions in Figure 5.17.

The cross-sectional velocity profile taken at the plane within the asymmetric instability parts is shown below. Radial velocity can be observed especially at the high-velocity regime in the colour coded graph in Figure 5.19, where fluid 2 flows.

(a)

(b)

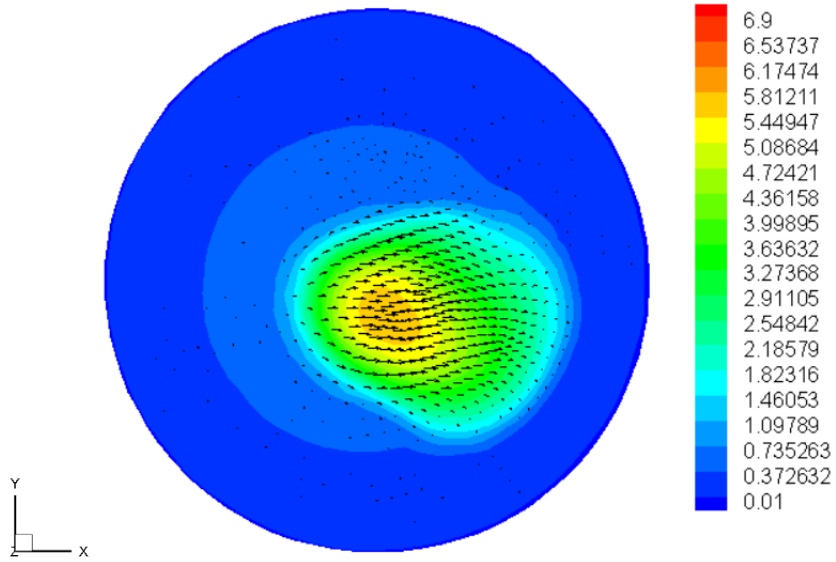

Figure 5.19 Cross-sectional velocity profile taken at the plane in (a) for the asymmetric unstable flows in circular channel. Unit of velocity magnitude: m s^{-1}.

In Figure 5.20, the mean fluid 2 velocity, which is calculated using the flow time after fluid 2 entering the channel and the distance fluid 2 travels in the channel, is subtracted from fluid 2 velocity field to reveal the circulation patterns near the fluid 2 tip region. In this case the mean velocity is calculated from the displacement of the fluid 2 tip within a known time. Figure 5.20a and b are the velocity profiles in the horizontal (*x*-*z*) plane near fluid 2 tip before and after velocity subtraction, Figure 5.20c shows the streamlines of the circulation patterns; the velocity magnitude is shown as the flood colour on the plot.

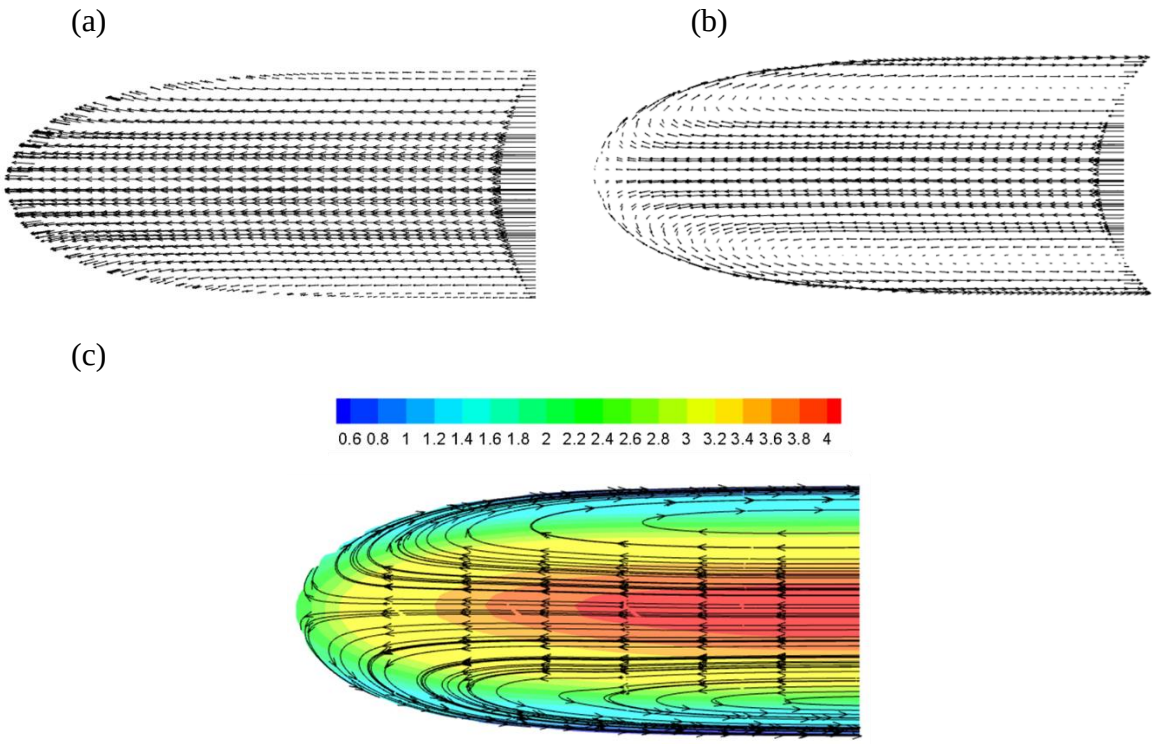

Figure 5.20 velocity profiles at the horizontal plane near fluid 2 tip, (a) before velocity subtraction; (b) after velocity subtraction and (c) streamlines of circulation patterns, velocity magnitude is superimposed with colour. Unit of velocity magnitude: m s^{-1}.

5.2.4 Circular channel flow "breakage"

During the simulation of circular channel, using a particular flow condition (Re_2 = 20, Ca_2 = 0.004) has resulted in the establishment of an intermittent flow regime, analogous to Taylor flow, which was not able to be reproduced in the experiment. Figure 5.21a shows the two views of this flow regime from simulation in circular channel. Figure 5.21b shows an example of the only intermittent flow regime which has been observed from experiments, which is believed to be caused by operational issues. These issues may include the inserting of the needle containing fluid 2 onto tubing, if the initial contact between fluid 1 and 2 at the needle tip is not strictly carried out in the way of fluid 2 pushing fluid 1, fluid 1 can sometimes exist between the first small amount of fluid 2 and the bulk of fluid 2. The reproducibility of these in experiments is

very low. In addition, the shape of the intermittent flows from simulation and experiment are very different. The tail part of each plugs in simulation results is almost flat compared to the curved shape in experiments. This very much resembles Taylor flow using certain fluids and operating conditions; Figure 5.21c shows the experimental image from (Haase, 2017), using hydrogen-glycerol two-phase flows ($u_{L,S}$ = 0.312 m s^{-1}, $u_{G,S}$ = 0.515 m s^{-1}).

The exact reason for the "breakage" taking place is not yet totally understood. But it is believed to be associated with simulation settings such as the cut off value of volume fraction. In this study a volume fraction cut off value of 1×10^{-6} was used in all cases, despite other settings such as mesh density.

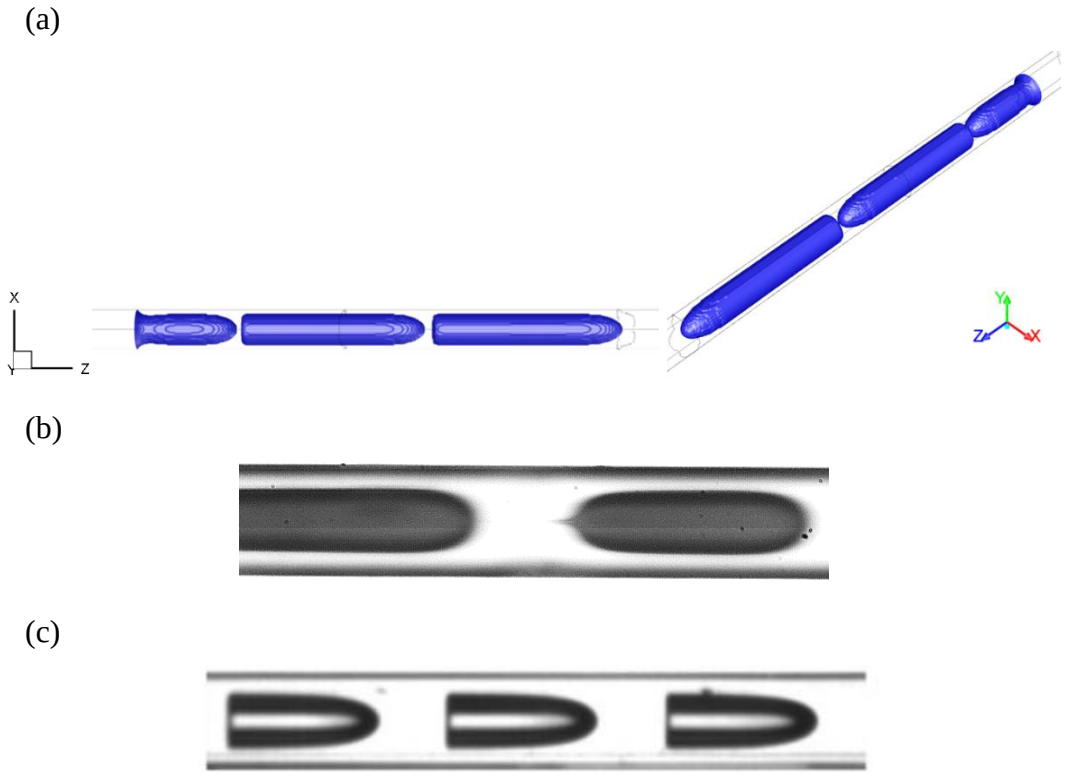

Figure 5.21 Intermittent (Taylor flow) regime in (a) simulation (circular channel, Re_2 = 20, Ca_2 = 0.004) and (b) experiment (believed to be caused by experimental operation instead of the dynamic of flows). (c) shows the similar flat-end Taylor flows from literature: hydrogen-glycerol two-phase flows ($u_{L,S}$ = 0.312 m s^{-1}, $u_{G,S}$ = 0.213 m s^{-1}, Ca = 152). (Haase, 2017).

Velocity profiles

The cross-sectional velocity profiles taken at the front, middle and tail position of a plug are shown below. As expected, the cross-sectional velocity profile at the plane near the tail shows inwards radial velocity compared to the plane in the middle, which shows almost no radial velocity. The velocity profile at the plane near the tip shows strong outwards radial velocity. These findings are in line with the results from Li and Angeli (2017).

(a)

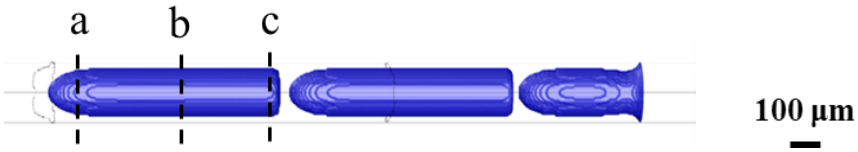

(b)

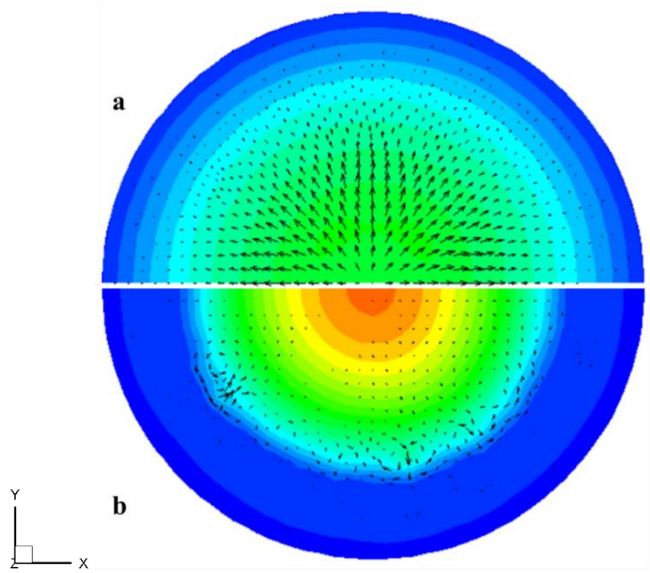

(c)

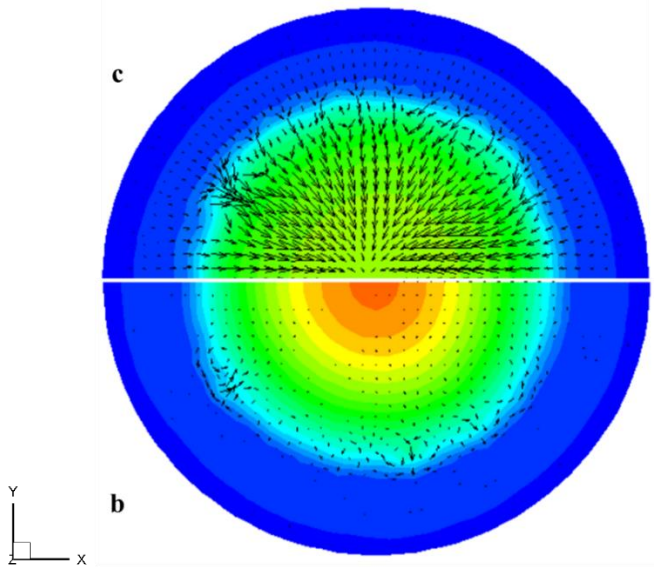

Figure 5.22 Velocity profiles taken at the three positions in (a), (b) velocity fields of position *a* and *b*, (b) velocity fields at positions *b* and *c*. Velocity contours showing total velocity magnitude while velocity vectors showing radial velocity.

Similar to above Figure 5.23a and b show the velocity patterns before and after velocity subtraction taken at the vertical middle plane of the regions near the front and rear of a plug in Figure 5.22 and Figure 5.23c shows the stream lines of the circulation patterns inside the plug. It is noticed that the circulation is asymmetric.

(a)

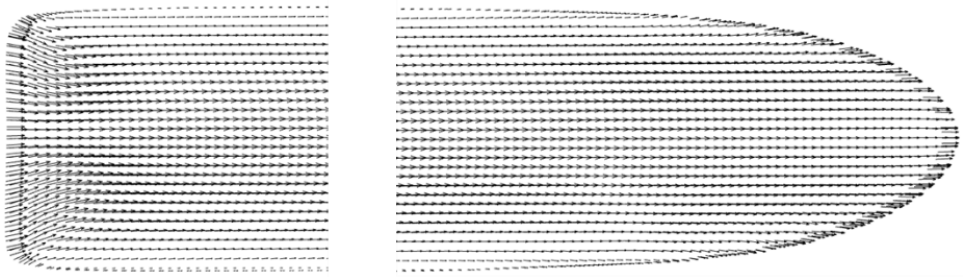

(b)

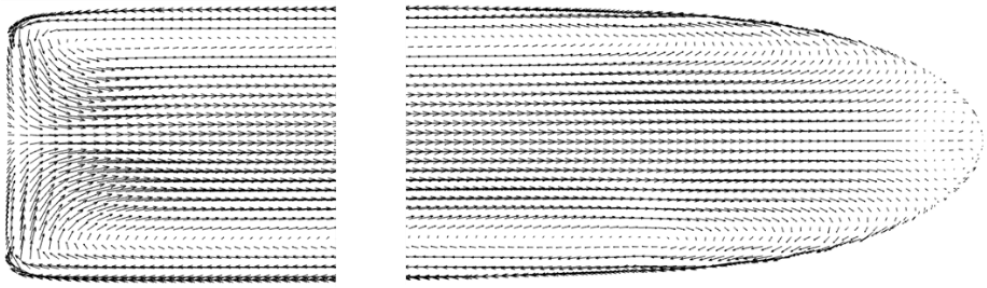

(c)

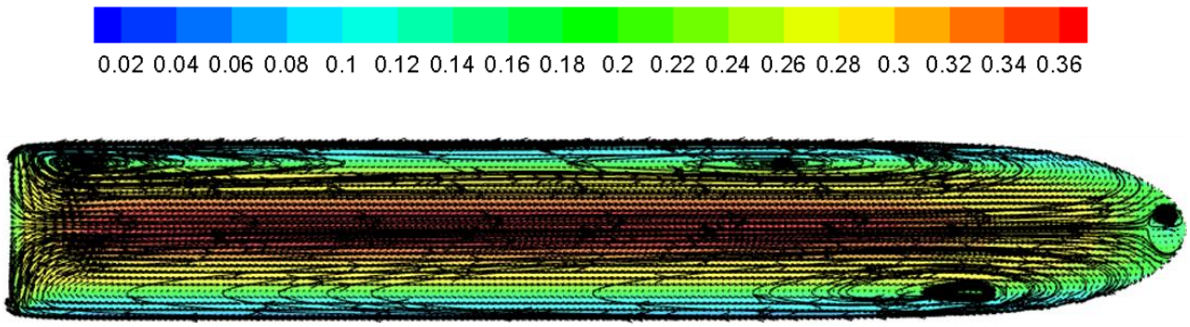

Figure 5.23 (a) Velocity fields at the front and tail before velocity subtraction; (b) mean fluid 2 velocity is subtracted; (c) streamlines of circulation patterns, velocity magnitude is superimposed with colour.

5.2.5 Circular channel summary

Figure 5.24 shows the tip curvature and film thickness measurement for all these three flow regimes for circular channel, flow conditions characterised by capillary number. The modified capillary number in experiment is based on the estimated real fluid 2 velocity which is different in simulation results where capillary number, Ca_2 based on the superficial velocity of fluid 2 is used for comparison. It can be seen although qualitatively the phenomena observed in experiments were able to be simulated relatively well and quantitatively, at smaller capillary number, the measurement of film thickness and fluid 2 tip curvature are very close but higher capillary number results in larger deviation between experiment and simulation. This may be because when the injection velocity increases, the Courant number, described in §5.1.1, becomes larger at a given time step size, which leads to the decrease of the numerical stability.

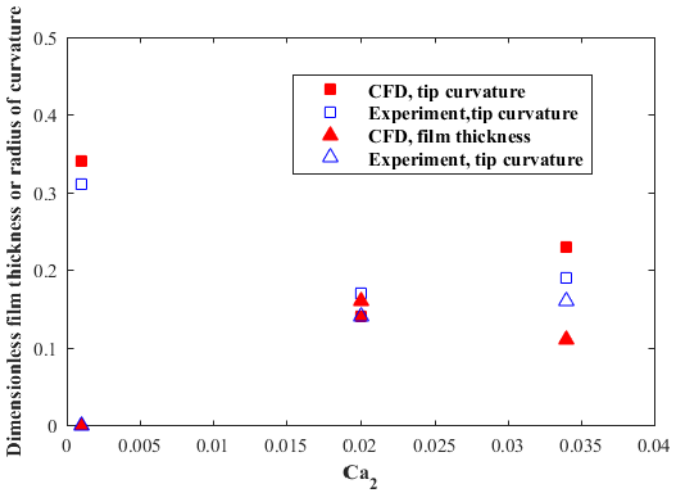

Figure 5.24 Plot of the film thickness and radius of fluid 2 tip curvature measurement from simulation and experimental results for circular channel.

5.3 Simulation results for near-semicircular channel

5.3.1 Near-semicircular channel axisymmetric unstable flow

Evolution of instabilities

For the simulation using near-semicircular and square channels, due to the limitation of computing resources, the stable regime (which is least interesting from a fluid dynamic point of view) was chosen not to be simulated. Axisymmetric and asymmetric unstable flows were simulated for these two geometries of channels.

Images in Figure 5.25 are the iso-surface created based on water volume fraction, indicating the position of water/oil interface from the simulation of immiscible displacement in near-semicircular channel (Re_2 = 50, Ca_2 = 0.01). In experiments it has only been possible to observe/record images from one view due to the limitation of the experimental set-up. Considering the interfacial instabilities must be three dimensional given the nature of the geometry, it was a priority to explore the 3-D topology of interfacial instabilities which is possible from the simulations. The film thickness following the advancing fluid 2 tip and fluid 2 tip curvature were obtained from simulation results. The dimensionless apparent film thickness for this result is ~0.3 and the dimensionless radius of tip curvature is ~0.32. Relevant experimental results for these two values are ~0.34 and ~0.31.

Figure 5.25 Evolution of the iso-surface generated based on water volume fraction indicating water/oil interface at different times. Axisymmetric instabilities from immiscible simulation in near-semicircular channel, viscosity ratio=100, Re_2 = 50, Ca_2 = 0.01. From left to right: flow time t = 3, 5, 7.62 and 12.1 (10^{-3} s).

Figure 5.26 shows the comparison between simulation and experimental results using the same flow conditions (immiscible displacement, viscosity ratio = 100, Re_2 = 50). The image from simulation results is the volume fraction contour in the *x-z* plane, which is the viewing direction in the experiment. Very similar axisymmetric interfacial instabilities are shown in simulation compared to experimental results. As aforementioned, it is believed that experimental images are reflecting the widest part of fluid 2 across the channel due to the non-transparent nature of the dye used (Nigrosin).

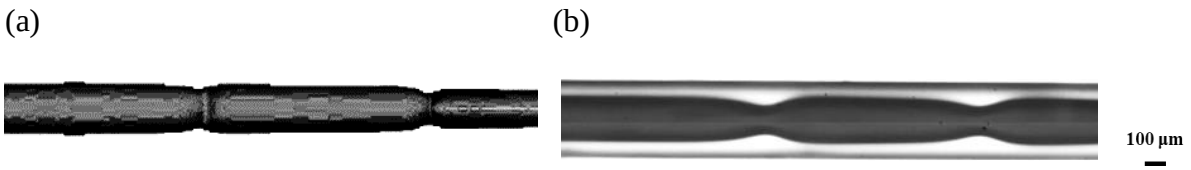

Figure 5.26 Example comparison between (a): simulation results and (b): experimental results. Flow conditions: immiscible displacement, viscosity ratio = 100, Re_2 = 50, Ca_2 = 0.01. Scale bar applies to both images.

Velocity profiles

Figure 5.27 shows simulation results presented by the water fraction contours taken at a vertical and a horizontal plane indicated respectively by dot-dash line and dashed line in the figure. It has shown a very different behaviour of flows if looking from side view, represented by vertical plane, other than the horizontal plane, which is believed to be very close what has been recorded in experimental images. Achieving these simulation results proves that the important role of CFD simulations that not only it can be used for comparing experimental results, but also it can enable visualisation of features which cannot be observed in a practical experiment.

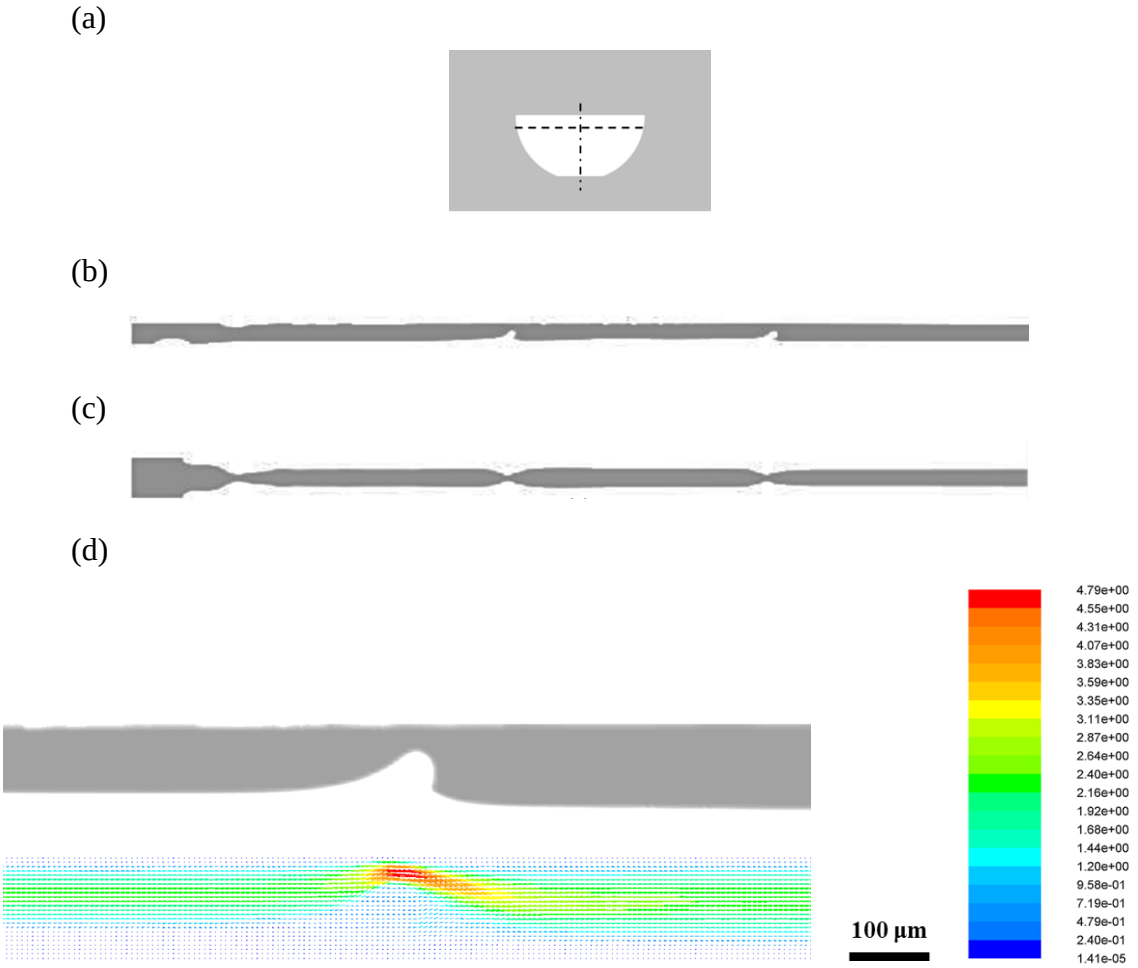

Figure 5.27 Simulation results of water fraction contours at two views indicated in (a). (b): vertical middle plane; (c): horizontal plane: 20 µm from the top of the channel. Flow time t = 0.01016s; (d) close up views of the velocity vectors at the unstable part taken from the plane in (b), velocity unit: m s^{-1}.

The cross-sectional velocity profile taken at the planes of close to fluid 2 tip and the pinching unstable part are shown in Figure 5.28. It can be seen radial velocity is presented at both these planes, the position close to tip presents outwards direction radial velocity while the position at the pinching part shows stronger inwards radial velocity.

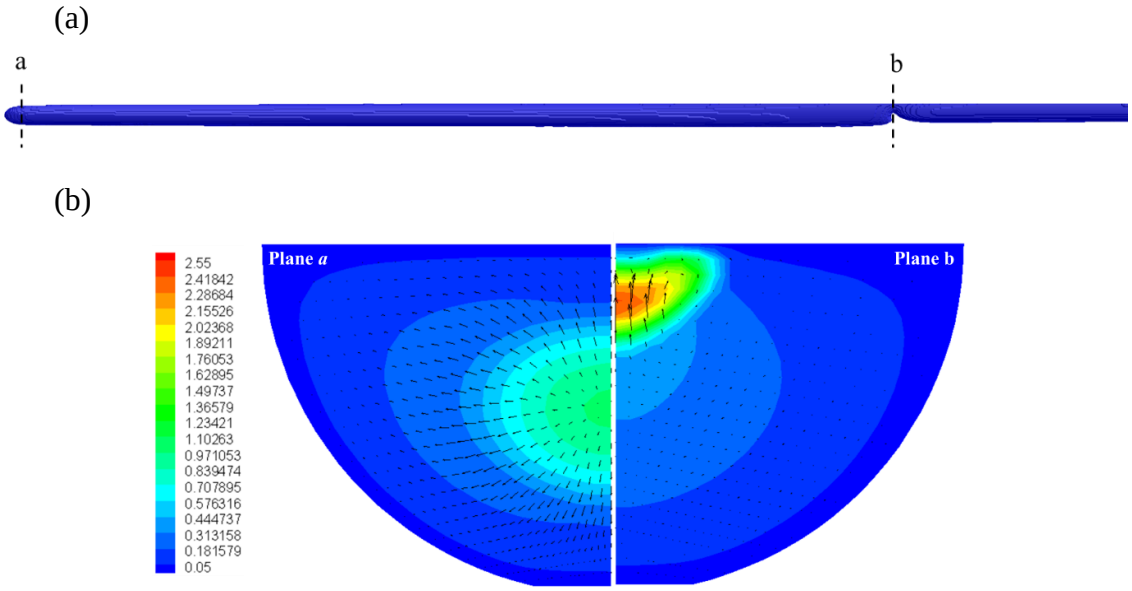

Figure 5.28 (a) Plane positions where cross-sectional velocity profiles are shown, (b) comparison of the velocity profiles at the two planes. Velocity contours showing total velocity magnitude while velocity vectors showing radial velocity. Velocity unit is m s^{-1}.

The velocity profiles at the horizontal and vertical central lines at a position between the *a* and *b* positions, position *c* in Figure 5.29a are shown below. The horizontal and vertical distances are normalised with the hydraulic diameter of the channel. It can also be seen from the vertical velocity plot that the maximum velocity does not appear at exactly in the middle of the vertical line since the non-circular channel causes the flow to be non-axisymmetric.

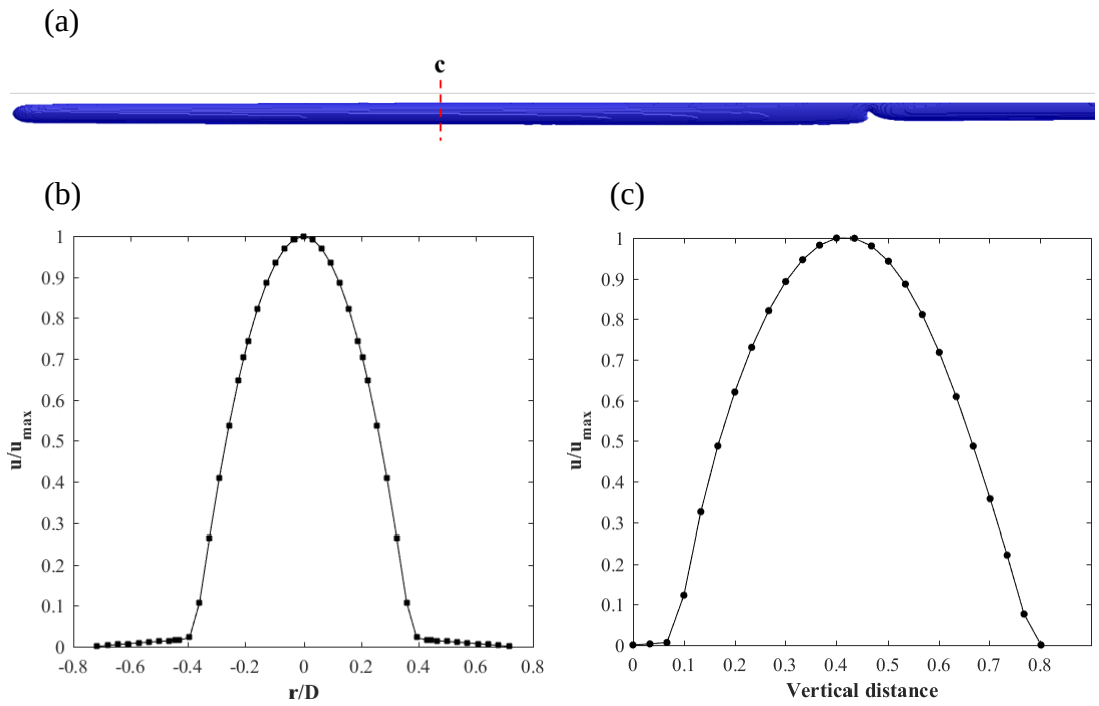

Figure 5.29 Velocity profiles taken at the (b) horizontal and (c) vertical line in the plane at position c in (a).

Mean fluid 2 velocity subtraction has been carried out in the tip regime of fluid 2 flow for both the horizontal and vertical plane, shown in Figure 5.30. The horizontal plane is taken at the vertical position of half of the channel height and the vertical plane is the vertical middle plane. The circulation patterns revealed from this operation support the analysis of the dynamic surface tension effect brought by the addition of surfactant on fluid 1 film thickness in experiments, which is discussed in previous section §4.3.2.

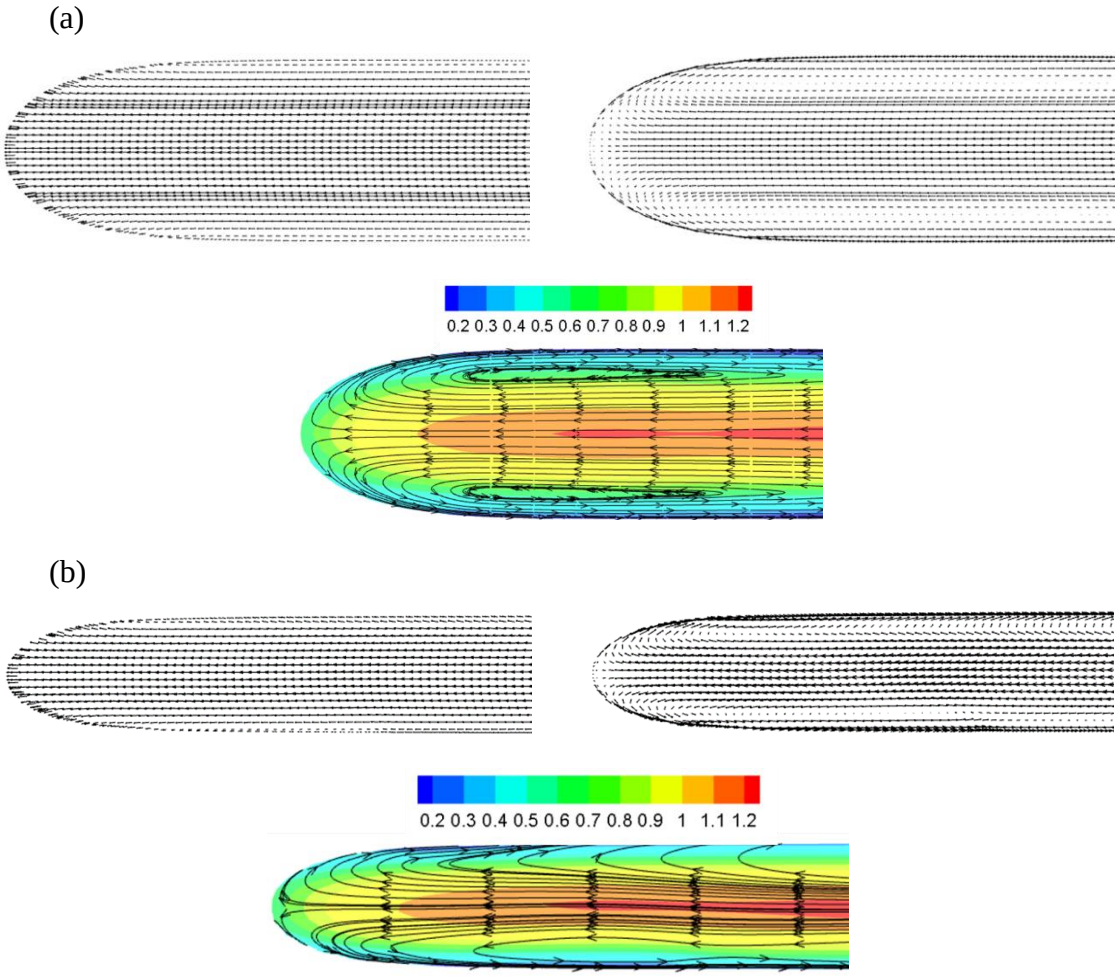

Figure 5.30 velocity field before and after subtracting mean fluid 2 velocity and the streamlines showing circulation patterns (velocity magnitude superimposed with colour) for (a) horizontal plane at the middle of channel height and (b) vertical middle plane. Unit of velocity m s^{-1}.

Fluid 2 flow cross-section shape

One of the most important feature of the displacement flows in the near-semicircular channel is the understanding of the cross-section shape of fluid 2. In Chapter 4, the shape of the cross-section interface is assumed to be an ellipse at low fluid 2 injection flowrate and a circle at high fluid 2 injection flowrate. The transition from elliptical to circular cross-section interface was estimated by the apparent film thickness because the minor axis of the ellipse is assumed to be constant (same with the height of the channel) while the major axis decreases when increasing

fluid 2 injection flowrate. From CFD simulations the cross-section interface can be obtained therefore providing understanding of this problem. Figure 5.31 is the cross-section view at the position where the film thickness is measured from simulation results, which is the constant film thickness region after the tip region of fluid 2. The dashed line in Figure 5.31 is a standard ellipse with the major and minor axis being the width and height of the fluid 2 interface measured from the image. This ellipse matches the interface very well therefore the assumption of elliptical cross-section is acceptable however the minor axis of this ellipse is not strictly the height of the channel. If the simulation reflects the true features of the flows, the actual mean film thickness proposed in the previous chapter is higher than estimated due to the residual liquid 1 at the top and bottom of the fluid 2 flows.

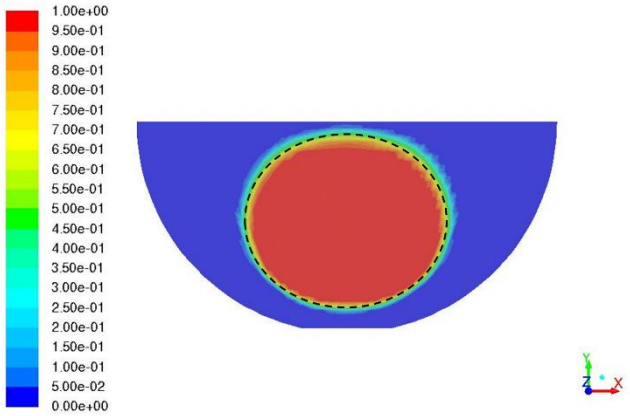

Figure 5.31 Cross-section view from simulation results in near-semicircular channel, based on water fraction value. Colour map indicates volume fraction of water.

Instead of a standard 3-D parabolic shape of fluid 2 tip in circular channel, the three-dimensional shape of fluid 2 tip in near-semicircular channel has also been revealed, shown in Figure 5.32.

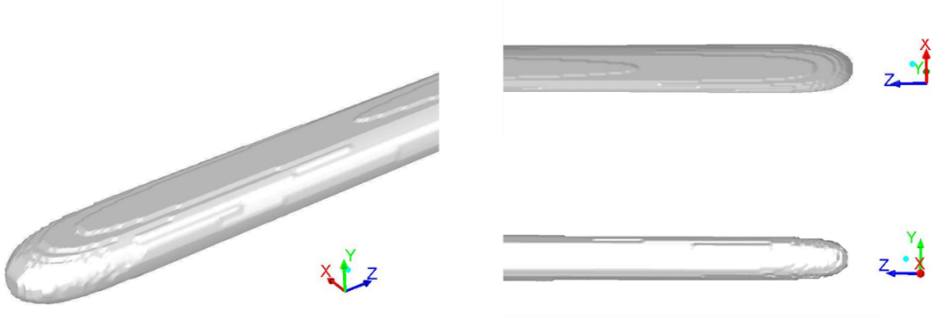

Figure 5.32 Three view of the fluid 2 tip in near-semicircular channel. $Re_2 = 50$, $Ca_2 = 0.01$.

5.4 Simulation results for square channel

5.4.1 Square channel axisymmetric unstable regime

Figure 5.33 shows some results from simulation of 100 cSt silicone oil displaced by water at $Re_2 = 50$.

Figure 5.33 Simulation of fluid displacement in square channel. $Re_2 = 50$, $Ca_2 = 0.01$, flow time from left to right: 4, 6, 7.7 and 9.8 ($\times 10^{-3}$) s.

The comparison between computational and experimental results is shown below. The film thickness and fluid 2 tip curvature measurement were also carried out, the results of which were compared with experimental measurement. The dimensionless apparent film thickness and fluid 2 tip curvature from this simulation is 0.09 and 0.25, which are in very good agreement for experimental measurement where the relevant results are 0.1 and 0.25.

Velocity profiles

Unlike the axisymmetric unstable flow in circular channel, the velocity profile at the pinching part of the flow in square channel did not has the sinuous shape profile as in Figure 5.13, see Figure 5.34. This may because the flow conditions in Figure 5.13, in circular channel, is in the transition regime that the flows would appeared to be asymmetric unstable with slightly increase in the inlet flowrate of fluid 2.

(a)

(b)

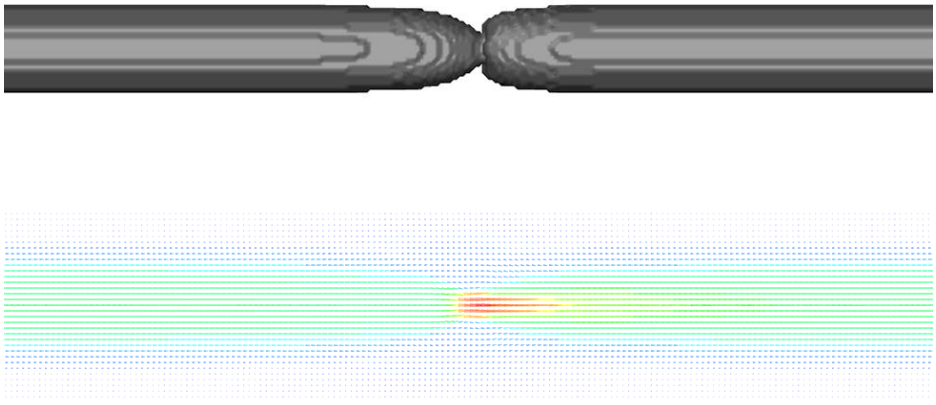

Figure 5.34 (a) Isosurface of volume fraction, (b) velocity profile at the pinching part at the axisymmetric unstable flows in square channel. Re_2 = 50, Flow time = 9.8 $\times 10^{-3}$ s. Flow direction from left to right.

The velocity profiles at the planes near fluid 2 tip (position *a*) and exactly at the narrowest unstable part of the flow (position *b*) are shown in Figure 5.35. The velocity profiles at the horizontal central lines of these two planes, plotted against horizontal positions (*x* axis) are also

shown. The velocity plotted is normalised by the maximum velocity at the chosen line. It can be seen the plane closer to fluid 2 shows strong outwards radial velocity compared to the plane at the narrowest part, which shows inwards direction radial velocity. In addition, the area where fluid 1 occupies does show significant radial velocities. The velocity profiles in Figure 5.35d show that the flows inside fluid 2 present parabolic velocity curves.

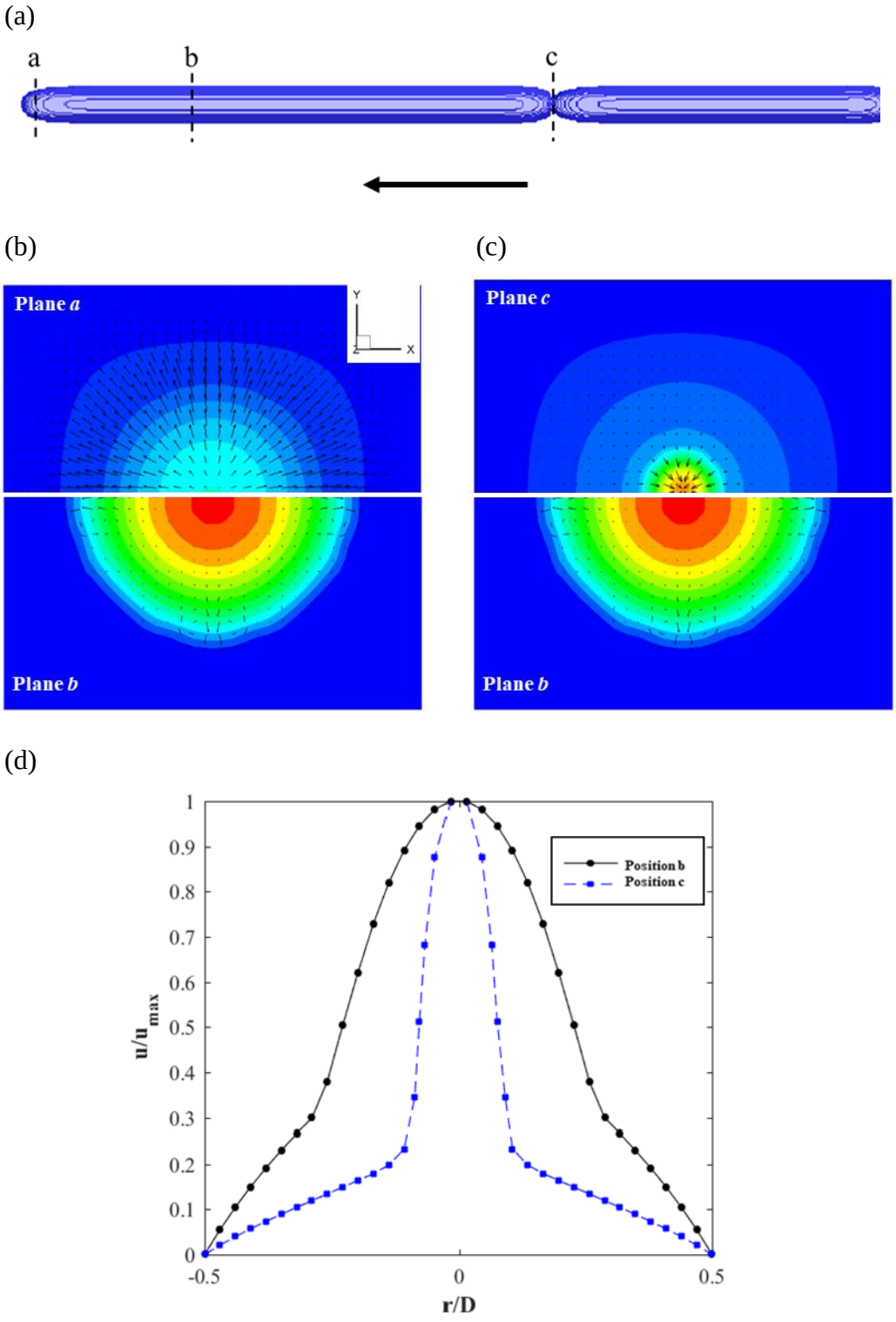

Figure 5.35 Cross-sectional velocity fields taken at the planes in (a); (b): comparison between the plane near fluid 2 tip (plane a), the plane in between fluid 2 tip and the pinching part (plane b) and the plane at the pinching part (plane c), (c): comparison between the plane at the unstable pinching part and the plane between fluid 2 tip and unstable flows; (d) Velocity profile at the horizontal central lines of the planes in (b) and (c). Velocity vectors represent radial velocity. Arrow indicates flow direction.

The velocity subtraction operation was also carried out in the region near fluid 2 tip in the square channel, shown in Figure 5.36 are the velocity magnitude before and after the fluid 2 velocity subtraction, as well as the circulation pattern streamlines.

(a)

(b)

(c)

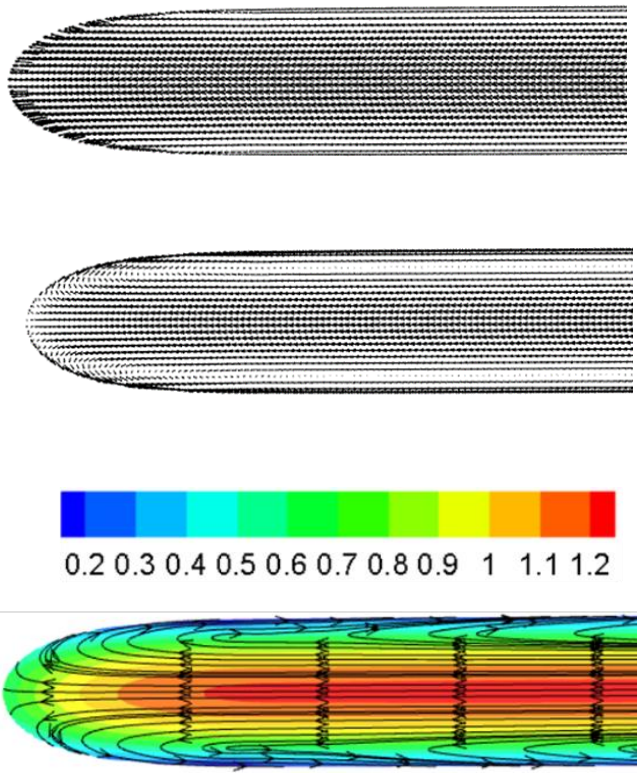

Figure 5.36 Circulation patterns revealed after the subtraction of fluid 2 mean velocity in square channel. (a) Velocity magnitude before subtraction, (b) velocity magnitude after subtraction and (c) circulation pattern streamlines, velocity magnitude superimposed by colours. Velocity unit is m s^{-1}.

5.4.2 Square channel asymmetric unstable regime

The asymmetric unstable regime has also been simulated in square channel, shown in Figure 5.37. The dimensionless film thickness from simulation results is 0.14 and the fluid 2 tip curvature is 0.21. The relevant measurement from experimental images under the same conditions are 0.13 and 0.21. These simulation results are also in line with the experimental

finding that asymmetric unstable flows take place after a short period of axisymmetric instabilities, which was observed in the immiscible displacement asymmetric unstable regime including the one using the same flow conditions with this simulation.

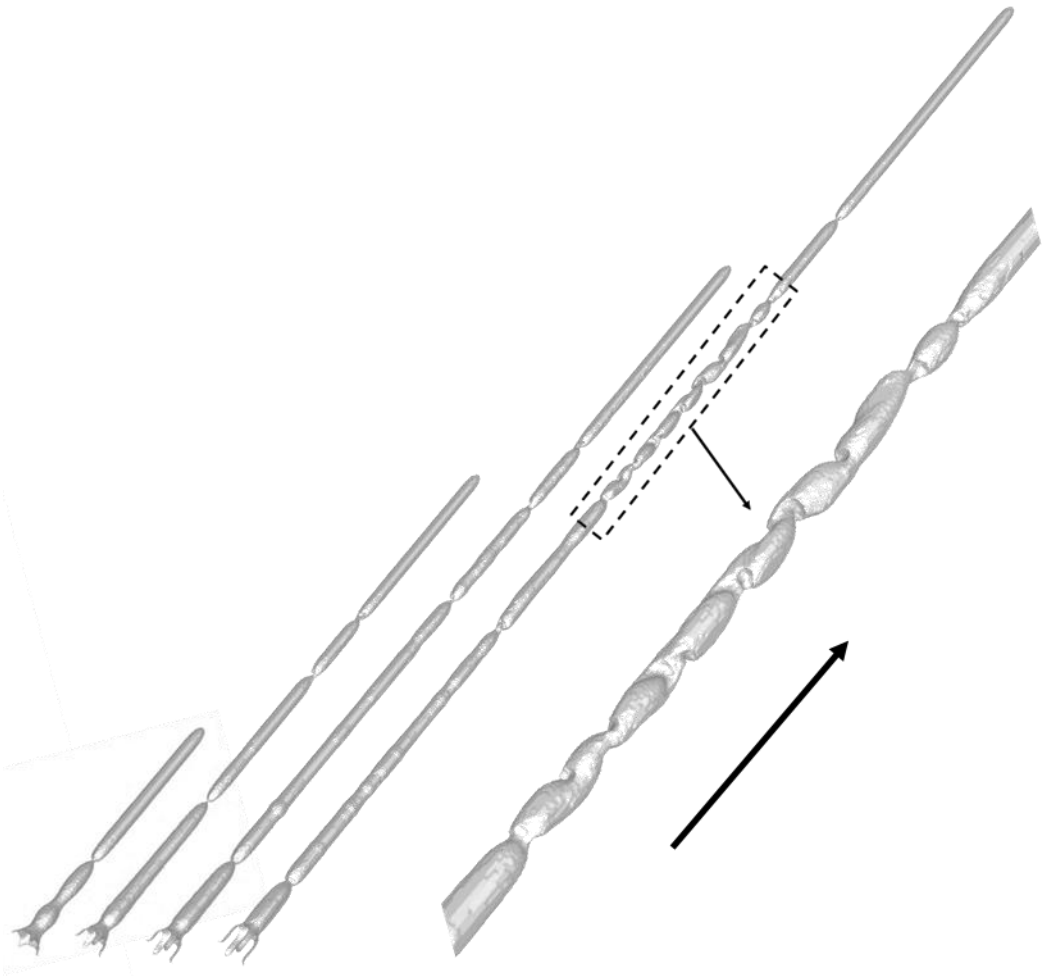

Figure 5.37 Evolution of the iso-surface generated based on water volume fraction indicating water/oil interface at different times. Asymmetric instabilities from immiscible simulation in square channel, viscosity ratio=100, Re_2 = 150, Ca_2 = 0.03, from left to right: flow time = 1.49, 3.49, 5.04 and 6.84 ($\times 10^{-3}$ s). A zoom-in image of the asymmetric instabilities on the right. Arrow indicates flow direction.

Velocity profiles

The volume fraction contour of the asymmetric unstable part of the flow and velocity profiles taken at the horizontal and vertical middle plane of the channel are shown below.

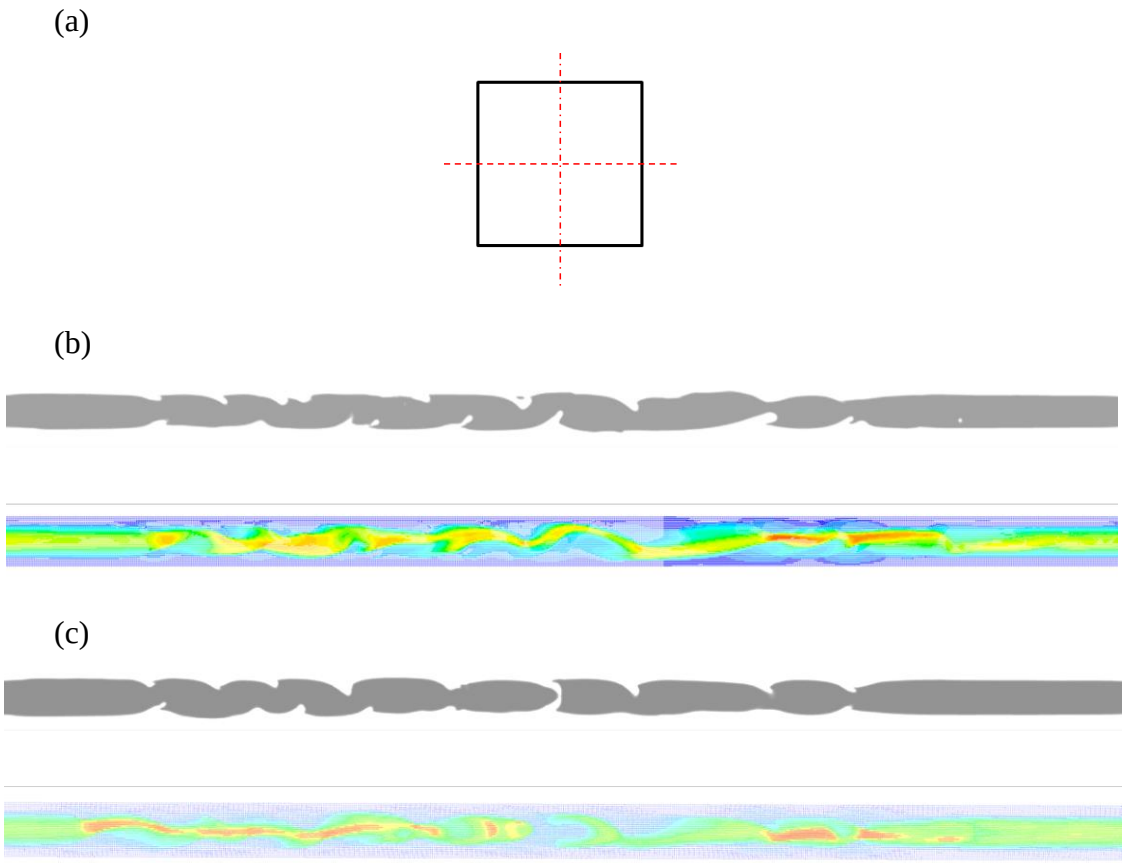

Figure 5.38 The flow pattern taken at the vertical and horizontal middle place of the channel and the velocity fields at these two planes. $Re_2 = 150$, $Ca_2 = 0.03$.

The velocity profiles taken at three planes are shown below: (a) near fluid 2 tip, (b) in the initial stable flow regime, between fluid 2 tip and unstable flows, and (c) inside the unstable flows. Similar to previous graphs, the velocity fields at the plane near fluid 2 tip show strong inwards direction radial velocity while at the position free from tip or unstable flow effects, the velocities show very small radial velocity elements. In the unstable flow regime, the radial velocity becomes more vortex-like, showing no certain patterns.

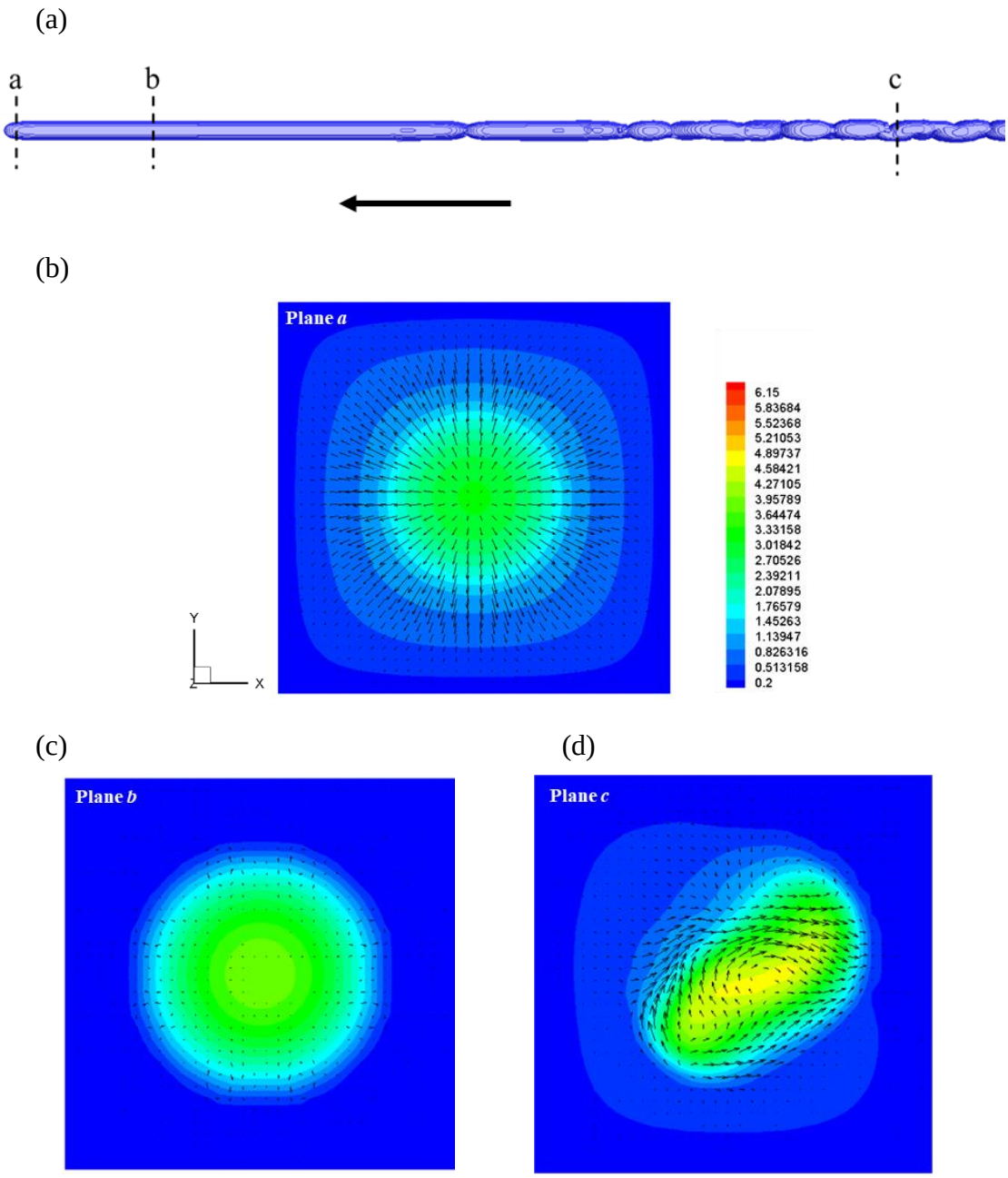

Figure 5.39 Cross-sectional velocity fields taken at the planes in (a), (b): the plane near fluid 2 tip; (c) the plane between fluid 2 tip and the unstable flows; (d) the plane at the unstable flows. Velocity unit: m s^{-1}. Arrow indicates flow direction. The length of velocity vectors indicates velocity magnitude and the same scale is applied in (a), (b) and (c).

The velocity profiles of the horizontal lines at the positions *a* and *b* above are shown below. The velocities are normalised by the maximum velocity at the chosen line and the *x*-axis position is normalised by channel hydraulic diameter.

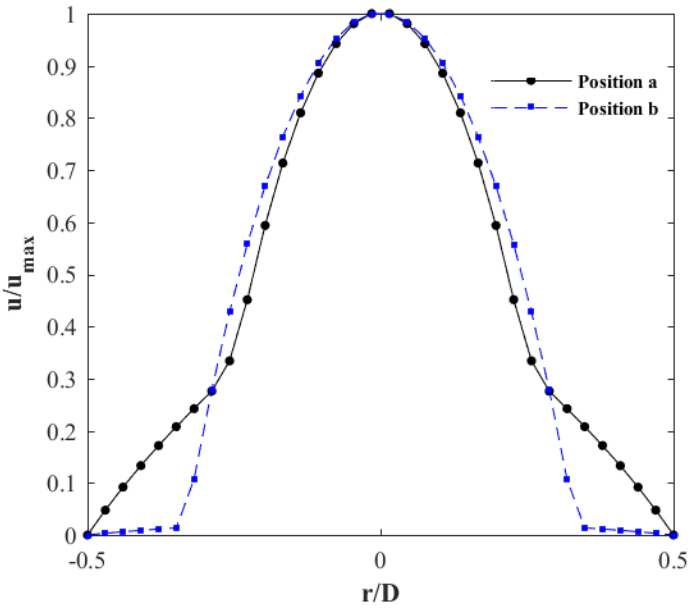

Figure 5.40 Velocity profiles of the horizontal central line of the planes at position *a* and *b* in Figure 5.39.

5.4.3 Square channel simulation summary

The difference in the measurement of film thickness and fluid 2 tip curvature is plotted below. Results from lower capillary number conditions (axisymmetric unstable flows) and higher capillary number conditions (asymmetric unstable flows) both show very good agreement.

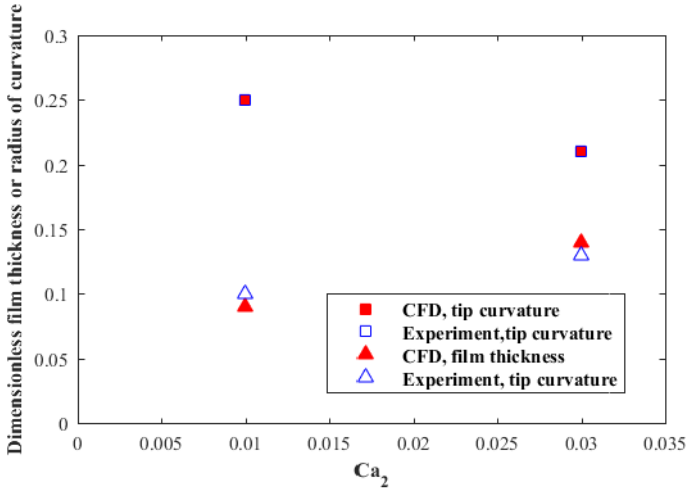

Figure 5.41 Plot of the film thickness and radius of fluid 2 tip curvature measurement from simulation and experimental results for square channel.

5.5 Summary

Computational Fluid Dynamic (CFD) simulations have been carried out using the commercial package Fluent. Circular, square and near-semicircular channels were used and immiscible fluid pair of 100 cSt silicone oil as fluid 1 and water as fluid 2 was simulated. Volume of Fluent (VoF) model was used and was proved to resolve the interface within 2 to 3 cells. Mesh independence study and the use of the inlet with parabolic velocity profile were first studied. The appearance of flow following the flow regimes of stable, axisymmetric unstable and asymmetric unstable were obtained for circular channel. Both axisymmetric and asymmetric unstable regimes were achieved for square channel while axisymmetric unstable flows were observed from the simulation using the near-semicircular channel.

Velocity patterns including the recirculation patterns near fluid 2 tip were shown from simulation results. The circulation patterns inside fluid 2 was revealed by subtracting fluid 2 velocity from the average velocity magnitude in all three channels. This confirms the previous discussion of the distribution of surfactant near fluid 2 tip region in Chapter 4. A Taylor-type plug flow was seen in one of the simulation cases using the circular channel, although no similar and reproducible flow phenomena was observed in the experiment. The flow behaviour, film thickness and the radius of fluid 2 tip curvature were compared between simulation and experimental results. For the square channel, very good agreement was shown for these comparisons. For the circular channel stable and axisymmetric unstable flows show good agreement while the asymmetric unstable, with the largest fluid 2 injection flowrate, flow show some variation between simulation and experiment results.

Chapter 6 FLUID DISPLACEMENT IN T-JUNCTION CHANNEL

Introduction

The immiscible displacement experiment has been carried out in a T-junction channel using two modes of injection (§6.2 and §6.3). One of the three ends of the T-channel was blocked in each injection mode, causing the displacing fluid to pass straight through or around a 90˚ bend through the junction. The behaviour of the flow just before and after the junction were particularly studied. Two methods of estimating fluid 2 cross-section interface shape were proposed. In the first method, fluid 2 cross-section is assumed to be elliptical with the width of fluid 2 and the height of channel as the major and minor axis. In the second method the top and bottom part of fluid 2 cross-section are assumed to be very close to the channel wall, and the interfaces at two sides are defined with a circle with the diameter equals to the width of fluid 2 flow.

Surfactant-free and surfactant-laden fluids were both used as the displacing fluid. Two types of surfactant, SDS and PmP, both at the concentrations above the CMC were used to study their effects upon flow behaviour. §6.4 describes a simple simulation case, using Fluent employing a single straight wide channel. The simulation results suggest that the first method of fluid 2 interface estimation provides a better approximation but some improvements are still needed.

6.1 Interfacial tension between fluid 1 and surfactant-laden fluid 2

The interfacial tension properties between silicone oil and SDS water solution are found in Chapter 4 (§4.1). The interfacial tension between 100 cSt silicone oil and Polyether-modified

Polysiloxane (PmP) solution was measured also using the Kruss K100 tensiometer with the Wilhelmy Plate method. Solutions with and without Nigrosin dye (10 g L^{-1}) were used as well as an additional measurement made with a PmP concentration at 20 times its CMC (1.8 g L^{-1}). The IFT results are shown in Table 6.1. It can be seen that by adding dye into the PmP solution or increasing the concentration from 10 CMC to 20 CMC did not affect significantly the IFT values.

Table 6.1 Equilibrium interfacial tension (IFT) values between fluid 1 and 2 used in junction channel experiment.

Fluid 1	Fluid 2	IFT (mN m-1)
	Water (dyed)	27.1
	Water+SDS (2CMC, dyed)	9.9
100 cSt silicone oil	Water+PmP (10 CMC, no dye)	5.7
	Water+PmP (10 CMC, dyed)	5.6
	Water+PmP (20 CMC, dyed)	5.9

As mentioned in §3.4.3, a stability test on the PmP solutions based on its surface tension values was carried out. Figure 6.1 shows the short-timesale surface tension measurement results for PmP water solution (1.8 g L^{-1}) dyed with Nigrosin (10 g L^{-1}). It can be seen from the results that this surfactant does have dynamic surface tension effects. The surface tension drops from over 42 mN m^{-1} at surface age ~ 0.12 s to the equilibrium surface tension of 23.8 mN m^{-1} (calculated from the average equilibrium values of all measurement). From the stability test it can be seen the surface tension values slightly increase particularly in the surface age time range 0.03 to 1 s. There is not a significant variation in terms of equilibrium surface tension values from measurement taken at all times. The standard deviation of all equilibrium surface tension values is 0.29.

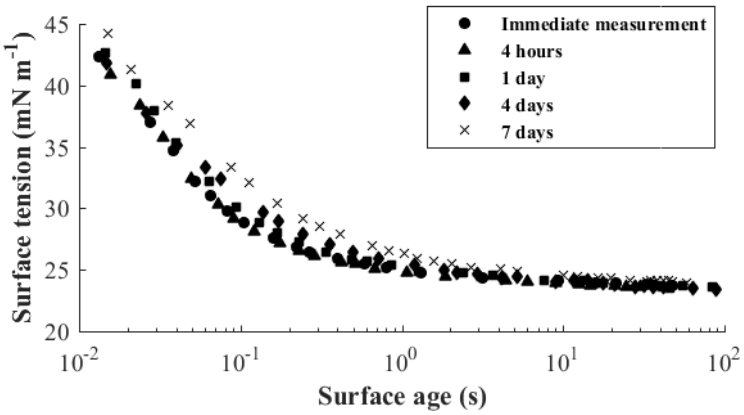

Figure 6.1 Surface tension measurement of water+PmP (dyed) at different times.

Table 6.2 Equilibrium surface tension values of water+PmP (dyed) solution measured at different times.

Time	Equilibrium surface tension (mN m-1)
Immediate	23.7
4 hours	23.8
1 day	23.3
4 days	23.4
7 days	24.0
Average	23.8
Standard deviation	0.29

The estimation of dynamic interfacial tension of PmP was carried out using the method mentioned in §4.2.1. Figure 6.2 shows the results.

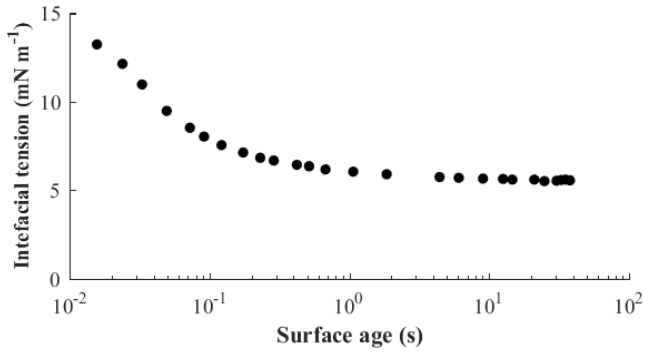

Figure 6.2 Estimation of dynamic IFT values between 100 cSt silicon oil and water+PmP solution (dyed), using the method described in §4.2.1.

For the cases where surfactant-laden fluid 2 was used, the time for fluid 2 to travel from the inlet to the junction (distance of 11.25 mm) was used as the surface age with regards to the estimation of dynamic interfacial tension effects. In this chapter the experiments using SDS water solutions resulted in the minimum time scale of ~ 0.02 s, which is within the regime of achieving equilibrium ST/IFT. Therefore the equilibrium interfacial tension values for silicon oil/SDS were used in further calculations. For the cases using PmP water solutions the smallest time scale (surface age) was ~ 0.03 s at which equilibrium SF/IFT values are not yet achieved. Thus the estimated dynamic interfacial tension values are used in the calculations.

6.1.1 Estimation of cross-section shape of fluid 2 interface

As already discussed extensively in previous chapters, the three-dimensional nature of the channel causes the apparent film thickness measured from experimental images to necessarily represent the film thickness across the entire cross-section of the channel. Two methods have been proposed to estimate the mean film thickness in the wide channel and the Taylor Law is used to compare the results of mean film thickness. The estimation of mean film thickness is similar to the non-circular channels in Chapter 4, based on the estimation of the cross-section area and perimeter of fluid 2 interface:

$$a_{mean} = \frac{A_c - A_2}{\frac{1}{2}(P_c + P_2)} \qquad \text{(Equation 6.1)}$$

Apart from providing us better understanding of the shape of the cross-section of fluid 2, the other important use of the estimation of fluid 2 cross-section area is the estimation of real fluid 2 velocity, which needs to be used in calculating the modified capillary number Ca_1'.

The largest apparent film thickness measured from experimental images for all cases is around 70 μm, meaning the width of fluid 2 for all cases is larger than 390-2×70 = 250 μm. Thus fluid 2 must exist within the semi-circular area of the channel.

In the first method, the shape of fluid 2 interface is assumed to be elliptical, with the major axis the width of fluid 2 and minor axis the height of the channel (190 μm). Figure 6.3 illustrates the assumed fluid 2 cross-section shape. The calculation of the area and perimeter of the interface is in the appendices.

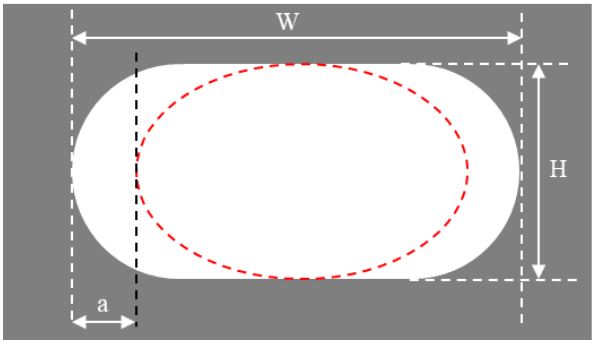

Figure 6.3 Illustration of the estimation of the cross-section shape of fluid 2 interface: Method 1.

The perimeter and cross-section are of fluid 2 interface using this method is calculated from:

$$P_2 = \pi\{3((\frac{W}{2} - a) + \frac{H}{2}) - \sqrt{(3(\frac{W}{2} - a) + \frac{H}{2})((\frac{W}{2} - a) + \frac{3H}{2})}\} \qquad \text{(Equation 6.2)}$$

$$A_2 = \pi(\frac{H}{2})(\frac{W}{2} - a) \quad \text{(Equation 6.3)}$$

The second method assumes the top and bottom part of fluid 2 nearly in ful contacts the channel wall, making the top and bottom part of fluid 2 flat, shown in Figure 6.4. The sides of the fluid 2 are assumed to be part of circle, with the diameter of the circle to be 390-2a. In this method the calculation of the area and perimeter of fluid 2 are further divided into two ways, with the critical apparent film thickness calculated: $a_{cr} = 100 + 95 - \sqrt{100^2 + 95^2} = 57.1\ \mu m$.

(a)

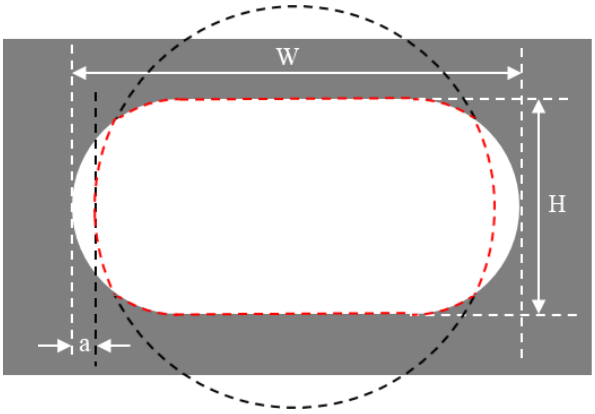

(b)

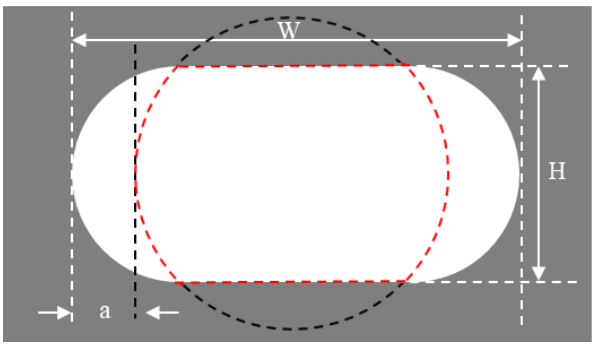

Figure 6.4 Illustration of the estimation of the cross-section shape of fluid 2 interface, Method 2. The red dashed lines represent the assumed fluid 2 interface for: (a) when $a < a_{cr}$; (b) when $a \geq a_{cr}$。 a: apparent film thickness, H and W: height and width of the channel.

The perimeter and cross-section area of fluid 2 when $a < a_{cr}$ (Figure 6.4a) are calculated from the equations below; a detailed explanation of the calculation is described in the Appendix A.

$$\begin{aligned} A_2 &= 4(A_{BCE} + A_{ABE} + A_{AEO}) + 2A_{AOJ} \\ &= 4(0.5(100-a)(\sqrt{9097 - \frac{(100-a)(290-a)}{200}}) \\ &\quad + 4(\frac{\cos^{-1}(\frac{l_{IF}+l_{FE}}{l_{BE}}) = (\frac{(\frac{95^2 - l_{BF}{}^2}{l_{EF}} - l_{EF})/2 + 100\tan\theta}{95})}{360} \times (9025\pi)) \\ &\quad + 4 \times 4750 + 19000 \end{aligned} \qquad \text{(Equation 6.4)}$$

Where A_{BCE}, A_{ABE}, A_{AEO} and A_{AOJ} are the area of the triangles with the vertexes marker with letter A, B, C, J, O.

$$\begin{aligned} P_2 = 4(BC + AB + l_{AG}) &= 4 \times \frac{\sin^{-1}(\sqrt{9097 - \frac{(100-a)(290-a)}{200}} / (195-a))}{360} \times (2\pi \times (195-a)) \\ &\quad + 4 \times \frac{\cos^{-1}(\frac{l_{IF}+l_{FE}}{l_{BE}}) = (\frac{(\frac{95^2 - l_{BF}{}^2}{l_{EF}} - l_{EF})/2 + 100\tan\theta}{95})}{360} \times (190\pi) \\ &\quad + 400 \end{aligned}$$

(Equation 6.5)

The perimeter and cross-section are of fluid 2 interface using this method and when $a \geq a_{cr}$ (Figure 6.4b), is calculated from:

$$A_2 = \frac{\sin^{-1}(\frac{95}{195-a})}{28.7} \times (195-a)^2 + 190\sqrt{(100-a)(290-a)} \qquad \text{(Equation 6.6)}$$

$$P_2 = \frac{\sin^{-1}\left(\frac{95}{195-a}\right)}{14.3} \times (195-a) + 4\sqrt{(100-a)(290-a)} \qquad \text{(Equation 6.7)}$$

The detailed calculation of cross-section area and perimeter of fluid 2 interface for these two ways are also shown in Appendix A.

6.2 Injection mode 1

The first mode of the injection of fluid 2 is carried out by blocking one of the channel ends to allow fluid 2 to travel through junction by turning through the 90-degree bend (Figure 6.5)

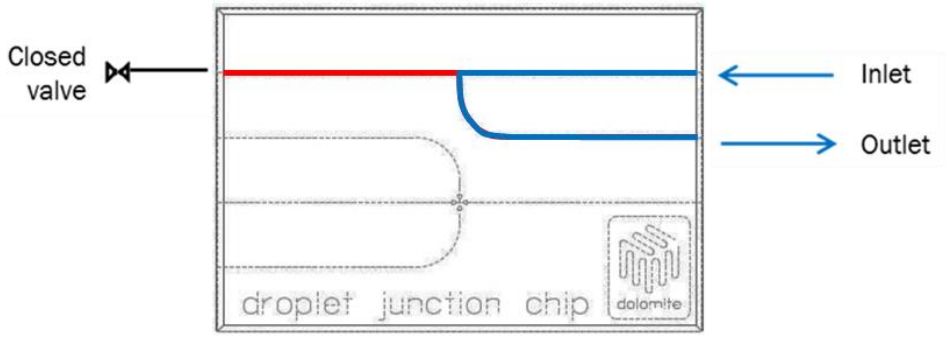

Figure 6.5 First injection mode in junction channel experiments. Size of chip: 22.5 × 15 mm.

Four important positions of fluid 2 in the channel are defined for the measurement to be carried out, shown in Figure 6.6. The first two positions are before fluid 2 passes through the junction, one located at the straight channel before fluid 2 enters the narrowing regime of the channel and one just before it enters the narrowest junction. The last two positions are after the fluid 2 passes through the junction, one located at the position where fluid 2 has just exited of the junction before narrowing regime of the wide main channel; the final position is when fluid 2 travelling in the main wide channel after passing through the junction. These four positions represent the effect of the narrowing of the channel on the flows as well as the junction.

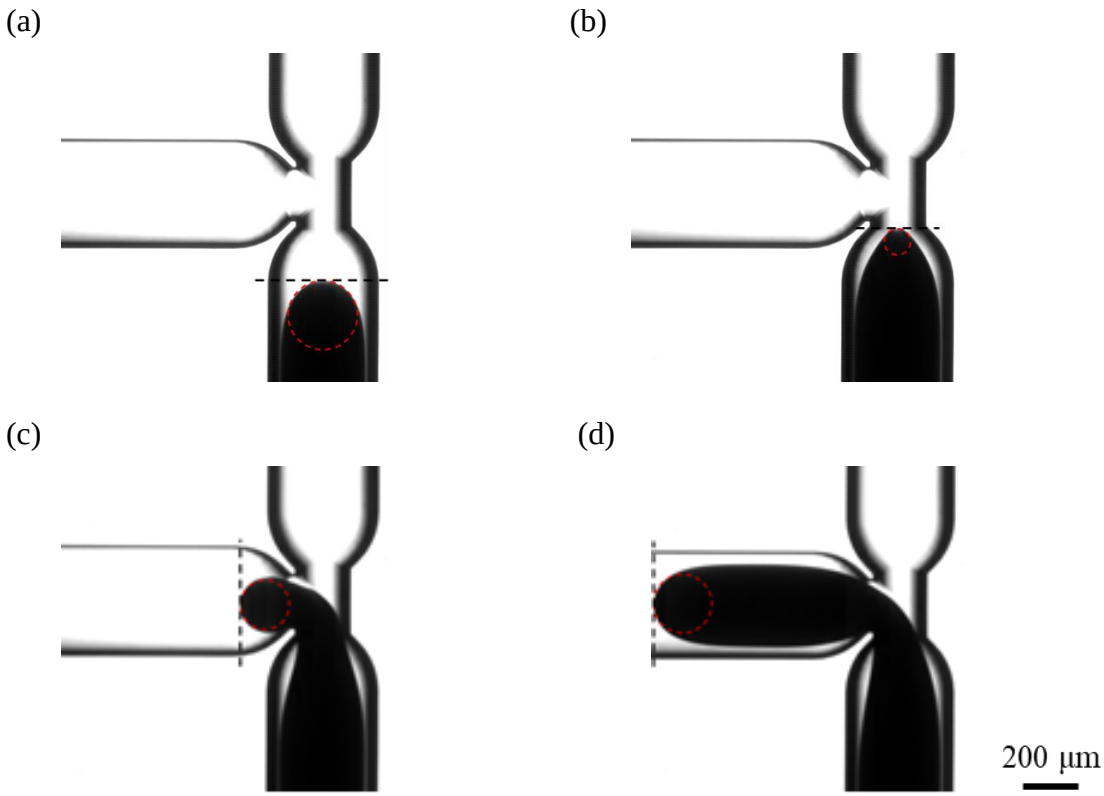

Figure 6.6 Four important position for the injection 1 for junction channel flows. (a) Fluid 2 in the wide channel before entering the narrowing regime of channel; (b) Fluid 2 at the position of just before entering the narrowest part of the junction; (c) Fluid 2 at the position just before entering the main wide channel after the narrowing regime; (d) Fluid 2 in the main wide channel after it passing the junction. Scale bar applies to all images.

The addition of surfactant into fluid 2 reduces the interfacial tension between the two fluids. Figure 6.7 shows the difference in the flows between surfactant-free and surfactant-laden fluid 2 at the same flowrate; the pictures are showing the flows at the same channel positions for these two cases. Considering the effect of interfacial tension on immiscible fluid pairs, capillary number is again chosen as the characteristic parameter.

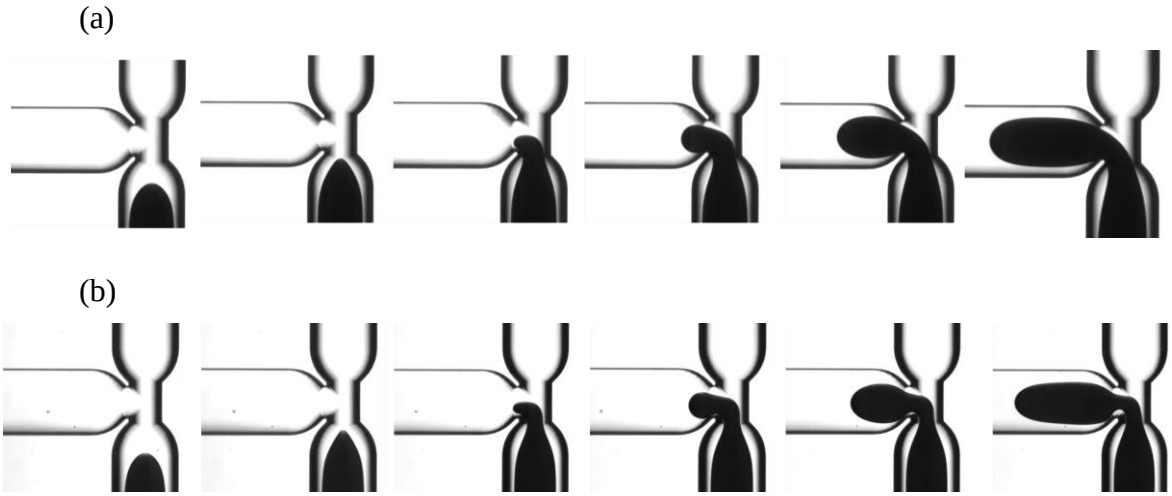

Figure 6.7 Illustration of the difference between (a) surfactant-free and (b) surfactant-laden (SDS) fluid 2 cases under the same fluid 2 injection flowrate: 500 mL min^{-1}.

6.2.1 Film thickness

The apparent film thickness was first measured at the position *a* and *d* in Figure 6.6 using ImageJ, shown in Figure 6.8. The real velocity of fluid 2, which depends on film thickness, is different from the two estimation methods because the difference in estimating film thickness. Therefore the relevant Ca_1 values are used which are calculated from the superficial velocity of fluid 2.

It can be seen from the figure that the film thickness does not change much between positions *a* and *d* especially for higher capillary number conditions. For small capillary number cases, the film thickness after the junction appears to be slightly larger. This may because the small cross-section area of the junction part provides a sudden increase in the velocity of fluid 2. This effect appears to be negligible for larger fluid 2 injection flow rate conditions. For the cases using SDS water solution as fluid 2, the effect on interfacial tension from surfactant seems to be well correlated by capillary number. This is shown from the very close results from water and surfactant-laden fluid 2 cases. There exists a decrease in film thickness values for the cases

using PmP solution as fluid 2, despite dynamic interfacial tension effect has been taken into consideration. This may first because the inaccuracy in the estimation of dynamic interfacial tension or the uneven distribution of surfactant molecules, or this may due caused by redistribution of surfactant from the circulation flows inside fluid 2, near tip region, as described in §4.3.1.

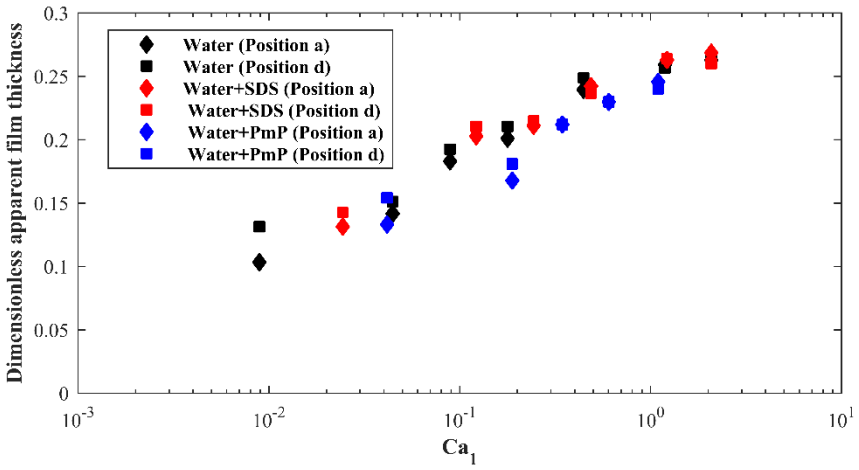

Figure 6.8 Apparent film thickness measurement (normalised by hydraulic diameter) at position *a* and *d* for injection mode 1.

Since the apparent film thickness measurement for three fluid pairs are close, only one set of data was chosen to validate the above two cross-section shape estimation methods. The film thickness using water as fluid 2 and the film thickness at position *d* was chosen as the working dataset. The apparent film thickness and the mean film thickness calculated from the two methods, together with the Taylor's Law, are plotted below (Figure 6.9). The mean film thickness values are plotted against Ca_1' while the apparent film thickness is plotted against Ca_1.

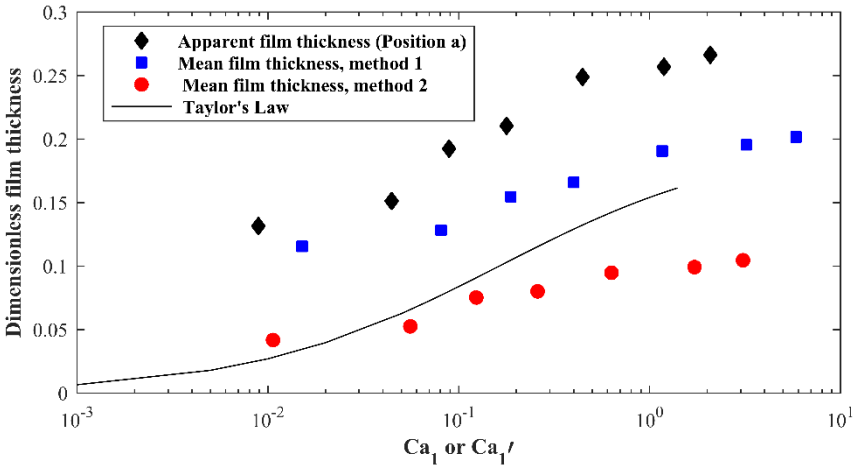

Figure 6.9 Mean film thickness obtained using both the two methods and the Taylor's Law.

It can be seen from Figure 6.9 that both methods fail to describe the mean film thickness across the whole range of capillary number using each single method. Due to the difference in the estimation of fluid 2 cross-sectional interface between the two methods, the modified capillary number also varies. Method 1 appears to be working better for larger capillary numbers while method 2 works better for small capillary numbers.

6.2.2 Liquid 2 tip curvature

The second measurement is the radius of fluid 2 tip curvature at all four positions in Figure 6.6. Figure 6.10 shows the measurement results for all four fluid pairs. Similar to film thickness measurement, due to the deviation exists on the estimation of fluid 2 cross-section shape, the capillary number based on the superficial velocity of fluid (Ca_1) is used as the characteristic parameter.

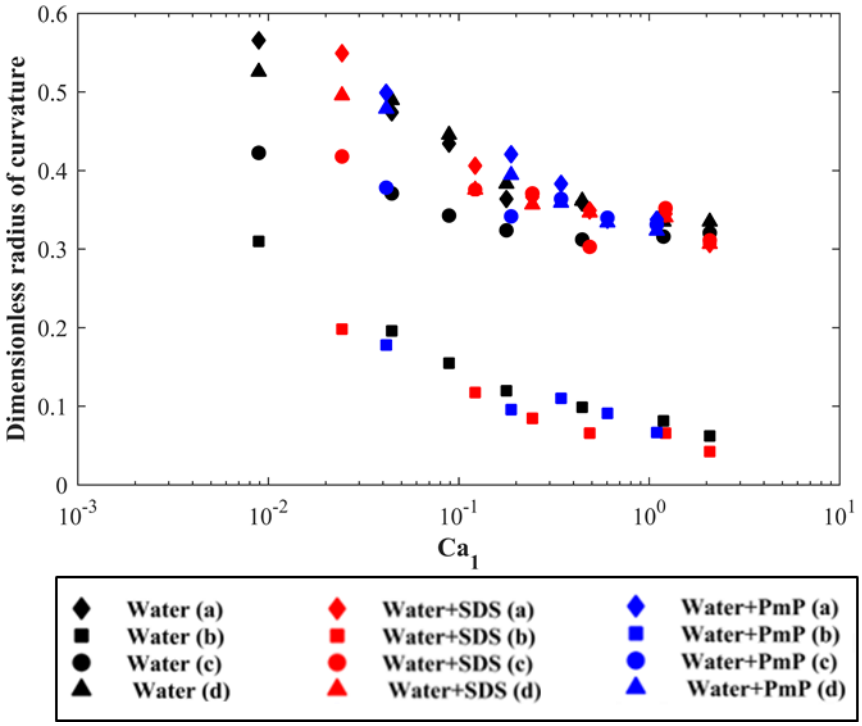

Figure 6.10 Measurement of radii of fluid 2 tip curvature for three fluid pairs at four positions.

From Figure 6.10, the general trend of decrease in tip radius of curvature as capillary number increases applies for this channel geometry. It can be seen that the radius of curvature for positions *a* and *d* follows the same trend for all three fluid pairs. For the cases using water and SDS water solution as fluid 2, the results appear to be very close whilst the results from PmP water solution cases appear to be slightly higher than the former two. This finding agrees with the finding of the measurement of film thickness, the estimation of interfacial tension between PmP and silicone oil, and the uneven distribution of surfactant molecules near the tip region may be the cause. The radius of curvature is also slightly larger at position *a* than that at position *d* especially for small capillary number conditions, which also in line with the phenomenon of larger film thickness at position *d* than *a*. This may because the sudden decrease of channel cross-section at the junction leads to a sudden increase of fluid 2 velocity after it passes the junction.

The results at position b show that the junction inlet has very similar effects on fluid 2 flows for these fluid pairs with different interfacial tensions, indicated by the close results in Figure 6.10 (square markers).

6.3 Injection mode 2

The second mode of injection involves the blockage of one of the channel ends for fluid 2 to flow straight passing the junction (Figure 6.11).

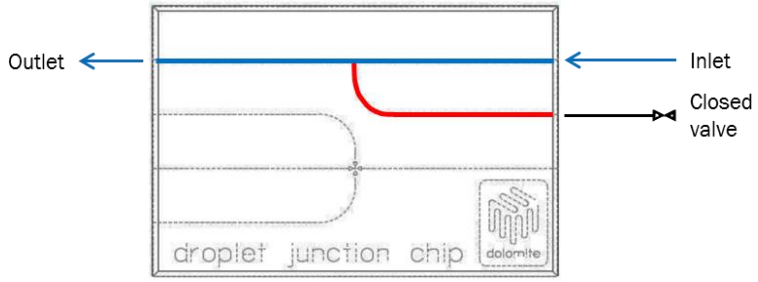

Figure 6.11 Second injection mode for junction channel experiment.

In Figure 6.12 are some example images from the second injection mode, showing the difference in flows passing the junction between surfactant-free and surfactant fluid 2 cases.

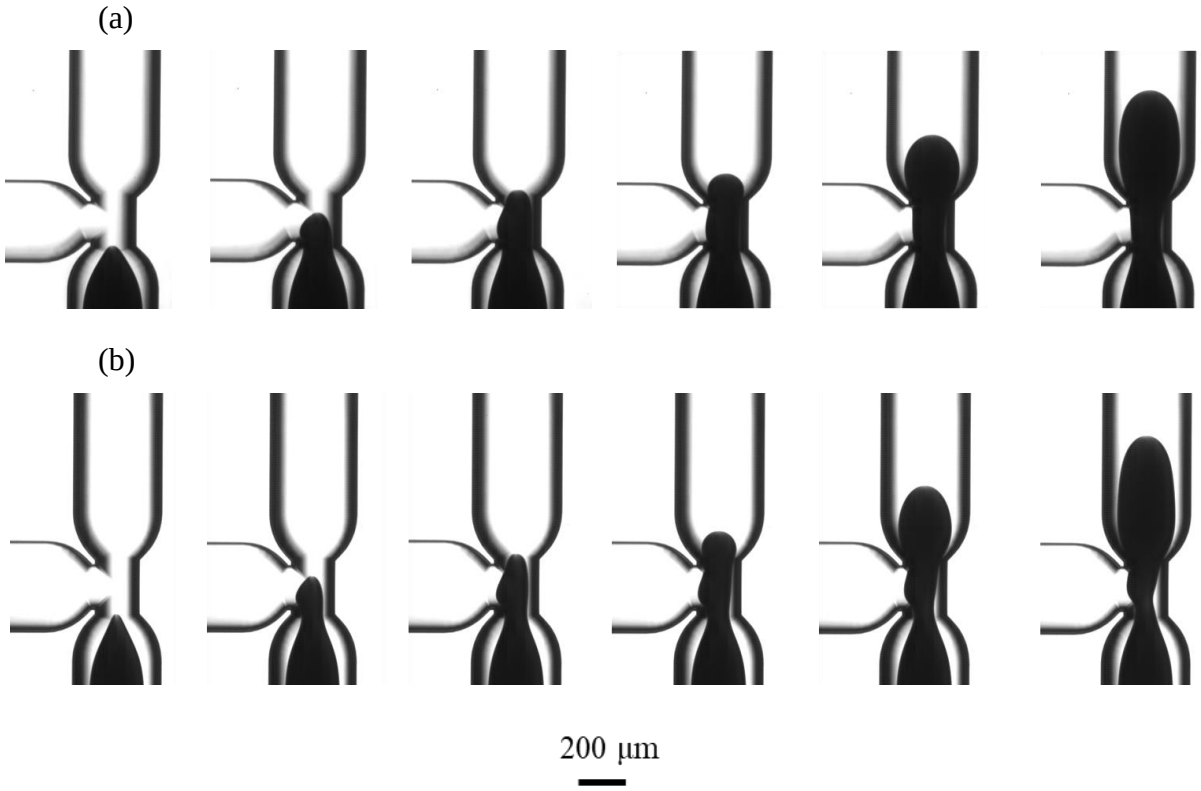

Figure 6.12 Illustration of the difference between (a) surfactant-free and (b) surfactant-laden (SDS) fluid 2 cases under the same fluid 2 injection flowrate: 500 mL min^{-1}.

The first measurement is the distance of fluid 2 expanded into the side channel when it passes the junction position. As shown in Figure 6.13, the position where this measurement is carried out is just before fluid 2 flows exit the junction. The values are normalised with the hydraulic diameter of the channel (266.3 μm). Measurement results are plotted against Ca_1, shown in Figure 6.14.

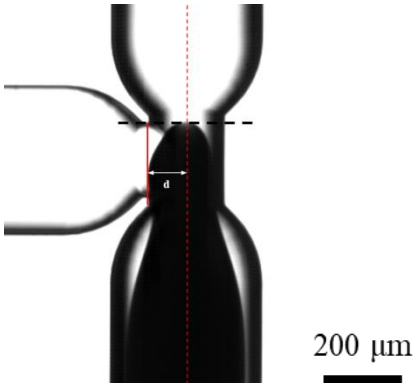

Figure 6.13 Measurement of the distance of the expansion of fluid 2 into the side channel at the junction.

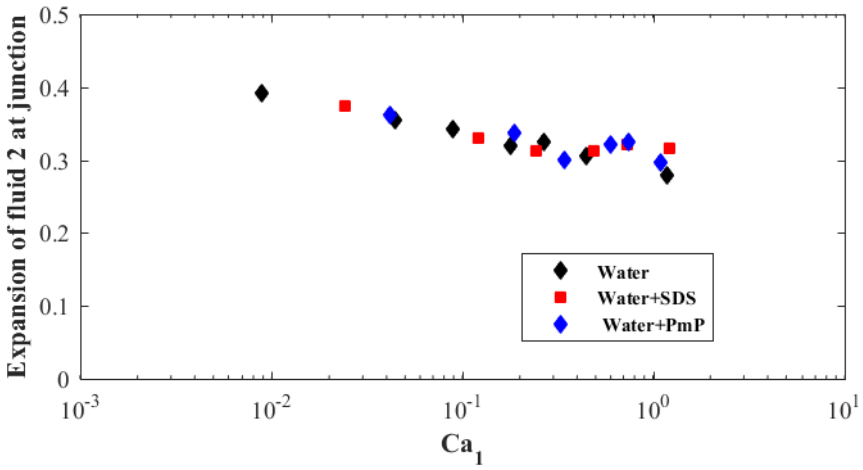

Figure 6.14 Expansion of fluid 2 at the junction for the second injection mode. Research normalised with hydraulic diameter of the channel.

The distance of the expanded part from central line decreases with the increase in capillary number. There does not appear a significant dependency with the surfactant added into fluid 2, since the results from three fluid pairs are close together, all characterised by capillary number. This indicates that although equilibrium interfacial tension isn't achieved for PmP-laden cases, the dynamic interfacial tension values used in calculating capillary number are good representatives to describe the effects of PmP.

The film thickness before and after fluid 2 passing through the junction were measured and plotted in Figure 6.15 against capillary number Ca_1. Similar to the first injection mode, an increase in film thickness after fluid 2 passing the junction can be observed and this effect is more obvious for small capillary number conditions. The use of SDS, which did not bring dynamic interfacial tension effects in this Chapter because of the time scale, did not influence the film thickness as the results are very close to those using water as fluid 2. On the other hand, similar to the finding from straight channel experiments (§4.3.1) and the injection mode 2 of T-junction channel, the other hand, the use of PmP, which shown some dynamic interfacial effects, introduced a slightly decreased trend on the film thickness, especially in high capillary number conditions. Although the inaccuracy of the estimated dynamic interfacial tension is believed to be a possible cause for this phenomenon but the results in Figure 6.14 indicates the values of dynamic interfacial tension values are very like to be acceptable. Therefore the distribution of surfactant molecules caused by recirculatory flows near the tip region is more likely to be the main reason for the finding. This is explained in detail in §4.3.1 (Figure 4.8).

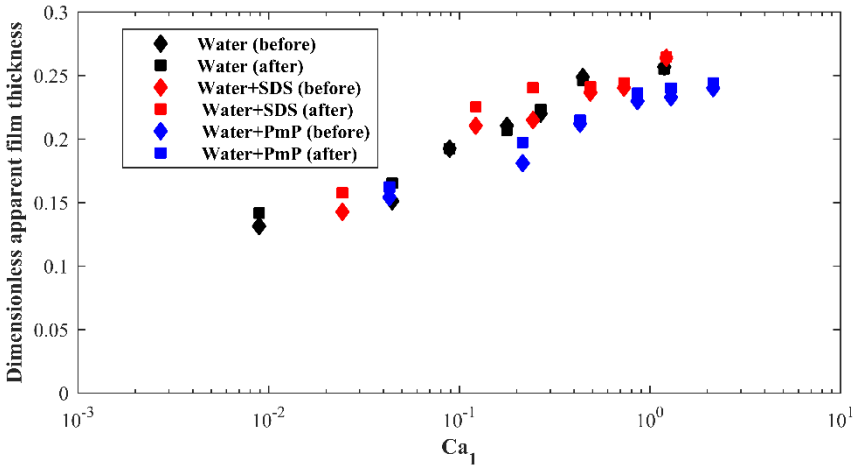

Figure 6.15 Film thickness measured before and after fluid 2 passing the junction for injection mode 2.

6.4 CFD simulation

ANSYS Fluent was used for simple cases mainly targeted to validate the assumptions of the cross-section shapes of fluid 2 in the wide straight part of the channel. The geometry used was a single straight channel without junction (Figure 6.16), with full channel cross-section.

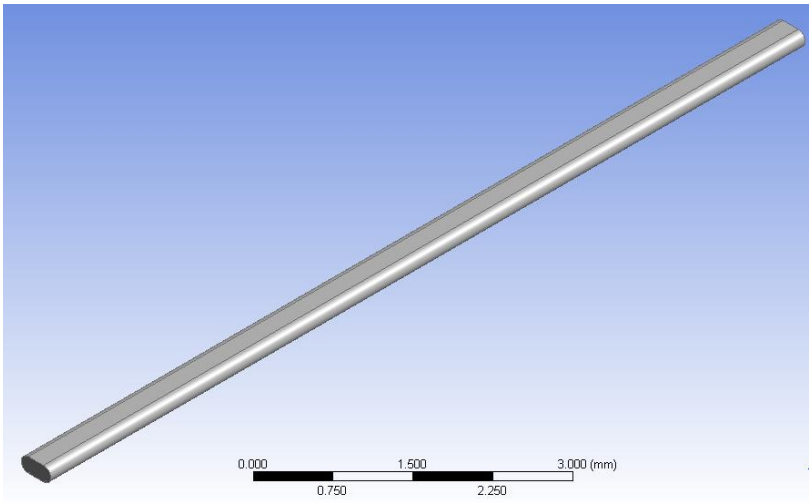

Figure 6.16 Geometry for computational simulation in wide channel.

The dimensions of the channel are the same with the wide part of the experimental channel. The fluid pair used was 100 cSt silicon oil as fluid 1 and water as fluid 2. Identical calculation settings as that in §5.1.1. were used.

The flow condition used for the simulation was 0.05 m s^{-1} for the velocity of fluid 2 injection, which corresponds to Ca_1 = 0.18. The apparent film thickness measurement using the same flow conditions is 56 and 53.5 μm for position *a* and *d* respectively. Either the method 1 or the first situation (Figure 6.9) of method 2 of the estimation of fluid 2 cross-section shape was expected to work and method 2 was expected to work better.

Figure 6.17 shows the fluid 2 cross-section interface shape from simulation results. Two methods of estimation of are marked on the graph with solid and dashed lines. Unlike the

prediction that the method 2 works better in the previous discussion, from the comparison between the mean film thickness using two interface estimation methods and the film thickness described using Taylor's law, the simulation result suggests method 1 (dashed line in Figure 6.17) is the better method. This may be because in CFD simulation, the result showed higher velocity than that in experiment, due to the different channel geometry (straight channel rather than junction channel). The higher velocity led to higher real capillary number and from Figure 6.9 it can be seen method 1 works better for high capillary number conditions. This is approve by calculating the velocity of fluid 2 and the capillary number from simulation results. The capillary number from simulation results is 0.33.

The interface at sides generally follows the curve of the ellipse but the interface at the top and bottom parts of the channel shows a much flatter curve than the ellipse. The film thickness at the top and bottom parts of the channel is ~15.8 μm. The height to width ratio of fluid 2 interface from this simulation results is 0.62, which is unfortunately not possible to be used as a universal reference for the height to width ratio in experiment. Because the height to width ratio of the channel is 0.49, meaning when film thickness is very small, i.e. fluid 2 interface very close to channel wall, the height to with ratio of the interface cannot theoretically exceed 0.49.

To this end the assumption of near zero film thickness at the top and bottom, inspired by the near zero film thickness at the corners in square channel at low capillary number (details in §4.3.1), may not suitable for the specific geometry of the wide channel in this Chapter.

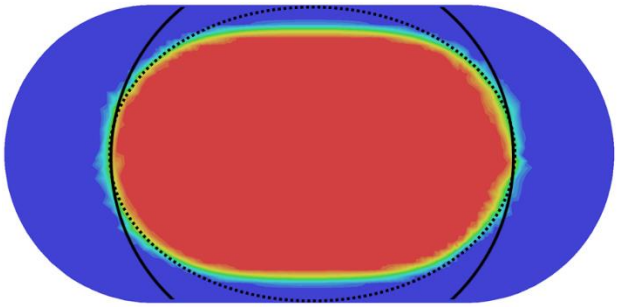

Figure 6.17 Cross-sectional view from simulation results. Dashed and solid lines represent the first and second method of fluid 2 cross-section estimation.

The 3-D shape of the fluid 2 tip revealed from simulation is shown in Figure 6.18.

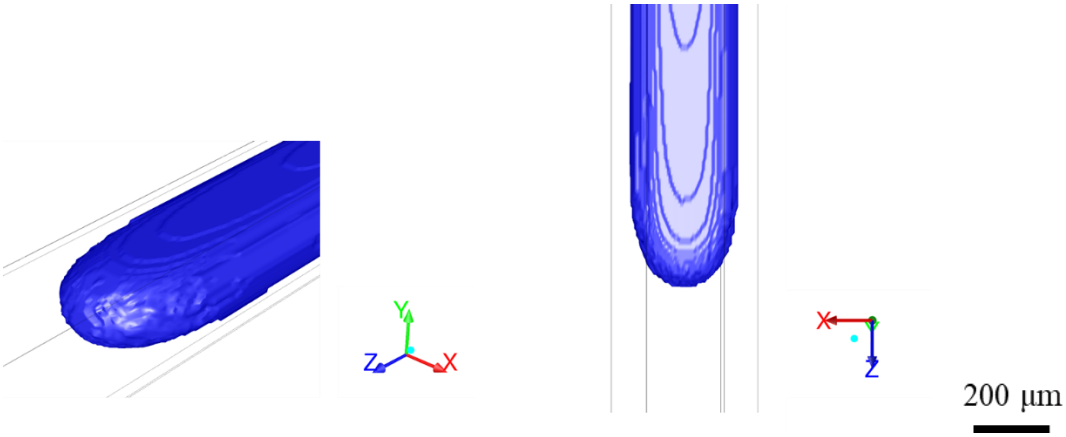

Figure 6.18 3-D view of the fluid 2 tip shape from simulation results.

Due to the fact that only the wide straight part of the channel has been used in the simulation, only qualitative information can be obtained from these simulation results. Quantitative information such as the film thickness cannot practically be compared to experimental results because the presence of the junction in experiment alters the pressure and velocity change in the channel consequently influences parameters such as film thickness. The apparent film thickness from using these flow conditions (Ca_1 = 0.18) is 69 μm, which is 23.2% and 29.0% larger than the film thickness measured from experimental images at positions *a* and *d*.

The simulation results have shown some flow features which were not observed in the experiment: the breakage of fluid 2 flows. Figure 6.19a shows the evolution of the occurrence of flow breakage, from two views. Unlike the flow breakage appears in the simulation of fluid displacement in circular channel, the plug formed in the wide channel may or may not has a flat tail depending on how the flow is viewed, see Figure 6.19d. This very much resemble the Taylor flow using certain fluids and operating conditions; Figure 6.19c shows the experimental image from (Haase, 2017), using hydrogen-water two-phase flows ($u_{L,S}$ = 0.007 m s^{-1}, $u_{G,S}$ = 0.006 m s^{-1}).

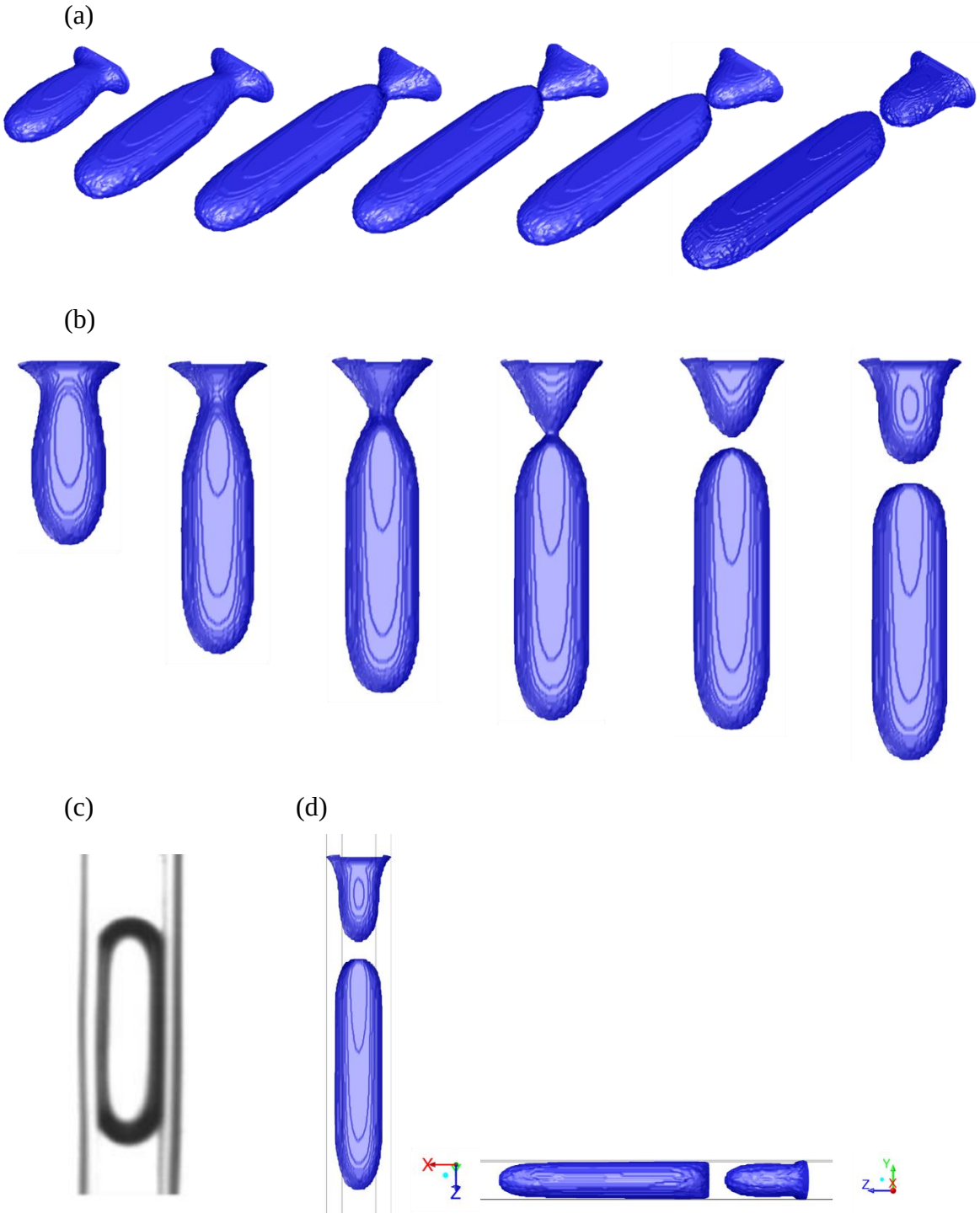

Figure 6.19 Simulation results showing the evolution of flow breakage at two views showing fluid volume fraction iso-surface, flow time from left to right: 1.0, 1.6, 1.8, 1.9, 1.95 and 2.11 ($\times 10^{-2}$) s; (c), experimental image show similar Taylor flows, hydrogen-water two phase flow, ($u_{L,S}$ = 0.007 m s^{-1}, $u_{G,S}$ = 0.006 m s^{-1}).

The circulation pattern inside fluid 2 was revealed by subtracting fluid 2 superficial velocity from the average flow velocity magnitude. Figure 6.20 shows the view of horizontal and vertical central planes. The velocity magnitude before and after velocity subtraction are shown, as well as the circulation streamlines.

(a)

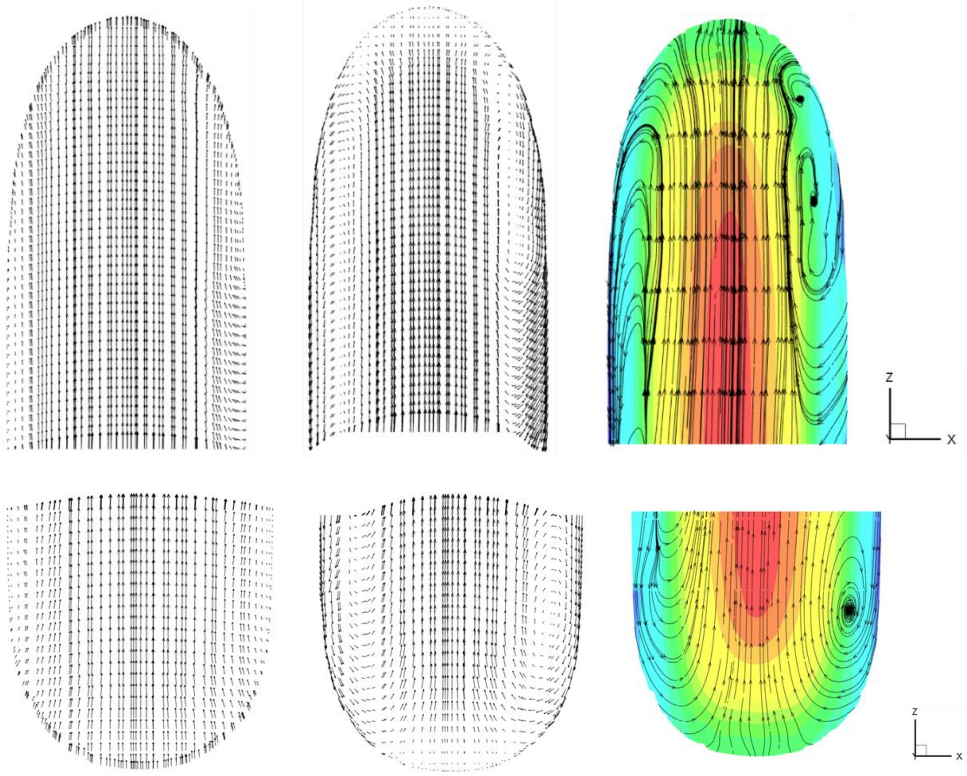

(b)

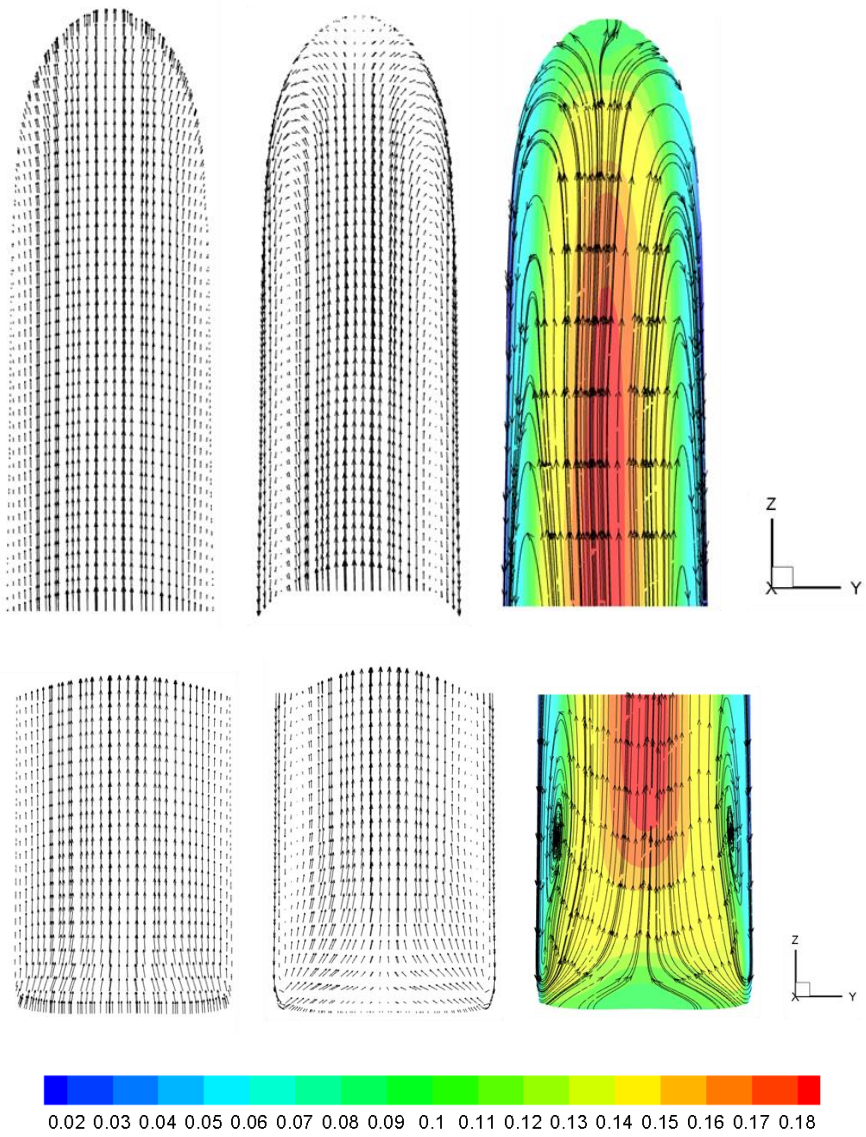

Figure 6.20 The circulation patterns inside fluid 2 revealed from velocity subtraction for (a) horizontal and (b) vertical middle planes. From left to right: velocity magnitude before velocity subtraction, velocity magnitude after velocity subtraction and the circulation streamlines with velocity superimposed with colours. Velocity legend in m s^{-1}.

6.5 Summary

The fluid displacement in a T-junction channel was carried out as well as a brief CFD simulation. The T-junction channel consists of the main wide channel part and the junction part. Two injection modes were used with one of the channel ends being blocked in each of the mode. The flow behaviour before and after the injection was particularly studied and the effects of introducing surfactants (SDS and PmP). An increase of the film thickness after the fluid passing through the junction was observed especially at small capillary conditions. This is believed to be caused by the sudden increase in fluid 2 velocity after passing the junction.

The cross-section shape of the interface between fluid 1 and 2 was studied following some geometrical assumptions. Two methods of interface estimation were proposed however both were shown to not able to accurately describe the shape of cross-section interface. The methods were assessed by comparing the mean film thickness, based on the cross-section area and perimeter of the interface estimated, with the literature correlation (Taylor's law). The mean film thickness approach was shown to be a valid tool to link the film thickness in non-circular channels to the literature models which were mostly developed using circular channels. Therefore further study is needed to understand the shape of interface in this non-circular channel because the accurate estimation of cross-section shape lead to more accurate estimate of the mean film thickness. The simulation results show a Taylor-style plug flow which is very similar to the results shown in §5.2.4. The cross-section of fluid 2 interface suggests the first method of interface estimation is closer, but improvement is needed.

Chapter 7 CONCLUSIONS AND FUTURE WORK

7.1 Conclusions

The work contained in this thesis describes experiments and CFD simulations of the displacement process of one fluid by another less viscous fluid in small scale channels. Three types of straight channels were used with hydraulic diameters ranging from 100 to 200 μm. Circular and square channels used were made in-house and a near-semicircular channel was used from a commercial microfluidic chip supplied by from Dolomite® microfluidics.

Both immiscible and miscible fluid pairs with various viscosity ratios, ranging from 20 to 100, were studied. For immiscible cases, the influence of adding surfactants in the displacing fluids was investigated.

The overall flow pattern and the interfacial behaviour such as the film thickness left on wall after the advancing displacing fluid, the curvature of the tip of the displacing fluid and interfacial instabilities were the parameters particularly studied in straight microchannels. The parameter investigated in the includes the residual which were particularly studied. For the displacement in T-junction channel, attention was mainly focused on the flow behaviour before and after passing through the junction.

CFD simulations were carried out using the commercial CFD package Fluent; Multiphase model Volume of Fluid (VoF) was chosen as the main model for better resolution of the fluid interfaces. Fluid displacement in all three straight channel geometries as well as the wide channel part of the T-junction channel were simulated. Quantitative and qualitative comparison between simulation and experimental results were carried out.

Details concerning how were the aims and objectives of this study achieved are described in the following sections.

7.1.1 Immiscible fluid displacement in straight microchannels

For immiscible fluid displacement experiment in straight channels, the initial film thickness was measured. It was found using the same fluid pair, the increase in fluid 2 injection caused to increase of film thickness. The capillary number was found to be the key parameter in this analysis. For near-semicircular channel and square channels, large deviation found between the film thickness using literature correlations for circular channels and the apparent film thickness (the film thickness measured directly from experimental images) suggested that the apparent film thickness was not the appropriate measure to represent the liquid film across the entire channel cross-section. Therefore, a mean film thickness approach, which based on the estimation of the cross-section interface shape of fluid 2, was proposed as an estimation of the film thickness across the whole channel. It was shown that by adapting the mean film thickness calculations as well as the real fluid 2 velocity, estimated from superficial velocity and film thickness, good agreement was achieved with literature correlations for circular channels. The recalculation of the results using film thickness correlation developed for square channel into mean film thickness also shows good alignment with the circular film thickness correlations. Therefore, the mean film thickness can be potentially applied to other channels with non-circular cross-sections. The analysis of the film thickness after adding a surfactant (SDS) into fluid 2 shows a thinning effect. This comes from the combined influence of the dynamic interfacial tension and the circulation flows inside fluid 2.

The analysis of the curvature of fluid 2 tip shows a decrease in the radius of curvature as capillary number increases. The width transition region between the tip and the constant film

thickness region was found to show a slightly decrease trend for surfactant-free fluid 2 cases, as capillary number increases. On the other hand, for surfactant-free cases, the transition region width was shown to stay almost unchanged as capillary number increases. This led to the proposition of a linear empirical correlation between the apparent film thickness and the radius of fluid 2 tip curvature.

Various types of interfacial instabilities between fluid 1 and 2 were observed as the injection flowrate of fluid 2 increases. These instabilities were categorised into three main flow patterns, namely the stable, axisymmetric unstable and asymmetric unstable regimes. It was found the use of different channel geometries did not affect the appearance of these unstable flows although various forms of the asymmetric unstable flows were observed in the experiments. Flow regime maps were developed to characterise the occurrence of these unstable flows based on the fluid pairs used (viscosity ratio) and capillary number. It was found the addition of a surfactant (SDS) into fluid 2 did not bring significant effects on the flow regime map when the capillary number was calculated using the viscosity and velocity of fluid 2. This may be because the unstable flow feature exists as a dynamic activity throughout the entire displacement process therefore the dynamic interfacial effect is compromised by the long-time contact between fluid 1 and 2. Therefore the alteration in equilibrium interfacial tension is the main effect that surfactant brings into the system. The use of a near-semicircular channel with hydrophobic wall showed that the wettability did change the conditions of the occurrence of the interfacial instabilities but did not show significant difference in the liquid film thickness on the wall. It was found the instabilities took place at lower fluid 2 injection rate for hydrophobic channel.

7.1.2 Miscible displacement in straight microchannels

The unstable flow features, i.e. interfacial instabilities, were the main observation for the displacement using miscible fluid pairs. Three flow regimes were categorised based on the appearance of unstable flows, namely the stable regime, wavy unstable and completely unstable regimes. The transition from wavy to completely unstable regimes does not have a strictly distinguishable change such as the change from axisymmetric to asymmetric forms for the immiscible cases. Therefore these two regimes were defined by the scale and the continuity of the unstable flows. From the flow regime maps developed for circular, near-semicircular and square channels, it was found the transition between stable and wavy unstable regimes and the transition from wavy to completely unstable appeared to take place at the smallest injection flowrate when using fluid pairs with viscosity ratio of 50.

By summarising the findings of immiscible and miscible fluid displacement in straight microchannels, the aims of the exploration of flow structures and interfacial behaviour, the effects of key parameters including the addition of surfactant on these behaviours and the development of flow regime maps (Aims and objectives 1, 2, 4 and 6 in §1.2) are considered achieved.

7.1.3 CFD simulations

Employment of the VoF model using Fluent successfully generated results showing sharp fluid interfaces resolved in only two to three cells. Reasonable measures were taken to increase the calculation speed such as the use of High Performance Computing facilities and the shortening of channel length. The unstable flow features were able to be simulated for all three channel geometries. In both circular and square channels, axisymmetric and asymmetric unstable flows were obtained and for near-semi-circular channel the axisymmetric unstable flow was obtained.

The comparison between simulation and experiment results were carried out both quantitatively and qualitatively.

The pinching part of the axisymmetric unstable flows in circular channel shows different appearance before and after fluid 2 traveling throughout the channel. However very similar pinching unstable features were seen after fluid 2 flowing throughout the entire channel. The asymmetric unstable flows from simulation results show very good agreement qualitatively when comparing with experimental results. For near-semicircular channel, the axisymmetric unstable regime was successfully simulated. It was revealed in the simulation results the side-view of the flow features of this type of unstable flows as this was not able to be recorded from experiments. The axisymmetric and asymmetric unstable flows in square channel both resemble the flow features observed in the experiments.

Quantitatively, the film thickness and radius of fluid 2 tip curvature were measured from simulation results using the same methods in the experiments. The results for near-semicircular and square channels shown very good agreement, represented by the very close match between experiment and simulation results. For circular channel, small capillary conditions, which account for stable and axisymmetric unstable regimes, show very good agreement while some variation was seen for higher capillary number condition, when the asymmetric unstable flow took place. This is believed to be caused by either the experimental operational error or the possible inaccuracy in the setting of time step or courant number in the simulation.

The velocity profiles obtained from simulation results in the circular channel reveal the sinuous flow inside the fluid 2 at the pinching part, when the macro appearance of the flow was actually axisymmetric. This was believed to be caused by the injection condition was close to trigger the occurrence of asymmetric instabilities because the axisymmetric unstable flow in square channel, which slower injection velocity was used, did not show the similar sinuous flows. The

subtraction of fluid 2 mean velocity from average velocity magnitude illustrated the circulation patterns inside fluid 2 near the tip region. This in addition proves the discussion of the redistribution of surfactant under the circulation patterns in the analysis of surfactant effects on film thickness in experiments.

From the summary and findings above, aim and objective 6 (§1.2) is achieved.

7.1.4 Immiscible displacement in T-junction channel

The flow features before and after fluid 2 passing the junction were investigated. For both injection modes, the film thickness increased after fluid 2 passed through the junction. This effect is more observable for small capillary number conditions. The sudden velocity increase after the junction, because of the cross-section area difference between the junction and wide main channel (wide main channel cross-section area is around 2.9 times that of the junction), is believed to be the main cause of the increase in film thickness. At high capillary number conditions, this effect is reduced, represented by film thickness before and after the junction being almost equal. Surfactant SDS and PmP with concentration of two and 10 times their CMC were used in the experiment. The addition of surfactant PmP, which has dynamic interfacial tension effects in the time scale in the experiment in this Chapter, in fluid2 shows a slightly thinning effect on the film thickness. This agrees with the finding of the experiment in straight channel. On the other hand, the addition of SDS in fluid 2 did not bring addition effects apart from the alteration of interfacial tension because equilibrium interfacial tension was achieved in the experimental timescale in this chapter.

Two methods of estimating the cross-section area and perimeter of the interface of fluid 2 were proposed: the first one assuming the cross-section shape of fluid 2 interface is elliptical and in the second method the interface at the sides are part of a circle with the diameter same with the

width of fluid 2. The top and bottom parts of the interface in the second method are assumed to be very close to the channel wall, i.e. very close to zero film thickness at these parts. By adapting the mean film thickness approach, both of the methods shown some variations. The CFD simulation of fluid displacement in a straight channel with the same cross-section of the wide channel part in the T-junction channel was carried out. The CFD result shows that the first method provides better approximation, but further investigation is needed to obtain an accurate calculation method. Similar to the CFD simulation using the straight circular channel, a Taylor-style plug flow was shown from the simulation in the wide channel, which was not observed from experiments. The exact mechanism for the breakage remains to be explored but it is believed to connected to calculation settings such as the cut off value of volume fraction.

Aim and objective 4 (§1.2) is achieved from this Chapter however some future studies are needed to provide full understanding of the T-junction flows, especially the estimation of fluid interface in the wide non-circular channel.

7.2 Future work

The results and discussion throughout this thesis provide some insights into the dynamics involved in the fluid displacement in microchannels, there still exists some gaps to be filled to give a complete picture on the topic. Following are some directions of future work:

1. Although it has been shown that the mean film thickness approach provides a valid link between the apparent film thickness in non-circular channel to the film thickness correlations developed in circular channel, the estimation of cross-section shape of the interface is the key element. A systematic study may need to be carried out analysing the cross-section shapes of the immiscible two-phase flows in non-circular channel, with varying interfacial tension and flow conditions. In this way the employment of the mean

film thickness approach can be widely broadened. Musterd, et al. (2015) successfully employed the interfacial energy minimisation principles to provide equations to calculate the cross-section area and perimeter of a droplet in non-circular channels. However capillary number needs to be smaller than 10^{-3} (quasi-static status), i.e. the film thickness near wall is very small compared to the size of channel, for their correlations to work. This could be a starting point to integrate flow momentum into the calculation.

2. The wettability of wall was shown to not affect the liquid film thickness left on the wall in this study. This could due to the very short contact between the wall and the aqueous phase (displacing fluid in this case) only near the inlet of channel. However only one type of hydrophobic channel was used therefore this analysis could be extended using coated channels with different contact angles. The laminar flow nature in this study means the displacing fluid does not normally touch the wall therefore it would be beneficial to introduce turbulence into the system to bring potentially more distinct effects in the displacement processes. In addition, when the displaced fluid in the channel is in the state of oil droplets on the wall, the wall wettability would have more impact on removing the droplets.
3. The flow regime maps developed in this project provide some guidance on the occurrence of interfacial phenomena in similar system and using similar fluids. However, more generalised flow pattern maps which can potentially be applied for different channel geometries and fluids are in need.
4. The time for fluid 1 to be completely cleared out from the channel was not able to be accurately obtained due to the limitation of camera capture time and the insufficient strategies to define the “clear out” status in the channel. This needs further investigations to provide more information to assist the concept of channel cleaning. The precise

measurement of the liquid from the outlet could be a possibility, as the volume of injected liquid is known from the injection flowrate. The use of fluorescent material in the displaced fluid can be potentially employed, with the help of high-energy laser and high-speed camera.

5. The velocity field was unfortunately unable to obtained in this study, due to the high-speed evolution of the time-dependent flows and the frequency and energy required from illumination source without damaging the optical components in the microscope. The measurement of velocity profiles from experiments using techniques such as (micro-) Particle Image Velocimetry (PIV) can be a great addition to the current work, as the velocity profiles have already been obtained from CFD simulations. The novel Ghost Particle Velocimetry (GPV) technique, which employs the speckles patterns of nano-scale particles, has also been tested in the current study. However due to the high velocity nature of the flow patterns especially in the complex unstable regime, GPV was not able to resolve the velocity fields using the existing instruments.
6. The transition between flow regimes are important to determine the desired fluid pairs and conditions in applications. CFD simulations using more flow conditions can generate flow regime maps from simulation results which can provide valuable information on the validation of CFD models on resolving the flow features in the transition regimes.
7. Only the flow region near fluid 2 tip was studied in the fluid displacement in the T-junction channel. More interfacial activities such as the behaviour of unstable flows at the junctions remain to be explored.

Bibliography

Adrian, R. J. and Westerweel, J., 2011. *Particle Image Velocimetry.* s.l.:Cambridge University Press.

Alvarez, M., 1998. *Aotomated Image Analysis Module for Axiymmetric Drop Shape Anaysis-Diameter,* Toronto: Department of Mechanical and Industrial Engineering, University of Toronto.

Anasasiou, A. D., Makatsoris, C., Gaviriilidis, A. and Mouza, A. A., 2013. Application of micro-PIV for investigating liquid film characteristics in an open inclined microchannel. *Experimental Thermal and Fluids Science,* 44, pp. 90-99.

Andersson, B. et al., 2015. *Computational Fluid Dynamics for Engineers.* 11th ed. Cambridge : Cambridge University Press.

Anti-Corrosion Methods and Materials, 2012. Global Report on the Surfactants Market. *Anti-Corrosion Methods and Materials,* 59(3).

Atencia, J. and Beebe, D. J., 2005. Controlled microfluidic interface. *Nature,* 437(29), pp. 648-655.

Aussillous, P. and Quere, D., 2000. Quick deposition of a fluid on the wall of a tube. *Physics of Fluids,* 12(10), pp. 2367-2371.

Ayirala, S. C. and Rao, D. . N., 2004. Multiphase flow and wettability effects of surfactants in porous media. *Colloids and Surfaces A: Physicochemical and Engineering Aspects,* 24(1), pp. 313-322.

Baker, O., 1954. Simultaneous flow of oil and gas. *Oil and Gas Journal,* 53(12), pp. 185.

Balasubramaniam, R., Rashidnia, N., Maxworthy, T. and Kuang, J., 2005. Instability of miscible interfaces in a clindrical tube. *Physics of Fluids,* 17(052103), pp. 1-11.

Barnea, D., Luninski, Y. and Taitel, Y., 1983. Flow pattern in horizontal and vertical two phase flow in small diameter pipes. *The Canadian Journal of Chemical Engineering,* 61(5), pp. 617-620.

Bentsen, R. G., 1985. A new approach to instability theory in porous media. *Society of Petroleum Engineers,* 25(5), pp. 765-779.

Bonfillon, A., Sicoli, F. and Langevin, D., 1994. Dynamic surface tension of ioninc surfactant solutions. *Journal of Colloid and Interface Science,* 168, pp. 497-504.

Boomkamp, P. A. and Miesen, R. H., 1996. Classification of instabilities in parallel two-phase flow. *Engineering Fluid Dynamics,* 22(1), pp. 67-88.

Boussinesq, M. J., 1868. Mémoire sur l'influence des frottements dans les mouvements réguliers des fluides. *JOURNAL DE MATHÉMATIQUES,* 13, pp. 377-438.

Brakke, K. A., 1992. The Surface Evolver. *Experimental Mathematics,* 1(2), pp. 141-165.

Brauner , N. and Maron, D. M., 1992. Identification of the range of 'small diameters' conduits, regarding two-phase flow pattern transitions. *International Communications in Heat and Mass Transfer,* 19(1), pp. 29-39.

Brennen, C. E., 2005. *Fundamentals of Multiphase Flows.* Cambridge: Cambridge University Press.

Bretherton, F. B., 1961. The motion of long bubbles in tubes. *Journal of Fluid Mechanics,* 10(2), pp. 166-188.

Brosseau, Q., Vrignon, J. and Baret, J.-C., 2014. Microfluidic Dynamic Interfacial Tensiometry. *Soft matter*, 10, pp. 3066-3076.

Buzzaccaro, S., Secchi, E. and Piazza, R., 2013. Ghost Particle Velocimetry: Accurate 3D Flow Visualization Using Standard Lab Equipment. *Physical Review Letters*, 111, p. 048101.

Casandra, A., Chung, M.-C., Noskov, B. A. and Lin, S.-Y., 2017. Adsorption Kinetics of sodium dodecyl sulfate on perturbed air-water interfaces. *Colloids and Surfaces A: PhysicoChemical and Engineering Aspects*, 518, pp. 241-248.

Chakrabarty, C. and Bentsen, R. G., 1991. Instability theory for immiscible displacements in tubular systems. *Journal of Petroleum Science and Engineering*, 6, pp. 15-35.

Chattopadhyay, A. and London, E., 1984. Fluorimetric determination of critical micelle concentration avoiding interference from detergent charge. *Analytical Biochemistry*, 139(2), pp. 408-412.

Chorin, A. J., 1968. Numerical solution of navier-stokes equations. *Mathematics of Computation*, 22, pp. 745-762.

Chung, P. M.-Y., Kawaji, M., Kawahara, A. and Shibata, Y., 2004. Two-phase flow through square and circular microchannels-Effects of Channel Geopmetry. *Journal of Fluids Engineering*, 126, pp. 546-552.

Coleman, J. W. and Garimella, S., 1999. Characterization of two-phase flow patterns in small diameter round and rectangular tubes. *International Journal of Heat and Mass transfer* , 42, pp. 2869-2881.

Collier, J. G., 1981. *Convective Boiling and Condensation.* 2nd ed. New York ; London: McGraw-Hill.

Cox, B. G., 1962. On driving a viscous fluid out of a tube. *Journal of Fluid Mechanics,* pp. 81-96.

Cuny, V. K. H. and Wolf, K. L., 1956. Präzisierung der Blasendruckmethode zur Bestimmung der Oberflächenspannung von Flüssigkeiten. *Annalen der Physik,* 452(2-3), pp. 57-77.

Dixon, J. K., Weith, Jun., A. J., Argyle, A. A. and Salley, D. J., 1949. Measurement of the Adsorption of Surface-Active Agent at a Solution-Air Interface by a Radiotracer Method.. *Nature,* 163, pp. 845.

Donnan, F. G. and Baker, J. T., 1911. An Experimental Investigation of Gibbs' Thermodynamical Theory of Interfacial Concentration in the Case of an Air-Water Interface. *Proceddings of the Royal Society A,* 85(152), pp. 557-573.

Dow, T. D. C. C., n.d. *Viscosity of Aqueous Glycerine Solutions in Centipoises/ mPa s.* [Online] Available at: http://msdssearch.dow.com/PublishedLiteratureDOWCOM/dh_0032/0901b803800322bd.pdf?filepath=glycerine/pdfs/noreg/115-00678.pdfandfromPage=GetDoc
[Accessed 6 1 2015].

Drelich , J., Fang, C. and White, C., 2002. Measurement of interfacial tension in fluid-fluid systems. In: P. Somasundaran, ed. *encyclopedia of surface and colloid science.* CRC Press, pp. 3152-3166.

Dukler, A. E. and Hubbard, M. G., 1975. A Model for Gas-Liquid Slug Flow in Horizontal and Near Horizontal Tubes. *Industrial and Engineering Chemistry Fundamentals,* 14(4), pp. 337-347.

Eastoe, J. and Dalton, J. S., 2000. Dynamic surface tension and adsorption mechanisms of surfactants at the air-water interface. *Advances in Colloid and Interface Science* , 85, pp. 103-144.

Ebnesajjad, S. and Landrock, A. H., 2014. *Adhesives Technology Handbook.* 3rd ed. s.l.:Elsevier.

Fainerman, V. B., Makievski, A. V. and Miller, R., 2004. Accurate analysis of the bubble formation process in maximum bubble pressure tensiometry. *Review of Scientific Instruments,* 75(1), pp. 213-221.

Fainerman, V. B. and Miller, R., 1995. Dynamic surface tensions of surfactant mixtures at the water-air interfaces. *Colloids and Surfaces A: Physicochemical and Engineering Aspects* , 97, pp. 65-82.

Fainerman, V. B. et al., 2010. Surface tension isotherms, adsoprtion dynamics and dilational visco-elasticity of soldium dodecyl sulphte solutions. *Colloids and Surfaces A: Physicochemical and Engineering Aspects* , 354, pp. 8-15.

Fairbrother, F. and Stubbs, A. E., 1935. Studies in electro-endosmosis. Part VI. The "Bubble-tube" method of measurement. *Journal of the Chemical Society,* 1, pp. 527-529.

Fendler, V. J. H., 1982. *Membrane Mimetic Chemistry.* New York: John Wiley and Sons, .

Ferguson, A., 1923. On a relation between surface tension and density. *Transactions of the Faraday Society,* 19, pp. 407-412.

Fleckenstein, S. and Bothe, D., 2013. A volume-of-fluid-based method for mass transfer processes at fluid particles. *Chemical Engineering Science,* 101, pp. 283-302.

Franses, E., Basaran, O. A. and Chang, C.-H., 1996. Techniques to measure dynamic surface tension. *Current Opinion in Colloid and Interface Science* , 1, pp. 296-303.

Furlong, D. N. and Hartland, S., 1979. Wall Effect in the Determination of Surface Tension Using a Wilhelmy Plate. *Journal of Colloiid and Interface Science,* 71(2), pp. 301-315.

Gaonkar, A. and Neuman, R., 1984. The Effect of Wettability of Wilhelmy Plate and du Nouy Ring on Interfacial Tension Measurements in Solvent Extraction Systems. *Journal of Colloid and Interface Science* , 98, pp. 112-119.

Girifalco, L. A. and Good, R. J., 1957. A Theory for the Estimation of Surface and Interfacial Energies. I. Derivation and Application to Interfacial Tension. *The Journal of Physical Chemistry,* 61(7), pp. 904-909.

Govier, G. W. and Omer, M. M., 1962. The horizontal pipeline flow of air-water mixtures. *The Canadian Journal of Chemical Engineeringgo,* 40(3), pp. 93-104.

Gravesen, P., Branebjerg, J. and Jensen, O. S., 1993. Microfluidics-a review. *Journal of Micromechanics and Microengineering,* 3, pp. 168-182.

Griffin, W. C., 1949. Classification of surface-active agents by "HLB". *Journal of Cosmetic Science* , pp. 311-326.

Griffith, P. and Snyder, G. A., 1964. *The Bubbly-Slug Transition in a High Velocity Two Phase Flow,* Cambridge, Boston: Massachusetts Institute of Technology.

Guggenheim, E. A., 1945. The Principle of Corresponding States. *The Journal of Chemical Physics,* 13(7), pp. 253-261.

Gunstensen, A. K., Rothman, D. H., Zaleski, S. and Zanetti, G., 1991. Lattice Boltzmann model of immisible fluids. *Physical Review A,* 43(8), pp. 4230-4237.

Gunther, A. and Jensen, K. F., 2006. Multiphase microfluidics:from flow characteristics to chemical and materials synthesis. *Lab Chip*, 6, pp. 1487-1503.

Haase, S., 2017. Characterisation of gas-liquid two-phase flow in minichannels with co-flowing fluid injection inside the channel, part II: gas bubble and liquid slug lengths, film thickness, and void fraction within Taylor flow. *International Journal of Multiphase Flow,* 88, pp. 251-269.

Halliday, H., 2008. Surfactants: past, present and future. *Journal of Perinatology*, 28, p. S47–S56.

Han, Y., Kanno, H., Ahn, Y.-J. and Shikazono, N., 2015. Measurement of liquid film thickness in micro tube annular flow. *International Journal of Multiphase Flow,* 72, pp. 264-274.

Han, Y. and Shikazono, N., 2009a. Measurement of the liquid film thickness in micro tube slug fow. *International Journal of Heat and Fluid Flow*, 30, pp. 842-853.

Han, Y. and Shikazono, N., 2009b. Measurement of liquid film thickness in micro square channel. *International Journal of Multiphase Flow,* 35, pp. 896-903.

Harkins, W. D. and Jordan, H. F., 1930. A Method for the Determination of Surface and Interfacial Tension from the Maximum Pull on a Ring. *Journal of the American Chemical Society*, 52(2), pp. 1751-1772.

Hassan, I., Vaillancourt, M. and Pehlivan, K., 2005. Two-phase Flow Regime Transitions in Microchannels: A Comparative Experimental Study. *Microscale Thermophysical Engineering*, 9, pp. 165-182.

Hewitt, G. F. and Hall-Taylor, N. S., 1970. *Annular Two-Phase Flow*. 1st ed. Oxford: Pergamon Press.

Hewitt, G. F. and Roberts, D. N., 1969. *Studies of Two-phase Flow Patterns by Simultaneous X-ray and Flash Photography,* Harwell, England: Atomic Energy Research Establishment.

He, X., Zhang, R. and Doolen, G., 1999. On the three-dimensional Rayleigh-Taylor Instability. *Physics of Fluid,* 11(1143), pp. 1143-1152.

Hickox, C. E., 1971. Instability due to viscosity and density stratification in axisymmetric pipe flow. *The physics of Fluids,* 14(252), pp. 1958-1988.

Hirsch, C., 2007. Intrduction: An initial guide to CFD and to this Volume. In: *Numerical computational of internal and external flows.* Elsevier, pp. 1-20.

Hoffmann, M., Schluter, M. and Rabiger, N., 2006. Experimental investigation of liquid-liqudi mixign in T-shaped micro-mixers using micro-LIF and micro-PIV. *Chemical Engineering Science,* 61, pp. 2968-2976.

Homsy, G. M., 1987. Viscous fingering in porous media. *Annual Review of Fluid Mechanics,* 19, pp. 271-311.

Hoogendoorn, C. J., 1959. Gas-liquid flow in horizontal pipes. *Chemical Engineering Science ,* 9, pp. 205-217.

Horozov, T. et al., 1996. Effect of the surface expansion and wettability of the capillary on the dynamic surface tension measured by the maximum bubble pressure method. *Colloids and Surfaces A: Physicochemieal and Engineering Aspects,* 113, pp. 117-126.

Huh, D. et al., 2007. A gravity-driven microfluidic particle sorting device with hydrodynamic separation amplification. *Analytical Chemstry,* 79(4), pp. 1369-1376.

Iliev, T. H. and Dushkin, C. D., 1992. Dynamic surface tension of micellar solutions studied by the maxium bubble pressure method. Part 1. *Colloid and Polymer Science ,* 270, pp. 370-376.

Inci, A. and Lee, B., 2014. Dynamic relations between stock returns and exchange rate changes. *European Financial Management,* 20(1), pp. 71-106.

Irandoust, S. and Andersson, B., 1989. Liquid film in Taylor flow through a Capillary. *Industrial and Engineering Chemistry Research,* 28, pp. 1684-1688.

Israelachvili, J. N., Mitchell, D. J. and Ninham, B. W., 1976. Theory of self-assambly of hydrocarbon amphiphiles into micelles and bilayers. *Journal of the Chemical Society, Faraday Transactions 2: Molecular and Chemical Physics,* 72, pp. 1525-1568.

Jahanmiri, M., 2011. *Particle Image Velocimetry: Fundamentals and Its applications,* Göteborg: Chalmers University of Technology.

Jamshed, S., 2015. *Using HPC for Computational Fluid Dynamics, Chapter 1 - Introduction to CFD.* Oxford: Elsevier.

Jeong, W. and Seong, J., 2014. Comparison of Effects on Technical Variances of Computational Fluid Dynamics Software Baed on Finite Element and Finite Volume Methods. *International Journal of Mechanical Sciences,* 78, pp. 19-26.

Kamisli, F. and Ryan, M. E., 2001. Gas-assisted non-newtonian $uid displacement in circular tubes and noncircular channels. *Chemical Engineering Science,* 56, pp. 4913-4928.

Kanellopoulos , A. G. and Owen, M. J., 1971. Adsorption of sodium dodecyl sulphate at the silicone fluid/water interface. *Transactions of the Faraday Society,* 67, pp. 3127-3138.

Kawahara, A., Chung, P.-Y. and Kawaji, M., 2002. Investigation of two-phase flow pattern, void fraction and pressure drop in a microchannel. *International Journal of Multiphase Flow,* 28, pp. 1411-1435.

Kew, P. A. and Cornwall, K., 1997. Correlations for the prediction of boilling heat transfer in small-diameter channels. *Applied Thermal Engineering* , 17(8-10), pp. 705-714.

Klevens, H. B., 1953. Structure and Aggregation in Surface Active Agents. *Journal of the American Oil Chemists Society,* 30(2), pp. 74-80.

Kobayashi, J. et al., 2004. A microfluidic device for conducting gas-liquid solid hydrogenation reactions. *Science* , 304, pp. 1305-1308.

Kolb, W. B. and Cerro, R. L., 1991. Coating the inside of a capillary of square cross section. *Chemical Engineering Science,* 46(9), pp. 2181-2195.

Kovalchuk, N., Roumpea, E., Nowak, E., Chinaud, M., Angeli, P. and Simmons, M., 2018. Effect of surfactant on emulsification in microchannels. *Chemical Engineering Science,* 176, pp. 139-152.

Koval'chuk, V. I., Dukin, S. S., Fainerman, V. B. and Miller, R., 1998. Lifetime Calculations Relative to Maximum Bubble Pressure Measurements. *Journal of Colloid and Interface Science,* 197(2), pp. 383-390.

KRÜSS Gmbh, 2017. *Du Noüy ring method.* [Online] Available at: https://www.kruss.de/services/education-theory/glossary/du-nouey-ring-method/ [Accessed 24 March 2017].

Kuang, J., Maxmorthy, T. and Petijeans, P., 2003. Miscible displacment between silicone oils in capillary tubes. *European Journal of Mechanics B/Fluids,* 22, pp. 271-277.

Kulkarni, V. S. and Shaw, C., 2016. *Essential Chemistry for Formulators of Semisolid and Liquid Dosages.* 1st ed. s.l.:Elsevier.

Leandro, J., Lopes, P., Fernandes de Carvalho, R. and Valentin, M. G., 2016. Assessment of the Ability of a Volume of Fluid Model to Reproduce the Efficiency of a Continuous Transverse Gully with Grate. *Journal of Irrigation and Drainage Engineering,* 142(10), pp. 1-9.

Lecomte du Noüy, P., 1919. A new apparatus for measuring surface tension. *The Journal of General Physiology* .

Lei, K. F., 2014. Materials and fabrication techniques for nano- and microfluidic devices. In: F. H. Labeed and H. O. Fatoyinbo, eds. *Microfluidics in detection science: lab-on-a-chip technologies.* Royal Society of Chemistry, pp. 1-28.

Li, H. et al., 2014. Flow pattern map and time–frequency spectrum characteristics of nitrogen–water two-phase flow in small vertical upward noncircular channels. *Experimental Thermal and Fluid Science,* 54, pp. 47-60.

Li, Q. and Angeli, P., 2017. Experimental and numerical hydrodynamic studies of ionic liquid-aqueous plug flow in small channels. *Chemical Engineering Journal,* 328, pp. 717-736.

Li, S. et al., 2013. Initial thickness measurement and insights into crystal growth of methane hydrate film. *AICheE Journal,* 59(6), pp. 2145-2154.

Lliescu, C. et al., 2012. A parctical guide for the fabrication of microfluidic devices using glass and silicon. *Biomicrofluidics,* 6, pp. 016505 1-16.

Lu, J. R. et al., 1993. Adsoption of Dedecyl Sulfate Surfactants with Monovalent Metal Counterions at the Air-Water Interface Studied by Neutron Reflection and Surface Tension. *Journal of Colloid and Interface Science,* 158, pp. 303-316.

Lunkenheimer, K. and Czichocki, G., 1993. On the Stability of Aqueous Sodium Dodecyl sulfate Solutions. *Cournal of Colloid and Interface Science,* 160(2), pp. 509-510.

Malhotra, S. and Sharma, M. M., 2014. Impact of fluid elasticity on miscible viscous fingering. *Chemical Engineering Science,* 117, pp. 125-135.

Mandhane, J. M., Gregory, G. A. and Aziz, K., 1974. A flow pattern map for gas-liquid flow in horizontal pipes. *International Journal of Multiphase Flow,* 1, pp. 537-553.

Manglik, R. M., Wasekar, V. M. and Zhang, J., 2001. Dynamic and equilibrium surface tension of aqueous surfactant and polymeric solutions. *Experimental Thermal and Fluid Science,* 25, pp. 55-64.

Marchessault, R. N. and Mason, S. G., 1960. Flow of entrapped bubbles through a ccapillary. *Industrial and Engineering Chemistry,* 52(1), pp. 79-84.

Martin, J. D. and Hudson, S. D., 2009. Mass transfer and interfacial properties in two-phase. *New Journal of Physics,* 11, p. 115005.

Mcquillan, K. W. and Whalley, P. B., 1985. Flow patterns in vertical two-phase flow. *International Journal of Multiphase Flow,* 11(2), pp. 161-175.

Mehta, S., Bhasin, K., Chauhan, R. and Dham, S., 2005. Effect of temperature on critical micelle concentration and thermodynamic behavior of dodecyldimethylethylammonium bromide and dodecyltrimethylammonium chloride in aqueous media. *Colloids and Surfaces A: Physicochemical and Engineering Aspects,* 255, pp. 153-157.

Menger, F. M. and Littau, C. A., 1991. Gemini-surfactants: synthesis and properties. *Journal of the American Chemical Society,* 113(4), pp. 1451-1452.

Menger, F. M. and Littau., C. A., 1993. Gemini Surfactants: A New Class of Self-Assembling Molecules. *Journal of American Chemical Scociety,* 115, pp. 11083-10090.

Menger, F. M., Zana, R. and Lindman, B., 1998. Portraying the Structure of Micelles. *Journal of Chemical Education,* 75(1), p. 115.

Mishama, K. and Ishii, M., 1984. Flow regime transition criteria for upward two-phase flow in vertical tubes. *International Journal of Heat and Mass Transfer ,* 27(5), pp. 723-737.

Mishima, K. and Hibiki, T., 1996. Some Characteristics of Air-water Two-phsae flow in small diameter vertical tubes. *International Journal of Multiphase Flow,* 4, pp. 703-712.

Mishra, M., Wit, A. D. and Sahu, K. C., 2012. Double diffusive effects on pressure-driven miscible displacement flows in a channel. *Journal of Fluid Mechanics ,* 712, pp. 579-597.

Miyake, M. and Yamashita, Y., 2017. Molecular Structure and Phase Behavior of Surfactants. In: K. Sakamoto, R. Lochhead, H. Maibach and Y. Yamashita, eds. *Cosmetic Science and Technology: Theoretical Principles and Applications.* 1st ed. Alsevier, p. 390.

Mohajeri, E. and Noudeh, G. D., 2012. Effect of Temperature on the Critical Micelle Concentration and Micellization Thermodynamic of Nonionic Surfactants: Polyoxythylene Sorbitan Fatty Acid Esters. *E-Journal of Chemistry,* 9(4), pp. 2268-2274.

Muijlwijk, K. et al., 2016. Interfacial tension measured at high expansion rates and within milliseconds using microfluidics. *Journal of Colloid and Interface Science,* 470, pp. 71-79.

Mukerjee, P., 1967. The nature of the association equilibria and hydrophobic bonding in aqueous solutions of association colloids. *Advances in Colloid and Interface Science,* 1(3), pp. 242-275.

Mukerjee, P. and Mysels, K. J., 1971. Critical Micelle Concentrations of Aqueous Surfactant Systems. *National Standard Reference Data Service,* 36.

Musterd, M., van Steijn, V., Kleijn, C. R. and Kreutzer, M. T., 2015. Calculating the volume of elongated bubbles and droplets in microchannels from a top view image. *Royal Society of Chemistry Advances*, 5, pp. 16042-16049.

Myers, D., 1992. *Surfactant Science an Technology.* 2nd ed. VCH publishers.

Mysels, K. J., 1986. Surface Tension of Solutions of Pure Sodium Dodecyl Sultfate. *Langmuir*, 2, pp. 423-428.

Nair K, L., Jagadeeshan, S., Nair, S. A. and Kumar , G. S. V., 2011. Evaluation of triblock copolymeric micelles of Valerolactone and poly (ethylene glycol) as a competent vector for doxorubicin delivery against caner. *Journal of Nanobiotechnology* , 9, p. 42.

Nakama, Y., 2017. Surfactants. In: K. Sakamoto, R. Lochhead, H. Maibach and Y. Yamashita, eds. *Cosmetic Science and Technology: Theoretical Principles and Applications.* 1st Edition ed. Elsevier, p. 232.

Navier, M., 1927. Mémoire sur les lois du mouvement des fluides. *Mémoires de l'Académie des sciences*, 6(2), pp. 389-440.

Nowak, E., Kovalchuk, N. M., Che, Z. and Simmons, M. J. H., 2016. Effect of surfactant concentration and viscosity of outer phase during the coalescence of a surfactant-laden drop with a surfactant-free drop. *Colloids and Surfaces A: Physicochemical and Engineering Aspects*, 505, pp. 124-131.

Ohnuki, A. and Akimoto, H., 2000. Experimental study on transition of ¯ow pattern and phase distrubution in upward air-water two-phase flow along a large vertical pipe. *International Journal of Multiphase Flow*, 26, pp. 367-386.

Okushima, S., Nisisako, T., Torii, T. and Higuchi, T., 2004. Controlled Production of Monodisperse Double Emulsions by Two-Step Droplet Breakup in Microfluidic Devices. *Langmuir,* 20(23), pp. 9905-9908.

Olgac, U. and Muradoglu, M., 2013. Effects of surfactant on liquid film thickness in the Bretherton problem. *International Journal of Multiphase Flow,* 48, pp. 58-70.

Oliveira, R. M. and Meiburg, E., 2011. Miscible displacements in Hele-Shaw cells: three-dimensional Navier-Stokes simulations. *Journal of Fluid Mechics,* 687, pp. 431-460.

Owens, D. K., 1969. The Dynamic Surface Tension of Sodium Dodecyl Sulfate Solutions. *Journal of Colloid and Interface Sicence,* 29(3), pp. 496-501.

Pamme, N., 2007. Continuous flow separation in microfluidioc devices. *Lab on a chip,* 7, pp. 1644-1659.

Pathak, A. and Raessi, M., 2016. A three-dimensional volume-of-fluid method for reconstructing and advecting three-material interfaces forming contact lines. *Journal of Computational Physics,* 307, pp. 550-573.

Patist, A. et al., 2000. On the Measurement of Critical Micelle Concentrations of Pure and Technical-Grade Nonionic Surfactants. *Journal of Surfactants and Detergents,* 3(1), pp. 53-58.

Peiro, J. and Sherwin, S., 2005. Finite difference, finite element and finite volume methods for partial differential equations. In: S. Yip, ed. *Handbook of Materials Modeling.* Berlin: Springer, pp. 2415-2446.

Perez-Rodrıguez, M. et al., 1998. A Comparative Study of the Determination of the Critical Micelle Concentration by Conductivity and Dielectric Constant Measurements. *Langmuir,* 14, pp. 4422-4426.

Petitjeans, P. and Maxworthy, T., 1996. Miscible displacement in capillary tubes. Part 1. Experiments. *Journal of Fluid Mechanics* , 326, pp. 37-56.

Phylaktis, K. and Ravazzolo, F., 2005. Stock prices and exchange rate dynamics. *Journal of International Money and Finance.*

Poisson, S. D., 1831. Mémoire sur les équations générales de l'équilibre et du mouvement des corps solides élastiques et des fluides. *Journal de l'École polytechnique,* 30, pp. 1-174.

Presto, W. C., 1948. Some Correlating Principles of Detergent Action. *The journal of Physical Chemistry,* 52(1), pp. 84-97.

Quintella, E. F., Souza Mendes, P. R. and Carvalho, M. S., 2007. Displacement flows of dilute polymer solutions in capillaries. *Journal of Non-Newtonian Fluid Mechanics,* 147, pp. 117-128.

Radovcich, N. A. and Moissis, R., 1962. *The Transition from Two Phase Bubble Flow to Slug flow,* Cambridge, Boston: Massachusetts Institute of Technology.

Rapp, B. E., 2016. *Microfluidics: Modeling, Mechanics and Mathematics.* 1st ed. s.l.:Elsevier.

Ratulowski, J. and Chang, H.-C., 1989. Transport of gas bubbles in capillaries. *Physics of Fluids A,* 1(10), pp. 1642-1655.

Ratulowski, J. and Chang, H.-C., 1990. Marangoni effects of trace impurities on the motion of long gas bubbles in capillaries. *Journal of Fluid Mechanics* , 210, pp. 303-328.

Ray, A. and Nemethy, G., 1971. Effects of Ionic Protein Denaturants on Micelle Formation by Nonionic Detergents. *Journal of the American Chemical Society,* 93(25), pp. 6787-6793.

Redapangu, P. R., Sahu, K. C. and Vanka, S. P., 2012. A study of pressure-driven displacement flow of two immiscible liquids using a multiphase lattice Boltzmann approach. *Physics of Fluids,* 24(102110), pp. 1-21.

Redapangu, P. R., Sahu, K. C. and Vanka, S. P., 2013. A Lattice Boltzmann simulation of three-dimensilonal displacement flow of two immiscible liquids in a square duct. *Journal of Fluids Engineering,* 135(121202), pp. 1-8.

Rennie, A. R. et al., 1989. Adsorption of poly(ethylene oxide) at the air-solution interface studied by neutron reflection. *Macromolecules,* 22(8), pp. 3466-3475.

Rosen, M. J., 2004. *Surfactants and Interfacial Phenomena.* 3rd ed. Hoboken, New York: Wiley-Interscience.

Sadatomi, M., Sato, Y. and Satuwatari, S., 1982. Two-phase flow in veritical noncircular channels. *International Journal of Multiphase Flow,* 8(6), pp. 641-655.

Sahu, K. C., 2013. Double Diffusive effects on pressure-driven miscible channel flows: Influence of varable diffusivity. *International Journal of Multiphase Flow,* 55, pp. 24-31.

Sahu, K. C., Ding, H., Valluri, P. and Matar, O. K., 2009. Linear stability analysis and numberical simulation of muscible two-layer channel flow. *Physics of Fluids,* 21(042104), pp. 1-19.

Saint-Venant, B., 1843. Mémoire sur la dynamique des fluides. *Comptes Rendus de l'Académie des Sciences,* 17, pp. 1240-1242.

Schramm, L. L., Stasiuk, E. N. and Marangoni, D. G., 2003. Surfactants and their applications. *Annual Reports Section "C" (Physical Chemistry),* 99, pp. 3-49.

Scoffoni, J., Lajeunesse, E. and Homsy, G. M., 2001. Interfacial instabilities during displacement of two miscible fluids in a vertical pipe. *Physics of Fluids,* 13(3), pp. 553-556.

Selvam, B., Merk, S., Govindarajan, R. and Meiburg, E., 2007. Stability of miscible core-annular flows with viscosity stratification. *Journal of Fluid Mechanics,* 592, pp. 23-49.

Serizawa, A., Feng, Z. and Kawara, Z., 2002. Two-phase flow in microchannels. *Experimental Thermal and Fluid Science,* 26, pp. 703-714.

Shah, R. K. and Bhatti, M. S., 1987. Laminar convective heat transfer in ducts. In: S. Kakac, R. K. Shah and W. Aung, eds. *Handbook of Single-Phase Convective Heat Transfer.* New York: Willy.

Shan, X. and Chen, H., 1993. Lattice Boltzmann model for simulating flows with multiple phase and components. *Physical Review E,* 47(3), pp. 1819-1820.

Shestopalov, L., Tice, J. D. and Ismagilov, R. F., 2004. Multi-step synthesis of nanoparticles performed on millisecond time scale in a microfluidic droplet-based system. *Lab chip,* 4, pp. 316-321.

Shimizu, K. and Iwatsuru, M., 1988. Measurement of the Critical Micelle Concentration of Nonionic Surfactant by the First Derivative Absorption Spectrum Method. *Chemical and Pharmaceutical Bulletin,* 36(10), pp. 4055-4059.

Shinoda, K., Nakagawa, T., Tamamushi , B.-I. and Isemura, T., 1965. *Colloidal surfactants: some physicochemical properties.* New York: Academic Press.

Shinoda, K. and Saito, H., 1969. The stability of 0/W type emulsions as functions of temperature and the hlb of emulsifiers: the emulsification by PIT-method. *Journal of Colloid and Interface Science,* 30(2), pp. 258-263.

Shukla, S., 2016. *Surfactants Market by Type (Cationic, Anionic, Non-ionic, Amphoteric) and Application (Household detergents, Personal Care, Industrial and Institutional Cleaners, Emulsion Polymerization, Food Processing, Oilfield Chemicals),* Allied Market Research .

Sia, S. K. and Whitesides, G. M., 2003. Microfluidic devices fabricated in poly(dimethylsiloxane) for biological studies. *Electrophoresis,* 24, pp. 3563-3576.

Si, H.-M., Cho, C. and Kwahk, S.-Y., 2003. A hybrid method for casting process simulation by combining FDM and FEM with an efficient data conversion algorithm. *Journal of Materials Processing Technology,* 133(3), pp. 311-321.

Silva, G., Leal, N. and Semiao, V., 2009. Determination of microchannels geometric parameters using micro-PIV. *Chemical Engineering Research and Disign,* 87, pp. 298-306.

Simmons, M. J. H. and Azzopardi, B. J., 2001. Drop size distributions in dispersed liquid–liquid pipe flow. *International Journal of Multiphase Flow,* 27(5), pp. 843-859.

Simons, M., 1851. Recherches Sur La Capillarité. *Annales de Chimie et de Physique,* 32, p. 5.

Sinton, D., 2004. Microscale flow visulisation. *Miirofluidic Nanofluid,* 1, pp. 2-21.

Skauge, A., Garnes, J. M., Mørner, O. J. and Torske, L., 1992. Optimization of a surfactant flooding prcess by core-flood experiments. *Journal of Petroleum Science and Engineering ,* 7(1-2), pp. 117-130.

Smits, A. J. and Lim., T. T., 2012. *Flow Visualizatiion: Techniques and Examples.* 2nd ed. London: Imperial College Press.

Soares, E. J., Carvalho, M. S. and Souza Mendes, P. R., 2005. Immiscible Liquid-Liquid displacement in Capillary Tubes. *Journal of Fluids Engineering ,* 127, pp. 24-31.

Soares, E. J., de Souza Mendes, P. R. and Carvallo, M. S., 2008. Immiscible liquid-liquid displacement in capillary tubes: viscoelastic effects. *J. Braz. Soc. Mech. Sci. and Eng,* 30(2), pp. 160-165.

Spedding, P. L. and Spence, D. R., 1993. Flow regimes in two-phase gas-liquid flow. *International Journal of Multiphase flow ,* 19(2), pp. 245-280.

Steegmans, M. L. J., Warmerdam, A., Schroen, K. G. P. H. and Boom, R. M., 2009. Dynamic Interfacial Tension Measurements with Microfluidic Y-Junctions. *Langmuir,* 25(17), pp. 9751-9758.

Stokes, G. G., 1880. On the Theories of the Internal Friction of Fluids in Motion, and of the Equilibrium and Motion of Elastic Solids. *Mathematical and Physical Papers,* 1, pp. 75-129.

Stone, H. A., Strook, A. D. and Ajdari, A., 2004. Engineering flows in small scale devices: microfluidics toward a lab-on-a-chip. *Annual Review of Fluid Mechanics ,* 36, pp. 381-411.

Stracca, L., 2015. Our currency, your problem? The global effects of the euro debt crisis. *European Economic Review,* pp. 1-13.

Swain, P. A., Karapetsas, G., Martar, O. K. and Sahu, K. C., 2015. Numerical simulation of pressure-driven displacement of a viscoplastic meterial by a Newtonian fluid using the lattice Boltzmann method. *European Journal of Mechanics B/Fluids,* 49, pp. 197-207.

Swift, M. R., Osborn, W. R. and Yeomans, J. M., 1995. Lattice Boltzmann simulation of nonodeal fluids. *Physical Review Letters,* 75(5), pp. 830-834.

Taghavi, S. M., Alba, K. and Frigaard, I. A., 2012. Buoyant miscible displacement flows at moderate viscosity ratios and low Atwood numbers in near-horizontal ducts. *Chemical Engineering Science,* 69, pp. 408-418.

Taitel, Y., Bornea, D. and Dukler, A. E., 1980. Modelling Flow Pattern Transitions for Steady Upward Gas-Liquid Flow in Vertical Tubes. *AIchE Journal,* 26(3), pp. 345-354.

Tajima, K., Muramatsu, M. and Sasaki, T., 1970. Radiotracer Studies on Adsoption of Surface Avtive Substance at Aqueous Surface. I. Accurate Measurement of Adsoption of Tritiated Soium Dodecylsulfate. *Bullentin of the Chemical Society of Japan,* 43, pp. 1991-1998.

Tanaka, T., 2013. Surface tension models. In: S. Seetharaman , ed. *Treatise on Process Metallurgy, 2: Process Phenomena.* Elsevier , pp. 35-59.

Taylor, D. J. F., Thomas , R. K. and Penfold, J., 2002. The adsorption of oppositely charged polyelectrolyte/surfactant mixtures: Neutron reflection from dodecyl trimethylammonium bromide and sodium poly(styrene sulfonate) at the air/water interface. *Langmuir,* 18(12), pp. 4748-4757.

Taylor, G. I., 1961. Deposition of a viscous fluid on the wall of a tube. *Fluid Mechnics,* 10, pp. 161-165.

Teh, S.-Y., Lin, R., Hung, L.-H. and Lee, A. P., 2008. Droplet microfluidics. *Lab Chip,* 8, pp. 198-220.

Thorsen, T., Mearkl, S. J. and Quake, S. R., 2002. Microfluidic large-scale integration. *Science ,* 298, pp. 580-584.

Thorsen, T., Roberts, R. W., Arnold, F. H. and Quake, S. R., 2001. Dynamics patterns formation in a vesicle-generating microfluidic device. *Physical Review Letters,* 86(18), pp. 4163-4166.

Troniewski, L. and Ulbrich, R., 1984. Two-phase gas-liquid flow in rectangular channels. *Chemical Engineering Science ,* 39(4), pp. 751-765.

Tsaoulidis, D. and Angeli, P., 2016. Effect of Channel Size on Liquid-Liquid Plug Flow in Small Channels. *AIChE Journal,* 62(1), pp. 315-324.

Tsuji, Y., 2000. Activities in discrete particle simulation in Japan. *Powder Technology,* 113, pp. 278-286.

Versteeg, H. K. and Malalasekera, W., 1995. *An introduction of computational fluid dynamics The finite volume method.* New York: Longman Group.

Wambsganss, M. W., Jendrzejczyk, J. A. and France, D. M., 1991. Two-phase flow patterns and transitions in a small, horizontal, rectangular channel. *International Journal of Multiphase Flow*, 17(3), pp. 327-342.

Wang, K., Zhang, L., Zhang W. and Luo, G., 2016. Mass-Transfer-Controlled Dynamic Interfacial Tension in Microfluidic Emulsification Processes. *Langmuir*. 32(13), pp. 3174-3185

Wang, K.-L., Zhang, L.-L. and Ming, Y.-Y., 2013. Experimental Study on the Properties and Displacement Effects of Polymer Surfactant Solution. *Journal of Chemistry,* 2013, pp. 1-6.

Weisman, J., Duncan, D., Gibson, J. and Grawford, T., 1979. Effects of fluid peoperies and pipe diameter on two-phase flow patterns in horizontal lines. *International Journal of Multiphase Flow*, 5, pp. 437-462.

Wereley, S. T., Gui, L. and Meinhart, C. D., 2002. Advanced algorithms for microscale particle image velocimetry. *AIAA Journal,* 40(6), pp. 1047-1055.

Westerweel, J., 1997. Fundamentals of digital particle image velocimetry. *Measurement Science and Technology,* 8, pp. 1379-1392.

Whitesides, G. M., 2006. The origins and future of microfluidics. *Nature*, 442, pp. 368-373.

Wilhelm, M. et al., 1991. Poly(styrene-ethylene oxide) Block Copolymer Micelle formation in water_a fluorescence probe study. *Macromolecules,* 24, p. 10331040.

Wilhelmy, L., 1864. Ueber die abhangigkeit der capillarita¨tsconstanten des alkohols von substanz und gestalt des benetzten fasten korpers.. *Ann. Phys. Chem.,* 4(29), pp. 177-217.

Woods, B. D. and Hanratty, T. J., 1996. Relation of slug stability to shedding rate. *International Journal of Multiphase Flow*, 22(5), pp. 809-28.

Xu, J., 1999. Experimental study on gas-liquid two-phase flow regimes in rectangular channels with mini gaps. *International Journal of Heat and Fluid Flow*, 20, pp. 422-428.

Xu, J., Cheng, P. and Zhao, T., 1999. Gas-liquid two-phase flow regimes in rectangular channels with mini/micro gaps. *Internatinoal Journal of Multiphase flow*, 25, pp. 411-432.

Yamada, M., Nakashima, M. and Seki, M., 2004. Pinched flow fractionation: continuous size seperation of particles utilizing a laminar flow profile in a piched microchannel. *Analytical Chemsitry* , 76(18), pp. 5465-5471.

Yih, C., 1967. Instability due to viscosity stratification. *Journal of Fluid Mechanics,* 27(2), pp. 337-352.

Yoshimura, T. et al., 2013. Equilibrium surface tension, dynamic surface tension, and micellization properties of lactobionamide-type sugar-based gemini surfactants. *Journal of Oleo Science,* 62(6), pp. 353-362.

Zhang, X., Jackson, J. K. and Burt , H. M., 1996. Determination of surfactant critical micelle concentration by a novel fluorescence depolarization technique. *Journal of Biochemical and Biophysical Methods,* 31, pp. 145-150.

Zuidema, H. H. and Waters, G. W., 1941. Ring Method for the Determination of Interfacial Tension. *Industrial and Engineering Chemistry,* 13(5), pp. 312-313

Appendix A Detailed calculations

Calculations near-semicircular channel

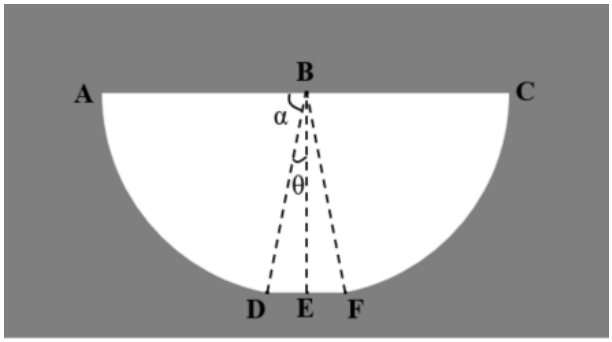

Figure A.1. Calculation of the cross-section area and perimeter of the near-semicircular channel.

All units of length for the calculation below are μm. Notation:

A, B, C, D, E, F are the points located at the intersection of lines.

l_{AB} : the straight distance between point A and B.

AD : the length of the arc from points A to B

$\triangle BDE$: The triangle with the vertex of pointe A, B and C.

A_{ABD}: The area of triangle or sector $\triangle ABD$

$\angle\alpha$: The degree of Angle α.

$$l_{DE} = \sqrt{l_{BD}{}^2 + l_{BE}{}^2} = \sqrt{102.5^2 + 100^2} = 22.5$$

$$\angle\theta = \sin^{-1}\frac{l_{DE}}{l_{BD}} = \sin^{-1}\frac{22.5}{102.5}$$

$$\angle\alpha = 90° - \angle\theta$$

$$A_2 = 2A_{ABD} + A_{BDF} = 2 \times \frac{\angle\alpha}{360} \times \pi \times 102.5^2 + 2 \times 22.5 \times 100 = 16420.81$$

$$P_2 = 2AD + l_{DE} + l_{AC} = 2 \times \frac{\angle\alpha}{360} \times \pi \times 2 \times 102.5 + 45 + 205 = 526.5$$

Calculations of the junction channel (wide channel).

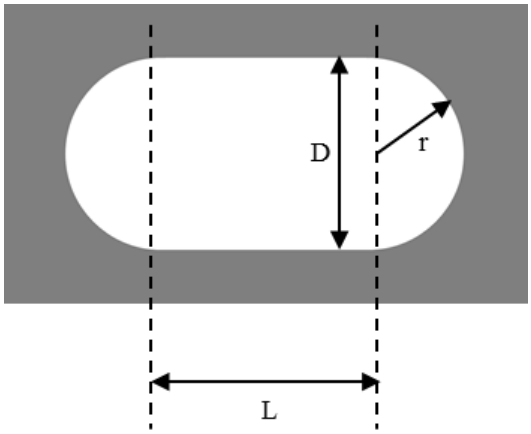

Figure A.2. Calculation of the cross-section area and perimeter of the wide channel part in the T-junction channel.

The cross-section consists of two semicircles, with 190 µm diameter, and a rectangular (size 190 × 200 µm), thus the cross-section:

$$A_c = 2 \times \left(\frac{\pi\, r^2}{2}\right) + L \times H = 2 \times \left(\frac{3.14 \times {}^{190}/_{2}{}^{2}}{2}\right) + 190 \times 200 = 66338.5\ \mu m^2$$

$$\mathrm{P} = \pi\mathrm{D} + 2 \times \mathrm{L} = 3.14 \times 190 + 2 \times 200 = 996.6\ \mu\mathrm{m}$$

Calculation of the perimeter and cross-section area of fluid 2 in junction wide channel, method 1.

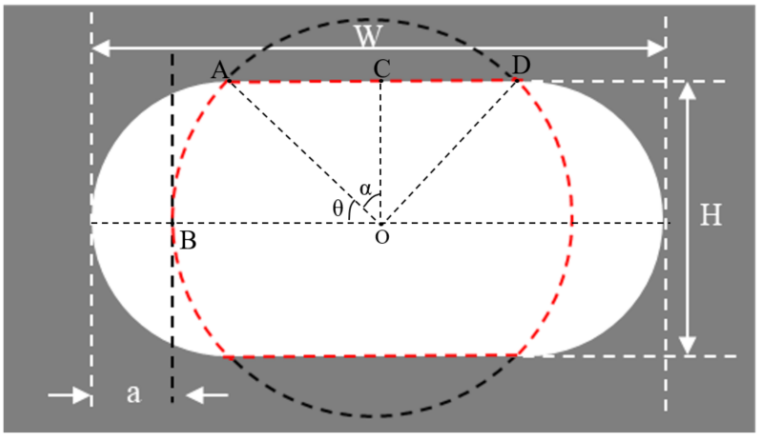

Figure A.3. Calculation of the cross-section area and perimeter of fluid 2 in junction channel (wide channel part) using method 1.

$$\angle\alpha = \tan^{-1}(\frac{l_{AC}}{l_{CO}}) = \tan^{-1}(\frac{100}{95})$$

$$\angle\theta = 90° - \angle\alpha$$

$$l_{AO} = \sqrt{{l_{AC}}^2 + {l_{CO}}^2} = 137.9$$

$$p_2 = 4AB + 2l_{AD} = 4\times\frac{\angle\theta}{360}\times\pi\times 2\times 137.9 + 2\times 200$$

$$A_2 = 4A_{ABO} + 2A_{ADO} = 4\times\frac{\angle\theta}{360}\times\pi\times 137.9^2 + 200\times 95$$

Calculation of the perimeter and cross-section area of fluid 2 in junction wide channel, method 2.

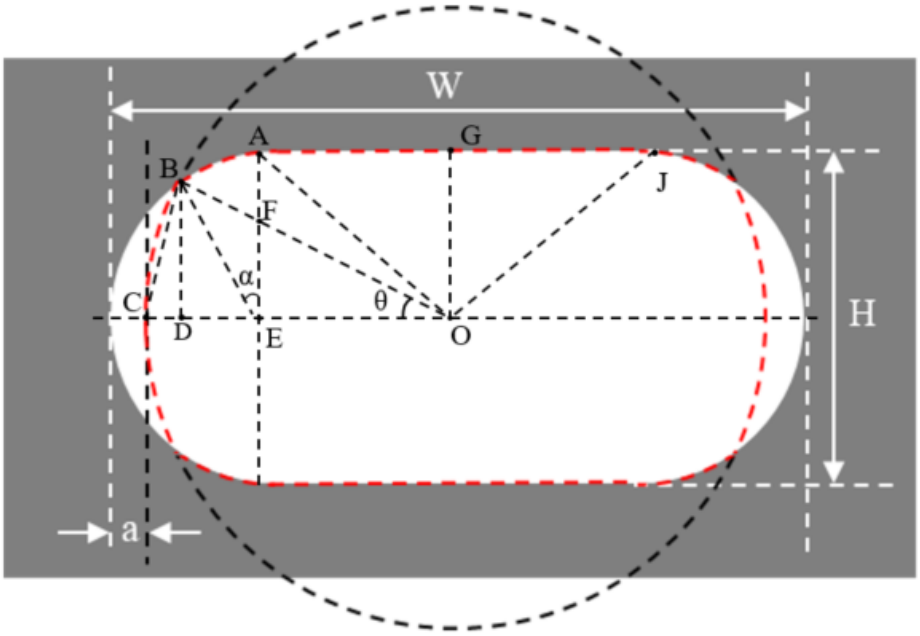

Figure A.4. Calculation of the cross-section area and perimeter of fluid 2 in junction channel (wide channel part) using method 2.

Several assisting lines are used to for calculation, illustrated in Figure A.4.

All units of length for the calculation below are μm. Notation:

A, B, C, D, E, F, O are the points located at the intersection of lines.

l_{AB} : the straight distance between point A and B.

AB : the length of the arc from points A to B

$\triangle ABC$: The triangle with the vertex of pointe A, B and C.

A_{ABO}: The area of triangle or sector $\triangle ABO$

$\angle\alpha$: The degree of Angle α.

The area of quadrangle ABCO is here approximated to be $A_{BCE}+A_{ABE}+A_{AEO}$ and the perimeter of fluid 2 is four times the length of $BC + AB + l_{AG}$.

$$l_{BD}^{\ 2} + l_{DE}^{\ 2} = l_{BE}^{\ 2}$$
$$l_{BD}^{\ 2} + (l_{DE} + l_{OE})^2 = l_{OB}^{\ 2}$$

From the dimensions of the channel: $l_{BE} = 95, \quad l_{OE} = 100, \quad l_{OB} = l_{OC} = 195 - a$, solve the two equations above we have: $l_{BD} = \sqrt{9097 - \frac{(100-a)(290-a)}{200}}$.

$$\angle\theta = \sin^{-1}(\frac{l_{BD}}{l_{OB}}) = \sin^{-1}(\sqrt{9097 - \frac{(100-a)(290-a)}{200}} / (195-a))$$

$$BC = \frac{\angle\theta}{360} \bullet (2\pi l_{OC}) = \frac{\sin^{-1}(\sqrt{9097 - \frac{(100-a)(290-a)}{200}} / (195-a))}{360} \bullet (2\pi \bullet (195-a))$$

$$A_{BCE} = 0.5(l_{CE} \bullet l_{BD}) = 0.5(100-a)(\sqrt{9097 - \frac{(100-a)(290-a)}{200}})$$

Some more assistant lines are created for $\triangle BEF$:

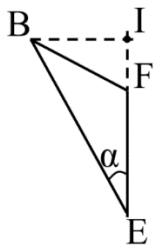

$$l_{BI}^{\ 2} + l_{IF}^{\ 2} = l_{BF}^{\ 2}$$
$$l_{BI}^{\ 2} + (l_{IF} + l_{FE})^2 = l_{BE}^{\ 2}$$

$l_{EF} = l_{OE} \times \tan\theta = 100\tan\theta$, $l_{BF} = l_{OB} - l_{OF} = 195 - a - 100\cos\theta$. Solving these two equations gives: $l_{IF} = (\frac{95^2 - l_{BF}{}^2}{l_{EF}} - l_{EF})/2$

$$\angle\alpha = \cos^{-1}(\frac{l_{IF} + l_{FE}}{l_{BE}}) = (\frac{(\frac{95^2 - l_{BF}{}^2}{l_{EF}} - l_{EF})/2 + 100\tan\theta}{95})$$

$$AB = \frac{\angle\alpha}{360} \times (2\pi l_{BE}) = \frac{\cos^{-1}(\frac{l_{IF} + l_{FE}}{l_{BE}}) = (\frac{(\frac{95^2 - l_{BF}{}^2}{l_{EF}} - l_{EF})/2 + 100\tan\theta}{95})}{360} \bullet (190\pi)$$

$$A_{ABE} = \frac{\angle\alpha}{360}(\pi l_{BE}{}^2) = \frac{\cos^{-1}(\frac{l_{IF} + l_{FE}}{l_{BE}}) = (\frac{(\frac{95^2 - l_{BF}{}^2}{l_{EF}} - l_{EF})/2 + 100\tan\theta}{95})}{360} \bullet (9025\pi)$$

$$A_{AEO} = 0.5 l_{AG} l_{OG} = 4750$$

$$\begin{aligned} A_2 &= 4 \times (A_{BCE} + A_{ABE} + A_{AEO}) + 2A_{AOJ} \\ &= 4(0.5(100 - a)(\sqrt{9097 - \frac{(100 - a)(290 - a)}{200}}) \end{aligned}$$

Therefore

$$\begin{aligned} &+ 4(\frac{\cos^{-1}(\frac{l_{IF} + l_{FE}}{l_{BE}}) = (\frac{(\frac{95^2 - l_{BF}{}^2}{l_{EF}} - l_{EF})/2 + 100\tan\theta}{95})}{360} \times (9025\pi)) \\ &+ 4 \times 4750 + 19000 \end{aligned}$$

$$P_2 = 4(BC + AB + l_{AG}) = 4 \times \frac{\sin^{-1}(\sqrt{9097 - \frac{(100 - a)(290 - a)}{200}} / (195 - a))}{360} \times (2\pi \times (195 - a))$$

$$\begin{aligned} &+ 4 \times \frac{\cos^{-1}(\frac{l_{IF} + l_{FE}}{l_{BE}}) = (\frac{(\frac{95^2 - l_{BF}{}^2}{l_{EF}} - l_{EF})/2 + 100\tan\theta}{95})}{360} \times (190\pi) \\ &+ 400 \end{aligned}$$

Appendix B Code used in the study (Matlab and UDF for Fluent)

Matlab code for image processing (identification of interface at a certain channel position)

```
%% set parameters here

folder='EXAMPLE';

VideoFileName='EXAMPLE.avi';

xposition=0.01; % 0~1, which cross section to use

iFrame0=14;  %1, first frame to process

NFrames=1000;  %0, how many frame to process, set to 0 for all frames

kSetWall=1;  % 1 or 0, whether to select wall in this run

fps=5000;  %frame rate

yA1=14;  %left wall position

yA2=114;  %right wall position

delta=20;  %1-20, a small number, trial

widthChannel=205;  % width of the channel in microns



%% read video file

videoObj = VideoReader([folder filesep VideoFileName]);

xpix=floor(xposition*videoObj.Height);
```

```
if(NFrames==0)
   NFrames=videoObj.NumberOfFrames;
end
IMxt=zeros(videoObj.Width,NFrames,'uint8');
for iFrame=iFrame0:NFrames+iFrame0-1
   IM=read(videoObj,iFrame);
   IMxt(:,iFrame-iFrame0+1)=IM(xpix,:);
   if(iFrame==iFrame0andandkSetWall==1)
      imshow(IM)
      title('Draw a line along the LEFT wall')
      xy1=getline;
      yA1=floor(mean(xy1(:,1)));
      title('Draw a line along the RIGHT wall')
      xy1=getline;
      yA2=floor(mean(xy1(:,1)));
      title('Ok, Wait ......')
   end

   if(mod(iFrame,50)==0)
       fprintf( [ num2str(iFrame) '/' num2str(NFrames) '\n']);
```

```
    end
end
scale=widthChannel/(yA2-yA1);
y1=yA1+delta;
y2=yA2-delta;

%% find fluid interface
xpos1=zeros(NFrames,1);
xpos2=zeros(NFrames,1);
xpos1wall=zeros(NFrames,1);
xpos2wall=zeros(NFrames,1);
size(IMxt)

for iFrame=1:NFrames
    y=smooth(double(IMxt(:,iFrame)));
    dy=diff(y);
    [~,xpos1(iFrame)]=max(dy(y1:y2));
    [~,xpos2(iFrame)]=min(dy(y1:y2));
    [~,xpos1wall(iFrame)]=min(dy(1:y1));
    [~,xpos2wall(iFrame)]=max(dy(y2:end));
```

```
end


%% post-processing and plot
xposRight=(xpos1+y1-0.5)*scale;
xposLeft=(xpos2+y1-0.5)*scale;
ywall1=mean(xpos1wall)*scale;
ywall2=mean(xpos2wall+y2-1)*scale;
t=(1:NFrames)/fps;
hold off


subplot(2,1,1)
imshow(IMxt)
hold on
plot(xposRight/scale,'r')
plot(xposLeft/scale,'b')
%legend('Right interface','Left interface','Location','East')
plot(xpos1wall*0+ywall1/scale)
plot(xpos2wall*0+ywall2/scale)


subplot(2,1,2)
```

```
hold on

plot(t,xposRight,'r') % plot of interface in micrometer

plot(t,xposLeft,'b')

legend('Right interface','Left interface','Location','East')

plot(t,xpos1wall*0+ywall1) %plot of wall

plot(t,xpos2wall*0+ywall2)

ylabel('Channel cross-section (\mum)')

xlabel('Time (s)')

axis([0 t(end)  0 ywall2*1.1])


result=[t' xposLeft xposRight xpos1wall*0+ywall1 xpos2wall*0+ywall2];

filename='EXAMPLE.xls';

xlswrite(filename,result)

% data format: time (s), left-interface (um), right-interface (um), left-wall1 (um), right-wall (um)
```

C Programme codes as UDF in Fluent to apply parabolic velocity profile at inlet.

```
#include "udf.h"

#define CHANNEL_DIAMETER 0.0002 // Set the diameter of channel in meters

#define AVG_Z_VELOCITY 0.5. // Set here the mean velocity at inlet in m/s

DEFINE_PROFILE(paraboloid_velocity, thread, position) { real x[ND_ND];
```

```
real coeff,r,v_max;

face_t f;

r = CHANNEL_DIAMETER/2.; //Calculating radius

v_max = 2.*AVG_Z_VELOCITY; //Calculating paraboloid vertex z (max velocity)

coeff = -v_max/pow(r,2.);

begin_f_loop(f, thread)

{

F_CENTROID(x,f,thread);

F_PROFILE(f, thread, position) = coeff*(pow(x[0],2.) + pow(x[1],2)) + v_max;

} end_f_loop(f, thread)

}
```